

Dislocation Interactions with  $(10\bar{1}2)$  Twin Boundary in Mg

---

A Dissertation

Presented to  
the faculty of the School of Engineering and Applied Science  
University of Virginia

---

in partial fulfillment  
of the requirements for the degree

Doctor of Philosophy

by

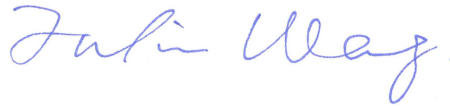
Fulin Wang

December

2017

APPROVAL SHEET

The dissertation  
is submitted in partial fulfillment of the requirements  
for the degree of  
Doctor of Philosophy



---

AUTHOR

The dissertation has been read and approved by the examining committee:

Sean R. Agnew

---

Advisor

James M. Howe

---

Jerrold A. Floro

---

Marek-Jerzy Pindera

---

Rodney J. McCabe

---

Accepted for the School of Engineering and Applied Science:



Craig H. Benson, Dean, School of Engineering and Applied Science

December  
2017



## ABSTRACT

$\{10\bar{1}2\}$  twinning is an important deformation mechanism of Mg alloys and, in fact, the most common twinning mode in all hexagonal metals. Under appropriate loading, these twins grow pervasively, consuming large volume fractions of the material while the migrating twin boundaries (TBs) undergo extensive interactions with dislocations. As such, the deformation behavior of the twins can dominate the subsequent stress-strain response of the polycrystalline aggregate. The present work focuses on investigating the interactions between basal dislocations within the surrounding matrix and  $(10\bar{1}2)$  TBs, with the ultimate aim of understanding the influences these interactions have on defects within the twin and on TB migration. The crystallography-based notion that 2 matrix dislocations with  $[a_1]_m$  or  $[a_3]_m$  Burgers vector can react to form a single dislocation with  $[c - a_2]_t$  or  $[c + a_2]_t$  Burgers vector within a  $(10\bar{1}2)$  twin and a residual twinning dislocation at the TB was confirmed, by *post-mortem* transmission electron microscopy (TEM) analyses. The twins are shown to contain abundant non-basal  $[c]$  and  $\langle c + a \rangle$  dislocations and basal  $I_1$  stacking faults (SF) in the vicinity of the TB.

To further elucidate the dislocations transformation process, *in situ* tension experiments were performed in a TEM. The impingement of gliding dislocations on a static, unloaded TB was observed to induce local twin growth, with profuse basal  $I_1$  SF in the wake of the advancing interface. In combination with molecular dynamics simulations, this evidence permitted the following unit process to be formulated. Each  $\langle a \rangle$  dislocation in the matrix transforms to a sessile partial dislocation, which is trailed by an  $I_1$  SF in the twin, with a residual dislocation left behind at the interface. As such, this individual reaction is a generalization of the classic Basinski mechanism, which was originally formulated for face centered cubic metals. The subsequent

transformation of a second  $\langle a \rangle$  dislocation can lead to termination of the SF. The net Burgers vector of the two sessile partial dislocations is  $\langle c + a \rangle$ , and the residual interfacial defects add to a unit twinning dislocation (disconnection). The observed twin growth was quantitatively evaluated and could be attributed completely to the dislocations transformation.

Finally, a formation mechanism for perfect  $\langle c + a \rangle$  dislocations was further proposed, with supporting evidence provided by additional *in situ* TEM results. TB migration is identified as a necessity and creates a thermodynamically favorable condition for the constriction of partial dislocations to form a single, perfect dislocation with large Burgers vector. The characteristic defects in the  $(10\bar{1}2)$  twins and the formation mechanisms reported in this study will contribute to the development of physically-based crystal plasticity models and the full field modeling of the twinning dominated mechanical response of hexagonal metals.

Keywords:

Hexagonal Crystal Structure; Dislocation; Twin Boundary; Stacking Fault; *In situ* TEM.

## ACKNOWLEDGEMENTS

I would firstly like to acknowledge the financial supports of the National Science Foundation (NSF) grant number CMMI 1235259 and the Army Research Laboratory under Cooperative Agreement Number W911NF-15-2-0025, which necessarily make this dissertation study possible.

I would like to most humbly and gratefully thank Professor Sean Agnew for advising me through the years of my PhD study and for supporting me to pursue various scientific opportunities. He guided me to learn and think as a researcher and as a person. His boundless energy and enthusiasm and positive mentality are contagious and encouraging. The critical thinking of “the big picture”, “what does it mean” and “who cares” helped me keep a clear mind. I am truly grateful for these valuable years, which certainly will benefit my career and life in the long run.

I would like to thank other committee members, Prof. Howe, Prof. Floro, Prof. Pindera and Dr. McCabe at Los Alamos National Laboratory (LANL), for their valuable time and input. I am especially grateful to Dr. McCabe, who granted me the opportunity to perform in situ straining experiments in TEM at LANL. His guidance on the operational details and even hands-on help are greatly appreciated.

I would like to thank the collaborators for their helpful input and many discussions. I am grateful for the time and effort of Dr. Laurent Capolungo and Dr. Christopher Barrett. Their intelligence and insights helped sharpen the theoretical understandings and broaden the vision of many aspects of the dissertation study.

Thanks to all the members of the Agnew group who have created a vibrant atmosphere. To Matt Steiner, Chris Calhoun, Jishnu Bhattacharyya and Md Shamsujjoha, the help from all of

you, and the stimulating discussions and chats with you have made every day of the graduate study easier and more enjoyable.

Lastly, I am grateful to my parents for raising me and supporting me to go on my own path. I would express my gratitude to my wife, Pei Cai, for her continuous support, encouragement and understanding.

# TABLE OF CONTENTS

<b>Abstract .....</b>	<b>i</b>
<b>Acknowledgements .....</b>	<b>iii</b>
<b>List of figures .....</b>	<b>ix</b>
<b>List of tables .....</b>	<b>xix</b>
<b>Chapter 1     Introduction.....</b>	<b>1</b>
1.1     Background and motivation .....	1
1.2     The $\{10\bar{1}2\}$ deformation twinning.....	7
1.3     Dislocation transformation at the $(10\bar{1}2)$ twin boundary.....	10
1.4     Specific research objectives.....	12
1.5     Layout of the dissertation .....	13
References .....	15
<b>Chapter 2     Dislocation-twin interactions in magnesium alloy AZ31 .....</b>	<b>19</b>
2.1     Introduction.....	19
2.2     Experimental methods.....	21
2.3     Results and discussion .....	23
2.3.1     TEM observations of dislocations.....	23
2.3.2     TEM observation of stacking faults associated with twins .....	32
2.4     Conclusions.....	34
References .....	35

<b>Chapter 3</b>	<b>Dislocation transmutation by tension twinning in magnesium alloy AZ31 .....</b>	<b>37</b>
<b>3.1</b>	<b>Introduction.....</b>	<b>37</b>
<b>3.2</b>	<b>Experimental procedures .....</b>	<b>39</b>
3.2.1	Sample preparation .....	39
3.2.2	Characterization .....	41
<b>3.3</b>	<b>Twinning relationship and dislocation transmutation reactions .....</b>	<b>42</b>
<b>3.4</b>	<b>Experimental results .....</b>	<b>44</b>
3.4.1	Dislocations near the $(10\bar{1}2)$ twin boundary from the perspective of ND.....	45
3.4.2	Dislocations near the $(10\bar{1}2)$ twin boundary from the perspective of TD.....	55
3.4.3	Defect structure inside the $(10\bar{1}2)$ twin .....	60
<b>3.5</b>	<b>Discussion .....</b>	<b>66</b>
3.5.1	The process of dislocation transmutation .....	67
3.5.2	The $\langle c \rangle$ dislocations and basal stacking faults inside twin.....	76
3.5.3	Effect of stress state on the $\langle c + a \rangle$ dislocations inside twin.....	79
<b>3.6</b>	<b>Conclusion .....</b>	<b>87</b>
	<b>References .....</b>	<b>88</b>
<b>Chapter 4</b>	<b>Characteristic dislocation substructure in <math>(10\bar{1}2)</math> twins in hexagonal metals .93</b>	
<b>4.1</b>	<b>Introduction.....</b>	<b>93</b>
<b>4.2</b>	<b>Experimental methods.....</b>	<b>95</b>
<b>4.3</b>	<b>Results .....</b>	<b>96</b>
<b>4.4</b>	<b>Discussions and conclusion .....</b>	<b>100</b>
	<b>References .....</b>	<b>104</b>

<b>Chapter 5</b>	<b>Dislocation induced twin growth and formation of basal stacking faults in</b>	
	<b>(10<math>\bar{1}2</math>) twins in pure Magnesium .....</b>	<b>106</b>
5.1	Introduction.....	106
5.2	Experimental methods.....	109
5.3	Molecular dynamics simulation.....	111
5.4	Experimental results .....	112
5.4.1	Local twin growth induced by dislocation impingement.....	112
5.4.2	Stacking faults in the wake of the advancing TB .....	118
5.5	MD simulations of the dislocation – TB interaction .....	122
5.6	Discussions .....	125
5.6.1	Defects analyses of the interfacial reaction .....	126
5.6.2	Slip-assisted twin growth model.....	130
5.6.3	Formation of interfacial facets .....	134
5.7	Conclusions.....	137
	References .....	138
<b>Chapter 6</b>	<b><math>\langle c + a \rangle</math> dislocation in (10<math>\bar{1}2</math>) twin: a kinematic requirement .....</b>	<b>141</b>
6.1	Introduction.....	141
6.2	Proposed procedures of the formation of $\langle c + a \rangle$ dislocations in twin .....	143
6.2.1	The sequential transformations of basal $\langle a \rangle$ dislocations .....	143
6.2.2	Formation of $\langle c + a \rangle$ dislocations from the advancing TB .....	147
6.3	<i>In situ</i> TEM observations of the $\langle c + a \rangle$ dislocations in twin.....	153
6.4	The evolution and morphology of the $I_1$ SFs in twin .....	160
6.5	Conclusions and outlook .....	163

<b>References .....</b>	<b>165</b>
<b>Chapter 7     Comprehensive summary and recommendations for future work.....</b>	<b>168</b>
<b>7.1     Motivations .....</b>	<b>168</b>
<b>7.2     Major conclusions .....</b>	<b>169</b>
<b>7.3     Significance of the work .....</b>	<b>171</b>
<b>7.4     Recommendations for future work .....</b>	<b>172</b>
7.4.1   Implementing the dislocation transformations in crystal plasticity (CP) models .....	173
7.4.2   Investigating the interactions of the defects in the twin.....	177
7.4.3   Investigating the critical dislocation configurations at the interface .....	178



## LIST OF FIGURES

Figure 1.1. Deformation modes in HCP crystals. The first row includes dislocation slip modes, and the second row twinning modes. Note that twinning is a polar mechanism, it is activated only in the positive direction of the twinning shear vector. 2

Figure 1.2. (a) Measured true stress - true strain curves typical of a rolled plate tested along normal direction (ND), transverse direction (TD) and rolling direction (RD) under tension (T) and compression (C) [8]. (b) Representative orientation image maps obtained by EBSD show the growing of twins (red) in the parent grains (blue), when an extruded Mg alloy AM30 is compressed into regimes I, II, and III [10]. Eventually the majority of the microstructure transformed to twins. 3

Figure 1.3. (a) Schematic illustration of a twinning dislocation (disconnection) that has a step  $h_p$  on the interface and a Burgers vector  $b_p$  connecting the vectors in the twin,  $t(t)$ , and matrix,  $t(m)$  [33]. (b) High resolution transmission electron microscope (TEM) observation of a twinning dislocation on the TB with a step [34]. (c) Lattice shearing (black open-headed arrow) and structure shuffling (blue full-headed arrow) in a  $(10\bar{1}2)$  twin, transforming the matrix lattice points (solid shapes) to twin lattice points (open shapes) [33]. 8

Figure 1.4. (a) High resolution TEM image showing a serrated  $\{10\bar{1}2\}$  TB in Co comprising segments of coherent twin boundary (CTB) and BP/PB facets [42]. (b) Schematics suggested by MD simulations demonstrating the ability of twinning dislocations ( $b_{2/2}$ ) to pass through the BP facets [29]. 10

Figure 2.1. Flow curves obtained for loading along the rolling direction under tension (RD-T) and compression (RD-C). Figure reproduced from [13]. 21

Figure 2.2. Orientation of the TEM disk in the compressed sample, the normal of the disk is parallel to the transvers direction (TD) of the rolled plate. 22

Figure 2.3. Straight  $\langle a \rangle$  type dislocations in the 0.5% sample. Dislocation bow-out around precipitates is indicated by short arrows in (c). The imaged area is close to a twin in the upper-right corner in (a, b and d). 24

Figure 2.4.  $\langle a \rangle$  type dislocations in the 0.5% sample. Plane traces are shown in (b). 25

Figure 2.5. Selected area diffraction pattern showing the matrix-twin orientation relationship ( $86^\circ$ ). The extension twinning plane is determined as  $(01\bar{1}2)$ . The close alignment of some diffraction vectors from twin and matrix is illustrated on the right. 26

Figure 2.6. Dislocation structure in the twin and the matrix in the 2.0% sample. The diffraction vectors are those from the matrix. The trace of the twinning plane is indicated in (a) by the dashed line. The dashed line box in (c) highlights the dislocations with  $[c]$  component in the matrix connected with the twin boundary. 28

Figure 2.7. WBDF images of dislocations in the twin by using two diffraction vectors. The dashed line box in (b) highlights the  $[c]$  containing dislocation in the matrix. 29

Figure 2.8. One area from Figure 2.7 to compare the visibility of dislocations in two diffraction conditions. The short arrows indicate the contrast from the same dislocation segment in both images. 31

Figure 2.9. Stacking faults emanating from twin boundary in an extension twin in the 0.5% sample. 32

Figure 2.10. Stacking faults at a twin boundary and twin boundary dislocations in the 0.5% sample. The dashed lines indicate the trace of basal plane. 33

Figure 3.1. (a) The flow curves of the rolled plate of AZ31, whose initial texture is shown in (b). RD-C denotes compression along the rolling direction, and RD-T denotes tension along the rolling direction. The flow curves and pole figures are reproduced from (Wu et al., 2010). (c) The disks for TEM characterization were machined from the TD and ND planes of the RD-C sample. 40

Figure 3.2. The  $180^\circ/\eta_1$  rotation relationship connecting the matrix and the twin is shown schematically in (a). (b) is a simulated diffraction pattern of the two lattices with  $[a_2]_{m,t}$  being the zone axis. The black dots represent the matrix spots, the red squares the twin spots. The reciprocal vectors  $(0002)$  and  $(10\bar{1}0)$  are drawn in the pattern for the matrix and the twin respectively. The real space twinning plane  $K_1$  is determined from the common diffraction spot.

43

Figure 3.3. Dislocations in the matrix and the twin adjacent to a  $(10\bar{1}2)$  twin boundary (TB) presented in DF images. Image (a) was obtained with the common diffraction vector for the matrix and the twin, the area highlighted by the dashed box outline is magnified for close inspection. The orientations of the two lattices are shown schematically in (b). Images (c) and (e) were obtained with two beam conditions for only the twin or the matrix, respectively. The selected dislocations are sketched schematically in (d). The dislocation segment AA' in (a), (c) and (d) is highlighted to guide the eye.

47

Figure 3.4. Two-beam DF images of dislocations in the matrix from the area shown in Figure 3.3. The corresponding diffraction vectors are under the images with arrows indicating the directions. Some dislocation segments are annotated by their Burgers vectors ( $a_1$ ,  $a_2$  or  $a_3$ ). The red arrows in (b) and (c) indicate the same dislocation segments which are invisible in (a).

49

Figure 3.5. Two-beam BF and DF images of the dislocations in the same region of the twin shown in Figure 3.3. The five diffraction vectors employed are shown below each column of BF and DF images. As explained in the text, the contrast reveals the AA' dislocation to be  $1/3[1\bar{2}13]$ , or  $[c - a_2]$ . The faint parallel fringes aligned diagonally from the upper left to lower right of the images in (d, e, i, j) are examples of the numerous basal faults within the twins.

51

Figure 3.6. Stereological analysis for dislocation line direction determination. (a) and (b) are images of the  $\langle c + a \rangle$  dislocations in the twin obtained at two-beam conditions from two zone axes. (c) presents the results from a trace analysis for dislocation segment i, conducted in the  $[10\bar{1}0]$  stereographic projection. The determined line directions for segment i, ii and iii are shown in the twin crystal lattice (d). The orientation of the lattice is consistent with Figure 3.3(b).

53

Figure 3.7. (a) A  $(10\bar{1}2)$  twin in a grain, whose grain boundary (GB) is delineated by black lines. The BF images were obtained with the same diffraction condition  $g_m = (10\bar{1}0)$  of the matrix from consecutive areas and were montaged. The dashed red line indicates the plane trace of the  $(10\bar{1}2)$  twinning plane. The area (b) was imaged with  $g_t = (0002)$ , in WBDF mode. The twin boundary is not only curved, it also has a serrated appearance. 56

Figure 3.8. Dislocations in the matrix (a), (b) and (c), and in the twin (e)-(g), (i)-(l) imaged with various diffraction vectors. All micrographs show the same area, and the red arrows in the images point at the same location to guide the eye. The orientations of the matrix and twin are shown schematically in (d), with only the basal and prismatic planes plotted for clarity. Selected features of the area are sketched in (h), where the curved lines represent dislocations and the double dashed lines represent SFs. 57

Figure 3.9. Defect structure inside the  $(10\bar{1}2)$  twin imaged with different diffraction vectors from two zone axes (indicated as beam direction  $B$ ). 60

Figure 3.10. (a) Two grains near the hole of the electropolished TEM foil, both including tension twins. The large image was obtained by secondary electron signals, and the images for the two grains were band contrast maps obtained by EBSD scan. (b) The IPF map of Grain 1, the lattice orientations of the matrix (G1) and the twin (T1) are shown below the map. (c) the IPF map of Grain 2, the lattice orientations of the matrix (G2) and the two twins (T2, T3) of the same variant are shown to the right of the map. The IPF map is color coded by the RD of the sample. 61

Figure 3.11. Defects inside T2 in Grain 2 from Figure 3.10(c). The twin was characterized with diffraction vectors (a)  $(10\bar{1}0)$ , (b)  $(0002)$  and (c)  $(11\bar{2}0)$  respectively. (c.1) highlights a dislocation feature from (c). In all the images, the basal plane is roughly horizontal. The red arrows point at the same locations in the twin at different imaging conditions to guide the eye. 64

Figure 3.12. Defects inside T3 in Grain 2 from Figure 3.10(c). The twin was characterized with diffraction vectors (a)  $(0002)$  and (b)  $(11\bar{2}0)$  respectively. (a.1) highlights a dislocation feature from (a). In all the images, the basal plane is roughly horizontal. The red arrows point at the same locations in the twin at different imaging conditions to guide the eye. 65

Figure 3.13. DF image obtained with  $g = (0004)_m$  showing basal stacking faults in a narrow  $(10\bar{1}2)$  twin. 66

Figure 3.14. The incorporation of one  $\langle a \rangle$  dislocation in the matrix and its transmutation to  $\frac{1}{2}\langle c + a \rangle_t$  at twin boundary. (a-d) depict the scenario of mobile dislocation in the matrix moving towards the stationary twin boundary. The dashed line indicates the basal plane trace in the matrix, which is approximately the prismatic plane trace in the twin. (e-h) depict the scenario of mobile twin boundary moving towards the stationary dislocation, realized by the glide of a twinning dislocation  $b_t$  on twinning plane. 68

Figure 3.15. (a) Dislocation lines and Burgers vectors in the matrix and the twin. (b)-(d) The incorporation and transmutation of the zeroth and first dislocations. The pile-up dislocations are depicted schematically in front of the twin boundary (TB). The wavy line in (d) indicates the fault created by the  $\frac{1}{2}\langle c + a \rangle_t$  dislocation. 73

Figure 3.16. The successive incorporation and transmutation of the first two basal dislocations from the matrix at twin boundary. The area filled by parallel red lines in (b) and (d) represents a stacking fault. Figure (d) presents the detailed configuration of dislocations junction as highlighted by dashed circle in (c). 75

Figure 3.17. A semi-looped  $\langle c + a \rangle$  with both ends on the twin boundary (TB). Part of the dislocation dissociates into  $\langle c \rangle$  and  $\langle a \rangle$  dislocations with length  $l$  and width  $w$ . 77

Figure 3.18. When compression load 100 MPa is applied along  $y_s$  to the two matrix orientations (a) and (e),  $(10\bar{1}2)[\bar{1}011]$  twinning is activated, the twinning plane and shear direction are projected onto the basal plane of each matrix crystal as indicated by the blue lines. The RSS on different systems are plotted as a function of twin aspect ratio  $q$  in (b, c, d) and (f, g, h) for the two orientations respectively. (b) and (f): RSS on the twin shear system due to the applied stress, internal stress and effective stress; (c) and (g): the magnitude of RSS on pyramidal  $\langle c + a \rangle$  slip systems due to the effective stress; (d) and (h): the magnitude of RSS on basal and prismatic  $\langle a \rangle$  slip systems due to the effective stress. 85

Figure 4.1. True stress – strain curve of pure Mg single crystal compressed along  $[10\bar{1}0]$  axis at room temperature. Schematics of the orientation and dimensions of the single crystal sample for compression test are shown in the inset. 96

Figure 4.2. Dislocation structure in a  $(10\bar{1}2)$  twin, within a pure Mg single crystal compressed along  $[10\bar{1}0]$  to 1.1% true strain. The images were taken at weak beam dark field (WBDF) condition with diffraction vectors of the twin crystal (a)  $g = (0002)_t$  and (b)  $g = (\bar{1}010)_t$ , whose directions are indicated by white arrows. (a) is at a lower magnification with the location of the TBs delineated by yellow lines. (b) is at higher magnification because the high dislocation density on the basal plane would otherwise obscure the image. 98

Figure 4.3. Another twin from pure Mg single crystal compressed along  $[10\bar{1}0]$  to 1.1% true strain. The WBDF images were taken with diffraction vectors of the twin crystal (a)  $g = (0002)_t$  and (b)  $g = (\bar{1}010)_t$ , whose directions are indicated by white arrows. The yellow arrows in (a) and (b) point to the same features at different sample tilt. 99

Figure 4.4. Dislocation substructure in  $(10\bar{1}2)$  twins in polycrystalline samples. (a) and (b) are in Mg alloy AZ31 compressed along rolling direction of a rolled plate [12, 25]. (c) and (d) are in pure Zr rolled plate undergone in-plane compression (IPC) [18]. 100

Figure 5.1. Orientations of the matrix and the two twin variants in the single crystal tensile specimen. During the *in situ* straining, the tension strain is applied in the vertical direction, which is also the axis of sample tilting, and the electron beam is perpendicular to the plane of the paper. (a) is the projected hexagonal lattices of the crystals. (b) is the stereographic projection of important plane poles and directions of the matrix and twins. The solid lines indicate the trace of basal planes, and the dash lines indicate the trace of  $(10\bar{1}0)$  prismatic planes. 110

Figure 5.2. Captured image sequence showing the local twin growth in two regions along the same TB, (a-c) and (d-f) respectively. The twin is the lower crystal in the images and the matrix the upper crystal. The dashed boxes in (b) and (e) highlight the regions of interest. (g) and (h) are difference images between (a), (b) and (c) for region I, and (i) and (j) are those between (d), (e) and (f) for region II. Schematics of the TB advancement are shown below. 113

Figure 5.3. Static images of a TB (a) before and (b) after the tensile loading in the vertical direction. The yellow arrows point to the same features in the two images, which conveniently function as fiducial markers. (c) is the WBDF image with  $g = 0002_t$  focusing on the grown region of the twin in (b). The position of the original flat TB is denoted by arrows outside the image frames. The diffraction patterns are obtained at state (b) from different regions: (d) the matrix – m, (e) matrix and the grown region – t', (f) matrix, the grown region and the original twin – t, and (g) the original twin. The circles in (e) highlight the coincident diffraction spots of matrix and the grown region. The red and green arrows point to the spots of the grown region and the original twin respectively.

115

Figure 5.4. Snapshots of the same twin (a) before and (b) after the impingement of localized basal dislocations from the matrix. (c) and (d) are the difference images of two areas along the TB, with the dashed line indicating the initial position of the TB and solid line the final position.

117

Figure 5.5. Defects inside the wedge-shaped twin extrusion from the twin in Figure 5.4. (a) and (b) are two-beam BF and WBDF images respectively using the diffraction vector  $g = 0002_t$  and  $g = 10\bar{1}0_t$ . (c) is a magnified view of (b), highlighting the fringe contrast of faults. The traces of the straight segments of the twin interface are shown by yellow lines aside the interface.

118

Figure 5.6. Montaged WBDF images at  $g = 0002_t$  two-beam condition showing the TB and defects inside twin after tensile straining of the twin in the vertical direction. The lower crystal in the images is the twin.

119

Figure 5.7. WBDF images of basal stacking faults in the wake of an advanced TB. The respective diffraction vectors  $g$  are (a)  $(000\bar{2})$ , (b)  $(10\bar{1}0)$ , (c)  $(10\bar{1}\bar{1})$  and (d)  $(10\bar{1}1)$ . (a-d) are montaged images of the same area with the arrows pointing to the same features. Selected SFs are presented in magnified views at the latter three diffraction conditions: (b1, c1 & d1) focus on SFs 1 and 4, and (b2, c2 & d2) focus on SFs 5 and 6.

120

Figure 5.8. Time-resolved sequences of dislocation interaction with TB by MD simulation. The  $(10\bar{1}2)$  TB is horizontal in the images with the matrix above and the twin below. The atoms are colored based on the component of the normalized local  $c$ -axis along the vertical direction of the

simulation box (the basal plane vector method [28]). The positions of the dislocations are indicated. The results shown correspond to a temperature of 50K, which, owing to minimal thermal fluctuation, facilitated the identification and analysis of defects structures. 125

Figure 5.9. Trichromatic pattern of the matrix ( $\mu$ ), the twin ( $\lambda$ ) and the third ( $\kappa$ ) lattices projected along the co-zone axis  $[a_2]$ . The horizontal black lines indicate the CTB, and the inclined blue lines the coherent plane between the  $\lambda$  and  $\kappa$  lattices. The dissociation of the matrix  $[a_3]$  dislocation is shown in (a). (b) and (c) show the total resultant Burgers vector in the twin crystal ( $[c + a_2]$ ) and the interface ( $b_{2/2}$ ) respectively after the transformation of two matrix dislocations. (d) is the schematic of the three lattices and their orientation relationships with respect to the twinning plane  $K_1$  and conjugate plane  $K_2$ . 128

Figure 5.10. The outline of the twin interface extracted from Figure 5.3(b). The length scale and the inclination of plane traces and vectors reflect the original experimental image. The parallel dashed lines represent the coherent  $(10\bar{1}2)$  twinning planes, with the twinning dislocation  $b_t$  and the step height  $h$  drawn schematically. 131

Figure 5.11. (a) and (b) show schematically the slip direction of opposite basal dislocations in the matrix with respect to the two twinning systems. (c) and (d) are the corresponding interface structure extracted from Figure 5.4, Figure 5.6 and Figure 5.3 after the dislocation-twin interaction. Note for the purpose of comparison, (c) is rotated from (a) such that the twinning shear direction ( $\eta_1$ ) is aligned with that in (d). 135

Figure 6.1. Proposed procedures of the incorporation of matrix dislocations by a moving TB and the evolution of defects in twin. The matrix crystal is in the front left in the perspective view, and the twin crystal in the back right. The basal plane in the matrix (green) and that in twin (orange) are at an angle of  $86^\circ$ , with the bisecting TB (blue) in between. The TB is depicted as a flat plane, ignoring the nanoscale interfacial steps. The step created by  $b_t$  is exaggerated in (c) and (d) to illustrate the jog of the matrix dislocation. Dislocations with different Burgers vectors are represented by different colors as indicated in the insets. 145



Figure 6.2. Extension of the fault with further TB advancement based on the scenario of Figure 6.1(g). (b) and (d) are two alternatives after (a). (c) and (e) are alternatives after (b). (b1) and (d1) depict the local dislocation configurations around the junction at TB in (b) and (d) respectively.

148

Figure 6.3. Extension of the fault with further TB advancement based on the scenario of Figure 6.1(h). (b) and (c) are two alternatives as TB advances. (b1) and (c1) presents the detailed dislocation lines and Burgers vectors connected to the nodes at TB in (b) and (c) respectively.

149

Figure 6.4. The dislocations configurations representing the two alternatives of (a) extension and (b) constriction. (c) is the total energy of the systems at various lengths of H and L. (d) is the projection of the energy surfaces, showing the intersection line in two-dimensions. The lengths are in the unit of lattice parameter  $a = 0.321$  nm.

153

Figure 6.5. Homogeneous TB migration and the evolution of defects in twin under a tension in the vertical direction. The twin is roughly horizontal in the middle of the images, with the matrix above and below it. The black arrows outside the frames in (b) and (c) indicate the position of TB at previous times. The yellow arrows point to the same dislocations that are extended by the boundary through (b) to (c).

155

Figure 6.6. Evolution of the dislocations in twin in the wake of the advancing TB. The images are rotated from Figure 6.5 such that the basal plane in twin is horizontal and that in matrix is almost vertical. (a-d) are taken at increasing times. (e) is the difference image of (c) and (b), with the white features represent those in (b) and dark features those in (c). The dislocation lines are extracted in (f) showing the original dislocations (dashed lines) and new dislocations (solid lines).

157

Figure 6.7. Collective slip activity of the  $[c]$  and  $\langle c + a \rangle$  dislocations on non-basal planes in twin. (a-d) are the initial dislocation structure in four different regions, and (e-h) are the respective final structure after being strained by the tension in the vertical direction for 500s. The difference images reveal the direction and distance of the dislocation movements, with the white representing the initial dislocations and the black the final dislocations. The directions of the

dislocation movements are indicated by red arrows. (a) and (e) are montaged images and therefore possess vertical stripes of different brightness. 159

Figure 6.8. The pinch-off of the  $\langle c + a \rangle$  dislocation dipole and the subsequent dissociation of the segments on basal plane. The partial dislocations  $p_1$  and  $p_2$  enclose an  $I_1$  fault on basal plane. The dislocation line directions are indicated by the arrows along the line. 161

Figure 6.9. WBDF image of basal  $I_1$  SFs inside a twin after extensive dislocation-TB interactions, as evidenced by the curvature of the TB. The diffraction condition is  $g = (10\bar{1}\bar{1})_t$ . The twin is the lower crystal in the image, the matrix is the upper one but does not exhibit diffraction contrast. 163

Figure 7.1. Schematic illustration of the dislocation density in the matrix ( $\rho_M$ ) and in the growing twin ( $\rho_T$ ). The twin grows by the lateral migration of both TBs from the time  $t_0$  to  $t_1$  and to  $t_2$ . Different regions of the twin have different dislocation densities resulting from the dislocation transformation mechanism. 175

Figure 7.2. Geometry of the incorporation of two basal dislocations at TB. 179

Figure 7.3. Possible geometric variables for the energetic evaluation of the two competing scenarios. 180

## LIST OF TABLES

Table 2.1. Diffraction conditions for TEM analysis. The three zone axes (ZA) are 30° apart along the (0002) Kikuchi band. The diffraction vectors are grouped by their respective ZAs, and (0002) is available at all ZAs. 23

Table 2.2. Schmid factors ( $m$ ) for possible dislocation types. The loading direction is taken as [0001]. And the absolute values of  $m$  are taken. 31

Table 3.1. Dislocation reactions across a  $(10\bar{1}2)$  twin boundary, the twinning relation is described by 180° rotation about the twinning direction,  $\eta_1$ .  $b_t = \frac{3-\gamma^2}{3+\gamma^2}\langle\bar{1}011\rangle = 0.0643\langle\bar{1}011\rangle$  (Serra, Bacon and Pond, 1988), with  $\gamma = 1.624$  for Mg. The subscripts  $m$  and  $t$  denote the matrix and the twin respectively. 44

Table 3.2. The  $g \cdot b$  values of  $\langle a \rangle$  dislocations with selected diffraction vectors from the zone axis of [0001]. The corresponding figures (a), (b) and (c) in Figure 3.4 for each  $g$  vector are indicated. 48

Table 3.3. The  $g \cdot b$  values of  $\langle c + a \rangle$  dislocations with selected diffraction vectors from the zone axes of  $[10\bar{1}0]$  and  $[11\bar{2}0]$ . The visibility of the dislocations in Figure 3.5 at each  $g$  vector is indicated in the last row. 50

Table 3.4. The  $g \cdot b$  values of  $\langle a \rangle$  dislocations in the matrix and  $\langle c \rangle$  containing dislocations in the twin with selected diffraction vectors. The corresponding image numbers in Figure 3.8 for each  $g$  vector are indicated. 58

Table 5.1. The  $g \cdot b$  values of the partial dislocations of  $I_1$  stacking fault at the four two-beam conditions. The Burgers vectors of the partial dislocations are arranged in dissociated pairs of perfect  $\langle c + a \rangle$  dislocations. The  $g \cdot b$  values smaller or equal to  $1/3$  are underlined. 121

Table 7.1. Dislocation transformation reactions for all the  $\{10\bar{1}2\}$  twin variants. The twinning dislocation  $b_t$  is the corresponding positive twinning shear vector of each twin variant. 174

## CHAPTER 1 INTRODUCTION

### 1.1 Background and motivation

Magnesium based light alloys have long been attractive as potential structural materials for the interest of weight reduction in components, especially in automotive industry where energy efficiency and decrease of greenhouse gas emission are desired [1, 2]. However, the application of wrought magnesium alloys remains minor compared to metallic counterparts such as steel and aluminum, largely due to the poor formability at ambient temperatures, strong texture developed during processing and hence poor mechanical behavior of the product.

Magnesium has a hexagonal close-packed (HCP) crystal structure. The available deformation modes include  $\langle a \rangle$  dislocation slip on basal plane, prismatic plane and pyramidal plane,  $\langle c + a \rangle$  dislocation slip on pyramidal plane,  $\{10\bar{1}2\}\{10\bar{1}1\}$  tension twinning and  $\{10\bar{1}1\}\{10\bar{1}2\}$  compression twinning (Figure 1.1). Deformation at room temperature is dominated by basal  $\langle a \rangle$  slip and  $\{10\bar{1}2\}\{10\bar{1}1\}$  tension twinning due to their much lower critical resolved shear stress (CRSS) values (e.g. [3]). The former provides only two independent slip systems, accommodating strain along  $\langle a \rangle$  directions of crystal. The latter provides extension strain in the  $[c]$  direction of the matrix crystal and in the meantime abruptly reorients the lattice,

that the  $c$ -axis of the twin is at an angle of  $86^\circ$  to that of the matrix. As a result, strong basal texture is developed in rolled sheet products or extruded bars [4, 5], where the basal plane is parallel to the rolling plane or the extrusion direction (ED).

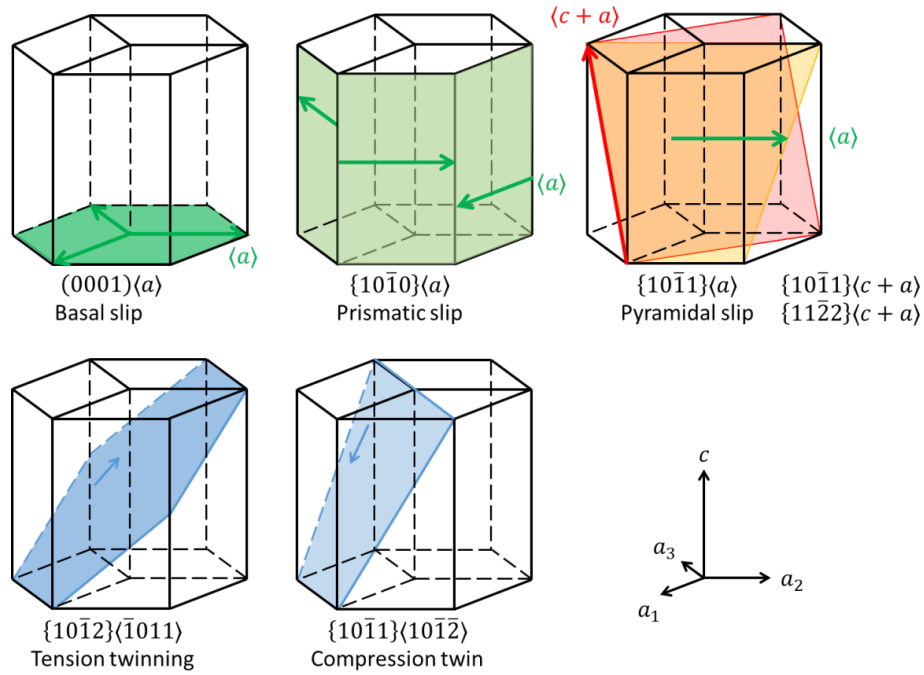


Figure 1.1. Deformation modes in HCP crystals. The first row includes dislocation slip modes, and the second row twinning modes. Note that twinning is a polar mechanism, it is activated only in the positive direction of the twinning shear vector.

The textured materials generally exhibit strength anisotropy, e.g. the stress-strain curve of compression along the normal direction (ND) as compared to that of compression along the rolling direction (RD) in Figure 1.2, and tension-compression asymmetry, e.g. the stress-strain curves of tension and compression respectively along the same direction RD. Due to the polar nature of deformation twinning, namely twinning can only be generated by stress in the twinning shear direction, the activity of twinning can be maximized or minimized by just inverting the

sign of the stress or by changing the strain direction. In a rolled material, for instance, in-plane tension (IPT) RD-T and through-thickness compression (TTC) ND-C minimize twinning activity, in-plane compression (IPC) RD-C or TD-C tends to maximize twinning activity. The stress-strain curves obtained from IPT or TTC exhibit the dislocation slip dominated flow behavior (Figure 1.2). Plasticity commences at a high initial hardening rate and decreases monotonically. The high yield stress and initial slope associated with IPT and TTC are attributed to the hard primary slip mode prismatic  $\langle a \rangle$  and pyramidal  $\langle c + a \rangle$  respectively (see e.g. [3, 6-9]).

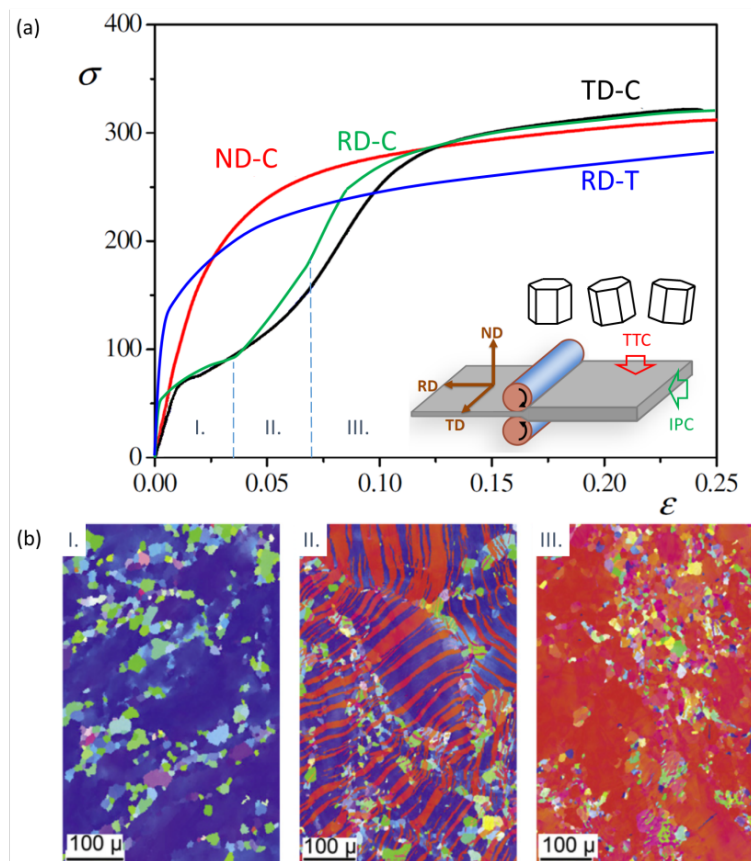


Figure 1.2. (a) Measured true stress - true strain curves typical of a rolled plate tested along normal direction (ND), transverse direction (TD) and rolling direction (RD) under tension (T) and compression (C) [8]. (b) Representative orientation image maps obtained by EBSD show the growing of twins (red) in the parent grains (blue), when an extruded Mg alloy AM30 is

compressed into regimes I, II, and III [10]. Eventually the majority of the microstructure transformed to twins.

In-plane compression (IPC) along RD/TD of rolled material or ED of extruded material induces a drastically different flow curve with sigmoidal shape. The straining is essentially compression perpendicular to the  $c$ -axis of most crystals. The easy slip mode basal  $\langle a \rangle$  has very low Schmid factor, and the CRSS of non-basal  $\langle a \rangle$  and pyramidal  $\langle c + a \rangle$  slip modes are not reached yet although they have higher Schmid factor, so  $\{10\bar{1}2\}$  tension twinning is activated as early as  $\sim 0.3\%$  plastic strain [11, 12], providing tension strain along the  $c$ -axis of matrix crystal and in the meantime rotating the twinned crystal such that its  $c$ -axis is close to the compression axis. The initial massive activation of twinning, i.e. the twin dominated compression, is characterized by a plateau of low hardening rate and termed regime I (Figure 1.2). Tension twins often grow very quickly and consume a large fraction of the matrix grains. For example, in a rolled Mg alloy AZ31 [11], up to  $\sim 6\%$  strain, twins occupy 80% volume fraction of polycrystals (e.g. the microstructure evolution in Figure 1.2(b) of an extruded Mg alloy AM30 when compressed along ED). When twinning starts to cease activity gradually in the polycrystals, the stress increases sharply [13], defined as regime II in the flow curve. Strain hardening slows as slip-based deformation commences inside twins (regime III). Note that the  $c$ -axes of twins are closely aligned with the compression axis, it is a similar loading orientation as in ND compression. Although of decreasing volume fraction, the untwinned matrix crystals are always subject to compression parallel to the basal plane, necessitating non-basal  $\langle a \rangle$  and pyramidal  $\langle c + a \rangle$  slip modes. While the majority of the crystals are subject to  $c$ -axis compression, as seen in the flow curves, the flow stress at large strains of RD-C is consistently higher than that of ND-C. Apparently, additional hardening arising from twinning is responsible for the elevated stress.

The contribution of generic deformation twinning to strain hardening has been attributed to three main mechanisms:

- A Hall-Petch effect due to the division of the grains by twin boundaries [14-18].

In Mg alloys undergoing profuse  $\{10\bar{1}2\}$  twinning, hardening through a Hall-Petch effect has been proven to be insignificant [9, 17, 19, 20]. As mentioned earlier, tension twins may eventually occupy ~80% volume fraction of polycrystals (see also the microstructure representative of regime III in Figure 1.2(b)), and some grains appear to be reoriented in their entirety they are hence not considered very effective in refining the grain size.

- Change of crystal to a hard or soft orientation.

In Mg and its alloys, the rapid strain hardening can be largely explained by the hard orientation of twins with respect to the loading axis. The sharp rise in stress in regime II of the flow curve coincides with the exhaustion of twinning. The twin crystals are subject to compression strain almost along  $c$ -axis, necessitating the operation of pyramidal  $\langle c + a \rangle$  slip systems whose CRSS has not been achieved. Lacking active deformation modes to accommodate the imposed strain, the twin crystals deform almost elastically, leading to a high strain hardening rate of the polycrystals, e.g. see the comprehensive study in [21]. In fact, pyramidal  $\langle c + a \rangle$  slip within the twins is predicted once twinning is activated according to plasticity modeling, e.g. [22], which may therefore mitigate the rigid response of the twins.

- The so-called Basinski mechanism originally developed in FCC metals that pre-existing glissile dislocations are transformed to sessile ones when the region is twinned [16, 18, 23].

It was argued [19] that since tension twins appear early in the deformation process before accumulation of significant dislocation densities in the matrix, the Basinski mechanism



may not contribute significantly to strain hardening as it does in FCC metals where twinning is activated late in deformation. El Kadiri and Oppedal [9] introduced the hardening effect of dislocation “transmutation” upon their incorporation in the twinned regions, and demonstrated the efficacy in crystal plasticity models by artificially changing the dislocation densities inside twin.

Upon the previous research endeavors, there is an urgent demand for the knowledge of the lower length scale defects structure in the  $\{10\bar{1}2\}$  twin crystals. The most pertinent question is: what types of dislocations do the  $\{10\bar{1}2\}$  twins possess? Considering the pervasive migration of the twin boundaries (TB), the dislocation-TB interaction is identified as an essential and fundamental interaction of crystal defects occurring during deformation. Such interactions would occur when a twin is nucleated in a grain and enlarges its volume by TB propagation into a region containing pre-existing dislocation, as well as when dislocations in the matrix glide toward and eventually be incorporated by a TB. Additionally, two seminal studies have proposed the twin growth mechanisms as a result of the incorporation of slip dislocations: the first by Yoo and Wei in 1966 [24] via crystallography based vector transformations, and the second by Serra and Bacon in 1996 [25] via molecular dynamics simulations. There has been progress in the understanding of deformation twinning, albeit being a fundamental mechanism, that the lateral thickening of twins (twin growth) is carried out by the gliding of twinning dislocations [26, 27] or twinning disconnections [28] on the twinning plane. In this context, the contribution of the gliding dislocations in the matrix to the generation of the twinning dislocations remains to be examined experimentally.

## 1.2 The $\{10\bar{1}2\}$ deformation twinning

Deformation twinning is an important mechanism in hexagonal structured metals, because of its ability to accommodate the strain along the  $[c]$  axis of the crystal. Among all the twinning systems, the relatively low shear of the  $\{10\bar{1}2\}$  mode and high mobility of the twin boundary make it the most frequently observed (e.g. [29]). For metals whose  $c/a$  ratio is smaller than  $\sqrt{3}$ , such as Mg, Ti, Zr and Be,  $\{10\bar{1}2\}$  twinning results in extension along the  $c$  axis, it is therefore commonly termed as extension, tension or tensile twinning [30].

The operation of twinning includes twin nucleation, driven by the local stress at grain boundaries, as well as forward twin propagation and lateral twin thickening, via the gliding of twinning dislocations on the twinning plane driven by long range stress across grains [31, 32]. Twinning dislocation (TD) is an interfacial line defect with both dislocation and step character ( $\mathbf{b}, h$ ). It is also termed as twinning disconnection since it connects two incompatible step vectors in either lattice across the interface (Figure 1.3 (a, b)). In Mg, the Burgers vector of a TD is  $0.0643\langle\bar{1}011\rangle$  [27], parallel to the twinning shear direction, and the step height is  $2d_{\{10\bar{1}2\}}$ , perpendicular to the twinning plane. The gliding of a TD therefore produces a characteristic shear strain of  $s = |\mathbf{b}|/h = 0.049 \text{ nm}/0.380 \text{ nm} = 0.13$ . Because of the step nature of a TD, the TB migrates along the TB normal direction by a height of  $h = 2d_{\{10\bar{1}2\}}$  via the gliding of each TD. The successive gliding of TDs on the twinning plane shears the matrix lattice points by vectors parallel to TD and magnitudes proportional to the distance from the interface. The sheared lattice points undergo further structure shuffles to reach the corresponding twin lattice points (Figure 1.3 (c)). Eventually, the shear strain accommodated by twinning is directly proportional to the volume fraction ( $f$ ) of the crystal that has twinned  $\gamma = f \cdot s$ .

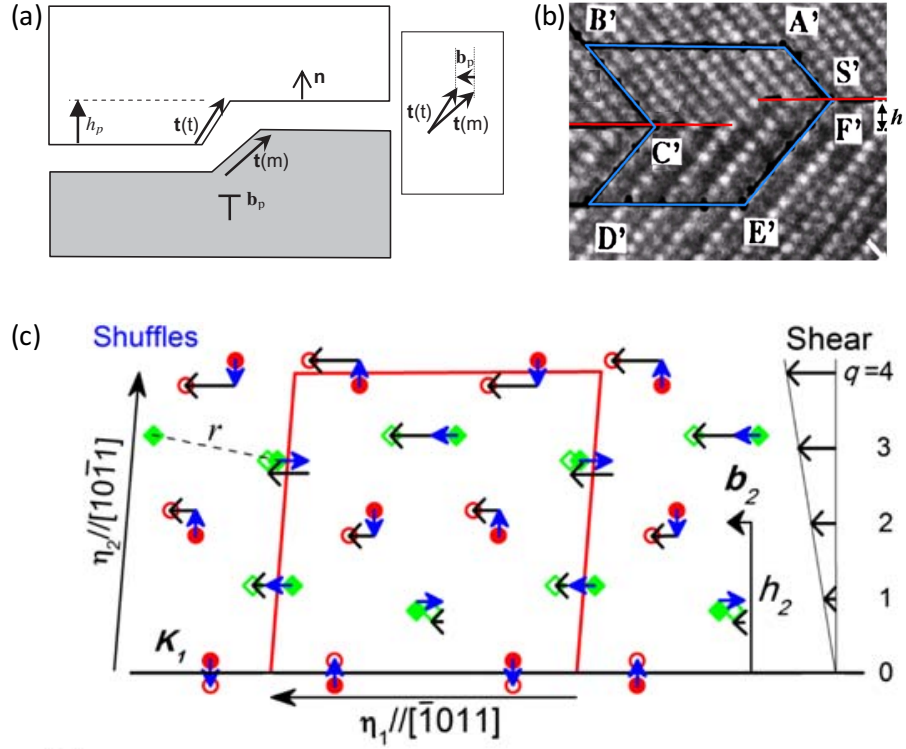


Figure 1.3. (a) Schematic illustration of a twinning dislocation (disconnection) that has a step  $h_p$  on the interface and a Burgers vector  $b_p$  connecting the vectors in the twin,  $t(t)$ , and matrix,  $t(m)$  [33]. (b) High resolution transmission electron microscope (TEM) observation of a twinning dislocation on the TB with a step [34]. (c) Lattice shearing (black open-headed arrow) and structure shuffling (blue full-headed arrow) in a  $(10\bar{1}2)$  twin, transforming the matrix lattice points (solid shapes) to twin lattice points (open shapes) [33].

The generation and gliding of twinning dislocations, and hence the twin growth process, have been shown to be a process independent of dislocation slip occurring in the surrounding crystal [22, 35]. On the other hand, it was proposed based on crystallographic transformation [24] and molecular dynamics (MD) simulations [25] that the incorporation of  $\langle a \rangle$  slip dislocations at the  $\{10\bar{1}2\}$  TB can generate TDs and cause TB migration. The former predicted that two  $\langle a \rangle$  dislocations would transform to a corresponding vector in the twin lattice while leaving behind one residual TD on the interface. The latter reported complete absorption of one  $\langle a \rangle$  dislocation

at the interface, which then decompose into interfacial steps and several TDs. Many studies have been conducted since then using MD simulations to study the incorporation of matrix dislocations at TB, with a focus on the resulting interfacial defects and aiming at understanding their effect on TB migration [29, 33, 36, 37]. However, the experimental evidence is lacking to quantitatively correlate the generation of TDs to boundary migration and support the mechanism of slip assisted twin growth.

Whereas the planar glide of TDs on coherent twin boundary (CTB) results in TB migration, TDs have to pass various interfacial facets on a serrated TB. It is well-accepted that the  $\{10\bar{1}2\}$  TBs migrate briskly and invasively into the matrix crystal, despite the fact that the boundaries deviate from the CTB, as evidenced by the commonly observed curved TBs on microscale in Figure 1.2 (b). High resolution TEM characterizations performed in Mg, Ti and Co [38-40] have resolved the interface structure at lower length scale and revealed that the interface consists (1) terraces of CTB, (2) facets close to the basal plane in the matrix or the prismatic plane in the twin (BP) and (3) those close to the prismatic plane in the matrix or the basal plane in the twin (PB) (Figure 1.4 (a)). MD simulations informed that the nanoscale BP/PB facets are formed by the relaxation of a pile-up of TDs that accumulate locally [29]. When a gliding TD on the CTB merges onto a BP/PB facet at one end, the facet tends to maintain a stable length by emitting a TD at the other end, whose continuous glide further induces boundary migration (Figure 1.4 (b)). This mechanism was believed to be responsible for the high growth rate of the  $\{10\bar{1}2\}$  twinning mode. When the BP/PB facets are extended beyond the stable length, however, misfit dislocations need to be formed at both ends of the facet to compensate the lattice misregistry [41], which may impede the passage of the twinning dislocations. Due to the small scale of the pertinent defects, this topic has been investigated primarily by MD simulations aided

by structural evidence obtained from HRTEM. In the current dissertation, the formation of TDs as a result of dislocation interactions with TB and its effect on TB morphology and migration are studied based on diffraction contrast TEM observations. Detailed investigations and discussions are included in Chapter 3 and Chapter 5.

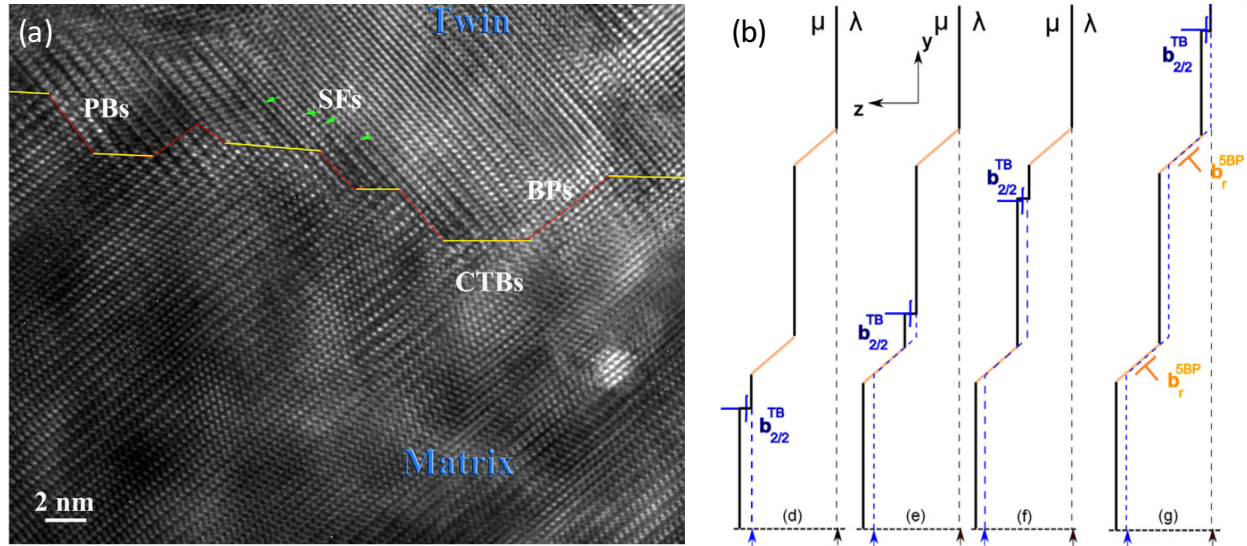


Figure 1.4. (a) High resolution TEM image showing a serrated  $\{10\bar{1}2\}$  TB in Co comprising segments of coherent twin boundary (CTB) and BP/PB facets [42]. (b) Schematics suggested by MD simulations demonstrating the ability of twinning dislocations ( $b_{2/2}$ ) to pass through the BP facets [29].

### 1.3 Dislocation transformation at the $\{10\bar{1}2\}$ twin boundary

The transformation of dislocations at twin boundary is often termed as the Basinski mechanism [23], which originally revealed a glissile to sessile transformation of dislocations upon incorporation by twins in face-centered cubic metals. In Mg, the primary slip dislocations are the basal  $\langle a \rangle$  dislocations. The crystallographic transformations of  $\langle a \rangle$  dislocations at the  $(10\bar{1}2)$  twin interface was firstly derived by Yoo and Wei for the hexagonal metal zinc in 1966

[24]. With respect to a  $(10\bar{1}2)$  twinning plane, the  $\langle a \rangle$  dislocations fall into two categories: (1) the  $1/3[\bar{1}2\bar{1}0]$  Burgers vector,  $[a_2]$ , is the co-zone axis of the matrix and the twin and is hence parallel to the interface, and (2) the  $1/3[2\bar{1}\bar{1}0]$  and  $1/3[\bar{1}\bar{1}20]$  Burgers vectors,  $[a_1]$  and  $[a_3]$ , are at  $60^\circ$  to the intersection line of the basal slip plane and twinning plane. When transformed from the matrix to the twin, the  $[a_2]$  Burgers vector is unchanged, leaving no residual defect at the interface and therefore not causing the twin boundary motion, whereas the  $[a_1]$  or  $[a_3]$  Burgers vector corresponds to a  $1/2[c \pm a_2]$  vector in the twin with a difference vector in the twinning shear direction. The latter transformation further poses the possibility that a unit  $\langle c + a \rangle$  dislocation can be produced in the twin by incorporating two  $[a_1]$  or  $[a_3]$  basal dislocations. In 2010, Niewczas [43] revisited the reaction suggested by Yoo and Wei [24] using the concept of the lattice correspondence matrix. This dissertation adopts the same crystallographic framework, and the vector transformations are presented in detail in Chapter 3.

The crystallography based dislocation transformation concept from  $\langle a \rangle$  dislocations in the matrix to  $\langle c + a \rangle$  dislocations in the  $\{10\bar{1}2\}$  twin is of great interest, because the former are the most readily activated glide dislocations in matrix and the latter represent the only slip mode in the twin crystals that is capable of accommodating strain along the  $[c]$ -axis. In fact, several crystal plasticity modeling studies [44-46] predicted that, in order to plastically accommodate the imposed strain, extensive pyramidal  $\langle c + a \rangle$  slip activity is necessitated in the twins. However, the investigations of the dislocations inside the  $\{10\bar{1}2\}$  twins in Mg alloys and in generic hexagonal metals are limited since the proposal by Yoo and Wei in 1966. The first experimental examination of the dislocation transformation concept was conducted in pure Zn single- and polycrystals [47, 48] in 1969. There were then scattered studies conducted in pure Mg [49] and in pure Zr polycrystals [50]. It is therefore the goal of the current dissertation study to thoroughly

examine the types and formation of various kinds of dislocations inside the  $\{10\bar{1}2\}$  twins in deformed microstructures, in order to understand the behavior of the defects and therefore their effects on the plastic response of the twin crystals.

#### 1.4 Specific research objectives

The primary objective of the current research is to investigate the interaction of basal  $\langle a \rangle$  dislocations in the matrix with  $\{10\bar{1}2\}$  twin boundaries. To achieve the overall goal, specific research objectives are set. The first objective is to assess the possibility that dislocations from the matrix would transform at the  $\{10\bar{1}2\}$  twin boundary into dislocations with a distinct Burgers vector consistent with the crystal geometry of the twin boundary. The dislocations are characterized using transmission electron microscope (TEM) and determined by diffraction contrast imaging at various two-beam conditions.

The second objective is to understand the condition of dislocation transformation at the twin interface, and the unit process of the interfacial reaction. The oriented single crystal samples are employed that allows the selection of defined loading conditions in order to activate specific deformation modes. *In situ* straining experiments in TEM are performed to identify the evolution of defects structures.

The third major objective is to investigate the interaction and relationship of various crystal defects involved in the vicinity of the twin boundary, including perfect dislocations, partial dislocations that bound stacking faults and interfacial defects with both dislocation and step characters (disconnections). This part of the study would contribute to the fundamental understanding of the effects of dislocation-TB interaction on the strain accommodation in the vicinity of the interface and on the boundary migration. The objective is achieved via both *in situ*

observations of defect evolutions in TEM and theoretical analyses, including (1) molecular dynamics (MD) simulation and the topological analyses of the vector transformations in the simulated results, (2) proposed formation mechanism of perfect  $\langle c + a \rangle$  dislocation from the interface and (3) evaluation of the proposed configurations using discrete dislocation calculations.

The comprehensive understanding of the scientific topics in this work and the investigation of the specific phenomena listed above necessitate appropriate tools at different length scales. The work would not be realized without the contributions of collaborators, which are included as coauthors in respective publications. The pure Mg single crystal samples were provided by Konstantin Molodov at RWTH Aachen University at Germany. The single crystal samples were deformed by Kavan Hazeli at University of Alabama, Huntsville. The in situ straining experiments in TEM were carried out at the Electron Microscopy Lab (EML) at Los Alamos National Laboratory (LANL) under the supervision of Rodney McCabe. The MD simulations were performed by Christopher Barrett at Mississippi State University. Preliminary calculations using a discrete dislocation code were performed by Yejun Gu at Johns Hopkins University.

## 1.5 Layout of the dissertation

The research of the dissertation is described in five chapters followed by a summary.

Chapter 2 includes the preliminary characterization of the dislocations in the matrix and the  $\{10\bar{1}2\}$  twin in a deformed polycrystalline Mg alloy AZ31, providing a basic and collective understanding of the deformation defect structure. This chapter is published as a conference proceeding in *Magnesium Technology 2015* [51].



Encouraged by the observations, Chapter 3 firstly establishes the crystallographic frame of the Burgers vectors transformations across a  $(10\bar{1}2)$  twin boundary, and then presents local evidences of the corresponding dislocation Burgers vectors on both sides of a TB via diffraction contrast analyses at various two-beam conditions in TEM. The crystallography based vector transformation is therefore confirmed and is referred to as dislocation transmutation reaction to distinct it from general transformations. The reaction processes at the interface and the stress conditions inside the twin are discussed based on the calculations of elastic stresses and energies. This chapter is published in the journal *International Journal of Plasticity* [52].

Chapter 4 aims to generalize the study in Chapter 3 to larger length scale than that of several dislocation segments, and to pure Mg and even other hexagonal metals. Furthermore, the use of single crystal pure Mg in this study create a controlled deformation condition of stimulating TB migration but not dislocations slip, providing a way to separate the motions of dislocation and interface which are convoluted in a polycrystalline environment. It therefore contributes as the first step to the understanding of the effect of boundary condition on the dislocations transmutation at TB. This chapter is published in the journal *Scripta Materialia* [53].

Chapter 5 and 6 are dedicated to probing the mechanism of the dislocation transmutation at the twin interface by performing in situ straining experiments in TEM and MD simulations to reveal details at lower length scale and time scale. The experimental observations and simulations motivate the proposal of a formation mechanism of perfect dislocations from the interface and the sequential evolutions of the defect configurations in the vicinity of the interface. The proposed mechanism is supported by dislocation theory and in situ TEM observations of certain steps of the defect evolutions. Preliminary quantitative evaluations of the energetics are conducted for the discretized dislocations using simplified dislocation geometries.

Finally, the last chapter summarizes the major conclusions of the dissertation and discusses the impact of the work on pertaining topics. Potential directions for future work, which would advance the study and broaden its implications, are put forward.

## References

- [1] S. Schumann and H. Friedrich, "Current and future use of magnesium in the automobile industry," *Mater. Sci. For.*, Vols. 419-422, pp. 51-56, 2003.
- [2] A. Luo, "Magnesium: current and potential automotive applications," *JOM*, vol. 54, pp. 42-48, 2002.
- [3] G. Proust, C. Tome, A. Jain and S. Agnew, "Modeling the effect of twinning and detwinning during strain-path changes of magnesium alloy AZ31," *Int. J. Pla.*, vol. 25, pp. 861-880, 2009.
- [4] S. Agnew, M. Yoo and C. Tome, "Application of texture simulation to understanding mechanical behavior of Mg and solid solution alloys containing Li or Y," *Acta Mater.*, vol. 49, pp. 4277-4289, 2001.
- [5] Q. Ma, H. El Kadiri, A. Oppedal, J. Baird, B. Li, M. Horstemeyer and S. Vogel, "Twinning effects in a rod-textured AM30 Magnesium alloy," *Int. J. Pla.*, vol. 29, pp. 60-76, 2012.
- [6] A. Oppedal, H. El Kadiri, C. Tome, S. Vogel and M. Horstemeyer, "Anisotropy in hexagonal close-packed structures: improvements to crystal plasticity approaches applied to magnesium alloy," *Phil. Mag.*, vol. 93, pp. 4311-4330, 2013.
- [7] A. Jain and S. Agnew, "Modeling the temperature dependent effect of twinning on the behavior of magnesium alloy AZ31B sheet," *Mater. Sci. Eng. A*, vol. 462, pp. 29-36, 2007.
- [8] X. Guo, A. Chapuis, P. Wu and S. Agnew, "On twinning and anisotropy in rolled Mg alloy AZ31 under uniaxial compression," *Int. J. Sol. Str.*, Vols. 64-65, pp. 42-50, 2015.
- [9] H. El Kadiri and A. Oppedal, "A crystal plasticity theory for latent hardening by glide twinning through dislocation transmutation and twin accommodation effects," *Journal of the Mechanics and Physics of Solids*, vol. 58, pp. 613-624, 2010.
- [10] A. Oppedal, H. El Kadiri, C. Tome, G. Kaschner, S. Vogel, J. Baird and M. Horstemeyer, "Effect of dislocation transmutation on modeling hardening mechanisms by twinning in magnesium," *International Journal of Plasticity*, Vols. 30-31, pp. 41-61, 2012.
- [11] D. Brown, S. Agnew, S. Abeln and et al., "The role of texture, temperature, and strain rate in the activity of deformation twinning," *Mater. Sci. For.*, Vols. 495-497, pp. 1037-1042, 2005.
- [12] S. Agnew, D. Brown and C. Tome, "Validating a polycrystal model for the elastoplastic

- response of magnesium alloy AZ31 using in situ neutron diffraction," *Acta Mater.*, vol. 54, no. 18, pp. 4841-4852, 2006.
- [13] O. Muransky, M. Barnett, V. Luzin and V. Vogel, "On the correlation between deformation twinning and Luders-like deformation in an extruded Mg alloy: in situ neutron diffraction and EPSC.4 modelling," *Mater. Sci. Eng. A*, vol. 527, pp. 1383-1394, 2010.
- [14] S. Asgari, E. El-Danaf, S. Kalidindi and R. Doherty, *Metall Mater Trans A*, vol. 28A, p. 1781, 1997.
- [15] E. El-Danaf, S. Kalidindi and R. Doherty, *Metall Mater Trans A*, vol. 30, p. 1223, 1999.
- [16] S. Kalidindi, A. Salem and R. Doherty, *Adv Eng Mater*, vol. 5, p. 229, 2003.
- [17] A. Salem, S. Kalidindi and R. Doherty, "Strain hardening of titanium: role of deformation twinning," *Acta Mater.*, vol. 51, pp. 4225-4237, 2003.
- [18] A. Salem, S. Kalidindi, R. Doherty and S. Semiatin, *Metall Trans A*, vol. 37, p. 259, 2006.
- [19] M. Knezevic, A. Levinson, R. Harris, R. Mishra, R. Doherty and S. Kalidindi, "Deformation twinning in AZ31: Influence on strain hardening and texture evolution," *Acta Mater.*, vol. 58, pp. 6230-6242, 2010.
- [20] C. Caceres, P. Lukac and A. Blake, "Strain hardening due to {10-12} twinning in pure magnesium," *Phil. Mag.*, vol. 88, pp. 991-1003, 2008.
- [21] P. Wu, X. Guo, H. Qiao, S. Agnew, D. Lloyd and J. Embury, "On the rapid hardening and exhaustion of twinning in magnesium," *Acta Mater.*, vol. 122, pp. 369-377, 2017.
- [22] L. Capolungo, I. Beyerlein and C. Tome, "Slip-assisted twin growth in hexagonal close-packed metals," *Scripta Mater*, vol. 60, pp. 32-35, 2009.
- [23] Z. Basinski, M. Szczerba, M. Niewczas, J. Embury and S. Basinski, "The transformation of slip dislocations during twinning of copper-aluminum alloy crystals," *Revue de Metallurgie*, vol. 94, pp. 1034-1044, 1997.
- [24] M. Yoo and C. Wei, *Phil. Mag.*, vol. 14, pp. 573-587, 1966.
- [25] A. Serra and D. Bacon, *Phil. Mag.*, vol. 73, pp. 333-343, 1996.
- [26] N. Thompson and D. Millard, "XXXVIII. Twin formation, in cadmium," *Philos. Mag.*, vol. 43, pp. 422-440, 1952.
- [27] A. Serra, D. Bacon and R. Pond, "The crystallography and core structure of twinning dislocations in H.C.P. metals," *Acta Metall.*, vol. 36, pp. 3183-3203, 1988.
- [28] J. Hirth and R. Pond, "Steps, dislocations and disconnections as interface defects relating to structure and phase transformations," *Acta Mater.*, vol. 44, pp. 4749-4763, 1996.
- [29] H. El Kadiri, C. Barrett, J. Wang and C. Tome, "Why are {10-12} twins profuse in magnesium?," *Acta Mater.*, vol. 85, pp. 354-361, 2015.
- [30] M. Yoo, "Slip, twinning, and fracture in hexagonal close-packed metals," *Metallurgical transactions A*, vol. 12A, pp. 409-418, 1981.
- [31] C. Tome, I. Beyerlein, J. Wang and R. McCabe, "A multi-scale statistical study of twinning

- in magnesium," *JOM*, vol. 63, pp. 19-23, 2011.
- [32] X. Liao, J. Wang, J. Nie, Y. Jiang and P. Wu, "Deformation twinning in hexagonal materials," *MRS Bulletin*, vol. 41, pp. 314-319, 2016.
- [33] H. Khater, A. Serra and R. Pond, "Atomic shearing and shuffling accompanying the motion of twinning disconnections in Zirconium," *Philos. Mag.*, vol. 93, pp. 1279-1298, 2013.
- [34] T. Braisaz, P. Ruterana, G. Nouet and R. Pond, "Investigation of  $\{1012\}$  twins in Zn using high-resolution electron microscopy: Interfacial defects and interactions," *Philos. Mag. A*, vol. 75, pp. 1075-1095, 1997.
- [35] P. Price, "Nucleation and growth of twins in dislocation-free zinc crystals," *Proceedings of the Royal Society of London. Series A, Mathematical and Physical Sciences*, Vols. 260-262, p. 251, 1961.
- [36] A. Serra, D. Bacon and R. Pond, "Dislocations in interfaces in the H.C.P. metals - I. defects formed by absorption of crystal dislocations.," *Acta Mater.*, vol. 47, pp. 1425-1439, 1999.
- [37] A. Serra and D. Bacon, *Phil. Mag.*, vol. 90, pp. 845-861, 2010.
- [38] Y. Li, Y. Chen, J. Walmsley, R. Mathinsen, S. Dumoulina and H. Roven, "Faceted interfacial structure of  $\{10-11\}$  twins in Ti formed during equal channel angular pressing," *Scripta Mater.*, vol. 62, pp. 443-446, 2010.
- [39] J. Tu, X. Zhang, C. Lou and Q. Liu, "HREM investigation of  $\{10-12\}$  twin boundary and interface defects in deformed polycrystalline cobalt," *Philos. Mag. Lett.*, vol. 93, pp. 292-298, 2013.
- [40] J. Tu, X. Zhang, Y. Ren, Q. Sun and Q. Liu, "Structural characterization of  $\{10-12\}$  irregular-shaped twinning boundary in hexagonal close-packed metals," *Mater. Charact.*, vol. 106, pp. 240-244, 2015.
- [41] C. Barrett and H. El Kadiri, "The roles of grain boundary dislocations and disclinations in the nucleation of  $\{10-12\}$  twinning," *Acta Mater.*, vol. 63, pp. 1-15, 2014.
- [42] J. Tu, X. Zhang, J. Wang, Q. Sun, Q. Liu and C. Tome, "Structural characterization of  $\{101-2\}$  twin boundaries in cobalt," *Appl. Phys. Lett.*, vol. 103, p. 051903, 2013.
- [43] M. Niewczas, "Lattice correspondence during twinning in hexagonal close-packed crystals," *Acta Materialia*, vol. 58, pp. 5848-5857, 2010.
- [44] G. Proust, C. Tome, A. Jain and S. Agnew, "Modeling the effect of twinning and detwinning during strain-path changes of magnesium alloy AZ31," *Int. J. Pla.*, vol. 25, pp. 861-880, 2009.
- [45] B. Clausen, C. Tome, D. Brown and S. Agnew, "Reorientation and stress relaxation due to twinning: modeling and experimental characterization of Mg," *Acta Mater.*, vol. 56, pp. 2456-2468, 2008.
- [46] P. Juan, S. Berbenni, M. Barnett, C. Tome and L. Capolungo, "A double inclusion homogenization scheme for polycrystals with hierarchical topologies: application to twinning

- in Mg alloys," *Int. J. Plas.*, vol. 60, pp. 182-196, 2014.
- [47] D. Tomsett and M. Bevis, "The formation of stacking faults in  $\{10\text{-}12\}$  twins in zinc as a result of slip dislocation-deformation twin interactions," *Phil. Mag.*, vol. 19, pp. 533-537, 1969.
- [48] D. Tomsett and M. Bevis, "The incorporation of basal slip dislocations in  $\{10\text{-}12\}$  twins in zinc crystals," *Philosophical Magazine*, vol. 19, no. 157, pp. 129-140, 1969.
- [49] S. Morozumi, M. Kikuchi and H. Yoshinaga, "Electron microscope observation in and around  $\{1\text{-}102\}$  twins in magnesium," *Trans. JIM*, vol. 17, pp. 158-164, 1976.
- [50] D. Bhattacharyya, E. Cerreta, R. McCabe, M. Niewczas, G. Gray III, A. Misra and C. Tome, "Origin of dislocations within tensile and compressive twins in pure textured Zr," *Acta Materialia*, vol. 57, pp. 305-315, 2009.
- [51] F. Wang and S. Agnew, "Dislocation-twin interactions in magnesium alloy AZ31," in *Magnesium Technology 2015*, A. S. M. A. a. N. R. N. M. V. Manuel, Ed., Hoboken, NJ, USA, John Wiley & Sons, Inc., 2015, pp. 139-144.
- [52] F. Wang and S. Agnew, "Dislocation transmutation by tension twinning in magnesium alloy AZ31," *Int. J. Plas.*, vol. 81, pp. 63-86, 2016.
- [53] F. Wang, K. Hazeli, K. Molodov, C. Barrett, T. Al-Samman, D. Molodov, A. Kontsos, K. Ramesh, H. El Kadiri and S. Agnew, "Characteristic dislocation substructure in  $\{10\text{-}12\}$  twins in hexagonal metals," *Scripta Mater.*, vol. 143, pp. 81-85, 2018.

## CHAPTER 2    DISLOCATION-TWIN INTERACTIONS IN MAGNESIUM ALLOY AZ31

### 2.1    Introduction

The  $\{10\bar{1}2\}$  extension twinning is an important mechanism of plastic deformation in magnesium alloys. It is able to produce extension along the c-axis during e.g. in-plane compression of the textured material. When twinning occurs, the material exhibits a characteristic plateau and subsequent rapid strain hardening as observed in the S-shaped uniaxial compression flow curve presented in Figure 2.1. Because of the basal texture in the rolled plate, compression along the RD promotes compression nearly perpendicular to the c-axis in a large volume fraction of the grains. Such a straining direction promotes the activation of extension twinning. The deformation mechanisms prior to and at the plateau regime have been studied extensively. Basal slip and extension twinning have been confirmed as the dominant deformation modes at room temperature in polycrystalline AZ31, and non-basal slip modes was reported to occur at boundaries where the stress state is perturbed [1].

Many in-situ neutron diffraction studies have shown that highly textured Mg alloys begin  $\{10\bar{1}2\}$  extension twinning by 0.5% strain (e.g. [2]), as indicated by a strong texture evolution

corresponding to the near  $90^\circ$  reorientation of c-axes. Through the use of in-situ neutron diffraction experiments and elasto-plastic [3] and elasto-viscoplastic [4] crystal plasticity modeling, it has also become clear that slip of  $\langle a \rangle$  type dislocations on basal planes precedes the onset of twinning. In fact, recent molecular dynamics simulations of a pile-up of basal dislocations on a low angle boundary was shown to result in the nucleation of a  $\{10.2\}$  extension twin [5]. The end of the plateau corresponds to the completion of Lüder's band propagation through the gage of the sample according to the picture proposed by Barnett et al. [6]. In short, a specified volume fraction of twinning has been produced within the entire gage region at this point. If further deformation (by twinning or otherwise) is to occur, higher stress levels are required. According to the twinning-detwinning (TDT) model of Wang et al. [7], this effect can be incorporated into the crystal plasticity models as the point at which further twinning becomes difficult.

Apparently, the distinct orientation of the twin relative to the loading direction, and the twin boundary have an influence on the deformation process. However, the interactions between slip and twinning which affect the strain hardening behavior are less understood. In addition to obstructing the dislocation slip, the coherent nature of the twin boundary allows the transmutation of dislocations [8-9], which has been invoked as an explanation for the high hardening rate within the twin interior [10], and hence, the surrounding polycrystal. According to this argument, in addition to the fact that extension twins do not generate any orientation favorable for subsequent slip of the soft, basal mechanism inside the twin, twins are additionally hardened by high density of dislocations [11-12]. The goal of the present study is to determine the dislocation character and arrangements in the twin and the adjacent matrix.

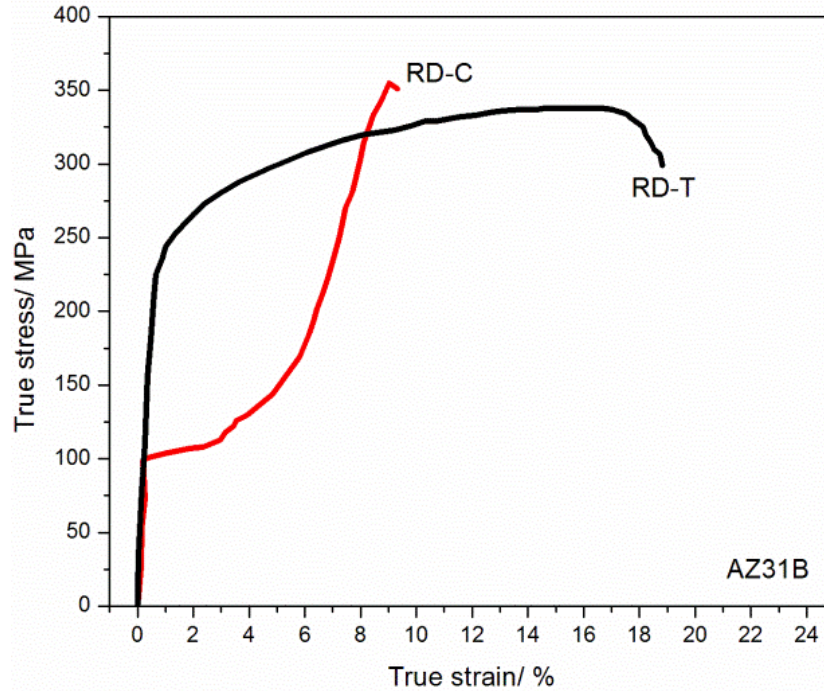


Figure 2.1. Flow curves obtained for loading along the rolling direction under tension (RD-T) and compression (RD-C). Figure reproduced from [13].

## 2.2 Experimental methods

The material used in this work is from a commercially rolled plate of magnesium alloy AZ31B with H24 temper (strain hardened and partially annealed). The nominal composition of the alloy is 3 wt% Al, 1 wt% Zn, and balance Mg). The rolled plate was subsequently compressed along the rolling direction (RD) at room temperature (RT). Compression samples with 0.5% and 2% strains were used to represent the start and end of the twinning-dominated strain hardening plateau.

For TEM analysis, thin sections parallel to the transverse plane were cut from the cuboidal compression sample using diamond saw (Figure 2.2). This orientation was selected to permit the twins to be observed primarily along the  $\{11\bar{2}0\}$  direction. The sections were mechanically ground to the thickness of  $\sim 200\ \mu\text{m}$  and then punched into 3 mm disks. The disks



were further thinned by 1200 grit SiC paper to  $\sim 80\ \mu\text{m}$ , prior to electropolish in a solution of 500 ml ethanol, 100 ml butyl cellosolve, 5.6 g magnesium perchlorate and 2.3 g lithium chloride, at 95 V and  $-50^\circ\text{C}$  maintained by a solution of liquid nitrogen and methanol within a Fischione double-jet polisher. After perforation, the disks were rinsed by ethanol.

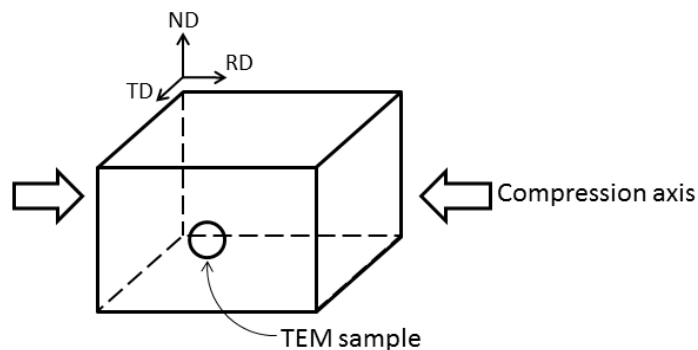


Figure 2.2. Orientation of the TEM disk in the compressed sample, the normal of the disk is parallel to the transvers direction (TD) of the rolled plate.

TEM observations were performed on a JEOL 2000FX TEM with a  $\text{LaB}_6$  cathode operating at 200 kV. Images of the dislocation and fault structure in and around extension twins were obtained using bright field (BF) and weak beam dark field (WBDF) imaging with the diffraction conditions listed in Table 2.1. When all such diffraction conditions were employed, a complete determination of the Burgers vector was possible. In many cases only selected reflections were employed to distinguish whether the Burgers vector of the dislocation is  $\langle a \rangle$  type or  $[c]$ -containing.

Table 2.1. Diffraction conditions for TEM analysis. The three zone axes (ZA) are 30° apart along the (0002) Kikuchi band. The diffraction vectors are grouped by their respective ZAs, and (0002) is available at all ZAs.

	ZA		$[\bar{1}2\bar{1}0]$			$[\bar{1}100]$	$[\bar{2}110]$		
Mode	$b/\vec{g}$	(0002)	$(10\bar{1}0)$	$(\bar{1}011)$	$(10\bar{1}\bar{1})$	$(11\bar{2}0)$	$(01\bar{1}0)$	$(0\bar{1}11)$	$(01\bar{1}\bar{1})$
<a>	$1/3[11\bar{2}0]$	0	1	1	-1	2	-1	-1	1
	$1/3[1\bar{2}10]$	0	0	0	0	-1	1	1	-1
	$1/3[\bar{2}110]$	0	-1	-1	1	-1	0	0	0
<c+a>	$1/3[11\bar{2}3]$	2	1	0	2	2	1	0	2
	$1/3[1\bar{2}13]$	2	0	1	1	-1	-1	2	0
	$1/3[\bar{2}113]$	2	-1	2	0	-1	0	1	1
	$1/3[11\bar{2}\bar{3}]$	-2	1	-2	0	2	1	-2	0
	$1/3[1\bar{2}1\bar{3}]$	-2	0	-1	-1	-1	-1	0	-2
	$1/3[\bar{2}11\bar{3}]$	-2	-1	0	-2	-1	0	-1	-1
[c]	[0001]	2	0	1	1	0	0	1	0

## 2.3 Results and discussion

### 2.3.1 TEM observations of dislocations

Regarding dislocations in the matrix at the onset of twinning (considered as 0.5% strain in this work), it is found that they are exclusively of <a> type, as indicated by their visibility in the  $[1\bar{1}01]$  and  $[1\bar{1}00]$  diffraction conditions and absence in the  $[0002]$  diffraction condition, Figure 2.3(d). Furthermore, stereological considerations indicated that the majority of these dislocations are lying within the basal plane (i.e., they are not prismatic or pyramidal

dislocations). More specifically, it is noted that they are long and relatively straight when looking down the (0001) basal planes (near edge-on perspective in Figure 2.3). This is not surprising, given the low stress level that is required to produce a strain of 0.5% in compression along the rolling direction, and the high stress level that is required to activate prismatic slip (e.g., see high flow stress in RD-tension Figure 2.1). However, it is yet an important observation since the immediate vicinity of the twin is likely under stress concentration associated with the demands of twin accommodation. Some authors (e.g. Jonas et al. [14]) have emphasized the role of prismatic  $\langle a \rangle$  dislocations in accommodating the twin strain within surrounding matrix grains. The present results suggest that this may not be necessary in the immediate matrix grain at low strain levels.

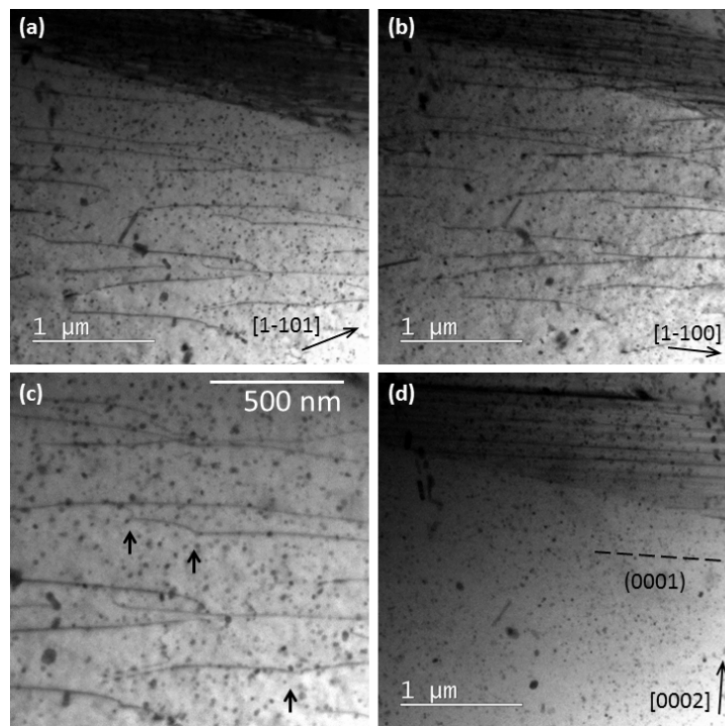


Figure 2.3. Straight  $\langle a \rangle$  type dislocations in the 0.5% sample. Dislocation bow-out around precipitates is indicated by short arrows in (c). The imaged area is close to a twin in the upper-right corner in (a, b and d).

Also note-worthy is the occurrence of dislocation bow-out at precipitates in Figure 2.3(c). As reported in [15], the manganese rich particles in AZ31 are suggested to contribute to precipitation hardening and hence an increase in tensile yield strength of this alloy. The alloy is not considered age hardenable, since there is no practical heat treatment schedule that leads to appreciable hardening. Presumably, the precipitates are either too easily bypassed or too sparse in the matrix.

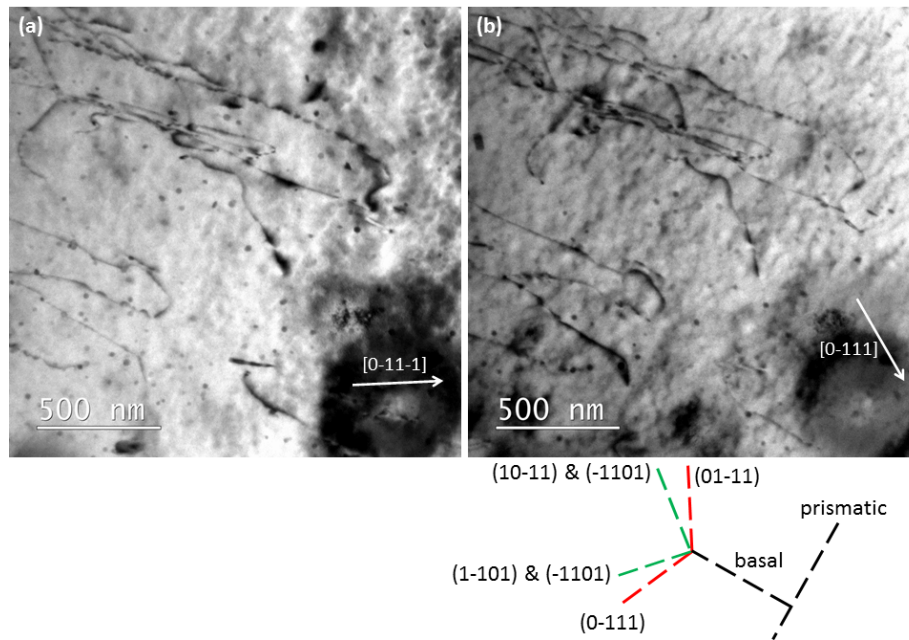


Figure 2.4.  $\langle a \rangle$  type dislocations in the 0.5% sample. Plane traces are shown in (b).

The  $\langle a \rangle$  type dislocations were occasionally observed to be operating on non-basal planes in the 0.5% sample. In Figure 2.4, dislocations are mainly on the basal plane while short segments are aligned with non-basal planes. It is observed, at least in this region, that the  $\langle a \rangle$  dislocations appear to be more readily operating on the first order pyramidal plane  $\{10\bar{1}1\}$  than on the prismatic plane  $\{10\bar{1}0\}$ . This has to be confirmed by examining the possibility of cross-

slip of the  $\langle a \rangle$  type dislocations. The presence of non-basal dislocations in both  $[0\bar{1}1\bar{1}]$  and  $[0\bar{1}11]$  reflections indicates that the  $\langle a \rangle$  dislocations have the Burgers vector of either  $[a_2]$  or  $[a_3]$ . In order for a screw dislocation to cross slip from the basal plane onto the pyramidal planes, the intercept of the basal and pyramidal planes has to be parallel to the Burgers vector. So  $(10\bar{1}1)$ ,  $(\bar{1}101)$ ,  $(1\bar{1}01)$  and  $(\bar{1}10\bar{1})$  are the possible gliding planes for the  $[a_2]$  or  $[a_3]$  dislocations in the figure. In fact, close inspection shows that the traces of these four planes align closely with most out of basal dislocation segments.

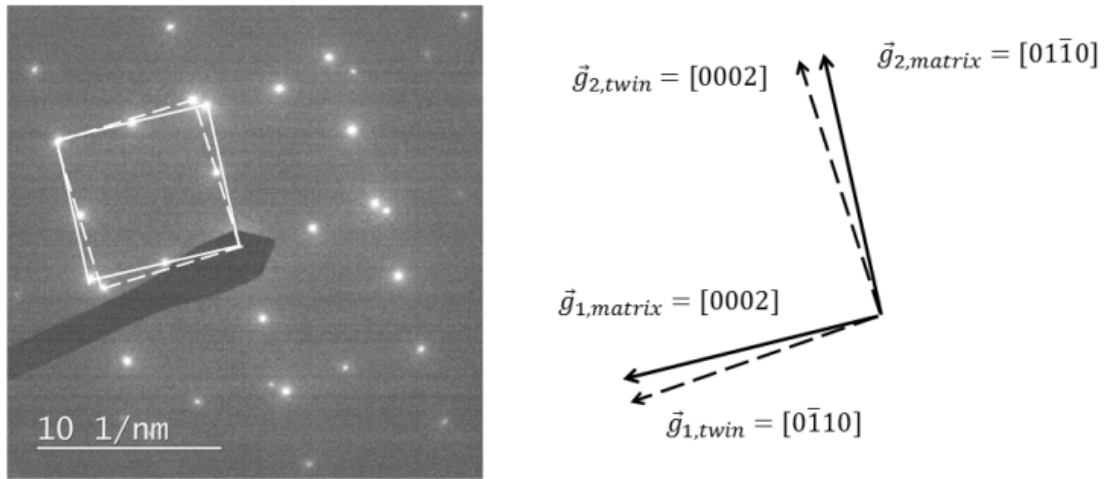


Figure 2.5. Selected area diffraction pattern showing the matrix-twin orientation relationship ( $86^\circ$ ). The extension twinning plane is determined as  $(01\bar{1}2)$ . The close alignment of some diffraction vectors from twin and matrix is illustrated on the right.

Extension twins assume a larger fraction of the microstructure at 2.0% strain. Dislocation analysis was focused in the vicinity of twins. The nearly  $90^\circ$  orientation relationship of directions from the matrix and the twin was utilized to compare the dislocation structure on both sides of a twin boundary, since it is possible to obtain a near two-beam diffraction condition on both the matrix and twinned regions. When the  $[0002]$  vector in the matrix is used as the two-beam

condition for imaging, the condition in the twin occurs naturally as close to  $[01\bar{1}0]$ , and vice versa. This relationship is schematically illustrated in Figure 2.5. The  $[0002]$  reflection will only give contrast to the  $[c]$  dislocations, and the  $[01\bar{1}0]$  reflection will give contrast to the  $\langle a \rangle$  containing dislocations. If a dislocation in either matrix or twin is visible in both diffraction conditions, it has both  $\langle a \rangle$  and  $[c]$  components.

At 2.0% strain, the most dislocations in the matrix are  $\langle a \rangle$  type, with the exception of a few in the vicinity of the twin boundary. Figure 2.6(c) shows segments of dislocation with  $[c]$  component in the matrix connected to the twin boundary. While they are present also in the condition of  $g = [01\bar{1}0]$  (Figure 2.6(b)), it is suggested that these are  $[c + a_2]$  or  $[c + a_3]$  dislocations, whose presence might be ascribed to the perturbed local stress state near the twin boundary or hint the emission from the twin boundary. Similar dislocations are also visible in Figure 2.7(b) on the right side and highlighted by the dashed line box. As is discussed in the previous paragraph, the  $[01\bar{1}0]$  vector in the twin naturally leads to the  $[0002]$  reflection in the adjacent matrix, which gives contrast to the dislocation having the  $[c]$  component.

The primary  $\langle a \rangle$  type dislocations in the matrix are accompanied by abundant  $[c]$  containing dislocations in the twin, as indicated by the dislocation contrast in both Figure 2.6(b) and (c). Furthermore, the coexistence of reflections  $[01\bar{1}0]$  in the matrix and  $[0002]$  in the twin reveals in the same figure the  $[a_2]$ ,  $[a_3]$  dislocations on the basal plane in the matrix and  $[c]$  containing dislocations in the twin. The dislocation transmutation has been suggested involving two  $\langle a \rangle$  type dislocations penetrating the  $\{10\bar{1}2\}$  twin boundary and producing a  $\langle c+a \rangle$  dislocation leaving a residual dislocation on the boundary [16, 17]. According to the correspondence matrix developed by M. Niewczas [9], a possible reaction is  $[a_3]$  dislocations on

the basal plane in the matrix produces a  $[c + a_2]$  dislocation on the prismatic plane in the extension twin.

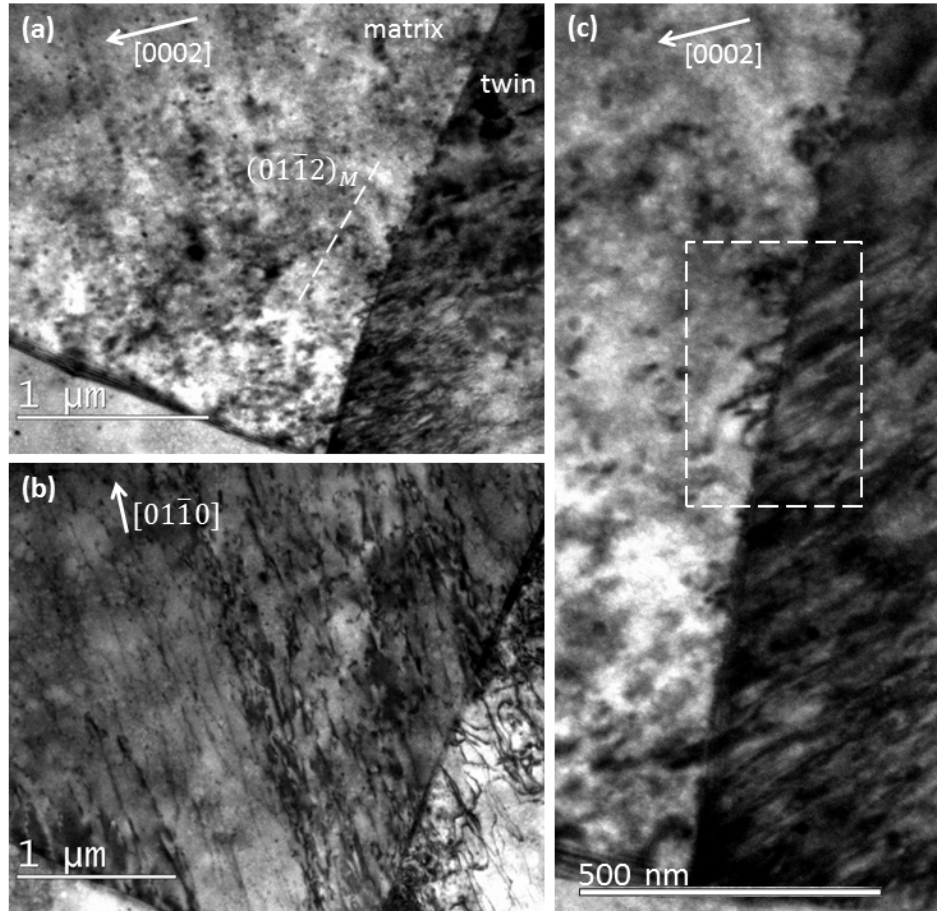


Figure 2.6. Dislocation structure in the twin and the matrix in the 2.0% sample. The diffraction vectors are those from the matrix. The trace of the twinning plane is indicated in (a) by the dashed line. The dashed line box in (c) highlights the dislocations with  $[c]$  component in the matrix connected with the twin boundary.

The dislocations inside the extension twin are displayed in Figure 2.7. The high density of dislocations and their large Burgers vectors ( $[c]$  containing) yield strong and overlapped strain field and therefore weak image contrast. Therefore, weak beam dark field (WBDF) technique is

helpful, to reveal the contrast of individual dislocations. In terms of the morphology, most dislocations have shorter segment on the basal plane and longer segment on the non-basal planes, which is in contrast to the dislocations in the matrix of the 0.5% sample having longer segments on the basal plane (Figure 2.4).

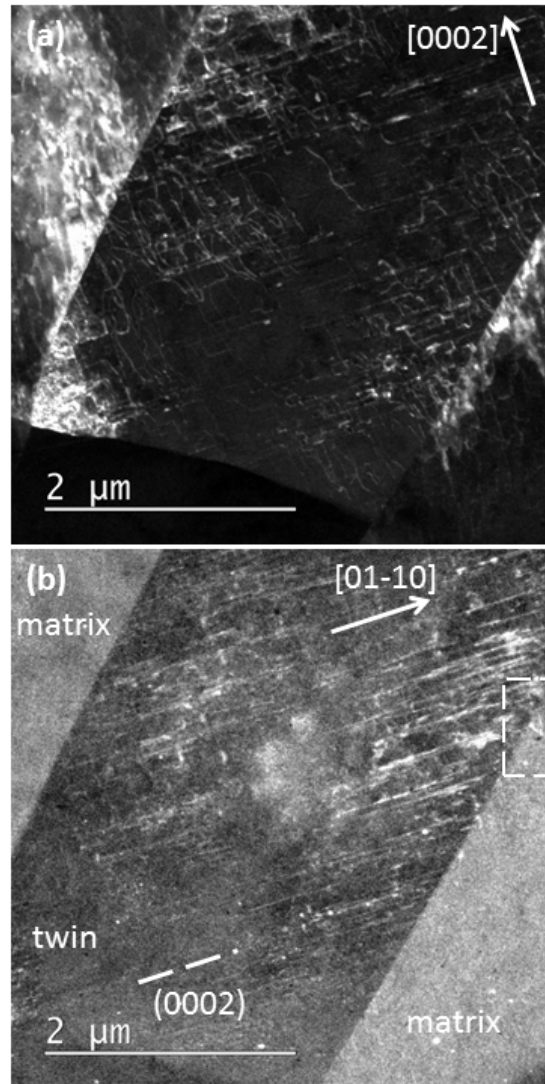


Figure 2.7. WBDF images of dislocations in the twin by using two diffraction vectors. The dashed line box in (b) highlights the [c] containing dislocation in the matrix.



According to the invisibility criterion for reflections  $[0002]$  and  $[01\bar{1}0]$ , in Figure 2.8, dislocations in (a) are either pure  $[c]$  or  $\langle c + a \rangle$ , and those in (b) are either  $a_2, a_3$  or  $[c+a_2]$ ,  $[c+a_3]$ . Therefore, those dislocations present in both reflections as indicated by the short arrows have the Burgers vector of  $[c+a_2]$  or  $[c+a_3]$ , and they are parallel to the basal plane; the non-rectilinear dislocations visible in Figure 8(a) but not in (b) have the Burgers vector of  $[c]$  or  $[c+a_1]$  and are operating on the non-basal planes. It should be noted that the  $\langle c + a \rangle$  dislocation could assume a dissociated configuration on the basal plane according to [18], therefore different contrast pattern follows than considering only the perfect dislocations. Analysis was focused here on the out of basal plane dislocations.

The existence of the possible Burgers vectors  $[c]$  or  $[c + a_1]$  for non-basal dislocations was further examined by Schmid factor analysis. The external loading direction is closely aligned with the basal plane of the matrix due to the pronounced texture, and is approximately aligned with the  $c$ -axis in the extension twin by the characteristic  $86^\circ$  rotation. The Schmid factors of the possible slip systems in the twin are hence calculated assuming the loading direction along the  $[0001]$  direction and are listed in Table 2.2. For  $\langle c + a \rangle$  dislocation, both the first and second order pyramidal planes are possible glide planes, and the Schmid factors for glide on the two planes are similar. The point of this section of the paper is to highlight the low probability that the contrast is due to  $c$ -type dislocations, rather than  $\langle c + a \rangle$ , so only the Schmid factors for  $\langle c + a \rangle$  on  $\{2\bar{1}\bar{1}2\}$  are listed for comparison. The absolute values of the Schmid factors are taken since negative value merely means dislocation gliding on the opposite direction. It is readily revealed that the activation of pure  $[c]$  dislocation in the analyzed twin is unfavorable, whereas the  $\langle c + a \rangle$  dislocations are necessary in terms of accommodating the imposed

deformation judging from the near maximum Schmid factor. By this analysis, the Burgers vectors of the out of basal, non-rectilinear dislocations are  $[c + a_1]$  and  $[c - a_1]$ .

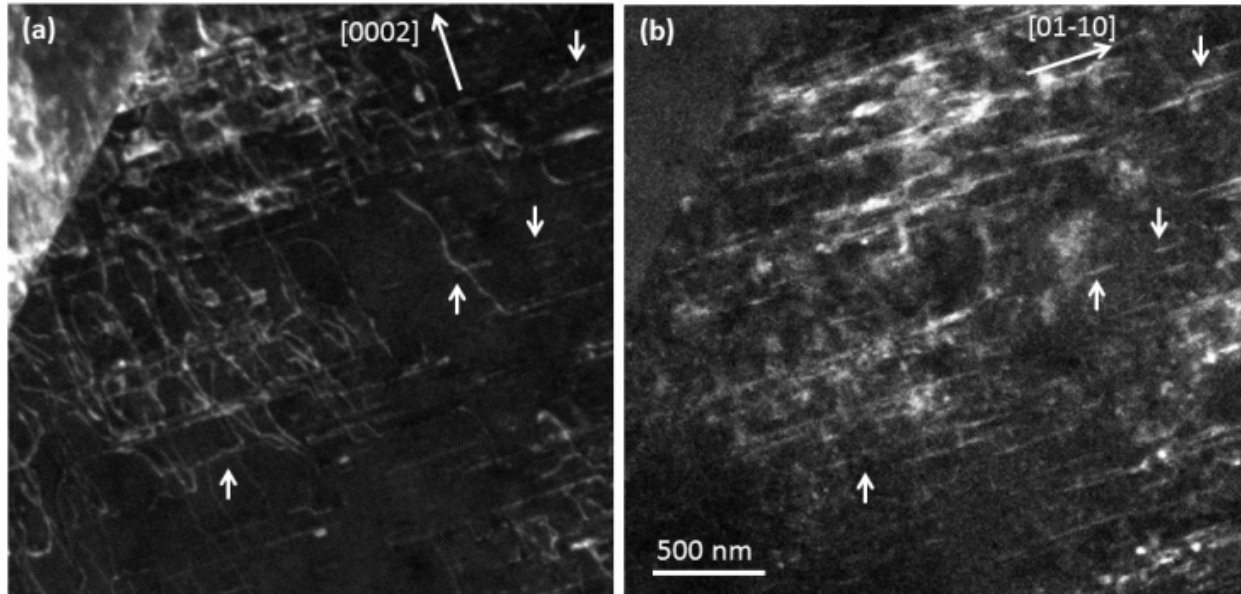


Figure 2.8. One area from Figure 2.7 to compare the visibility of dislocations in two diffraction conditions. The short arrows indicate the contrast from the same dislocation segment in both images.

Table 2.2. Schmid factors ( $m$ ) for possible dislocation types. The loading direction is taken as  $[0001]$ . And the absolute values of  $m$  are taken.

Type	$b$	Slip plane	$m$
$[c-a_1]$	$1/3[\bar{2}113]$	$(2\bar{1}\bar{1}2)$	0.45
$[c+a_1]$	$1/3[\bar{2}113]$	$(\bar{2}11\bar{2})$	0.45
$[c]$	$[0001]$		0

### 2.3.2 TEM observation of stacking faults associated with twins

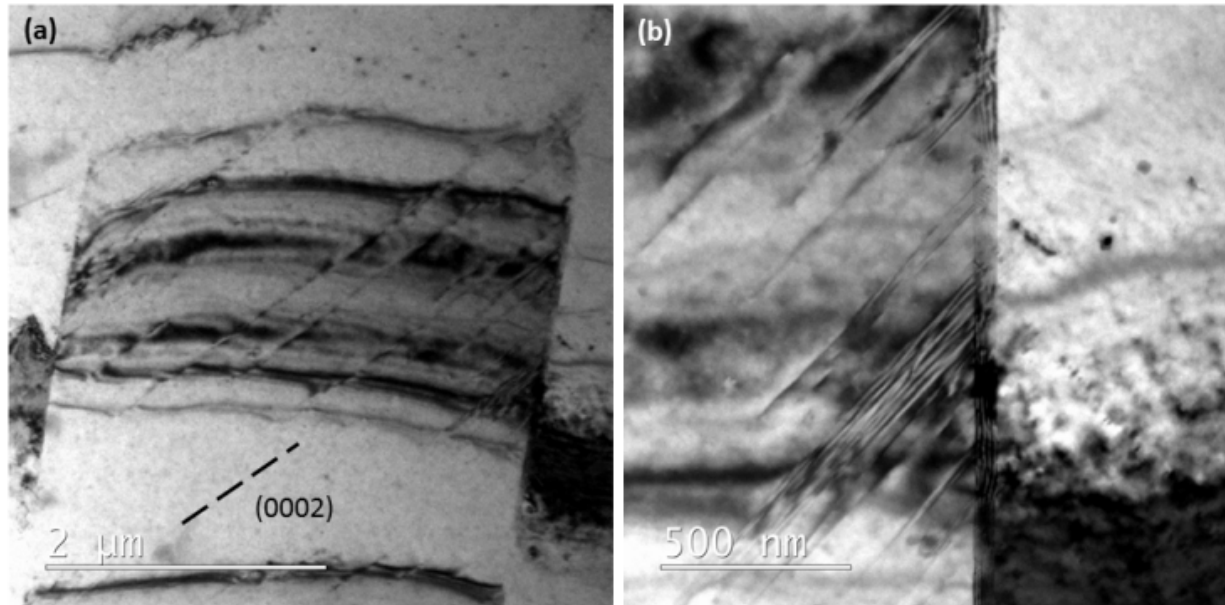


Figure 2.9. Stacking faults emanating from twin boundary in an extension twin in the 0.5% sample.

At 0.5% strain, there are very few dislocations of any type within the twins (Figure 2.9). On the other hand, there are wide stacking faults lying in the basal plane, being either  $I_1$  or  $I_2$  type. Although in the figure SFs seem to terminate in the interior of the twin, this is ascribed to the loss of contrast outside the bend contour, which is the dark horizontal band in the middle of Figure 2.9(a). At the bottom of this figure where a dark band exists, the SF is again visible. Considering the extended width of a few SFs at the center of Figure 2.9 (a), it is valid to conclude the SFs may span the entire twin. SFs traversing the twin were also reported by other authors, e.g. [19]. This is consistent with the twin growth (boundary migration) mechanism that has been proposed by J. Tu et al. [20]. Via molecular dynamic modeling, they suggest that the twin growth (migration of extension twin boundary) is accomplished by the migration of either

the coherent twin boundary (CTB) or the prismatic/ basal interface (PB/ BP), both of which result in the emission of a leading Shockley partial dislocation on the basal plane from the twin boundary, leaving a SF in the swept region, which is  $I_2$  type.

Figure 2.10 displays the SFs emitted from a twin boundary. Noteworthy is the lines with faint contrast parallel to the basal plane in the matrix, and these lines are connected with the SFs in the twin at the twin boundary. In the meantime, the contrast on the twin boundary superimposing on the boundary fringes is indicative of interface or twin dislocations. Further examination of these associated defects is required to reveal or prove the mechanism of SFs emission from twin boundary.

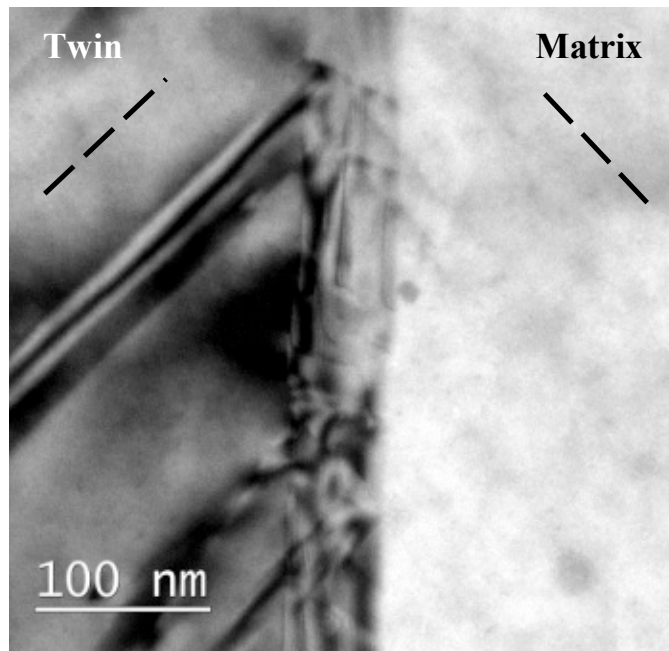


Figure 2.10. Stacking faults at a twin boundary and twin boundary dislocations in the 0.5% sample. The dashed lines indicate the trace of basal plane.

Finally, it is noted that no stacking faults are apparent within the matrix at the magnification employed in this study up to the strain of 2.0%. This is not surprising, even though

the I2 stacking fault energy is relatively low, because the equilibrium spacing of Shockley partials is only about 3 to 5 Burgers vectors or 6 to 16 Angstroms, as predicted by ab initio calculations [21].

## 2.4 Conclusions

By TEM analysis of the defect structure in the AZ31 RD-compression samples, specifically in the extension twin and the proximate matrix, the following conclusions can be drawn:

1. It is confirmed that in the matrix basal slip occurs firstly, as reported by the in-situ neutron diffraction and crystal plasticity modeling [3, 4].
2. At 0.5% strain where extension twinning begins to occur, the matrix is dominated by  $\langle a \rangle$  dislocation on the basal plane, and dislocation density is low in the twin interior. However, SFs on the basal plane are present. And the morphology is consistent with the SFs emission mechanism from twin boundaries proposed by MD modeling [20].
3. At 2.0% strain, there is a higher density of  $\langle a \rangle$  dislocations in the matrix. Dislocations with  $[c]$  component are observed emanating from the twin boundary into the matrix.
4. An abundant  $\langle c + a \rangle$  dislocations were identified in the extension twin at 2.0% strain. These  $\langle c + a \rangle$  dislocations have shorter length aligned with the basal plane and longer non-rectilinear segments on the non-basal planes. Their presence can be related to the higher hardening rate of the twin.

In addition to the above conclusions, several issues remain to be investigated in the future:

1. The  $\langle a \rangle$  dislocation transmutation across an extension twin boundary might result in  $\langle c + a \rangle$  dislocation in the twin. This provides a mechanism and explanation of higher dislocation density in the twin and the consequently high hardening rate.
2. Alternatively, the twin boundary may serve as a source mechanism for  $\langle c + a \rangle$  dislocations apart from transmutation. Perhaps it is aided by the stress concentration provided by  $\langle a \rangle$  dislocation pile-ups.
3. The twin boundary defect structure, specifically the interface dislocations can provide insights on the emission mechanism of stacking faults into the twin and the matrix.

## References

- [1] J. Koike, "Enhanced deformation mechanisms by anisotropic plasticity in polycrystalline Mg alloys at room temperature," *Metall. Mater. Trans. A*, vol. 36, p. 1689–1696, 2005.
- [2] D.W. Brown et al., "Internal strain and texture evolution during deformation twinning in magnesium," *Mat. Sci. Eng. A*, vol. 399, no. 1-2, pp. 1-12, 2005.
- [3] S.R. Agnew, D.W. Brown, and C.N. Tome, "Validating a polycrystal model for the elastoplastic response of magnesium alloy AZ31 using in situ neutron diffraction," *Acta Mater.*, vol. 54, no. 18, pp. 4841-4852, 2006.
- [4] H. Wang et al., "Study of lattice strains in magnesium alloy AZ31 based on a large strain elastic-viscoplastic self-consistent polycrystal model," *Int. J. Solids Struct.*, vol. 49, pp. 2155-2167, 2012.
- [5] J. Wang, J. Beyerlein, and C.N. Tome, "An atomic and probabilistic perspective on twin nucleation in Mg," *Scripta Mater.*, vol. 63, no. 7, pp. 741-746, 2010.
- [6] M.R. Barnett, M.D. Nave, and A. Ghaderi, "Yield point elongation due to twinning in a magnesium alloy," *Acta Mater.*, vol. 60, no. 4, pp. 1433-1443, 2012.
- [7] H. Wang et al., "A constitutive model of twinning and detwinning for HCP polycrystals," *Mater. Sci. Eng. A*, vol. 555, pp. 93-98, 2012.
- [8] L. Remy, "Twin-slip interaction in f.c.c. crystals," *Acta Metallurgica*, vol. 25, no. 6, pp. 711-714, 1977.
- [9] M. Niewczas, "Lattice correspondence during twinning in hexagonal close-packed crystals," *Acta Mater.*, vol. 58, no. 17, p. 5848–5857, 2010.

- [10] Z.S. Basinski et al., *Revue de Metallurgie*, vol. 94, p. 1037, 1997.
- [11] M.R. Barnett et al., "Influence of grain size on the compressive deformation of wrought Mg–3Al–1Zn," *Acta Mater.*, vol. 52, no. 17, p. 5093–5103, 2004.
- [12] S.R. Agnew et al., "Study of slip mechanisms in a magnesium alloy by neutron diffraction and modeling," *Scripta Mater.*, vol. 48, no. 8, pp. 1003–1008, 2003.
- [13] L. Wu et al., "The effects of texture and extension twinning on the low-cycle fatigue behavior," *Mater. Sci. Eng. A*, vol. 527, pp. 7057–7067, 2010.
- [14] J.J. Jonas et al., "The role of strain accommodation during the variant selection of primary twins in magnesium," *Acta Mater.*, vol. 59, no. 5, pp. 2046–2056, 2011.
- [15] N. Stanford, D. Atwell, "The Effect of Mn-rich Precipitates on the Strength of AZ31 Extrudates," *Metall. Mater. Trans. A*, vol. 44, pp. 4830–4843, 2013.
- [16] S. R. Agnew, O. Duygulu, "Plastic anisotropy and the role of non-basal slip in magnesium alloy AZ31B," *International Journal of Plasticity*, vol. 21, p. 1161–1193, 2005.
- [17] S. Morozumi, M. Kikuchi, and H. Yoshinaga, "Electron Microscope Observation in and around {1-102} Twins in Magnesium," *Transactions of the Japan Institute of Metals*, vol. 17, no. 3, pp. 158–164, 1976.
- [18] S.R. Agnew, L. Capolungo, and C.A. Calhoun, "Connections between the basal II "growth" fault and  $\langle c+a \rangle$  dislocations," *Acta Mater.*, 2014. Accepted.
- [19] B. Li et al., "Transmission electron microscopy study of stacking faults and their interaction with pyramidal dislocations in deformed Mg," *Acta Materialia*, vol. 58, pp. 173–179, 2010.
- [20] J. Tu et al., "Structural characterization of {10-12} twin boundaries in cobalt," *Applied Physics Letters*, vol. 103, p. 051903, 2013.
- [21] J.A. Yasi et al., "Basal and prism dislocation cores in magnesium: comparison of first-principles and embedded-atom-potential methods predictions," *Modelling Simul. Mater. Sci. Eng.*, vol. 17, p. 055012, 2009.

## CHAPTER 3    DISLOCATION TRANSMUTATION BY TENSION TWINNING IN MAGNESIUM ALLOY AZ31

### 3.1 Introduction

Deformation twinning is an important mechanism in hexagonal structured metals, because of its ability to accommodate the strain along the  $c$  axis of the crystal. Among all the twinning systems, the relatively low shear of the  $\{10\bar{1}2\}$  mode and high mobility of the twin boundary make it the most frequently observed (e.g., El Kadiri, Barrett, Wang and Tome, 2015). For metals whose  $c/a$  ratio is smaller than  $\sqrt{3}$ , such as Mg, Ti, Zr and Be,  $\{10\bar{1}2\}$  twinning results in extension along the  $c$  axis, it is therefore commonly termed extension, tension or tensile twinning (Yoo, 1981).

When profuse tension twins are activated, some materials exhibit tension-compression asymmetry, including a change of concavity in the flow curve and a rapid hardening regime (Reed-Hill, 1973; Kelley and Hosford Jr., 1968). In addition to normal dislocation-dislocation interaction (Taylor hardening a la Kocks and Mecking (Kocks and Mecking, 2003)), the hardening due to deformation twinning was classically attributed to two effects (Kalidindi, 2001; Proust, 2009): the composite strengthening effect associated with reorienting the twinned crystal



from a soft to a hard orientation, and twin-dislocation interaction by considering twin boundary as obstacles to subsequent slip and twinning deformation (Serra et al., 2002). Recently, a theory for latent hardening through dislocation transmutation by twinning was developed (El Kadiri and Oppedal, 2010), which hypothesizes that a rapid increase in the dislocation density or type inside twins is responsible for the larger hardening rate of the twin than that observed in the matrix. According to the dislocation transmutation theory, Oppedal et al. (2012) introduced in their model a fitting parameter called the “twin storage factor” that allows the twins harden more than the parent and showed its dominant effect on the increased hardening rate. Ma et al. (2012) showed that the incorporation of dislocation transmutation theory into latent hardening of twin-dislocation will more accurately simulate the texture and stress-strain data of magnesium alloy AM30, and suggested that at least the upper-half of the rapid hardening regime in the flow curve should be characterized by slip dominance within the twins.

Dislocation transmutation refers to the change of slip plane and Burgers vector of a dislocation when incorporated into the twin. Dislocation reactions at the  $\{10\bar{1}2\}$  twin boundary have been anticipated by Price (1961) and Yoo and Wei (1966) based primarily on geometric analysis. Tomsett and Bevis (1969a) were the first to study the transmutation of dislocations using the transmission electron microscope (TEM), and they showed the consistent appearance of  $\langle a \rangle$  dislocations in the matrix and  $\langle c + a \rangle$  dislocations in the  $\{10\bar{1}2\}$  twin, as suggested by the previous geometric analysis; thus, the transmutation concept was confirmed. Morozumi et al. (1976) observed  $\langle c + a \rangle$  dislocations near and within the  $\{10\bar{1}2\}$  twins in Mg. Lay and Nouet (1994) studied the interaction of slip dislocations with a  $(01\bar{1}2)$  twin in Zn, but did not observe the  $\langle a \rangle \rightarrow \langle c + a \rangle$  transmutation reaction. However, they only examined dislocation movement and penetration of the twin boundary *in situ*, under the influence of electron beam heating in the

TEM. Due to the weak stress field resulting from differential heating of the beam, their observations of dislocation interactions were limited to direct transfer of  $\langle a \rangle$  type dislocations whose Burgers vectors were parallel to the common axis of matrix and twin. Bhattacharyya et al. (2009) explored the origin of the dislocations within both tensile and compressive twins in textured Zr. Rather than invoking the transmutation argument, the  $c$ -type dislocations inside the tensile twin were hypothesized to be the remnants of dislocation interactions related to the formation of the twin itself. So far, the experimental evidence of dislocation transmutation has not been explored thoroughly, and no systematic explanation of the dislocation structure observed within twins has been advanced.

The current work explores the dislocation transmutation reaction at the boundaries of  $\{10\bar{1}2\}$  twins in a conventional Mg alloy using a TEM. The origin of the dislocations inside twin will be studied by focusing on the defect structure in the vicinity of twin boundary. We seek to understand the configuration and process of transmutation reactions. Finally, the potential operation of the dislocations inside the twin will be discussed in terms of the stress state.

## 3.2 Experimental procedures

### 3.2.1 Sample preparation

The studied material is a commercially rolled plate of magnesium alloy AZ31B in the H24 temper (strain hardened and partially annealed), with an average grain size of  $\sim 15 \mu\text{m}$  (Wu et al., 2010). The nominal composition of the alloy is 3 wt% Al, 1 wt% Zn, and balance Mg. The rolled plate possesses a preferred crystallographic orientation with the  $[c]$  axis of the crystals roughly parallel to the normal direction (ND) of the plate. The plate was subsequently compressed along the rolling direction (RD) at room temperature and individual samples were

strained to various levels (0.5, 1, 2, 4 and 8%). For TEM characterization, the samples from the plateau region in the flow curve (Figure 3.1a), up to 2.0% strain, were examined. Thin sections with the foil normal parallel to the transverse direction (TD) and ND respectively were cut from the cuboidal compression samples using a diamond saw (Figure 3.1c).

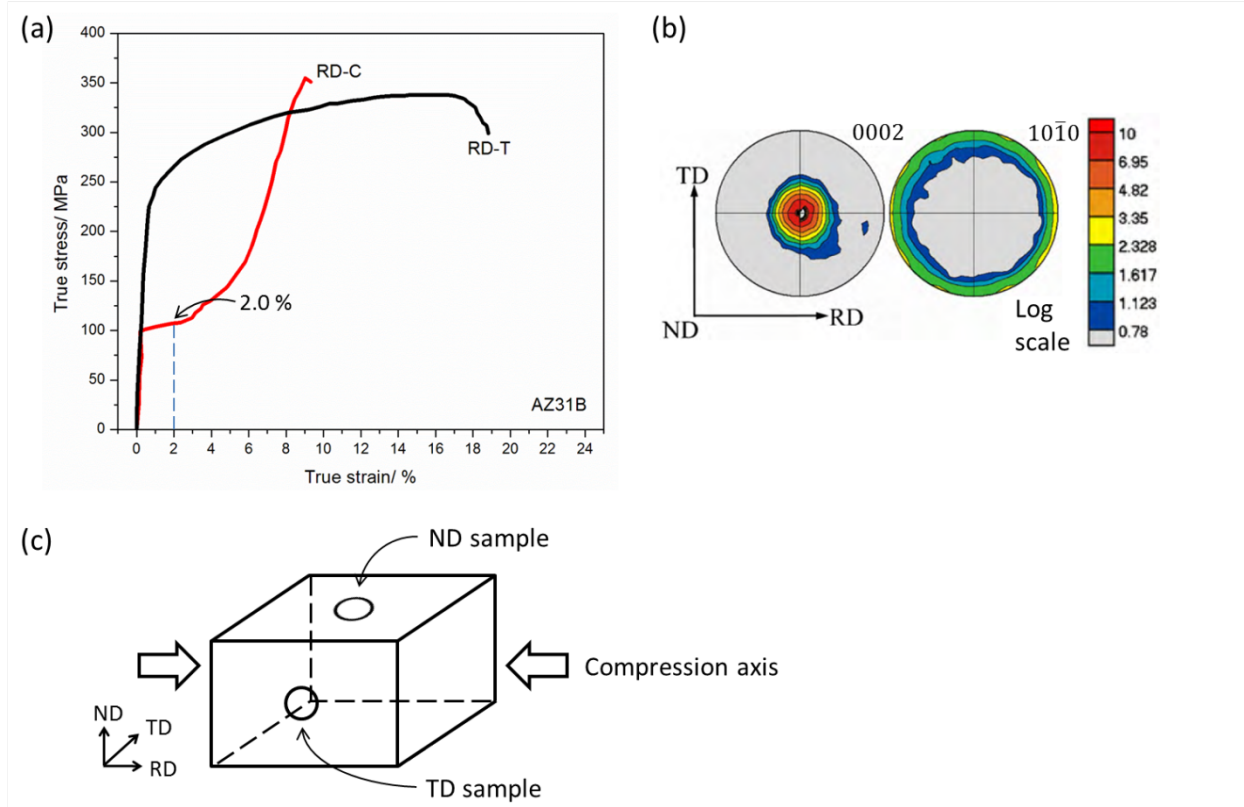


Figure 3.1. (a) The flow curves of the rolled plate of AZ31, whose initial texture is shown in (b). RD-C denotes compression along the rolling direction, and RD-T denotes tension along the rolling direction. The flow curves and pole figures are reproduced from (Wu et al., 2010). (c) The disks for TEM characterization were machined from the TD and ND planes of the RD-C sample.

The two foil orientations provide two perspectives for the characterization of the (10 $\bar{1}2$ ) twin: in the TD sample, the basal planes in the matrix and the twin, as well as the twinning plane

itself are all close to edge-on (the crystallographic plane is perpendicular to the plane of the foil); in the ND sample, the basal plane in most matrix grains is close to face-on (the crystallographic plane is parallel to the plane of the foil). The thin sections were mechanically ground to a thickness of  $\sim 250\ \mu\text{m}$  and then punched into 3 mm disks. The disks were further thinned by 1200 grit SiC paper to  $\sim 150\ \mu\text{m}$ . Thinning to electron transparency was achieved by electropolishing in a solution of 500 ml methanol, 100 ml butyl cellosolve, 11.16 g magnesium perchlorate and 5.3 g lithium chloride, at c.a. 100 V, 20 mA and  $-50^\circ\text{C}$  maintained by a solution of liquid nitrogen and methanol within a Fischione double-jet polisher. After perforation, the disks were rinsed in ethanol.

### 3.2.2 Characterization

TEM observations were performed on a JEOL 2000FX TEM with a  $\text{LaB}_6$  cathode operating at 200 kV. A double tilt sample stage was used to achieve various sample orientations. The Burgers vectors of dislocations were determined based on diffraction contrast analysis criteria (Fultz and Howe, 2001; Williams and Carter, 2009) by judging their visibility or invisibility in bright-field (BF) images and axial dark-field (DF) images under different two beam diffraction conditions. Weak-beam dark-field (WBDF) imaging was employed in areas of relatively large distortion due to, e.g. dense defect content. Simulated selected area electron diffraction (SAED) patterns and the stereographic projections used to navigate orientation space were generated by the software, Desktop Microscopist.

In specific cases, the TEM thin foil was characterized by an electron backscattered diffraction (EBSD) type technique known as transmission Kikuchi diffraction (TKD) (Keller and Geiss, 2012; Trimby, 2012) to quantitatively obtain the orientation of individual crystals with

respect to the sample coordinate system. For this purpose, the rolling direction was marked on the edge of TEM foil with a notch. EBSD was performed on a FEI Quanta 650 scanning electron microscope (SEM) equipped with AZtecHKL software.

### 3.3 Twinning relationship and dislocation transmutation reactions

The crystallographic frames of the two lattices (twin and matrix) were established based on the orientation relation investigated comprehensively by many authors (e.g. (Bevis and Crocker, 1969; Partridge, 1967)), and more recently reviewed by Christian and Mahajan (1995). With the twinning plane  $K_1 = \{10\bar{1}2\}$  and the shear direction  $\eta_1 = \langle\bar{1}011\rangle$ , it is a compound twin according to the categorization in Christian and Mahajan (1995). Throughout this work, the observed extension twins are arbitrarily indexed as  $(10\bar{1}2)$  with the direction  $a_2 = [1\bar{2}10]$  being the common axis of matrix and twin. The crystallographic relationship is depicted in Figure 3.2 in both real space (a) and reciprocal space (b). The mirror symmetry of the matrix and twin and the characteristic  $\sim 86^\circ$  rotation of the  $c$  axis of  $\{10\bar{1}2\}$  twinning is revealed in the diffraction pattern from the common zone axis  $[a_2]$ . This diffraction pattern is accessible in the TD samples in this work and was used to confirm that the twins were of the  $\{10\bar{1}2\}$  extension type. It should be noted that in the thin TEM foil, double diffraction commonly occurs, i.e. the  $(0001)$  diffraction spots are excited, and this effect is present in the simulated pattern (Figure 3.2b).

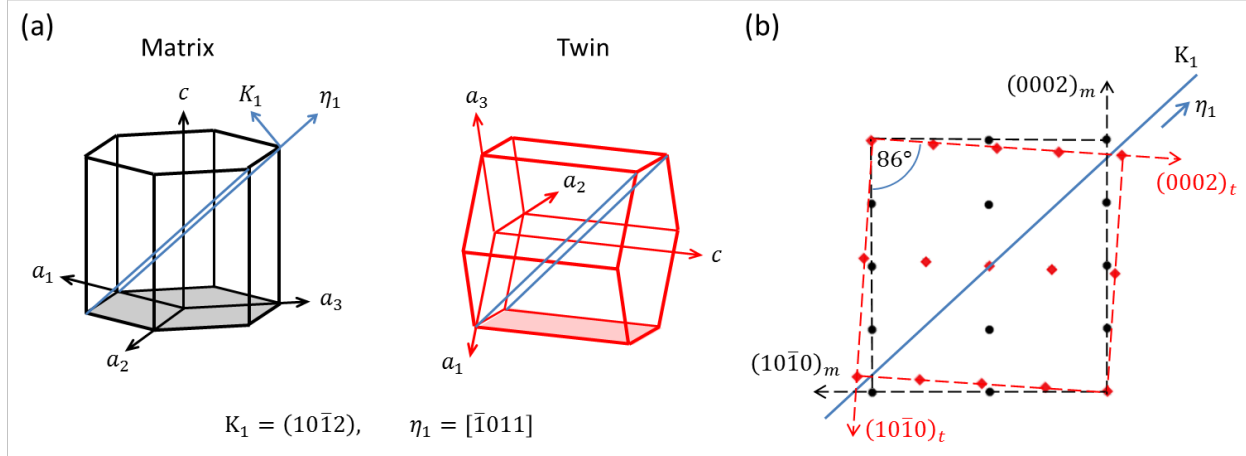


Figure 3.2. The  $180^\circ/\eta_1$  rotation relationship connecting the matrix and the twin is shown schematically in (a). (b) is a simulated diffraction pattern of the two lattices with  $[a_2]_{m,t}$  being the zone axis. The black dots represent the matrix spots, the red squares the twin spots. The reciprocal vectors  $(0002)$  and  $(10\bar{1}0)$  are drawn in the pattern for the matrix and the twin respectively. The real space twinning plane  $K_1$  is determined from the common diffraction spot.

Based on the crystallographic frames of the matrix and the twin lattices and using the correspondence matrix developed by Niewczas (2010), a vector in either lattice can be transformed into the other, and the dislocation transmutation reactions were formulated as in Table 3.1. Presently, focus was laid on the reactions involving the transmutation of  $\langle a \rangle$  dislocations from the matrix, and the reactions fall into two types: I. the transmutation of the common  $[a_2]$  dislocations from the plane of  $(0001)_m$  to  $(10\bar{1}0)_t$ , and II. the transmutation of  $[a_1]$  or  $[a_3]$  on the  $(0001)_m$  plane into  $\langle c \pm a_2 \rangle_t$  on the  $(10\bar{1}0)_t$  plane. The basal planes in the matrix and the indicated  $(10\bar{1}0)_t$  prismatic planes in the twin are closely aligned (Yoo and Wei, 1966). For type II reactions, a residual dislocation is left on the twin boundary with the magnitude of  $0.0643[\bar{1}011]$ , which is the twinning dislocation  $b_t$ , also known as the twinning disconnection  $b_{-2/-2}$  (Serra, Bacon and Pond, 1988). It should be emphasized that the  $\langle c + a \rangle_t$

dislocation which results from this mechanism contains the particular  $\langle a \rangle$  direction that is common to the matrix and twin, i.e.  $[a_2]$ .

Table 3.1. Dislocation reactions across a  $(10\bar{1}2)$  twin boundary, the twinning relation is described by  $180^\circ$  rotation about the twinning direction,  $\eta_1$ .  $b_t = \frac{3-\gamma^2}{3+\gamma^2}\langle\bar{1}011\rangle = 0.0643\langle\bar{1}011\rangle$  (Serra, Bacon and Pond, 1988), with  $\gamma = 1.624$  for Mg. The subscripts  $m$  and  $t$  denote the matrix and the twin respectively.

I.	$2 \times \frac{1}{3} [\bar{1}2\bar{1}0]_m \rightarrow 2 \times \frac{1}{3} [1\bar{2}10]_t$	$2 a_{2m} \rightarrow -2 a_{2t}$
II.	$2 \times \frac{1}{3} [\bar{1}\bar{1}20]_m \rightarrow 0.0643[\bar{1}011] + \frac{1}{3}[\bar{1}2\bar{1}3]_t$	$2 \times a_{3m} \rightarrow b_t + [c + a_2]_t$
	$2 \times \frac{1}{3} [\bar{2}110]_m \rightarrow 0.0643[\bar{1}011] + \frac{1}{3}[1\bar{2}13]_t$	$2 \times -a_{1m} \rightarrow b_t + [c - a_2]_t$

### 3.4 Experimental results

In the rolled material where the  $c$ -axes of the crystals are roughly parallel to the ND of the plate, deformation along RD reveals a pronounced tension-compression asymmetry, which is related to tension twinning (Figure 3.1a). Whereas basal slip is active in grains with orientations which deviate from the prominent texture component, compression along RD will activate tension twinning, though it is unable to accommodate tensile strain along RD, which will generally require prismatic slip. During compression, tension twinning is preferentially activated as early as  $\sim 0.3\%$  plastic strain, preceded by  $\langle a \rangle$  dislocation slip on the basal plane in matrix (Brown et al., 2005; Agnew, Brown and Tome, 2006; Wang, Wu, Tome and Wang, 2012). After tension twinning is activated, basal and prismatic  $\langle a \rangle$  slip systems remain the dominant slip systems in matrix (e.g., Clausen et al., 2008). The twinning-dominated compression is often characterized by a plateau in the flow curve, followed by a rapid strain hardening effect which

coincides with the exhaustion of twinning, and ultimately, strain hardening slows as slip-based deformation occurs inside twins (e.g., Muransky et al., 2010). Basal slip activity is dominant when twin volume fraction is low, and it drops in favor of pyramidal slip as twin grows. Viscoplastic self-consistent (VPSC) (Proust et al., 2009) and elastoplastic self-consistent (EPSC) (Juan et al., 2014) polycrystal models predicted that pyramidal slip activity inside twin commences near the end of the plateau regime ( $\sim 4\%$  strain), and increases rapidly before reaching steady state at higher strains. In a previous study, we examined some of the dislocation structures near the  $\{10\bar{1}2\}$  twin boundary in both matrix and twin at 2% RD compressed material (Wang and Agnew, 2015). While the matrix contains mostly  $\langle a \rangle$  dislocations and rarely  $[c]$ -containing dislocations, abundant  $[c]$ -containing dislocations were surprisingly common in the twin, even at such low stress level, and it was thus suggested that they are the product of dislocation transmutation reactions.

In this study, samples compressed along RD up to 2% true strain were selected, in order to pursue the origin of the  $[c]$ -containing dislocations and the activity of pyramidal slip systems inside tension twins.

### 3.4.1 Dislocations near the $(10\bar{1}2)$ twin boundary from the perspective of ND

Characterization was performed firstly from the ND perspective, where the basal plane in the matrix and the prismatic plane in the twin are close to face-on orientation, and the twinning plane is inclined (Figure 3.3b). This orientation allows the “plan-view” examination of the planes on which the dislocation transmutation occurs. Dictated by the twinning relationship, the  $[0001]_m$  and  $[10\bar{1}0]_t$  zone axes are only  $\sim 4^\circ$  away from each other. Since the characteristic  $[\bar{1}2\bar{1}0]$  diffraction pattern (Figure 3.2b) is not available in the ND sample, the  $(10\bar{1}2)$  twin was



identified by comparing the  $[0002]_m$  and  $[10\bar{1}0]_t$  diffraction patterns of the two crystals and their common  $(1\bar{2}10)$  diffraction spots.

In all the dark field (DF) images in Figure 3.3, the matrix is on the right side and the twin on the left side. Since the  $(10\bar{1}2)$  twinning plane is  $43.2^\circ$  inclined to the basal plane, twin boundary appears as a wide band as delineated in Figure 3.3(a) below the DF image. With a common diffraction vector  $g = (1\bar{2}10)$  operating simultaneously in both matrix and twin, the  $\langle a \rangle$  and  $\langle c + a \rangle$  dislocations are visible, but pure  $[c]$  dislocations are invisible according to the invisibility criterion. Thus, Figure 3.3(a) presents the scenario of  $\langle a \rangle$  dislocations in the matrix and  $\langle c + a \rangle$  dislocations in the twin, corresponding to the type II reaction in Table 3.1. The straight lines of bright contrast in the range of the twin boundary have line directions parallel to the line of intersection of twinning plane and basal plane. They represent the defects on the twin boundary, such as twinning disconnections with edge character.

In Figure 3.3(a), within the range of the inclined twin interface, the contrasts of the dislocations from both crystals are projected into the image. Thus, the sample was oriented such that two-beam diffraction operated in one crystal but no diffracted beam was strongly excited in the other crystal. In this way, the dislocations can be isolated to either the matrix or the twin. As shown in Figure 3.3(c) and (e), the diffraction vector of the twin  $g_t = (1\bar{2}12)$  and that of the matrix  $g_m = (1\bar{1}00)$  respectively reveal the contrast of dislocations in each crystal. The selected dislocation segments, for consideration, are sketched schematically in Figure 3.3(d), and a critical junction is indicated by an arrow in Figure 3.3(d), which connects one dislocation segment in the twin and two segments in the matrix.

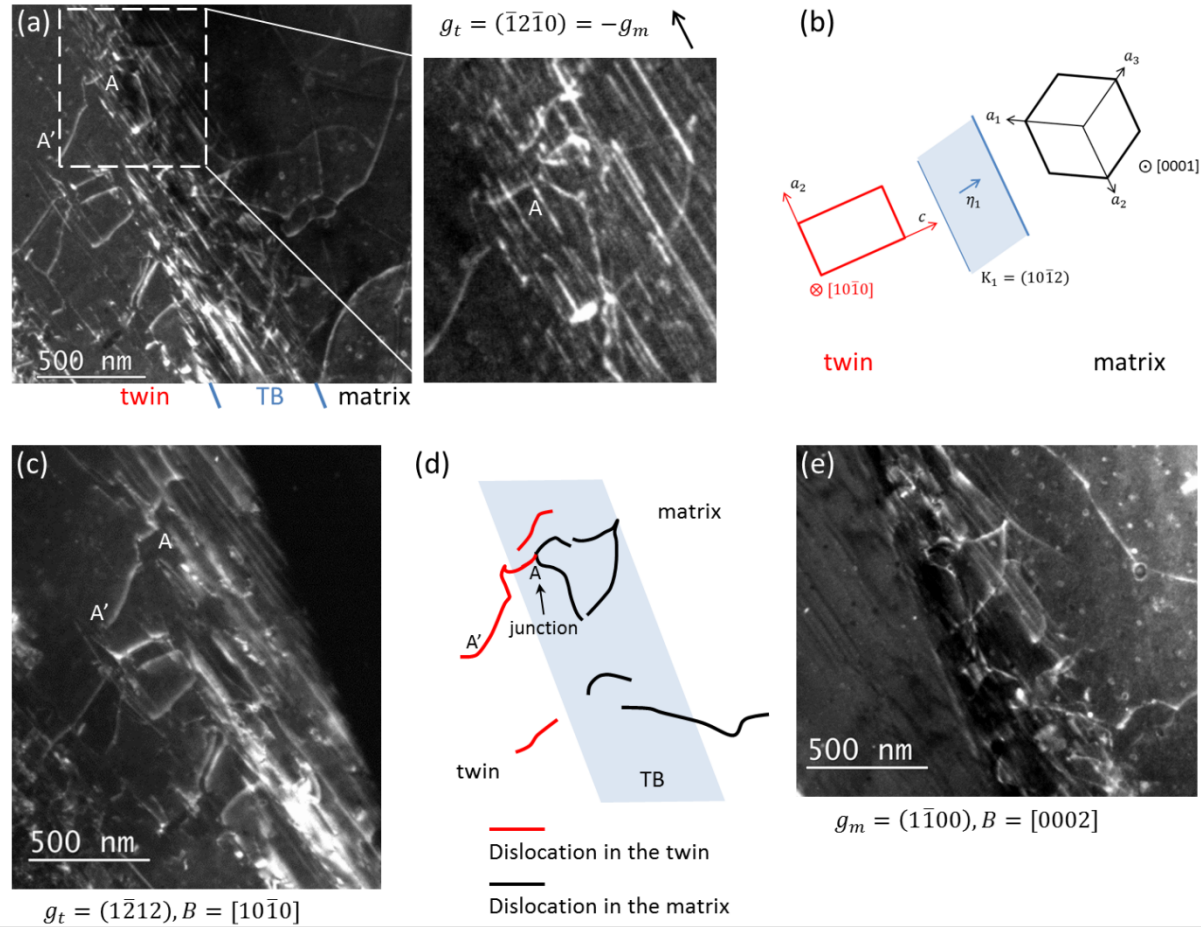


Figure 3.3. Dislocations in the matrix and the twin adjacent to a  $(10\bar{1}2)$  twin boundary (TB) presented in DF images. Image (a) was obtained with the common diffraction vector for the matrix and the twin, the area highlighted by the dashed box outline is magnified for close inspection. The orientations of the two lattices are shown schematically in (b). Images (c) and (e) were obtained with two beam conditions for only the twin or the matrix, respectively. The selected dislocations are sketched schematically in (d). The dislocation segment AA' in (a), (c) and (d) is highlighted to guide the eye.

The orientation of the matrix allows using the diffraction vectors  $(0\bar{1}10)$ ,  $(\bar{1}010)$  and  $(1\bar{1}00)$  to identify the three types of  $\langle a \rangle$  Burgers vectors according to the invisibility criterion (Table 3.2). The corresponding images are shown in Figure 3.4. At the lower left part of all three images, the twin crystal appears dark and void of dislocation contrast because these sample

orientations do not result in any strongly excited diffraction beam in the twin. Inside the matrix, dislocations of all three types of Burgers vector are present, and because the basal plane on which the dislocations lie on is roughly parallel to the foil surface, dislocations appear long before they terminate at a dislocation junction, an internal boundary, or the foil surface. The dislocation segments indicated by the red arrows have the Burgers vector of  $[a_1]$ . Some are connected with the twin boundary, and include the segments identified as being connected with the  $\langle c + a \rangle$  dislocation segment AA' in the twin (Figure 3.3d and e).

Table 3.2. The  $g \cdot b$  values of  $\langle a \rangle$  dislocations with selected diffraction vectors from the zone axis of  $[0001]$ . The corresponding figures (a), (b) and (c) in Figure 3.4 for each  $g$  vector are indicated.

	ZA	[0001]		
Mode	$b \setminus g$	$(0\bar{1}10)$ , (a)	$(\bar{1}010)$ , (b)	$(1\bar{1}00)$ , (c)
$\langle a \rangle$	$1/3[11\bar{2}0]$	-1	-1	0
	$1/3[1\bar{2}10]$	1	0	1
	$1/3[\bar{2}110]$	0	1	-1

For the dislocations in the twin, it is determined with the diffraction vector  $(\bar{1}2\bar{1}0)$  that their Burgers vector is of  $\langle c + a \rangle$  type, because the  $c$ -type dislocations would be invisible (Figure 3.3a). The exact determination of the Burgers vectors necessitates the diffraction vectors from the zone axes  $[10\bar{1}0]$  and  $[11\bar{2}0]$  (Table 3.3), and the corresponding two-beam BF and DF images are shown in Figure 3.5. The images are from the same area as Figure 3.3(c), and the dislocation segment AA' is indicated in Figure 3.5(f). Between the images obtained with the first three diffraction vectors, the  $\langle c + a \rangle$  dislocations are visible with sharp contrast in Figure 3.5(a, f) and (b, g), they are of diffuse contrast in Figure 3.5(c, h). Between the images obtained with the

last two diffraction vectors, dislocations are defined by clearer and sharper contrast in Figure 3.5(d, i) than in Figure 3.5(e, j). They are completely invisible in Figure 3.5(j). Since images (e) and (j) were obtained at the same two-beam condition with  $+g$  (BF) and  $-g$  (DF) respectively, dislocations are expected to display the same visibility in both images. This distinction is attributed to residual contrast, which is more apparent in BF mode than in DF mode. The visibility of the dislocations inside twin at the selected diffraction conditions suggests that their Burgers vector is  $\frac{1}{3}[1\bar{2}13]$ , or  $[c - a_2]$  (Table 3.3).

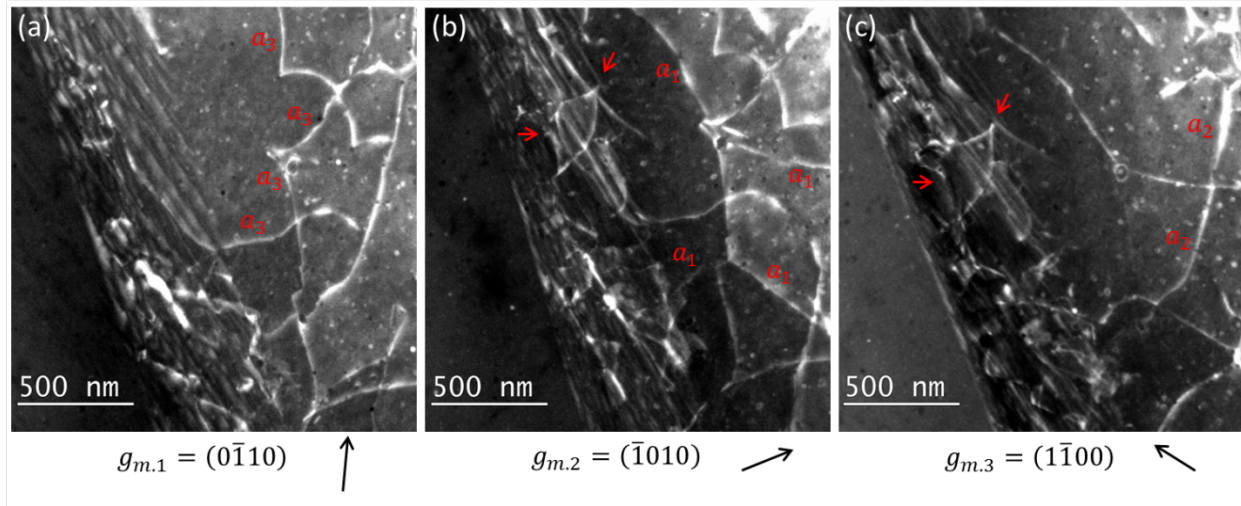


Figure 3.4. Two-beam DF images of dislocations in the matrix from the area shown in Figure 3.3. The corresponding diffraction vectors are under the images with arrows indicating the directions. Some dislocation segments are annotated by their Burgers vectors ( $a_1$ ,  $a_2$  or  $a_3$ ). The red arrows in (b) and (c) indicate the same dislocation segments which are invisible in (a).

Table 3.3. The  $g \cdot b$  values of  $\langle c + a \rangle$  dislocations with selected diffraction vectors from the zone axes of  $[10\bar{1}0]$  and  $[11\bar{2}0]$ . The visibility of the dislocations in Figure 3.5 at each  $g$  vector is indicated in the last row.

	ZA	$[10\bar{1}0]$			$[11\bar{2}0]$	
Mode	$b \setminus g$	$(\bar{1}2\bar{1}0)$	$(1\bar{2}12)$	$(1\bar{2}1\bar{2})$	$(1\bar{1}01)$	$(1\bar{1}0\bar{1})$
$\langle c + a \rangle$	$1/3[11\bar{2}3]$	-1	1	-3	1	-1
	$1/3[1\bar{2}13]$	2	4	0	2	0
	$1/3[\bar{2}113]$	-1	1	-3	0	-2
	$1/3[11\bar{2}\bar{3}]$	-1	-3	1	-1	1
	$1/3[1\bar{2}1\bar{3}]$	2	0	4	0	2
	$1/3[\bar{2}11\bar{3}]$	-1	-3	1	-2	0
Visibility*		v	v	d	v	i

\* v: visible, d: diffuse, i: invisible.

Additionally, the straight and parallel extinction fringes are observed in the interior of the twin in Figure 3.5, they are characteristic of stacking faults (SFs). These SFs are parallel to the trace of the basal planes, they are visible in Figure 3.5 because the high tilt employed to achieve the two-beam conditions has oriented the basal plane at a large deviation from the initial edge-on orientation (e.g. as in Figure 3.3). Tomsett and Bevis (1969b) suggested that the basal SF inside the  $(10\bar{1}2)$  twin can be formed as a result of dislocation transmutation.

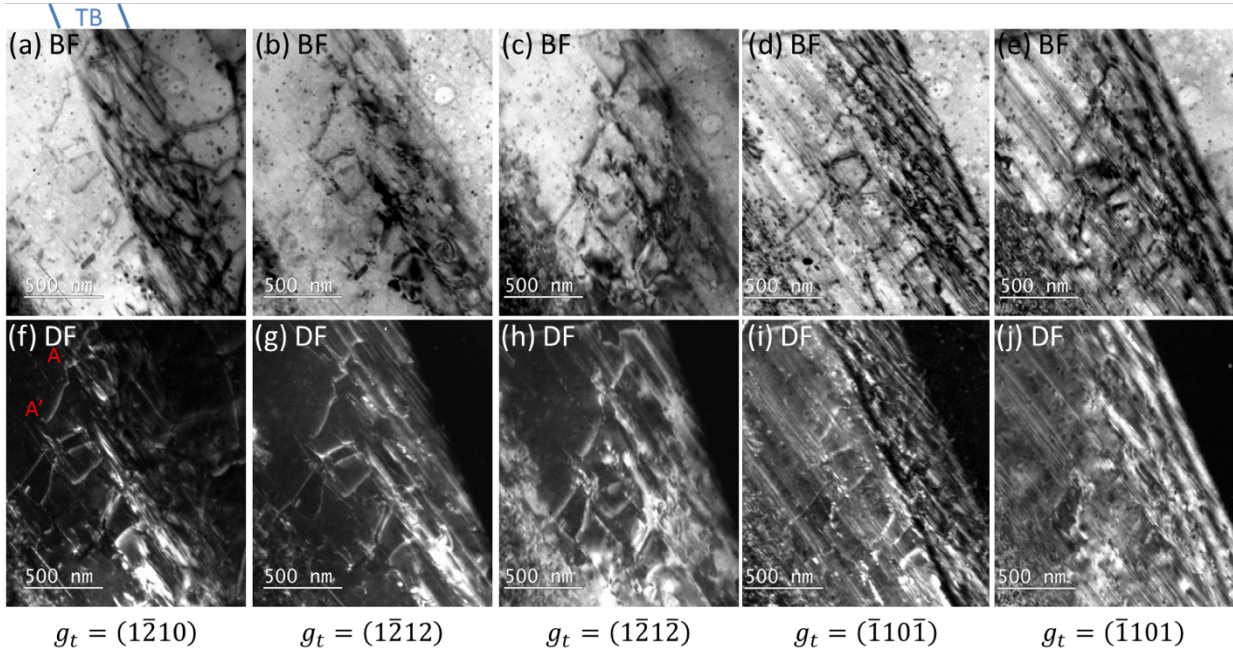


Figure 3.5. Two-beam BF and DF images of the dislocations in the same region of the twin shown in Figure 3.3. The five diffraction vectors employed are shown below each column of BF and DF images. As explained in the text, the contrast reveals the AA' dislocation to be  $1/3[1\bar{2}13]$ , or  $[c - a_2]$ . The faint parallel fringes aligned diagonally from the upper left to lower right of the images in (d, e, i, j) are examples of the numerous basal faults within the twins.

Different from the curved morphology of the dislocations in the matrix, the dislocations in the twin are mostly rectilinear. As shown in Figure 3.6, the  $[c - a_2]$  dislocations in the twin were observed using two-beam conditions from two zone axes, the dislocation segments i, ii and iii are straight for most of their length. (The dislocation segment iii (AA') is the same one as in Figure 3.3(c).) Segments i and ii clearly belong to one dislocation line, and the connection between them is blunt in Figure 3.6(a) and sharp in (b), indicating that the line direction of the connection is parallel to the beam direction  $[11\bar{2}0]$ . Segments i and iii are approximately parallel in both Figure 3.6(a) and (b), thus they have the same line direction. The line directions of segments i and ii were determined by trace analysis (Edington, 1976), and the analysis for

segment i is shown in Figure 3.6(c) as an example. Procedurally, it is preferential to use images obtained at three non-coplanar zone axes, in order to gain three projections of the dislocation line and a quantitative sense of uncertainty. But mathematically, images taken from two zone axes suffice for the determination. Using the conventional stereological techniques, the line direction of dislocation segments i and iii is determined to be  $[4\bar{7}3\bar{9}]$ .

---

The procedure involving the use of the stereographic projection in Figure 3.6 (c), which yields this result  $[4\bar{7}3\bar{9}]$ , is demonstrated here for segment i. To determine the crystallographic direction of an observed dislocation line from 2-dimensional images, the object needs to be observed from at least two distinct perspectives, e.g. two zone axes. In each image, the most convenient reference direction within the plane of the image is the diffraction vector used to record the image. The angle between the projected dislocation line in the image with the diffraction vector can be used to define one crystallographic plane the dislocation lies on. Since the projection of any dislocation on that plane will have the same angle between the diffraction vector, a different plane where the dislocation also lies on needs to be found by observation from a different perspective, and the common direction of both planes is the dislocation line direction.

Firstly, the angle between the diffraction vector  $g$  and the normal to the dislocation line is measured in Figure 3.6 (a) and (b) respectively. The former represents the pole of a chosen plane, and the latter represents the plane the dislocation lies on. The positive direction of the normal to segment i is arbitrarily taken as pointing to the upper left in the images. The angles are  $174^\circ$  and  $7^\circ$  for  $g_1$  and  $g_2$  respectively. With these angles, the  $(\bar{2}4\bar{2}\bar{5})$  pole is obtained  $174^\circ$  counter-clockwise from the  $(1\bar{2}12)$  pole around the  $[10\bar{1}0]$  zone axis, and the  $(19\bar{1}9\ 0\ 25)$  pole is obtained  $7^\circ$  clockwise from the  $(1\bar{1}01)$  pole around the  $[11\bar{2}0]$  zone axis (Figure 3.6c) (it is equivalent to  $(\bar{1}9\ 19\ 0\ \bar{2}\bar{5})$  pole from the  $(\bar{1}10\bar{1})$  pole, although both are in the negative hemisphere of the stereograph). This means that the dislocation lies on both  $(\bar{2}4\bar{2}\bar{5})$  and  $(19\bar{1}9\ 0\ 25)$  planes. The arcs corresponding to the two planes intersect approximately at the pole  $[4\bar{7}3\bar{9}]$ , which is the line direction of dislocation segments i and iii.

---







$[10\bar{1}0]$  stereographic projection. The determined line directions for segment i, ii and iii are shown in the twin crystal lattice (d). The orientation of the lattice is consistent with Figure 3.3(b).

As shown in Figure 3.6(c), the line direction  $[4\bar{7}3\bar{9}]$  of segments i and iii is very close to the periphery of the stereographic projection, and is  $113^\circ$  from the Burgers vector  $[1\bar{2}13]$ . It suggests that segments i and iii are primarily of edge character and remain on the  $(10\bar{1}0)$  plane after transmutation. Following the same procedures, dislocation segment ii was determined to have the line direction  $u = [01\bar{1}\bar{3}]$ , which is distant from the periphery of the stereographic projection and is  $163^\circ$  from the Burgers vector  $[1\bar{2}13]$ . Thus, this dislocation segment is of primarily screw character and has probably undergone cross-slip after transmutation. The cross product of the line direction  $u = [01\bar{1}\bar{3}]$  and Burgers vector  $b = [1\bar{2}13]$  were used to determine a possible glide plane normal. And this analysis suggests  $(11\bar{2}1)$  as a potential glide plane. The preferred glide planes of  $\langle c + a \rangle$  dislocations reported in literature include the first-order pyramidal planes  $\{1\bar{1}01\}$  and second-order pyramidal planes  $\{1\bar{2}12\}$  (Sandloebes et al., 2013; Obara, Yoshinga and Morozumi, 1973; Li and Ma, 2009). It is possible that the observed dislocation has undergone wavy slip involving a combination of these planes (Geng et al., 2015).

With this complete crystallographic knowledge of the  $[c - a_2]$  dislocations in the twin, the connection of the segment AA' on the twin boundary was confirmed. It was presented in Figure 3.3 that the segment AA' is connected with two dislocation segments in the matrix on the twin boundary. The segments ii and iii (AA') terminate within the range of the twin boundary in the image, thus they intersect the boundary within the foil thickness (Figure 3.6a, b, d). Segment i, on the other hand, terminates within the interior of the twin, away from the twin boundary fringes. Thus, it terminates at the foil surface before reaching the twinning plane.

In conclusion, a dislocation transmutation reaction comprised of two  $[a_1]$  dislocation segments in the matrix and one  $[c - a_2]$  dislocation in the twin was observed. The reaction is consistent with the type II reaction in Table 3.1. The junction of the associated dislocations on the twin boundary was confirmed by stereological analysis.

### 3.4.2 Dislocations near the $(10\bar{1}2)$ twin boundary from the perspective of TD

In the ND sample, since the basal plane in the matrix and prismatic plane in the twin on which the reaction occurs, are roughly parallel to the foil surface, only a limited number of  $\langle c + a \rangle$  dislocations were observed through the thin foil thickness. In contrast, characterization of the transmutation reaction on multiple layers was realized in the TD sample, where the basal, prismatic and twinning planes are all nearly edge-on. Figure 3.7 presents a grain scale picture of a  $(10\bar{1}2)$  twin and the associated dislocation structure. When the matrix diffraction vector  $g_m = (10\bar{1}0)$  is used for imaging, the close alignment with  $g_t = (0002)$  of the twin enables the observation of only  $\langle a \rangle$  containing dislocations in the matrix and  $[c]$  containing dislocations in the twin. In the matrix, dislocations are well aligned with the basal plane trace, so they are most likely lying on the basal plane. Inside the  $(10\bar{1}2)$  twin, the dislocations are either  $\langle c + a \rangle$  or  $[c]$ . It is readily revealed that there are abundant dislocations near the left twin boundary, and the boundary deviates from the  $(10\bar{1}2)$  plane trace indicated by the red dashed line, whereas in other areas of the twin, dislocations appear only occasionally. It is also note-worthy that at the two-beam condition of  $g_t = (0002)$ , there is contrast on the basal plane inside the twin (Figure 3.7b), suggesting that the defects on the basal plane have a  $\langle c \rangle$  component. They are possibly  $\langle c + a \rangle$  dislocations or dissociation products lying on the basal plane, e.g. the  $I_1$  fault, which has been

suggested to be intimately connected with  $\langle c + a \rangle$  dislocations (Sandloebes et al., 2012; Sandloebes et al., 2013; Agnew, Capolungo and Calhoun, 2015; Wu and Curtin, 2015).

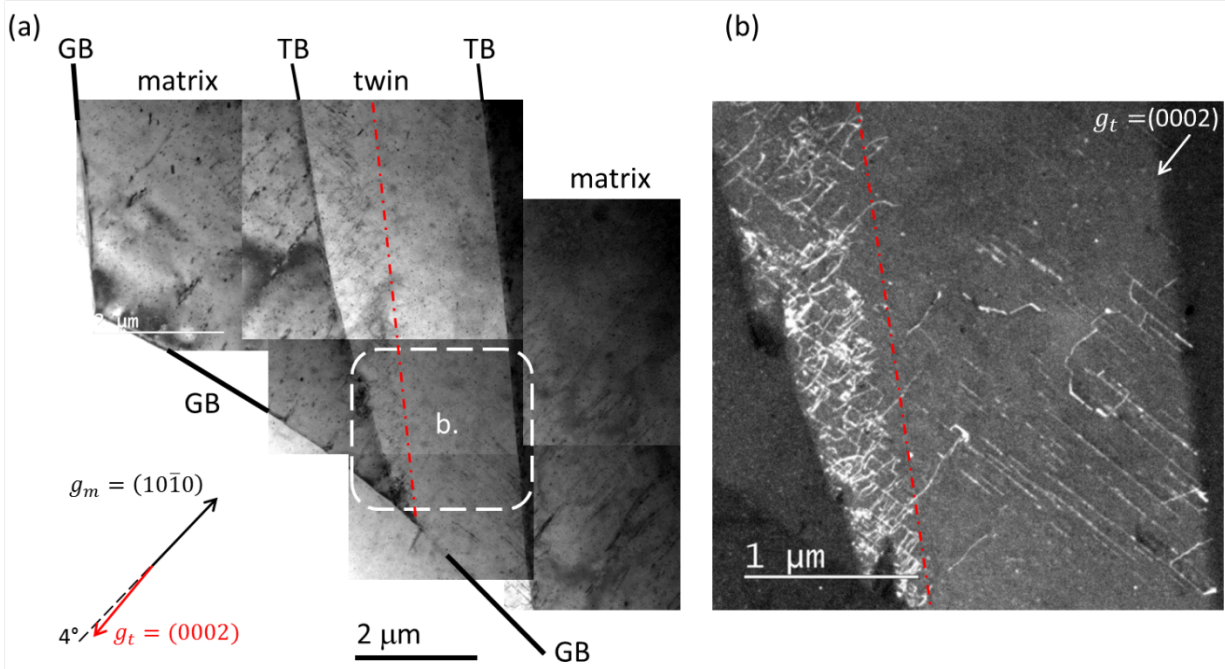


Figure 3.7. (a) A  $(10\bar{1}2)$  twin in a grain, whose grain boundary (GB) is delineated by black lines. The BF images were obtained with the same diffraction condition  $g_m = (10\bar{1}0)$  of the matrix from consecutive areas and were montaged. The dashed red line indicates the plane trace of the  $(10\bar{1}2)$  twinning plane. The area (b) was imaged with  $g_t = (0002)$ , in WBDF mode. The twin boundary is not only curved, it also has a serrated appearance.

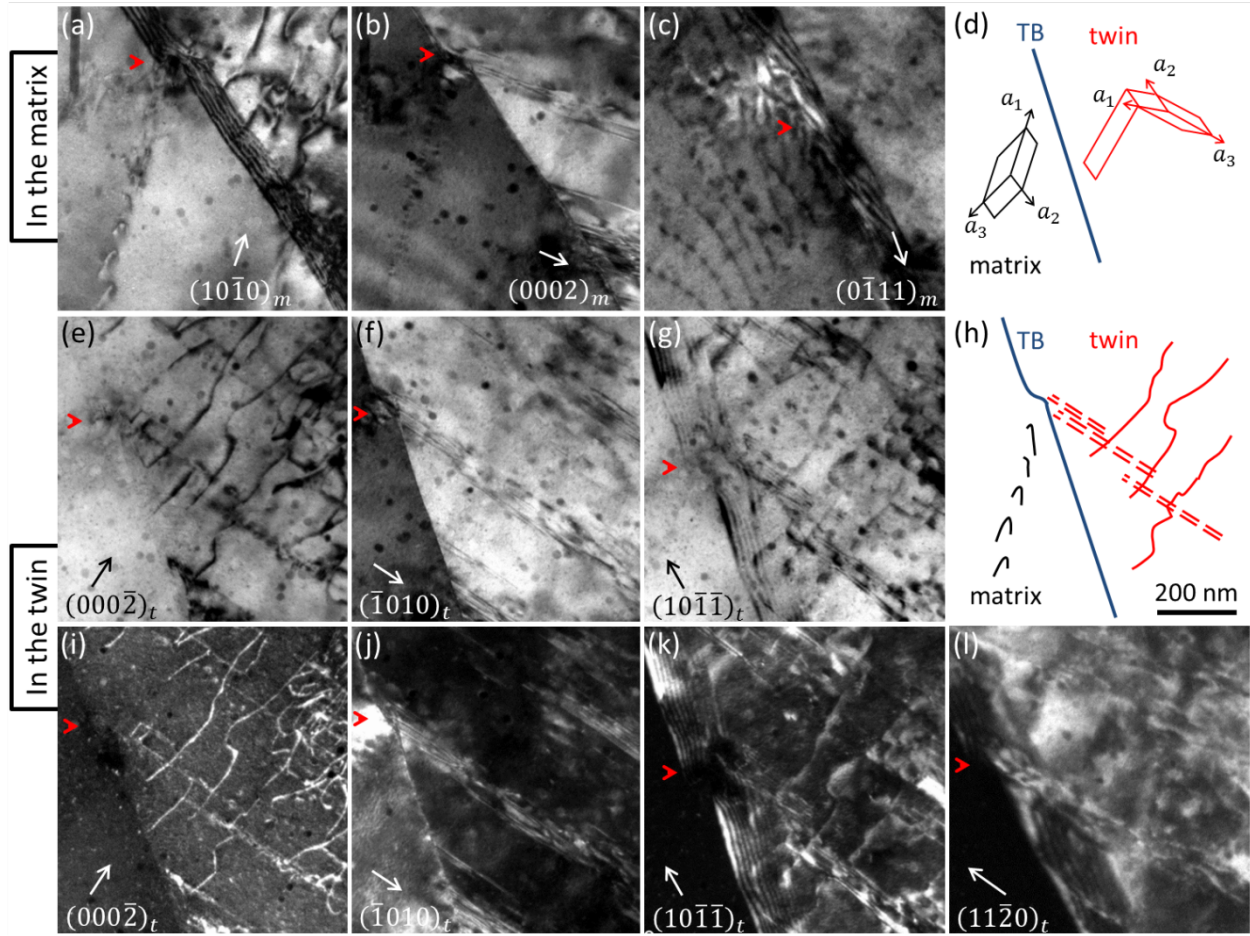


Figure 3.8. Dislocations in the matrix (a), (b) and (c), and in the twin (e)-(g), (i)-(l) imaged with various diffraction vectors. All micrographs show the same area, and the red arrows in the images point at the same location to guide the eye. The orientations of the matrix and twin are shown schematically in (d), with only the basal and prismatic planes plotted for clarity. Selected features of the area are sketched in (h), where the curved lines represent dislocations and the double dashed lines represent SFs.

Closer examination of the left twin boundary in Figure 3.7(b) is presented in Figure 3.8. In the matrix (Figure 3.8a-c), a train of dislocations is lying on the basal plane, potentially in a pile-up configuration directed to a point on the twin boundary, as indicated by the red arrow. At the orientation where  $g = (10\bar{1}0)$  is excited (Figure 3.8a), the basal plane is close to edge-on, and the dislocations appear short and sharply curved; when  $g = (0\bar{1}11)$  is excited (Figure 3.8c),

large deviation from the edge-on orientation of the basal plane reveals long and only slightly bowed appearance of the same set of dislocations. The Burgers vector of these dislocations was determined to be  $[a_3]$  due to their visibility in Figure 3.8(a) and (c) and invisibility in (b) (Table 3.4, the rows for Mode  $\langle a \rangle$ ).

Table 3.4. The  $g \cdot b$  values of  $\langle a \rangle$  dislocations in the matrix and  $\langle c \rangle$  containing dislocations in the twin with selected diffraction vectors. The corresponding image numbers in Figure 3.8 for each  $g$  vector are indicated.

	ZA	$[\bar{1}2\bar{1}0]$			$[\bar{1}100]$	$[\bar{2}110]$
Mode	b \ g	(0002)	(10 $\bar{1}$ 0)	( $\bar{1}$ 011)	(11 $\bar{2}$ 0)	(0 $\bar{1}$ 11)
Dislocation in the matrix		(b)	(a)			(c)
$\langle a \rangle$	$1/3[11\bar{2}0]$	0	1	1	2	-1
	$1/3[1\bar{2}10]$	0	0	0	-1	1
	$1/3[\bar{2}110]$	0	-1	-1	-1	0
Dislocation in the twin		(e, i)	(f, j)	(g, k)	(l)	
$\langle c + a \rangle$	$1/3[11\bar{2}3]$	2	1	0	2	0
	$1/3[1\bar{2}13]$	2	0	1	-1	2
	$1/3[\bar{2}113]$	2	-1	2	-1	1
	$1/3[11\bar{2}\bar{3}]$	-2	1	-2	2	-2
	$1/3[1\bar{2}1\bar{3}]$	-2	0	-1	-1	0
	$1/3[\bar{2}11\bar{3}]$	-2	-1	0	-1	-1
$\langle c \rangle$	[0001]	2	0	1	0	1

For the dislocations inside the twin, they are visible with  $g = (000\bar{2})$  and invisible with  $g = (\bar{1}010)$  (Figure 3.8e,i and f,j respectively), confining the possible Burgers vectors to  $\langle c + a \rangle$  and  $[c]$  (Table 3.4). They are of weaker contrast with  $g = (10\bar{1}\bar{1})$  and invisible with  $g =$

( $11\bar{2}0$ ) (Figure 3.8g,k and l respectively). Therefore, their Burgers vector is determined as  $[c]$ . The stronger diffraction contrast in BF images with (0002) than with ( $10\bar{1}\bar{1}$ ) is consistent with the larger  $g \cdot b$  value of the former than the latter.

Besides the  $[c]$  dislocations in the twin, fringes parallel to the basal plane are visible in Figure 3.8(f), (g) and (l), characteristic of SFs. At the diffraction condition of  $g = (0002)$ , which reveals defects with a  $[c]$  component, there is also contrast on the basal plane (Figure 3.8e and i). However, the contrast is discontinuous and diffuse if one compares the fringes which appear at the same locations imaged with other diffraction vectors. Although the identity of these defects was not determined definitively, it is reasonably suggested that some are of  $I_2$  (Shockley) type and those visible with  $g = (0002)$  are most likely  $I_1$  type.

In terms of the distribution of these  $[c]$  dislocations and basal SFs in the twin, the faults appear in stacks, with each group of SFs separated by about 200 nm (e.g. Figure 3.8j and k, Figure 3.9), and the mostly straight  $[c]$  dislocations connect these groups of SFs. This combination of a  $[c]$  and a dissociated  $\langle a \rangle$  dislocation is one of the  $\langle c + a \rangle$  decomposition configurations originally proposed by Bevis and Tomsett (1969b) and recently revealed by molecular dynamics simulation (Wu and Curtin, 2015). Figure 3.9 presents the dislocations in the twin from a nearby area imaged at two-beam conditions from two zone axes  $[\bar{1}2\bar{1}0]$  and  $[\bar{2}110]$ . Most dislocations in this field of view have a  $[c]$  Burgers vector, but the segment in the middle of the images is identified as having a  $[c + a_2]$  Burgers vector, whose diffuse contrast with  $g = (01\bar{1}\bar{1})$  (Figure 3.9c) is ascribed to residual contrast. The observations of  $[c]$  dislocations from these two perspectives reveal that most dislocations remain rectilinear and perpendicular to the basal plane, which is conveniently delineated by the SFs in Figure 3.9(b).

This morphology means that the line direction of the  $[c]$  dislocations in the twin is close to the  $[0001]$  direction, i.e., they are mostly of screw type.

To summarize this section, a train of  $[a_3]$  dislocations in the matrix with  $[c]$  dislocations and basal SFs in the twin were observed in the close vicinity of each other. According to the dislocation transmutation reactions listed in Table 3.1, the  $[a_3]$  dislocation in the matrix can transmute into  $[c + a_2]$ . The resultant dislocation may further dissociate into  $c + I_2$  SF or into a basal  $I_1$  SF bounded by two  $c$ -containing partial dislocations. These reactions are consistent with the observation, although the precise identity of the SFs in the images remains to be confirmed.

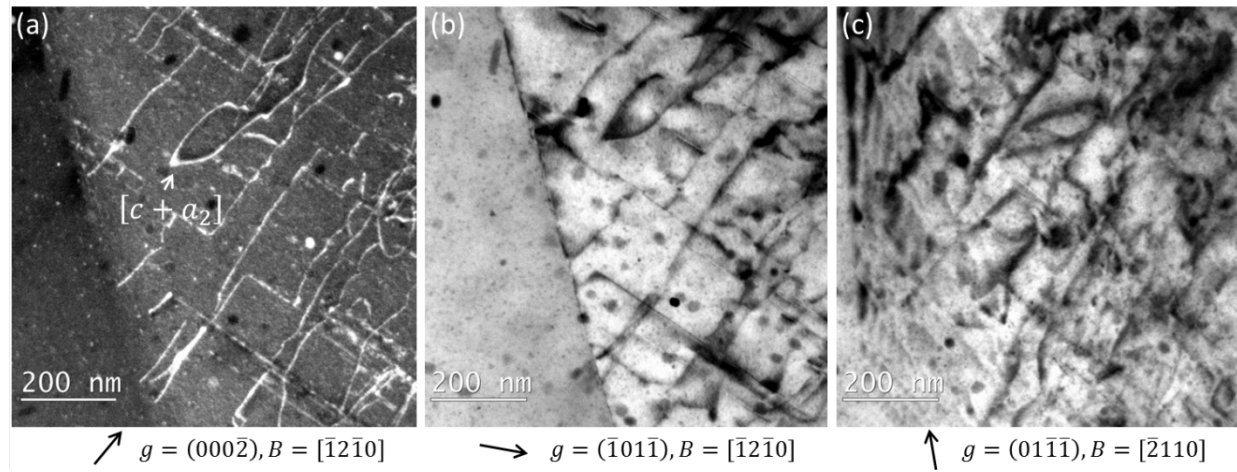


Figure 3.9. Defect structure inside the  $(10\bar{1}2)$  twin imaged with different diffraction vectors from two zone axes (indicated as beam direction  $B$ ).

### 3.4.3 Defect structure inside the $(10\bar{1}2)$ twin

In order to develop a collective understanding of the defect structure inside the twin as a result of dislocation transmutation, the  $(10\bar{1}2)$  twins in differently oriented grains were characterized. Figure 3.10 shows two grains near the hole of a TEM sample sectioned from the TD plane. The external directions RD and ND were marked during the sample preparation to



relate the crystal orientation to the loading direction. TEM analyses of dislocations were subsequently performed within the twins T1 in Grain 1 and T2 & T3 in Grain 2.

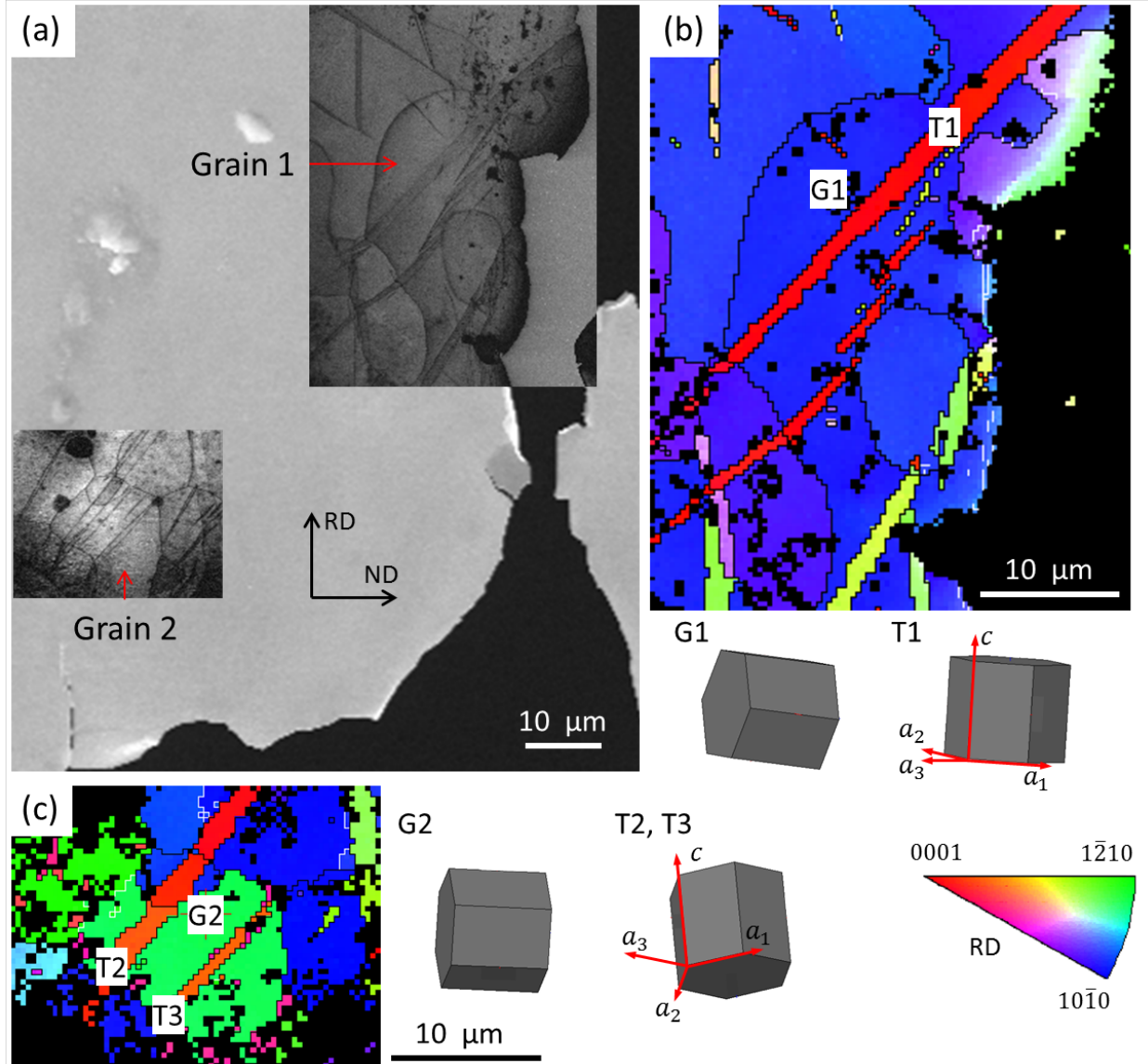


Figure 3.10. (a) Two grains near the hole of the electropolished TEM foil, both including tension twins. The large image was obtained by secondary electron signals, and the images for the two grains were band contrast maps obtained by EBSD scan. (b) The IPF map of Grain 1, the lattice orientations of the matrix (G1) and the twin (T1) are shown below the map. (c) the IPF map of



Grain 2, the lattice orientations of the matrix (G2) and the two twins (T2, T3) of the same variant are shown to the right of the map. The IPF map is color coded by the RD of the sample.

Figure 3.11 presents the defects inside the  $(10\bar{1}2)$  twin T2 in Grain 2. The images at three different two-beam conditions suggest that the defect structure in this twin is qualitatively consistent with the local observations in the previous sections: the twin contains basal stacking faults and  $[c]$  containing dislocations, and the dislocations preferentially populate the vicinity of the twin boundary. The diffraction vector  $(10\bar{1}0)$  yields  $[a_2]$ ,  $\langle c \pm a_2 \rangle$  and  $[c]$  dislocations invisible, and the vectors  $(0002)$  and  $(11\bar{2}0)$  give contrast to  $[c]$ -containing dislocations and  $\langle a \rangle$  containing dislocations respectively (Table 3.4). A collective comparison between the visibility of the dislocations at three conditions determines that most inclined non-basal dislocations are  $\langle c \pm a_2 \rangle$ , while some are pure  $[c]$ . For the  $\langle a \rangle$  containing dislocations on the basal plane, as shown at the  $(11\bar{2}0)$  condition (Figure 3.11c), it is noticed that some are visible at the  $(0002)$  condition, indicating they are  $[c]$ -containing as well. As revealed by the local observations in the TD sample in the previous section (Figure 3.8), the  $[c]$ -containing dislocation segments on the basal plane may be related to faults, namely the bounding partials of the  $I_1$  SF. On the other hand, it is also possible that these segments are edge-type perfect  $\langle c + a \rangle$  dislocation lying on the basal plane. An example is shown in the magnified view Figure 3.11 (c.1), where a dislocation semi-loop has its both ends connected to the dislocation segments on the basal plane.

Whereas most non-basal dislocations in the twin T2 within Grain 2 are  $\langle c \pm a_2 \rangle$ , those in T3 in Grain 2 and T1 in Grain 1 are mainly  $[c]$  dislocations. Figure 3.12 includes the images of T3 in Grain 2 obtained at two conditions. At the  $(0002)$  diffraction condition, many visible  $[c]$ -containing dislocations are straight and perpendicular to the basal plane, and they are invisible at the condition of  $(11\bar{2}0)$ . It is therefore determined that they are pure  $[c]$  dislocations. In the

meantime, this twin contains some  $\langle c \pm a_2 \rangle$  dislocations, based on their visibility in both the (0002) and (11 $\bar{2}$ 0) diffraction conditions. An example is shown in Figure 3.12(a.1). The  $\langle c \pm a_2 \rangle$  dislocation is not perpendicular to the basal plane, and has its both ends connected to the twin boundary, which is a strong indication that it originates from the dislocation transmutation reaction. Additionally, it should be noted that this morphology is very similar to the local observation obtained on ND plane as in Figure 3.6, if it is inspected with the electron beam in the horizontal direction of the image.

Finally, in much narrower twins, only basal stacking faults were observed (Figure 3.13). In (Tomsett and Bevis, 1969b), such basal SFs inside a tension twin were identified as  $I_2$  and were attributed to the decomposition of the transmuted  $\langle c + a \rangle$  dislocation and the subsequent dissociation of  $\langle a \rangle$  dislocation into Shockley partial dislocations. While it is possible that some are  $I_2$  faults formed by this reaction, or other reactions, such as dissociation of  $[a_2]$  dislocations. However, some of the faults give contrast for the  $g = (0002)$  diffraction condition, suggesting that they are of  $I_1$  type. Definitive conclusion with respect to the type of basal stacking faults necessitates the Burgers vector determination of the bounding partial dislocations on twin interface with the assistance of image simulation, which is beyond the scope of the present work. Regardless of being  $I_2$  or  $I_1$  type, the basal stacking fault is confirmed to be a typical kind of defect structure inside the tension twin, their possible origins will be discussed subsequently.

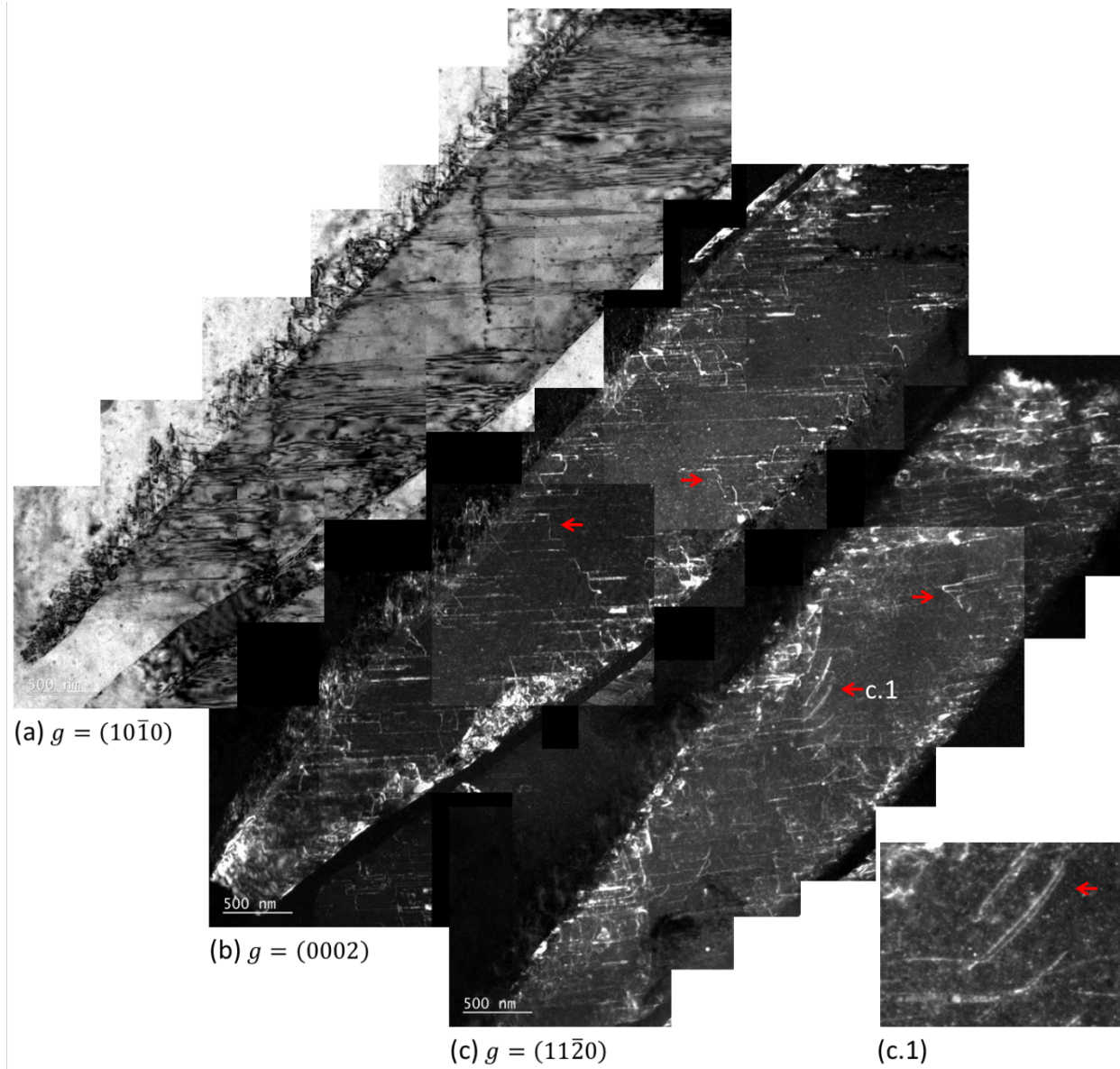


Figure 3.11. Defects inside T2 in Grain 2 from Figure 3.10(c). The twin was characterized with diffraction vectors (a)  $(10\bar{1}0)$ , (b)  $(0002)$  and (c)  $(11\bar{2}0)$  respectively. (c.1) highlights a dislocation feature from (c). In all the images, the basal plane is roughly horizontal. The red arrows point at the same locations in the twin at different imaging conditions to guide the eye.

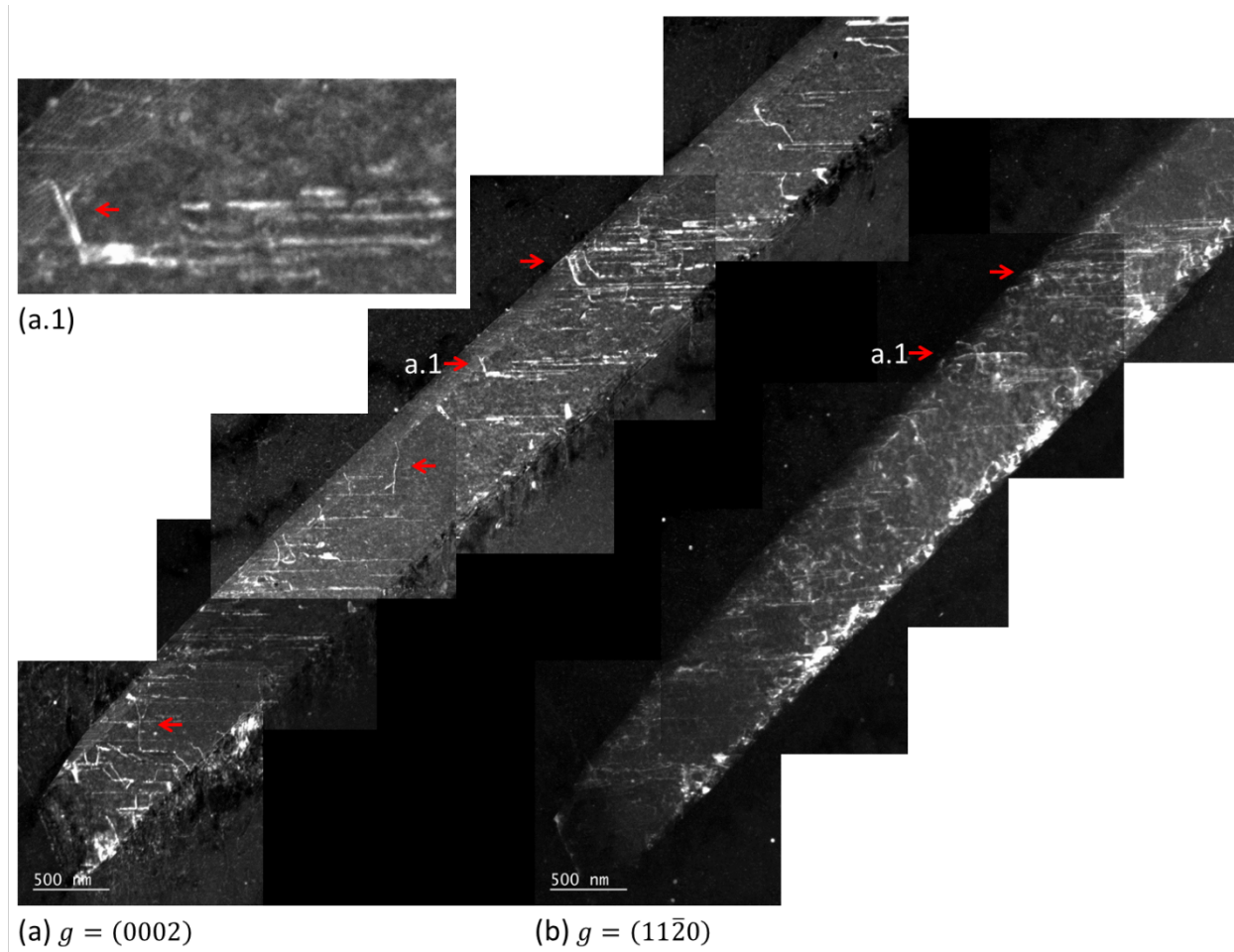


Figure 3.12. Defects inside T3 in Grain 2 from Figure 3.10(c). The twin was characterized with diffraction vectors (a)  $(0002)$  and (b)  $(11\bar{2}0)$  respectively. (a.1) highlights a dislocation feature from (a). In all the images, the basal plane is roughly horizontal. The red arrows point at the same locations in the twin at different imaging conditions to guide the eye.

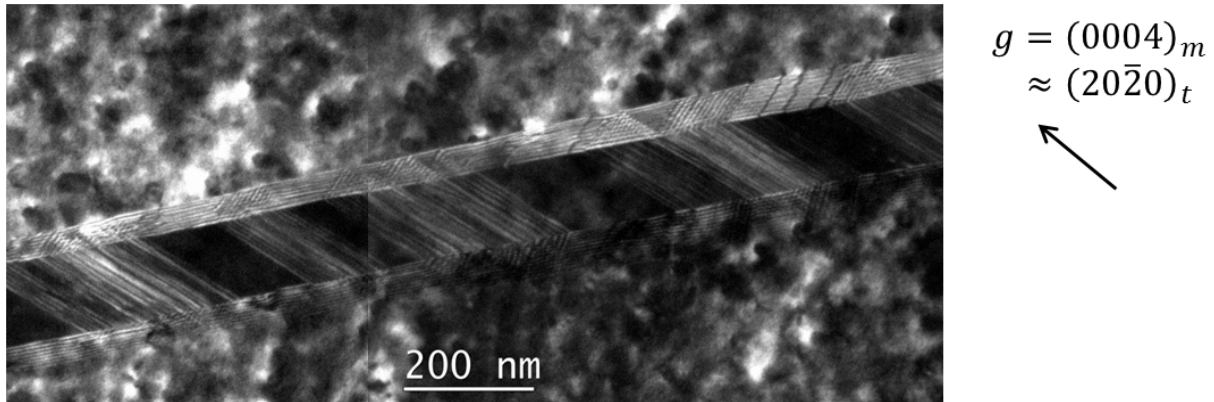


Figure 3.13. DF image obtained with  $g = (0004)_m$  showing basal stacking faults in a narrow  $(10\bar{1}2)$  twin.

### 3.5 Discussion

The current work aims to clarify dislocation transmutation across the  $(10\bar{1}2)$  tension twin boundary by TEM characterization. The incorporation and transmutation of basal  $[a_1]$  and  $[a_3]$  dislocations from the matrix has been observed. From the perspective of the sheet ND, two  $[a_1]$  dislocations from the matrix formed a junction on the twin boundary with a  $[c - a_2]$  dislocation in the twin, the junction was confirmed by stereological analysis of the dislocation segments. From the perspective of TD, a train of  $[a_3]$  dislocations in the matrix were observed to impinge upon the boundary where primarily  $[c]$  dislocations and basal stacking faults (as well as an occasional  $\langle c + a \rangle$ ) were observed in the adjacent twin. Both observations accord with the type II reactions in Table 3.1.

The  $\langle c + a \rangle$  dislocations inside the  $(10\bar{1}2)$  twins preferentially populate the vicinity of twin boundary. At the low global stress level of about 100 MPa, they are generally not expected to be activated in this alloy with this grain size (e.g., Agnew, Brown and Tome, 2006). Therefore, the generation of  $\langle c + a \rangle$  dislocations is attributed to dislocation transmutation. According to the

crystallographic derivation and experimental observation (especially the collective invisibility at the two-beam condition of  $(10\bar{1}0)$ ), these  $\langle c + a \rangle$  dislocations in the  $(10\bar{1}2)$  twin are exclusively  $\langle c \pm a_2 \rangle$ , not any other variant. Therefore, the  $(10\bar{1}2)$  twin provides a suitable location to study the behavior of a specific set of  $\langle c \pm a_2 \rangle$  dislocations. In the following, the process of dislocation transmutation across twin boundary, the origin of  $[c]$  dislocations and the operation of the  $\langle c + a \rangle$  dislocations inside twin are discussed.

### 3.5.1 The process of dislocation transmutation

In the type II dislocation transmutation formulae in Table 3.1, two  $\langle a \rangle$  dislocations are required in order to produce a unit  $\langle c + a \rangle$  dislocation. According to Frank's rule (which is reasonably applied for Mg, given the near elastic isotropy) there is a penalty of  $\Delta b^2 = 1.66a^2$ , with  $a$  being the lattice parameter of Mg. Obviously, this reaction is energetically unfavorable. If the reaction is carried out in two steps successively, each time one unit  $\langle a \rangle$  dislocation is incorporated and transmutes into one half  $\langle c + a \rangle$  dislocation,

$$\langle a \rangle \rightarrow \frac{1}{2}\langle c + a \rangle + \frac{1}{2}b_t$$

Frank's rule yields  $\Delta b^2 = -0.0848a^2$ , revealing a slight energetic incentive for this reaction. When the transmutation of a second  $\langle a \rangle$  dislocation of the same Burgers vector occurs, another  $\frac{1}{2}\langle c + a \rangle$  is generated, which may associate with the first  $\frac{1}{2}\langle c + a \rangle$  to form a perfect  $\langle c + a \rangle$  dislocation in the twin.

Regarding the incorporation and transmutation of one unit  $\langle a \rangle$  dislocation, two possible scenarios and procedures are proposed. The first scenario, illustrated in Figure 3.14 (a-d), shows a mobile dislocation in the matrix moving towards the twin boundary. When the  $\langle a \rangle$  dislocation reaches the twin boundary (TB), transmutation reaction occurs (Figure 3.14 c and d), resulting in

$\frac{1}{2}\langle c + a \rangle_t$  and  $\frac{1}{2}b_t$  on the TB. While the exact interface structure is better addressed by atomistic simulation (e.g., Serra and Bacon (1996) and El Kadiri, Barrett, Wang and Tome (2015)), what is of interest at present is the behavior of the  $\frac{1}{2}\langle c + a \rangle_t$  dislocation. When the second basal dislocation approaches, it is subject to a repulsive force from the  $\frac{1}{2}\langle c + a \rangle_t$  dislocation due to their very similar Burgers vector. Consequently, a pile-up configuration would be required to force the combination of the two repulsive dislocations. On the other hand, if the  $\frac{1}{2}[c + a]$  dislocation is repelled and able to glide into the twin with a fault trailing on its glide plane (Yoo and Wei, 1966), the stress required of the pile-up is somewhat dissipated.

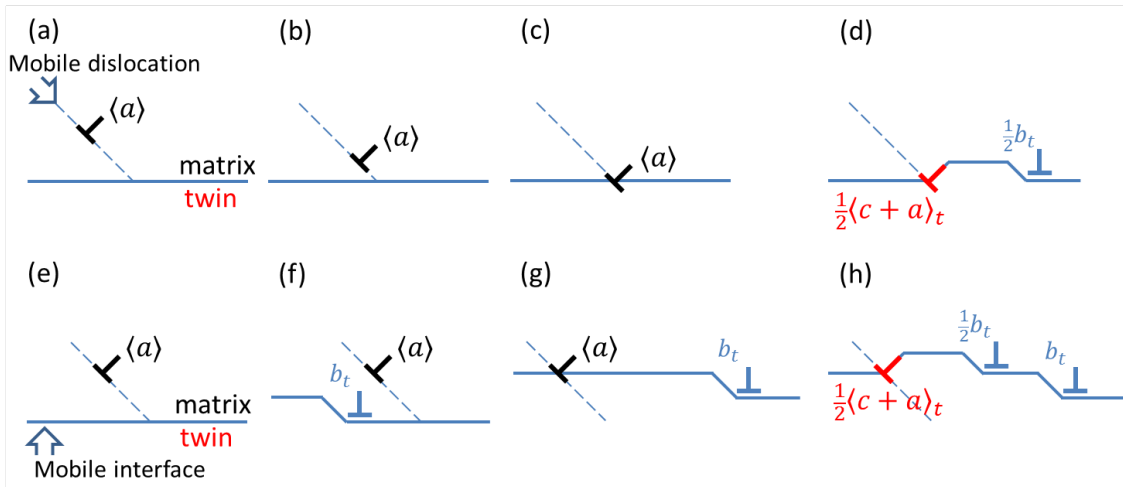


Figure 3.14. The incorporation of one  $\langle a \rangle$  dislocation in the matrix and its transmutation to  $\frac{1}{2}\langle c + a \rangle_t$  at twin boundary. (a-d) depict the scenario of mobile dislocation in the matrix moving towards the stationary twin boundary. The dashed line indicates the basal plane trace in the matrix, which is approximately the prismatic plane trace in the twin. (e-h) depict the scenario of mobile twin boundary moving towards the stationary dislocation, realized by the glide of a twinning dislocation  $b_t$  on twinning plane.

The second scenario, illustrated in Figure 3.14(e-h), describes a mobile twin boundary moving towards the stationary  $\langle a \rangle$  dislocation. It is conventionally held that the twin boundary

moves by the glide of twinning dislocations on the twinning plane (Serra and Bacon, 1996). When the TB finally meets the  $\langle a \rangle$  dislocation in the matrix after successive glide of twinning dislocations, the  $\langle a \rangle$  dislocation is incorporated and transmutes to  $\frac{1}{2}\langle c + a \rangle_t$  and  $\frac{1}{2}b_t$  on the TB (Figure 3.14 g and h). During further advancement of the TB, the transmuted  $\frac{1}{2}\langle c + a \rangle_t$  dislocation may either move along with the TB or detach, leaving a fault in its wake. In either case, again a pile-up structure would be necessary to force the second matrix dislocation to be incorporated by the TB rather than being repelled, due to the same reason as discussed in the first scenario. In fact, the relative movement of the matrix dislocations and TB remain virtually the same between the two scenarios in Figure 3.14.

In both scenarios, successive transmutation reactions generate a large number of twinning dislocations. On one hand, their glide along the twinning plane as well as the basal/ prismatic facets on the twin interface results in TB movement (El Kadiri, Barrett, Wang and Tome, 2015). On the other hand, abundant defects that populate the twin boundary vicinity, including the dislocation pile-ups in the matrix, the trailing faults, and perfect  $\langle c + a \rangle$  and  $\langle c \rangle$  dislocations inside twin, could impede the glide of twinning dislocations on twin boundary and therefore contribute to twin hardening. It is suggested that, if the twinning dislocations accumulate locally, they may contribute to the formation of steps on the TB with large height. This is consistent with the observation in Figure 3.7(b), where the twin boundary that is accompanied by abundant  $[c]$ -containing dislocation not only is curved but also exhibits serrated appearance.

Regarding the necessity of a pile-up of matrix dislocations to force the combination of two repulsive dislocations, the present TEM observations show that basal dislocations appear to have formed a pile-up structure in front of the twin boundary in the TD sample (Figure 3.8a and c). No obvious evidence of pile-ups was observed in the ND sample (Figure 3.4). The dislocation



pile-up in question has been modelled recently using Discrete Dislocation Dynamics (DDD) (Fan et al., 2015), where the initial  $\frac{1}{2}\langle c + a \rangle$  dislocation is assumed to be sessile on the TB. As discussed above, it is also possible that the  $\frac{1}{2}\langle c + a \rangle$  dislocation detaches TB and creates a fault on its glide plane, which was suggested by Yoo and Wei (1966) to be prismatic plane because of its close alignment with the basal plane in matrix. In hcp metals, the faults associated with  $\langle c + a \rangle$  dissociation are reported to be more probable on the pyramidal planes (Numakura, Minonishi and Koiwa, 1990; Ghazisaeidi, Curtin and Hector Jr., 2014) and basal plane (Sandloebes et al., 2013; Agnew, Capolungo and Calhoun, 2015; Wu and Curtin, 2015), and no stable stacking fault was found on the  $\{10\bar{1}0\}$  prismatic plane using the Lennard-Jones model (Bacon and Liang, 1986). On the second order pyramidal  $\{11\bar{2}2\}$  plane, the dissociation of  $\langle c + a \rangle$  into two  $\frac{1}{2}\langle c + a \rangle$  dislocations enclosing a stable stacking fault was predicted in Zr (Morris et al., 1997) and more recently in Mg (Ghazisaeidi, Curtin and Hector Jr., 2014).

In the following, the elastic strain energies of possible configurations of the dislocations involved in the transmutation reaction is considered. The twinning dislocation  $b_t$  is neglected in the subsequent stress and energy calculation, which seems valid because the interfacial step created by  $\frac{1}{2}b_t$  is small, and its stress field is weak due to the small Burgers vector ( $0.076a$  as compared to  $a$  of a unit basal dislocation). Furthermore, the  $\frac{1}{2}b_t$  will be repelled by the dislocations in matrix and twin and, hence, likely glide away on the twin boundary (Fan et al., 2015).

Figure 3.15 presents a model for the energetic evaluation. The matrix  $\langle a \rangle$  dislocations of the same Burgers vector pile up in front of the twin boundary. The pile-up is maintained by the external stress  $\tau$  and comprises  $N$  dislocations up to a distance  $L$  away from the twin boundary. Since the zeroth dislocation is on the twin boundary, it has transmuted and has the Burgers

vector of  $\frac{1}{2}\langle c + a \rangle$  (Figure 3.15c), a step is also created on TB as in Figure 3.14 (d) and (h). This represents the configuration of a sessile  $\frac{1}{2}\langle c + a \rangle$  dislocation on the twin boundary. If the  $\frac{1}{2}\langle c + a \rangle$  dislocation can glide into the twin with a fault trailing on its glide plane, until the 1st dislocation reaches the twin boundary, a new pile-up configuration comprising  $(N-1)$  dislocations with a length  $L'$  is formed (Figure 3.15d). According to (Hirth and Lothe, 1982; Eshelby, Frank and Nabarro, 1951), if one reasonably assumes the Mg alloy is elastically isotropic (Capolungo, Beyerlein and Wang, 2010), the length  $L$  is correlated with the number of dislocations  $N$  under the same loading  $\tau$ ,

$$L = \frac{2NA}{\tau}$$

where  $A_s = \mu b/2\pi$  for screw and  $A_e = \mu b/2\pi(1 - \nu)$  for edge dislocations,  $b$  is the magnitude of the Burgers vector,  $\mu$  is the shear modulus and  $\nu$  is the Poisson's ratio; the latter two materials constants take the value of 16.5 GPa and 0.035 respectively for this simple analysis. For the mixed dislocations of the present case,

$$A = A_s \cos \phi + A_e \sin \phi$$

$\phi$  is the angle between the Burgers vector and line direction, which is  $60^\circ$  for  $\langle a \rangle$  and  $58.4^\circ$  for  $\frac{1}{2}\langle c + a \rangle$ .

For state (b), the energy of the system is the energy of the pile-up, which is treated as one super dislocation with the Burgers vector of  $Nb$ ,

$$E_b = \frac{Gb_{\langle a \rangle}^2 N^2}{4\pi} \left( \cos^2 60^\circ + \frac{\sin^2 60^\circ}{1 - \nu} \right) \left( \ln \frac{R}{r_0} + 1 \right)$$

$R/r_0$  is the ratio of the cut-off radius and the core radius of dislocation, and the value of  $\ln \frac{R}{r_0} + 1 = 12$  is taken, representing  $R/r_0 \approx 6 \times 10^4$ . It can be seen from the equation that the total energy depends only on the number of dislocations  $N$  in the pile-up.

For state (d), the zeroth dislocation will be at equilibrium when the repulsive force due to the pile-up and the attractive force due to the fault are equal. As a first approximation, the  $\frac{1}{2}\langle c + a \rangle$  dislocation is assumed to be on the prismatic plane, the  $4^\circ$  difference between the basal plane in the matrix and the prismatic plane in the twin is neglected, since the width of the fault  $w$  is expected to be much smaller than the length of the pile-up  $L$ . The energy of the fault led by the  $\frac{1}{2}\langle c + a \rangle$  dislocation takes the value of the fault energy on the second order pyramidal plane  $\gamma = 328 \text{ mJ/m}^2$  (Yang et al., 2013), since that on the prismatic plane has not been reported in the literature yet. Note that the difference between the present calculation and one which examines  $\frac{1}{2}\langle c + a \rangle$  partial dislocation emission from the boundary on a second order pyramidal plane is only different by a small geometrical factor. The force equilibrium is

$$\sigma_{pile-up} \cdot b_{\frac{1}{2}[c+a]} = \gamma$$

and  $\sigma_{pile-up} = \tau \cdot \sqrt{\frac{2(N-1)A}{\tau \cdot w}}$  near the tip of the pile-up, where  $w \leq L'$ . Note that the pile-up comprises  $(N-1)$  dislocation in state (d) (Figure 3.15).

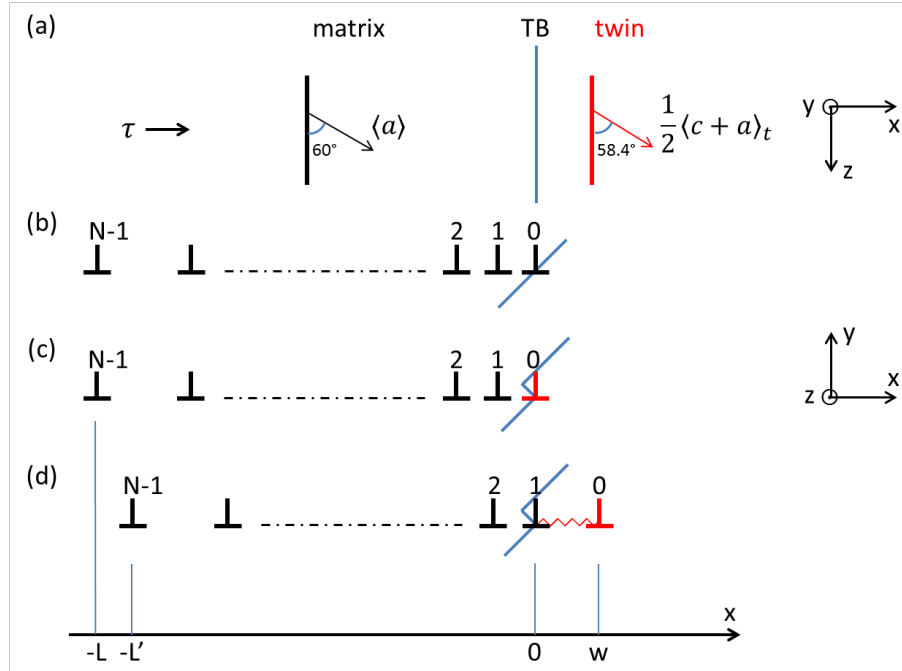


Figure 3.15. (a) Dislocation lines and Burgers vectors in the matrix and the twin. (b)-(d) The incorporation and transmutation of the zeroth and first dislocations. The pile-up dislocations are depicted schematically in front of the twin boundary (TB). The wavy line in (d) indicates the fault created by the  $\frac{1}{2}\langle c + a \rangle_t$  dislocation.

A calculation with an external stress  $\tau = 100$  MPa and a large number of dislocations in the pile-up  $N = 10$  yields that the length of the pile-up  $L$  is 236 nm, and the equilibrium fault width  $w$  is 1.85 nm, so the aforementioned approximations related to the relative lengths  $w$  and  $L$  are valid. The energy of the system is the sum of the energy of the pile-up, fault energy and energy of the  $\frac{1}{2}\langle c + a \rangle$  dislocation,

$$E_d = \frac{Gb_{\langle a \rangle}^2(N-1)^2}{4\pi} \left( \cos^2 60^\circ + \frac{\sin^2 60^\circ}{1-\nu} \right) \left( \ln \frac{R}{r_0} + 1 \right) + w \cdot \gamma$$

$$+ \frac{Gb_{\frac{1}{2}[c+a]}^2}{4\pi} \left( \cos^2 58.4^\circ + \frac{\sin^2 58.4^\circ}{1-\nu} \right) \left( \ln \frac{R}{r_0} + 1 \right)$$

The energy of the states (b) and (d) in Figure 3.15 are evaluated as a function of the external stress  $\tau$  for different number of dislocations in the pile-up  $N$ . For a given number of dislocations in the pile-up, the energy of the state (b) is constant regardless of the external stress, because the length of the pile-up varies with stress, but the energy of the ensemble depends only on the number of dislocations. The energy of state (d) increases with increasing stress, since the increasing stress tends to increase the width of the fault led by the  $\frac{1}{2}\langle c + a \rangle$  dislocation in the twin. The comparison of the energy between the two states reveals that, in the range of plausible stress ( $\leq 4$  GPa) and for a given number of dislocations ( $N \leq 20$ ) in the pile-up, the state (d) has lower overall energy than the state (b). Assuming that the dislocation core energies are not a strong function of applied stress, the energy difference is on the order of  $10^{-8} \text{ J/m}$  ( $\sim 20 \text{ eV/b}$ ).

Finally, the above calculation suggests that, at the first step of the dislocation incorporation and transmutation, the  $\frac{1}{2}\langle c + a \rangle$  dislocation is likely to leave the twin boundary (or be left by it) with a trailing fault in the twin (Figure 3.16a and b). Such configuration necessitates a pile-up of dislocations in the matrix in front of the TB to maintain the force balance. With increasing number of dislocations in the pile-up or increasing external stress, the second matrix dislocation will be incorporated and transmuted. At this point, the second  $\frac{1}{2}\langle c + a \rangle$  partial dislocation would recover some energy as it erases the fault created by the first partial and form a perfect  $\langle c + a \rangle$  dislocation (Figure 3.16c). Note that if the  $\frac{1}{2}\langle c + a \rangle$  partial dislocation is effectively sessile within the twin, motion of the TB could increase the fault length even further than suggested by the force balance computed above, rendering the subsequent formation of a perfect  $\langle c + a \rangle$  even more energetically favorable. After passing this critical step, it is reasonably hypothesized that subsequent motion of the TB will force continued “zipping up” of the two repulsive  $\langle a \rangle$  dislocations into a perfect  $\langle c + a \rangle$  dislocation at the junction shown in Figures 16

(c) & (d). The resulting picture is consistent with the observations, such as those presented in Figure 3.3.

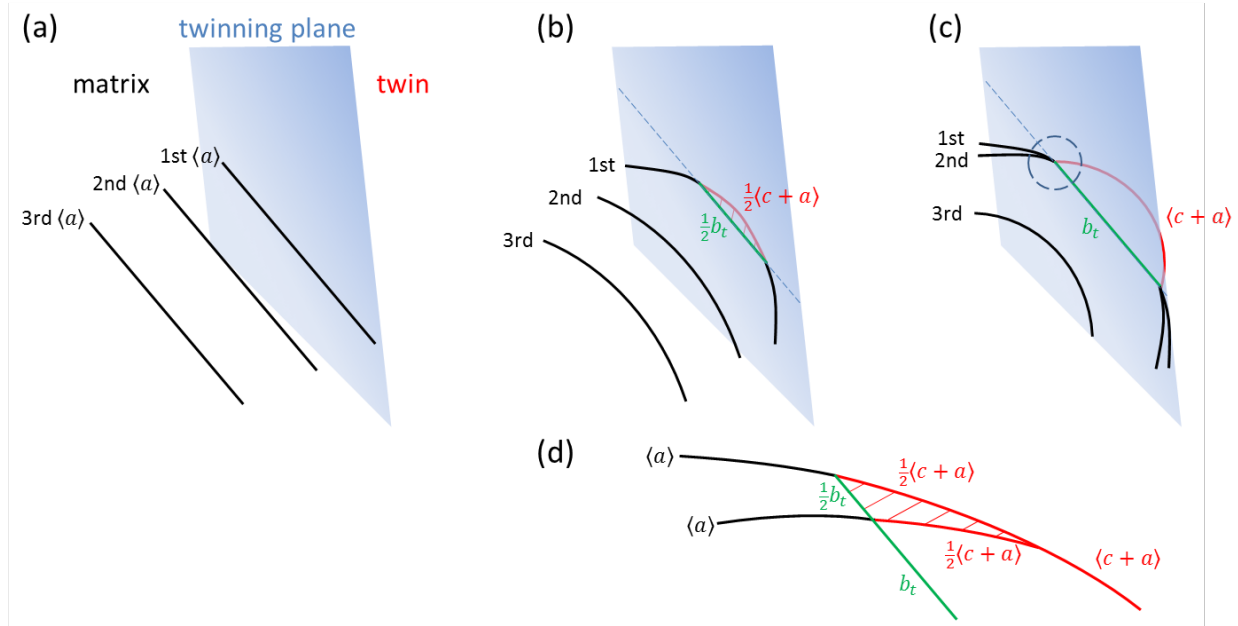


Figure 3.16. The successive incorporation and transmutation of the first two basal dislocations from the matrix at twin boundary. The area filled by parallel red lines in (b) and (d) represents a stacking fault. Figure (d) presents the detailed configuration of dislocations junction as highlighted by dashed circle in (c).

Admittedly, the model may not capture all the critical kinetic and interfacial structural details. Previous results from Serra and Bacon (1996) and El Kadiri, Barrett, Wang and Tome (2015) showed that a basal dislocation only decomposes into interfacial defects when incorporated by the  $\{10\bar{1}2\}$  twin boundary, and that slip is not transferred from one crystal to another. The current model is not considered in disagreement with the preceding work. Rather, it provides additional possibilities, which are consistent with the experimental evidence, and may be tested by additional atomistic modeling, perhaps with distinct interatomic potentials and boundary conditions.

### 3.5.2 The $\langle c \rangle$ dislocations and basal stacking faults inside twin

In some of the twins surveyed, not only perfect  $\langle c + a \rangle$  dislocations, but also  $[c]$  dislocations and basal stacking faults were observed, sometimes even exclusively. In the work of Tomsett and Bevis (1969b), based on the coexistence of basal dislocation in the matrix and  $I_2$  SF in the twin, and the premise of  $\langle a \rangle$  dislocation transmuted into  $\langle c + a \rangle$  dislocation, they reported the decomposition of the resultant  $\langle c + a \rangle$  dislocation in the twin into  $\langle c \rangle$  and  $\langle a \rangle$  dislocations. Further dissociation of the  $\langle a \rangle$  dislocation into two Schockley partial dislocations gives rise to the formation of  $I_2$  SF. A general expression of the dissociation is

$$\frac{1}{3}\langle \bar{1}2\bar{1}3 \rangle \rightarrow \langle 0001 \rangle + \frac{1}{3}\langle \bar{1}2\bar{1}0 \rangle \rightarrow \langle 0001 \rangle + \frac{1}{3}\langle 01\bar{1}0 \rangle + \frac{1}{3}\langle \bar{1}100 \rangle$$

Assuming elastic isotropy and ignoring the core contributions, the dissociation of  $\langle c + a \rangle \rightarrow \langle c \rangle + \langle a \rangle$  results no reduction in elastic strain energy for a dislocation line. This reaction was proved possible recently by molecular dynamics simulations (Wu and Curtin, 2015) based on a reduction in dislocation total energy, despite being a smaller reduction than that of other possible decomposition reactions. Further, the atomistic simulations showed that this decomposition is the dominant one at high loads. The current results involve a different scenario where the  $\langle c + a \rangle$  dislocation assumes a specific configuration, e.g. both ends terminating at twin boundary or connecting with dislocation segments on the basal plane (e.g. Figure 3.6, Figure 3.11, Figure 3.12). The approximate geometry is depicted in Figure 3.17, and the energy evaluation using Frank's rule proves that even this simple decomposition is favorable without resorting to considerations of partial dislocations:

$$\langle c + a \rangle^2 \times (2l + w) > c^2 \times (2l + w) + a^2 \times w$$

Only the elastic self-energy of dislocation is considered here using the abstract lengths of dislocation segments; this simple analysis ignores the core energy and the interaction energy between segments. Recall that the observed  $\langle c \rangle$  dislocations within the twins were observed to lie on the prismatic plane with the majority of the length perpendicular to the basal plane. This suggests the  $\langle c \rangle$  dislocations have limited mobility, at least for the loading scenario under consideration.

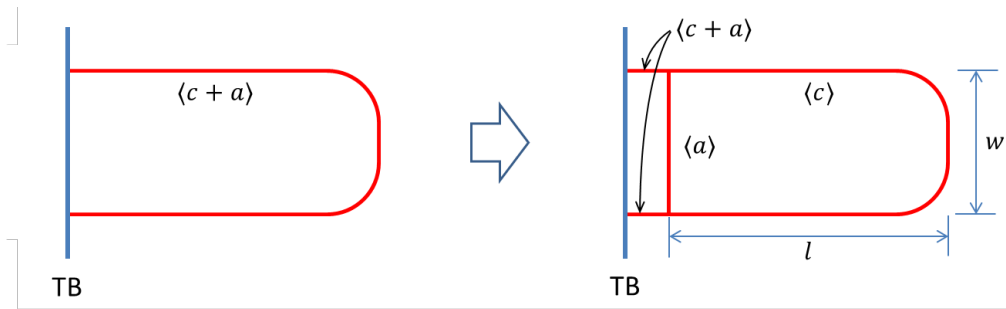


Figure 3.17. A semi-looped  $\langle c + a \rangle$  with both ends on the twin boundary (TB). Part of the dislocation dissociates into  $\langle c \rangle$  and  $\langle a \rangle$  dislocations with length  $l$  and width  $w$ .

An alternative mechanism was proposed by Westlake (1961) that a  $\langle c \rangle$  dislocation can be formed by the transmutation of a  $\langle 10\bar{1}0 \rangle$  dislocation. Following the notations in this work, by adding the two different reactions of type II in Table 3.1, it gives

$$\frac{1}{3}[\bar{2}110]_m + \frac{1}{3}[\bar{1}\bar{1}20]_m \rightarrow \frac{1}{2}b_t + \frac{1}{6}[1\bar{2}13]_t + \frac{1}{2}b_t + \frac{1}{6}[\bar{1}2\bar{1}3]_t$$

In a concise form, the transmutation is

$$[\bar{1}010]_m \rightarrow b_t + [0001]_t$$

Therefore, we identify that this mechanism is a variant of the basic transmutation reactions as listed in Table 3.1. Procedurally, this transmutation is realized by the incorporation of two different dislocations, in the current notation  $[a_1]$  and  $[a_3]$ , and the two dislocations react either



in the matrix or in the twin. In the former case, when the two basal dislocations form a junction, the third dislocation connected to the junction has the Burgers vector of  $[\bar{1}010]_m$  based on the continuity of dislocation (Hirth and Lothe, 1982). If the line direction of the third dislocation is parallel to the twin boundary, it is of edge type. The subsequent transmutation of the  $[\bar{1}010]_m$  results in  $[0001]_t$ . In the latter case, the two basal dislocations would undergo transmutation sequentially, resulting in  $\frac{1}{2}[c + a_2]_t$  and  $\frac{1}{2}[c - a_2]_t$ , respectively. The subsequent reaction of the two yields a pure  $\langle c \rangle$  dislocation in the twin. While the concurrent presence of both  $\langle c \rangle$  dislocations and basal SFs in our results is in agreement with the reaction of  $\langle c + a \rangle$  decomposition, it does not exclude the possibility of the mechanism of Westlake (1961). In fact, the reaction of two different  $\langle a \rangle_m$  or  $\langle c + a \rangle_t$  dislocations might be easier in terms of dislocation interaction than the reaction of two dislocations of the same Burgers vector as discussed in the previous section. The two different  $\langle a \rangle_m$  vectors,  $[-a_1]$  and  $[a_3]$ , are  $60^\circ$  to each other, and the two  $\langle c + a \rangle_t$  vectors,  $[c + a_2]$  and  $[c - a_2]$ , are  $63.2^\circ$  to each other. These dislocations are subject to smaller repulsive forces than the case of two dislocations of the same Burgers vector.

Rather than forming an  $I_2$  stacking fault from the decomposition of  $\langle c + a \rangle$  dislocation, according to (Stohr and Poirier, 1972), a possible non-planar dissociation of  $\langle c + a \rangle$  dislocation can result in an  $I_1$  stacking fault on the basal plane:

$$\frac{1}{3}\langle \bar{1}2\bar{1}3 \rangle \rightarrow \frac{1}{6}\langle 02\bar{2}3 \rangle + \frac{1}{6}\langle \bar{2}203 \rangle$$

It was recently proven as a low energy dissociation product of  $\langle c + a \rangle$  dislocations by elasticity considerations (Agnew, Capolungo and Calhoun, 2015) and molecular dynamics simulations (Wu and Curtin, 2015), though it requires climb of the leading partial dislocation into the basal plane. Notably, this faulted configuration is expected to be sessile. In the current study, two types of SF were observed and discriminated using the (0002) two-beam diffraction condition. Those

became invisible at that condition were presumably of  $I_2$  type and those remained visible were presumably of  $I_1$  type.

Finally, if transmutation of  $[a_2]$  occurs, although not captured in the current observations, the product inside twin is  $[a_2]$  (the type I reaction in Table 3.1). The subsequent dissociation of  $[a_2]$  inside twin into two Shockley partial dislocations will create a SF on basal plane. The balance between the repulsive force of the two bounding partials and the attractive force of the stacking fault energy renders an equilibrium fault width on the order of 20 nm (23.9 nm from isotropic continuum elasticity and 16.7 nm from ab initio modeling (Yasi et al., 2009)). However, it is suggested that if the two bounding partials are attached to opposing twin boundaries, a larger fault width may be realized. This is similar to the emission of partial dislocation from grain boundary with a trailing fault in nanocrystalline metals, e.g. Al (Yamakov et al., 2002). And this may be a possible explanation for the traversing basal stacking faults in narrow twins (Figure 3.13, the twin width is 260 nm).

### 3.5.3 Effect of stress state on the $\langle c + a \rangle$ dislocations inside twin

Abundant  $\langle c + a \rangle$  dislocations were observed in the  $(10\bar{1}2)$  twins, in material loaded into the plateau regime of the RD compression flow curve. In light of the prediction by polycrystal plasticity modeling that pyramidal slip inside twin commences at the end of the plateau ( $\sim 4\%$  macroscopic strain) (Proust et al., 2009; Juan et al., 2014), it is of interest to study the stress state imposed on these  $\langle c + a \rangle$  dislocation, in order to assess their activity.

In a suitably oriented grain under external loading, the occurrence of deformation twinning strongly modifies the stress and strain state of the surrounding (Lebensohn and Tome, 1993). The twin thusly experiences a back stress from the surrounding, counteracting with the

forward stress that promotes twin boundary advancement. If the sum of the resolved shear stress (RSS) on the twin shear system of the applied stress and twin internal stress (one of whose components is back stress as will be introduced below) is zero, or at least smaller than the friction stress of moving a twinning dislocations, the twin is at equilibrium. In the meantime, potential plasticity in the surrounding is able to relax the constraint on the twin and reduce the magnitude of back stress (Barnett et al., 2013), so further twin growth is allowed. Relaxation is induced by dislocation slip and twinning in not only the parent grain but also the suitably oriented neighboring grain. For instance, twins in the neighboring grains can be initiated to maintain strain compatibility at grain boundaries, and in this manner twinning spreads progressively over the sample (Barnett, Nave and Ghaderi, 2012; Wang et al., 2014). In Figure 3.10 (a), the twins T1 in G1 and T2 in G2 are accompanied by twins in the adjacent grain, forming twin pairs, but the twin T3 in G2 is not. It is expected that the internal stress in these twins is modified accordingly.

The exact determination of the net effective stress inside twin necessitates grain scale experimental characterization (Aydiner et al., 2009) or simulation, considering various extents of plastic relaxation of the stress. In the present work, the effective stress is calculated at two limiting cases. The first case assumes that the elastic internal stress of the twin is completely relaxed by plastic deformation in the surroundings. Therefore, the twin interior is subject to only the external applied stress. The second case assumes that the elastic internal stress of twin is preserved, without plastic relaxation from the surrounding grains. In this case, the effective stress inside twin is the superposition of the applied stress and internal stress. The studied material of this work is at the applied stress of  $\sim 100$  MPa, which is much smaller than the macroscopic yield stress (more than 200 MPa as taken from the RD tension flow curve in Figure 3.1a). At this stage,

plasticity in the surrounding is unlikely to relax all the back stress acting on a twin (Barnett et al., 2013). So the effective stress in most twins should be within the limiting bounds.

In order to calculate the internal stress, the twin is treated as an elastic inclusion of oblate spheroidal shape ( $a_1 = a_2 > a_3$ ), and the elastic constants are assumed to be the same for the twin and the matrix, based on the fact that magnesium is nearly elastically isotropic. In the spatial coordinate system of  $x_1$  parallel to the shear direction  $\eta_1$ ,  $x_2$  perpendicular to the twinning plane  $K_1$  and  $x_3$  perpendicular to the other two axes, the deviation of the stress, internal stress  $\sigma_{ij}^i$ , within the twin from the external applied stress  $\sigma^0$  stress can be calculated as (Lebensohn and Tomé, 1993)

$$\sigma_{ij}^i = C_{ijkl} (S_{klmn} \varepsilon_{mn}^p - \varepsilon_{kl}^p)$$

where  $C_{ijkl}$  is the stiffness tensor of Mg, and  $S_{klmn}$  is the Eshelby tensor, relating the eigenstrain to the actual total (elastic and transformation) strain of the inclusion when imbedded in a body (Eshelby, 1957; Kuykendall et al., 2012). In the above equation, both tensors are transformed to the same set of spatial coordinate axes  $x_1$ ,  $x_2$  and  $x_3$ . Analytical expressions of the Eshelby tensor  $S$  for inclusion in an isotropic body have been derived by Mura (1982) for particular inclusion shapes, with its components being functions of the inclusion shape and the elastic constants of the matrix. The exact components of  $S$  are not presented here for the interest of space.  $\varepsilon^p$  is the plastic transformation associated with twin. In the spatial coordinate system, it takes the form of

$$\varepsilon_{mn}^p = \frac{1}{2}s(\delta_{m1}\delta_{n2} + \delta_{m2}\delta_{n1})$$

where  $s$  is the characteristic twinning shear ( $s = 0.13$  for tension twinning in Mg), and  $\delta_{ij}$  is the Kronecker delta function. From the above two equations and based on the traits of the Eshelby tensor, for an oblate spheroidal twin in a given matrix, the only variable that influences the stress

components is the twin aspect ratio ( $q = \text{width}/\text{diameter}$ ), and the internal stress is uniform in the case of ideal elasticity. In the spatial coordinate system of the twin and with the approximated elastic isotropy, the internal stress takes the simple form of

$$\sigma^i = \begin{pmatrix} 0 & \sigma_{12} & 0 \\ \sigma_{12} & 0 & 0 \\ 0 & 0 & 0 \end{pmatrix}$$

The only non-zero stress component  $\sigma_{12}$  acts on the twinning plane (normal to  $x_2$ ) along the shear direction (parallel to  $x_1$ ), and is often referred to as the back stress.

In what follows, calculations were performed for twins inside the matrix at two ideal orientations under a fixed applied uniaxial compression of 100 MPa. The twins have aspect ratio  $q$  ranging from 0.01 to 0.2, covering most of the twins experimentally observed in our material, e.g. from 0.10 to 2  $\mu\text{m}$  twins inside grains of 10  $\mu\text{m}$  in diameter. This is representative of the situation of twins at different stages of growth in the textured material from the plateau regime of the RD compression flow curve, as evident by Figure 3.10. As shown in Figure 3.18 (a) and (e), the two orientations are referred to as  $[10\bar{1}0]$  compression and  $[11\bar{2}0]$  compression, respectively, based on the alignment of the crystallographic direction with the uniaxial sample compression axis  $y_s$ . For  $[10\bar{1}0]$  compression, the twinning system  $(10\bar{1}2)[\bar{1}011]$  is preferentially activated, the twin crystal has its  $c$ -axis almost parallel to the compression axis with a  $\sim 4^\circ$  deviation arising from the twin-matrix relation, and the  $[a_2]$  axis perpendicular to the compression axis; for  $[11\bar{2}0]$  compression, the twinning system  $(10\bar{1}2)[\bar{1}011]$  and  $(01\bar{1}2)[0\bar{1}11]$  are equally stressed, the angles between the compression axis and the twin  $[c]$  and  $[a_2]$  axes are approximately  $30^\circ$  and  $60^\circ$  respectively. For consistency, only the  $(10\bar{1}2)$  twin variant is considered. The pyramidal  $\langle c \pm a_2 \rangle$  and basal and prismatic  $[a_2]$  slip systems inside the twin are of special interests, based on the observed dislocation transmutation reactions.

In the first limiting case, the twin interior is subject to only the external applied stress, and the stress is invariant to twin aspect ratio. For  $[10\bar{1}0]$  compression, all six pyramidal slip systems inside twin experience very similar RSS due to the symmetry of the slip systems with respect to the loading direction. The RSS on pyramidal  $\langle c \pm a_2 \rangle$  slip systems is 44.5 MPa, and 46.8 or 41.8 MPa on others. Since  $[a_2]$  is perpendicular to the stress axis, it experiences zero RSS on either basal or prismatic plane. For  $[11\bar{2}0]$  compression, the pyramidal  $[c - a_2]$  is stressed the most among all the six systems with a RSS of 41.6 MPa and the pyramidal  $[c + a_2]$  the least with a RSS of 2.7 MPa. In contrast to the former orientation, the  $[a_2]$  experiences a much higher RSS of 43.2 MPa on basal plane, but only 2.8 MPa on prismatic plane due to the  $\sim 4^\circ$  deviation of the prismatic plane from the parallel position to the compression axis. At both matrix orientations, the external loading of 100 MPa yields a less than 50 MPa RSS on all six pyramidal slip systems, they are very unlikely active at this stress level (Proust et al., 2009; Juan et al., 2014).

In the second limiting case, dislocations inside twin are subject to not only the external applied stress but also the internal stress of twin, and the effective stress  $\sigma_{eff}$  is given by

$$\sigma_{eff} = \sigma^0 + \sigma^i$$

The applied stress, internal stress and effective stress are firstly resolved to the twinning shear system, and the RSS is plotted with respect to twin aspect ratio for two orientations as in Figure 3.18 (b) and (f). The RSS of the above three stresses represent respectively the twin forward stress, back stress and the net effective shear stress. The applied stress is independent of the twin aspect ratio and results in a RSS of 49.4 MPa and 37.4 MPa for the two orientations respectively. On the other hand, the internal stress increases in magnitude with increasing  $q$  but is independent of the matrix crystal orientation. The sign of the RSS of the internal stress is negative, indicating

that it opposes the twin shear. The RSS associated with the net effective stress exhibits two striking features. First, the effective shear stress on the twinning system is zero or close to zero at a very low aspect ratio  $q \sim 0.01$ . For twins with larger aspect ratios, apart from plastic accommodation of the twinning shear, the effective shear stress on the twin shear system is negative, i.e., it would cause the twin to shrink. The only reason twins are able to thicken beyond the equilibrium aspect ratio is due to plastic accommodation within the surrounding and the twin. Second, the effective shear stress within purely elastic twins reaches a high magnitude exceeding 600 MPa at  $q = 0.2$ . To be clear, the calculation at the limiting case of full elasticity is only for the purpose of illustrating the rank order of the effective RSS values experienced by various slip systems. Focus should be laid to the range of low  $q$  values, where plastic relaxation in the surrounding may only be at small scale and the calculated stress values in the plots are realistic.

When the applied stress is superimposed with the internal stress, the six pyramidal  $\langle c + a \rangle$  slip systems have distinct RSS values (Figure 3.18c and g), as compared to the case of considering only the applied stress. The RSSs on all the slip systems increase monotonically with twin aspect ratio, but some start from negative values, indicating that the stress is in the reversed direction of the defined Burgers vector. Since the slip activity of interest is affected by the magnitude of the RSS, rather than the direction, the absolute values  $|RSS|$  are employed for plotting.

For both matrix orientations, the magnitude of RSS on the transmuted  $\langle c \pm a_2 \rangle$  dislocations is higher than the others only at low  $q$  values, but becomes the lowest for all larger  $q$  values among six pyramidal systems. The RSS curves of  $[c + a_2]$  and  $[c - a_2]$  overlap at the orientation of  $[10\bar{1}0]$  compression (Figure 3.18c), due to the crystal symmetry with respect to the stress, so do those of  $[c + a_1]$  and  $[c - a_3]$ ,  $[c - a_1]$  and  $[c + a_3]$ . At the orientation of

$[11\bar{2}0]$  compression (Figure 3.18g),  $[c + a_2]$  and  $[c - a_2]$  systems have distinct values, yet still remain the lowest.

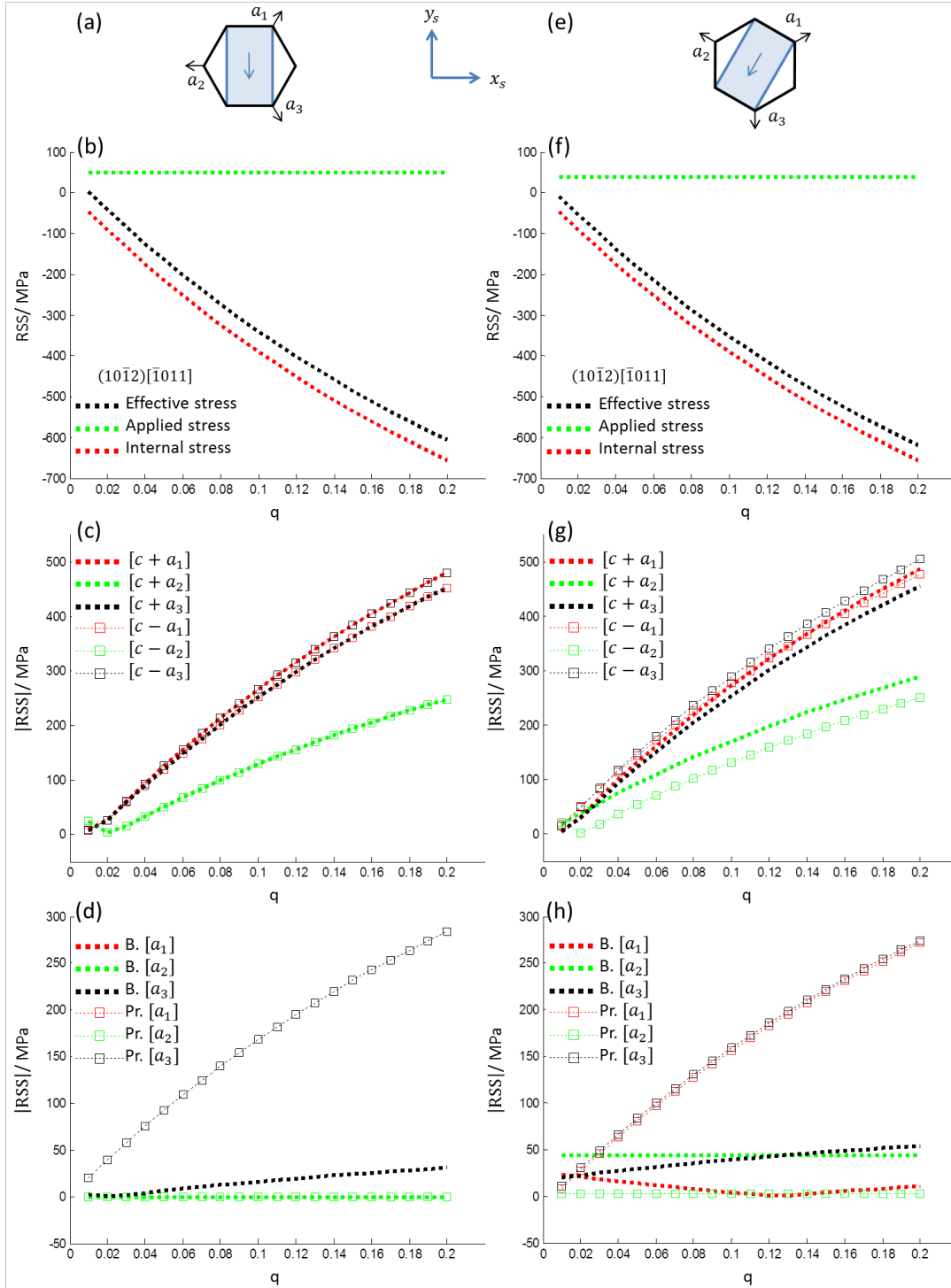




Figure 3.18. When compression load 100 MPa is applied along  $y_s$  to the two matrix orientations (a) and (e),  $(10\bar{1}2)[\bar{1}011]$  twinning is activated, the twinning plane and shear direction are projected onto the basal plane of each matrix crystal as indicated by the blue lines. The RSS on different systems are plotted as a function of twin aspect ratio  $q$  in (b, c, d) and (f, g, h) for the two orientations respectively. (b) and (f): RSS on the twin shear system due to the applied stress, internal stress and effective stress; (c) and (g): the magnitude of RSS on pyramidal  $\langle c + a \rangle$  slip systems due to the effective stress; (d) and (h): the magnitude of RSS on basal and prismatic  $\langle a \rangle$  slip systems due to the effective stress.

Since the non-zero component of the twin internal stress is along the twin shear direction on twinning plane, which is perpendicular to the  $[a_2]$  direction, the RSS on  $[a_2]$  dislocation is invariant to  $q$ , it is only affected by the external loading. The  $[a_2]$  dislocation on basal plane experiences zero RSS at the orientation of  $[10\bar{1}0]$  compression (Figure 3.18d), but the highest RSS for most twin aspect ratios at the orientation of  $[11\bar{2}0]$  compression (Figure 3.18h) among all three basal slip systems. The prismatic  $[a_2]$  slip system has zero RSS at the former orientation and only a small value of 2.8 MPa at the latter one.

The above two limiting cases establish the bounds for effective stress state inside twin. Although the magnitude of the stress in the second limiting case, which assumes full elasticity, may be lower in reality due to plastic relaxation, the results are able to provide some general insights of the dislocation behavior. In both limiting cases, the magnitude of the RSS on the transmuted  $\langle c \pm a_2 \rangle$  dislocations is not high enough to render them active. However, the TEM characterization shows that the  $(10\bar{1}2)$  twins contain exclusively  $\langle c \pm a_2 \rangle$  dislocations among all 6 possible symmetrically equivalent variants. This simultaneously suggests that the  $\langle c \pm a_2 \rangle$  dislocations are the result of dislocation transmutation across the twin boundary and that the operation of  $\langle c + a \rangle$  dislocations is source limited. With increasing applied stress in subsequent

straining,  $\langle c \pm a_2 \rangle$  dislocations would be activated and become a dominant slip system as predicted by polycrystal plasticity models (Proust et al., 2009; Juan et al., 2014). Furthermore, acknowledging the fact that the current investigation is conducted in samples from the plateau region of the flow curve, toward the onset of rapid hardening, the transmuted  $\langle c + a \rangle$  dislocations act as forest dislocations inside twin and will strongly contribute to latent hardening, due to the strong interactions of the pyramidal  $\langle c + a \rangle$  dislocation with basal and prismatic  $\langle a \rangle$  dislocations (Bertin et al., 2014). Therefore, the observed defect structures inside twins establish a basis for subsequent rapid hardening.

### 3.6 Conclusion

In the present work, Mg alloy AZ31B plate was compressed into the plateau region of the flow curve and samples were obtained to study the possibility of dislocation transmutation across the  $(10\bar{1}2)$  twin boundary. The character and configuration of dislocations within the twin and in the adjacent matrix were determined using TEM. Reactions were confirmed which involve  $[a_1]$  and  $[a_3]$  matrix dislocations that “transmute” into  $[c - a_2]$  and  $[c + a_2]$  dislocations, respectively, in the  $(10\bar{1}2)$  twin. Collective observation of a number of twins in different grains further showed that the  $(10\bar{1}2)$  twins contain only  $\langle c \pm a_2 \rangle$  among all six possible  $\langle c + a \rangle$  dislocations, and dislocations form a particular distribution inside twin, preferentially populating the vicinity of the twin boundary. The formation of a unit  $\langle c + a \rangle$  dislocation in the twin is proposed to involve consecutive incorporation and transmutation of two matrix dislocations of the same Burgers vector. This process necessitates dislocation pile-up in the matrix in front of the twin boundary, and the associated dislocation configuration was evaluated in terms of elastic strain energy.

Stress analyses were performed inside twin at two limiting bounds. It was shown that  $\langle c \pm a_2 \rangle$  dislocations are only moderately stressed in the plateau regime of the RD compression flow curve, and they experience either similar or lower effective resolved shear stress (RSS) as compared to other  $\langle c + a \rangle$  dislocations. Their exclusive presence suggests that the  $\langle c + a \rangle$  slip mode is source limited and that the transmutation concept provides an obvious source mechanism, which could be activated at later stages of deformation. It is hypothesized that the  $\langle c \pm a_2 \rangle$  dislocations are effectively sessile at this stress level. As evidence of this fact, note that they remain only in the vicinity of twin boundary and not uniformly distributed throughout the twin. Further, it is suggested that some of the interfacial defects introduced by transmutation may induce a dragging effect on twin boundary advancement. The abundant  $\langle c \pm a_2 \rangle$  dislocations (and faults) resulting from the transmutation mechanism will also contribute to hardening within the twin itself, during subsequent deformation. Finally, it is noted that the observed  $\{10\bar{1}2\}$  twin provides a suitable location for future study of  $\langle c + a \rangle$  dislocation behavior at a rather low global applied stress of about 100 MPa in a common alloy system.

## References

- Agnew, S.R., Brown, D., Tome, C.N., 2006. Validating a polycrystal model for the elastoplastic response of magnesium alloy AZ31 using in situ neutron diffraction. *Acta Materialia* 54, 4841-4852.
- Agnew, S.R., Capolungo, L., Calhoun, C.A., 2015. Connections between the basal II “growth” fault and  $\langle c + a \rangle$  dislocations. *Acta Materialia* 82, 255-265.
- Aydiner, C.C., Bernier, J.V., Clausen, B., Lienert, U., Tomé, C.N., Brown, D.W., 2009. Evolution of stress in individual grains and twins in a magnesium alloy aggregate. *Physics Review B* 80, 024113.
- Bacon, D. and Liang, M., 1986. Computer simulation of dislocation cores in h.c.p. metals I. Interatomic potentials and stacking-fault stability. *Philosophical Magazine A* 53, 163.
- Barnett, M., Nave, M.D., Ghaderi, A., 2012. Yield point elongation due to twinning in a magnesium alloy. *Acta Materialia* 60, 1433-1443.

- Barnett, M., Stanford, N., Ghaderi, A., Siska, F., 2013. Plastic relaxation of the internal stress induced by twinning. *Acta Materialia* 61, 7859-7867.
- Bertin, N., Tome, C.N., Beyerlein, I.J., Barnett, M.R., Capolungo, L., 2014. On the strength of dislocation interactions and their effect on latent hardening in pure Magnesium. *International Journal of Plasticity* 62, 72-92.
- Bevis, M. and Crocker, M., 1969. Twinning modes in lattices. *Proceedings of the Royal Society of London A* 313, 509-529.
- Bhattacharyya, D., Cerreta, E., McCabe, R., Niewczas, M., Gray III, G., Misra, A. and Tome, C.N., 2009. Origin of dislocations within tensile and compressive twins in pure textured Zr. *Acta Materialia* 57, 305-315.
- Brown, D., Agnew, S.R., Bourke, M., Holden, T., Vogel, S. and Tome, C.N., 2005. Internal strain and texture evolution during deformation twinning in magnesium. *Materials Science and Engineering A* 399, 1-12.
- Capolungo, L., Beyerlein, I. and Wang, Z., 2010. The role of elastic anisotropy on plasticity in hcp metals: a three-dimensional dislocation dynamics study. *Modelling and simulation in materials science and engineering* 18, 1-16.
- Christian, J. and Mahajan, S., 1995. Deformation twinning. *Progress in Materials Science* 39, 1-157.
- Clausen, B., Tome, C.N., Brown, D.W., Agnew, S.R., 2008. Reorientation and stress relaxation due to twinning: modeling and experimental characterization of Mg. *Acta Materialia* 56, 2456-2468.
- Edington, J., 1976. *Practical electron microscopy in materials science*. New York: Van Nostrand Reinhold Co.
- El Kadiri, H. and Oppedal, A., 2010. A crystal plasticity theory for latent hardening by glide twinning through dislocation transmutation and twin accommodation effects. *Journal of the Mechanics and Physics of Solids* 58, 613-624.
- El Kadiri, H., Barrett, C., Wang, J. and Tome, C.N., 2015. Why are {10-12} twins profuse in magnesium. *Acta Materialia* 85, 354-361.
- Eshelby, J., Frank, F. and Nabarro, F., 1951. The Equilibrium of Linear Arrays of Dislocations. *Philosophical Magazine* 42, 351-364.
- Eshelby, J., 1957. The determination of the elastic field of an ellipsoidal inclusion, and related problems. *Proceedings of the Royal Society of London A* 241, 376-396.
- Fan, H., Aubry, S., Arsenlis, A. and El-Awady, J., 2015. The role of twinning deformation on the hardening response of polycrystalline magnesium from discrete dislocation dynamics simulations. *Acta Materialia* 92, 126-139.
- Fultz, B. and Howe, J., 2001. *Transmission electron microscopy and diffractometry of materials*. New York: Springer.
- Geng, J., Chisholm, M.F., Mishra, R.K., Kumar, K.S., 2015. An electron microscopy study of dislocation structures in Mg single crystals compressed along [0001] at room temperature. *Philosophical Magazine* 95, 3910-3932.

- Ghazisaeidi, M., Curtin, W., Hector Jr., L., 2014. First-principles core structures of  $\langle c+a \rangle$  edge and screw dislocations in Mg. *Scripta Materialia* 75, 42-45.
- Hirth, J. and Lothe, J., 1982. *Theory of dislocations*. New York: Wiley.
- Juan, P.-A., Berbenni, S., Barnett, M.R., Tome, C.N., Capolungo, L., 2014. A double inclusion homogenization scheme for polycrystals with hierarchical topologies: application to twinning in Mg alloys. *International Journal of Plasticity* 60, 182-196.
- Kalidindi, S.R., 2001. Modeling anisotropic strain hardening and deformation textures in low stacking fault energy materials. *International Journal of Plasticity* 17, 837-860.
- Keller, R. and Geiss, R., 2012. Transmission EBSD from 10 nm domains in a scanning electron microscope. *Journal of Microscopy* 245, 245-251.
- Kelley, E. and Hosford Jr., W., 1968. Plane-strain compression of magnesium and magnesium alloy crystals. *Transactions of the Metallurgical Society of AIME* 242, 5-13.
- Kocks, U. and Mecking, H., 2003. Physics and phenomenology of strain hardening: the FCC case. *Progress in materials science* 48, 171-273.
- Kuykendall, W.P., Cash, W.D., Barnett, D.M., Cai, W., 2012. On the existence of Eshelby's equivalent ellipsoidal inclusion solution. *Mathematics and Mechanics of Solids* 17, 840-847.
- Lay, S. and Nouet, G., 1994. Interaction of slip dislocations with the (01-12) twin interface in zinc. *Philosophical Magazine A* 70, 1027-1044.
- Lebensohn, R. and Tome, C.N., 1993. A study of the stress state associated with twin nucleation and propagation in anisotropic materials. *Philosophical Magazine A* 67, 187-206.
- Li, B. and Ma, E., 2009. Pyramidal slip in magnesium: Dislocations and stacking fault on the  $\{10\bar{1}1\}$  plane. *Philosophical Magazine* 89, 1223-1235.
- Ma, Q., El Kadiri, H., Oppedal, A.L., Baird, J.C., Li, B., Horstemeyer, M.F., Vogel, S.C., 2012. Twinning effects in a rod-textured AM30 Magnesium alloy. *International Journal of Plasticity* 29, 60-76.
- Morozumi, S., Kikuchi, M. and Yoshinaga, H., 1976. Electron microscope observation in and around  $\{1-102\}$  twins in magnesium. *Trans. JIM* 17, 158-164.
- Morris, J., Scharff, J., Ho, K., Turner, D., Ye, Y. and Yoo, M., 1997. Prediction of a  $\{1122\}$  hcp stacking fault using a modified generalized stacking-fault calculation. *Philosophical Magazine A* 76, 1065-1077.
- Mura, T., 1982. *Micromechanics of defects in solids*. Hague: Martinus Nijhoff Publishers.
- Muransky, O., Barnett, M.R., Luzin, V., Vogel, V., 2010. On the correlation between deformation twinning and Luders-like deformation in an extruded Mg alloy: In situ neutron diffraction and epsc.4 modelling. *Mater. Sci. Eng.: A*, 527(6), 1383 - 1394.
- Niewczas, M., 2010. Lattice correspondence during twinning in hexagonal close-packed crystals. *Acta Materialia* 58, 5848-5857.
- Numakura, H., Minonishi, Y. and Koiwa, M., 1990. Atomistic study of  $1/3\langle 11-23 \rangle\{101-1\}$  dislocations in hcp crystals. II. Motion of the dislocations. *Philosophical Magazine A* 62, 545-556.

- Obara, T., Yoshinga, H. and Morozumi, S., 1973.  $\{11\text{-}22\} < 1123 >$  Slip system in magnesium. *Acta Metallurgica* 21, 845-853.
- Oppedal, A., El Kadiri, H., Tome, C., Kaschner, G., Vogel, S., Baird, J. and Horstemeyer, M., 2012. Effect of dislocation transmutation on modeling hardening mechanisms by twinning in magnesium. *International Journal of Plasticity* 30-31, 41-61.
- Partridge, P., 1967. The crystallography and deformation modes of hexagonal close-packed metals. *Metallurgical Reviews* 12, 169.
- Price, P., 1961. Nucleation and growth of twins in dislocation-free zinc crystals. *Proceedings of the Royal Society of London* 260, 251-262.
- Proust, G., Tome, C.N., Jain, A., Agnew, S.R., 2009. Modeling the effect of twinning and detwinning during strain-path changes of magnesium alloy AZ31. *International Journal of Plasticity* 25, 861-880.
- Reed-Hill, R., 1973. Role of deformation twinning in determining the mechanical properties of metals. In R. Reed-Hill (Ed.), *The inhomogeneity of plastic deformation* (pp. 285-311). Metals Park, OH: American Society for Metals.
- Sandloebes, S., Friak, M., Neugebauer, J. and Raabe, D., 2013. Basal and non-basal dislocation slip in Mg-Y. *Materials Science and Engineering A* 576, 61-68.
- Sandloebes, S., Friak, M., Zaefferer, S., Dick, A., Yi, S., Letzig, D., Pei, Z., Zhu, L.-F., Neugebauer, J. and Raabe, D., 2012. The relation between ductility and stacking fault energies in Mg and Mg-Y alloys. *Acta Materialia* 60, 3011-3021.
- Serra, A., Bacon, D.J., Pond, R.C., 1988. The crystallography and core structure of twinning dislocations in H.C.P. metals. *Acta Metallurgica* 36, 3183-3203.
- Serra, A., Bacon, D.J., 1996. A new model for  $\{10\text{-}12\}$  twin growth in hcp metals. *Philosophical Magazine* 73, 333-343.
- Serra, A., Bacon, D.J., Pond, R.C., 2002. Twins as barriers to basal slip in hexagonal-close-packed metals. *Metallurgical and Materials Transactions A* 33, 809-812.
- Stohr, J. and Poirier, J., 1972. Etude en Microscopie Electronique du Glissement Pyramidal  $\{11\text{-}22\} < 11\text{-}23 >$  dans le Magnesium. *Philosophical Magazine* 25, 1313-1329.
- Tomsett, D. and Bevis, M., 1969a. The incorporation of basal slip dislocations in  $\{10\text{-}12\}$  twins in zinc crystals. *Philosophical Magazine* 19, 129-140.
- Tomsett, D. and Bevis, M., 1969b. The formation of stacking faults in  $\{10\text{-}12\}$  twins in zinc as a result of slip dislocation-deformation twin interactions. *Philosophical Magazine* 19, 533-537.
- Trimby, P., 2012. Orientation mapping of nanostructured materials using transmission Kikuchi diffraction in the scanning electron microscope. *Ultramicroscopy* 120, 16-24.
- Wang, F., Sandloebes, S., Diehl, M., Sharma, L., Roters, F., Raabe, D., 2014. In situ observation of collective grain-scale mechanics in Mg and Mg-rare earth alloys. *Acta Materialia* 80, 77-93.

- Wang, F. and Agnew, S., 2015. Dislocation-twin interactions in magnesium alloy AZ31. In A. S. M. V. Manuel (Ed.), *Magnesium Technology 2015* (pp. 139-144). Hoboken, NJ, USA: John Wiley & Sons, Inc.
- Wang, H., Wu, P., Tome, C.N. and Wang, J., 2012. Study of lattice strains in magnesium alloy AZ31 based on a large strain elastic-viscoplastic self-consistent polycrystal model. *International Journal of Solids Structures* 49, 2155-2167.
- Westlake, D., 1961. Twinning in zirconium. *Acta Metallurgica* 9, 327-331.
- Williams, D. and Carter, C., 2009. *Transmission electron microscopy: a textbook for materials science*. Springer.
- Wu, L., Agnew, S., Ren, Y., Brown, D., Clausen, B., Stoica, G., Wenk, H.R. and Liaw, P.K., 2010. The effects of texture and extension twinning on the low-cycle fatigue behavior of a rolled magnesium alloy, AZ31B. *Materials Science and Engineering A* 527, 7057-7067.
- Wu, Z., Curtin, W.A., 2015. The origin of high hardening and low ductility in magnesium. *Nature* 526, 62-67.
- Yamakov, V., Wolf, D., Phillpot, S.R., Mukherjee, A.K., Gleiter, H., 2002. Dislocation processes in the deformation of nanocrystalline aluminium by molecular-dynamics simulation. *Nature Materials* 1, 45-49.
- Yang, Z., Chishom, M., Duscher, G., Ma, X. and Pennycook, S., 2013. Direct observation of dislocation dissociation and Suzuki segregation in a Mg–Zn–Y alloy by aberration-corrected scanning transmission electron microscopy. *Acta Materialia* 61, 350-359.
- Yasi, J.A., Nogaret, T., Trinkle, D.R., Qi, Y., Hector Jr., L.G., Curtin, W.A., 2009. Basal and prism dislocation cores in magnesium: comparison of first-principles and embedded-atom-potential methods predictions. *Modelling and Simulation in Materials Science and Engineering* 17, 055012.
- Yoo, M., 1981. Slip, twinning, and fracture in hexagonal close-packed metals. *Metallurgical transactions A* 12A, 409-418.
- Yoo, M. and Wei, C., 1966. Growth of deformation twins in zinc crystals. *Philosophical Magazine* 14, 573-587.
- Yoo, M. and Wei, C., 1966. Application of anisotropic elasticity theory to the plastic deformation in hexagonal zinc. *Philosophical Magazine* 13, 759.

## CHAPTER 4      CHARACTERISTIC DISLOCATION SUBSTRUCTURE IN $\{10\bar{1}2\}$ TWINS IN HEXAGONAL METALS

### 4.1 Introduction

$\{10\bar{1}2\}$  twins are ubiquitous in pure hexagonal close packed metals and many of their alloys. For example,  $\{10\bar{1}2\}$  twins are activated early during the deformation of textured Mg alloys due to their relatively low critical resolved shear stress (CRSS), and they may consume a large volume fraction of the material under appropriate loading, such as compression parallel to the working direction (e.g., rolling or extrusion direction) of wrought Mg alloys [1]. The subsequent mechanical response of the bulk material can be dominated by that of the twinned crystals. Often, a sigmoidal stress – strain curve is produced, including a strain hardening plateau followed by rapid hardening. Numerous crystal plasticity modeling studies have been devoted to describing and understanding this stress – strain response over the past two decades, especially the rapid hardening which accompanies twin exhaustion. Three main mechanisms have been identified: (1) texture hardening arising from the crystal rotation by  $\{10\bar{1}2\}$  twinning, e.g. [2]; (2) a Hall-Petch effect due to the division of parent grains by twin boundaries, e.g. [3, 4]; (3) transformation of pre-existing dislocation in the matrix by an advancing twin boundary (TB).



The former two mechanisms have been evaluated quantitatively by means of crystal plasticity modeling [3-7]. The third one requires investigation of dislocations on smaller length-scales and remains relatively less studied.

Transformation of dislocations by twin boundaries is often termed as the Basinski mechanism [8], which originally revealed a glissile to sessile transformation of dislocations upon incorporation by twins in face-centered cubic metals. Niewczas [9] recently used the concept of the lattice correspondence matrix to describe the previously suggested reaction [10, 11] in which two  $\langle a_{1,3} \rangle$  Burgers vector dislocations transform into a single  $[c \pm a_2]$  dislocation in the twin by  $(10\bar{1}2)[\bar{1}011]$  twinning shear. Notably, this reaction was recently confirmed by TEM analysis in a textured Mg alloy AZ31 polycrystals [12]. This specific reaction by  $\{10\bar{1}2\}$  twinning in hexagonal metals has also been referred to as dislocation transmutation [13]. Although details of the interfacial reaction are not yet fully understood, the transformation from  $\langle a \rangle$  to  $\langle c + a \rangle$  dislocations by  $\{10\bar{1}2\}$  twin boundaries is of great interest, because the former are the most readily activated glide dislocations in matrix and the latter represent the only slip mode beside twinning that is capable of accommodating strain along the  $[c]$ -axis in hexagonal crystals. Furthermore,  $\langle c + a \rangle$  slip is considered to be a hard deformation mode, perhaps source-limited, which also poses a strong hardening effect on primary slip systems [14].

Acknowledging the potential effect these dislocation-twin boundary interactions may have on hardening [15], this article aims to establish a characteristic dislocation substructure in  $\{10\bar{1}2\}$  twins within hcp crystals, a topic which has received scattered attention since the 1960s, including pure Mg [16] and Mg alloy AZ31 polycrystals [12], pure Zn single- and poly-crystals [11, 17], and pure Zr polycrystals [18]. The current experimental effort employed pure Mg single crystals oriented to preferentially activate  $\{10\bar{1}2\}$  twinning, which involves the advancement of

twin boundaries into the matrix crystal. This is similar to the process that occurs during compression along the prior working direction of wrought Mg alloys and permits characterization of the dislocation substructure inside the twins using transmission electron microscopy (TEM).

## 4.2 Experimental methods

The commercially pure Mg (99.95 pct) single crystal was grown using the Bridgeman method, as detailed in [19]. The material was furnace-cooled overnight after crystal growth. Cuboidal shaped samples were electrical discharge machined from the as-grown cylinder. Uniaxial compression tests were performed using a MTS universal testing system at room temperature and a constant strain rate of  $5 \times 10^{-4} \text{ s}^{-1}$ . Compression was applied along  $[10\bar{1}0]$  direction, which has a maximum Schmid factor of 0.5 on  $(10\bar{1}2)[\bar{1}011]$  and  $(\bar{1}012)[10\bar{1}1]$  twinning systems and 0.12 for the other four  $\{10\bar{1}2\}$  twinning variants.

In order to characterize the two preferred twin variants from the common zone axis with matrix  $[\bar{1}2\bar{1}0]$ , thin slices of about 700  $\mu\text{m}$  thickness were cut by diamond saw from the  $(\bar{1}2\bar{1}0)$  face of the cuboidal shaped sample. They were then ground to  $\sim 250 \mu\text{m}$  and punched to produce the 3 mm disks. The final thinning to electron transparency was achieved by electropolishing using the electrolyte and conditions given in [12]. The final chemical polishing effectively removes surface deformation layer introduced during previous mechanical preparations. TEM characterizations were carried out on a JEOL 2000FX operated at 200 kV.

### 4.3 Results

The stress – strain response of the  $[10\bar{1}0]$  compressed single crystal is shown in Figure 4.1(a) and exhibits the typical sigmoidal shape similar to the in-plane compression data of Mg single crystal from Kelley and Hosford [20]. During the initial plateau regime, the plastic strain is accommodated predominantly by twin nucleation and growth. Several noticeable stress drops in this regime correspond to nucleation of new twins [21]. For the two preferred twin variants, the  $[c]$ -axes of the twins are only  $4^\circ$  away from the compression axis at ideal orientation. Twin crystals are thus not capable of readily accommodating strain by easy slip modes. A thorough discussion of the subsequent rapid hardening regime, during which the strain hardening rate approaches the elastic modulus, can be found in [7].

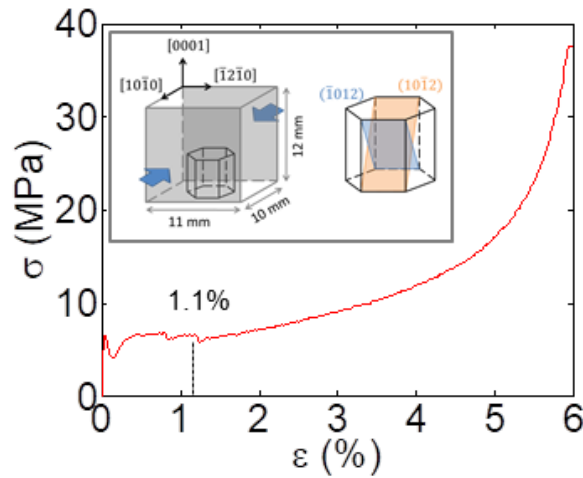


Figure 4.1. True stress – strain curve of pure Mg single crystal compressed along  $[10\bar{1}0]$  axis at room temperature. Schematics of the orientation and dimensions of the single crystal sample for compression test are shown in the inset.

Figure 4.2 presents the typical dislocation structure inside a  $(10\bar{1}2)$  twin from the sample compressed to 1.1% true strain. At the diffraction condition of  $g = (0002)_t$ , basal planes inside

the twin are in an edge-on orientation. Based on the  $g \cdot b = 0$  invisibility criterion, all the visible dislocations have a Burgers vector with a  $[c]$ -component. These dislocations lie on both basal and non-basal planes. Since basal planes are edge-on, dislocations contained within them appear as straight lines parallel to the  $(0001)_t$  traces. The long and curved dislocations are on non-basal planes. When the foil is tilted to the  $g = (10\bar{1}0)$  diffraction condition, basal planes are inclined, revealing a high density of dislocations lying within the basal planes. A noticeable feature is that all of these dislocations are concentrated in the vicinity of the twin boundary, whereas the central area of the twin is almost void of defects, and the line demarcating regions of low and high defect density is almost parallel to the trace of TB, as indicated by the black arrows outside the frame of Figure 4.2 (a).

The  $[c]$ -containing defects are more clearly illustrated in another twin of lower defect density (Figure 4.3). Near the left TB, a long dislocation is lying inclined to the basal plane at the diffraction condition of  $g = (0002)$ , and is invisible at  $g = (10\bar{1}0)$ . According to the  $g \cdot b = 0$  invisibility criterion, visibility at the former condition suggests a  $[c]$  component in its Burgers vector and invisibility at the latter constrains the possibilities to either pure  $[c]$  or  $[c \pm a_2]$ , i.e.  $1/3[1\bar{2}13]$  and  $1/3[\bar{1}2\bar{1}3]$ . Note both  $[c]$  and  $[c \pm a_2]$  dislocations are consistent with the predictions of lattice correspondence [9] or dislocation transmutation reaction [12], that  $[a_1]$  or  $[a_3]$  dislocations in the matrix could be transformed by  $(10\bar{1}2)$  twinning to  $[c \pm a_2]$  dislocations in the twin. Similar to the twin in Figure 4.2, linear contrast on basal plane was observed at  $g = (0002)$  when basal plane is edge-on, as indicated by arrows in Figure 4.3 (a). When the basal plane is inclined (Figure 4.3 (b)), the basal dislocations are accompanied by parallel dark/bright fringes characteristic of stacking faults. Clearly, these stacking faults are on the basal plane and the bounding partial dislocations possess a  $[c]$  component. Therefore, it is suggested that these

defects are the so-called  $I_1$  stacking faults, which are bounded by partial dislocations of  $1/6\langle 20\bar{2}3 \rangle$  type [22-24]. These faults in Figure 4.3 (b) have a large projected width of 60nm to 110 nm from the perspective of  $[\bar{1}2\bar{1}0]$ .

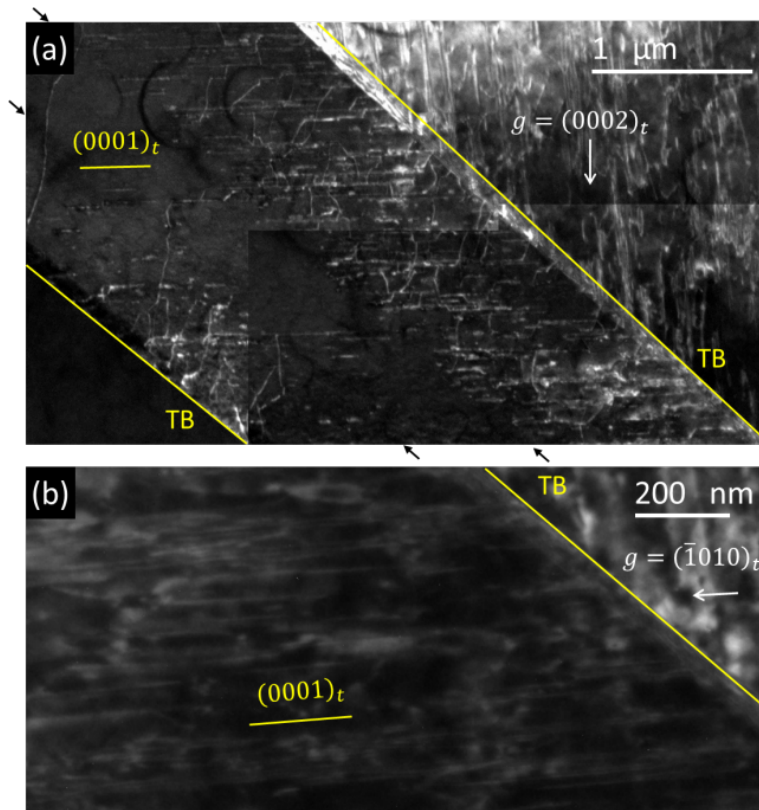


Figure 4.2. Dislocation structure in a  $(10\bar{1}2)_t$  twin, within a pure Mg single crystal compressed along  $[10\bar{1}0]$  to 1.1% true strain. The images were taken at weak beam dark field (WBDF) condition with diffraction vectors of the twin crystal (a)  $g = (0002)_t$  and (b)  $g = (\bar{1}010)_t$ , whose directions are indicated by white arrows. (a) is at a lower magnification with the location of the TBs delineated by yellow lines. (b) is at higher magnification because the high dislocation density on the basal plane would otherwise obscure the image.

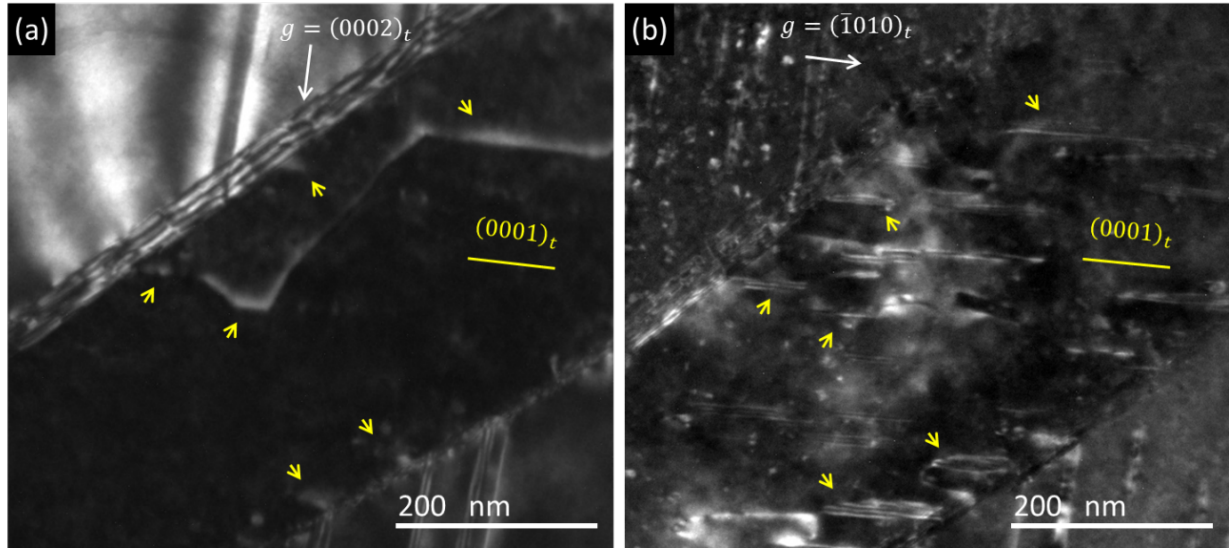


Figure 4.3. Another twin from pure Mg single crystal compressed along  $[10\bar{1}0]$  to 1.1% true strain. The WBDf images were taken with diffraction vectors of the twin crystal (a)  $g = (0002)_t$  and (b)  $g = (\bar{1}010)_t$ , whose directions are indicated by white arrows. The yellow arrows in (a) and (b) point to the same features at different sample tilt.

This dislocation substructure, observed in  $(10\bar{1}2)$  twins in a pure Mg single crystal, finds similarities to observations in previous studies. Representative examples are reproduced from the literature in Figure 4.4. The selected images all have a diffraction vector  $g = (0002)_t$  to highlight the  $[c]$ -containing dislocations. All the twins possess abundant  $[c]$ -containing defects. They are distributed in a band in the vicinity of TB, and the apparent line separating them from the twin interior that has lower defect density is approximately parallel to the trace of TB, as indicated by arrows outside the frame of each image. The  $[c]$ -containing dislocations appear both as long and curved perfect dislocations on non-basal planes (both  $[c]$  and  $\langle c + a \rangle$  Burgers vectors have been definitively determined in previous works [12, 18]) and linear contrast parallel to the traces of the basal planes. When the basal plane is inclined, stacking fault fringe contrast was reported [12, 16-18].

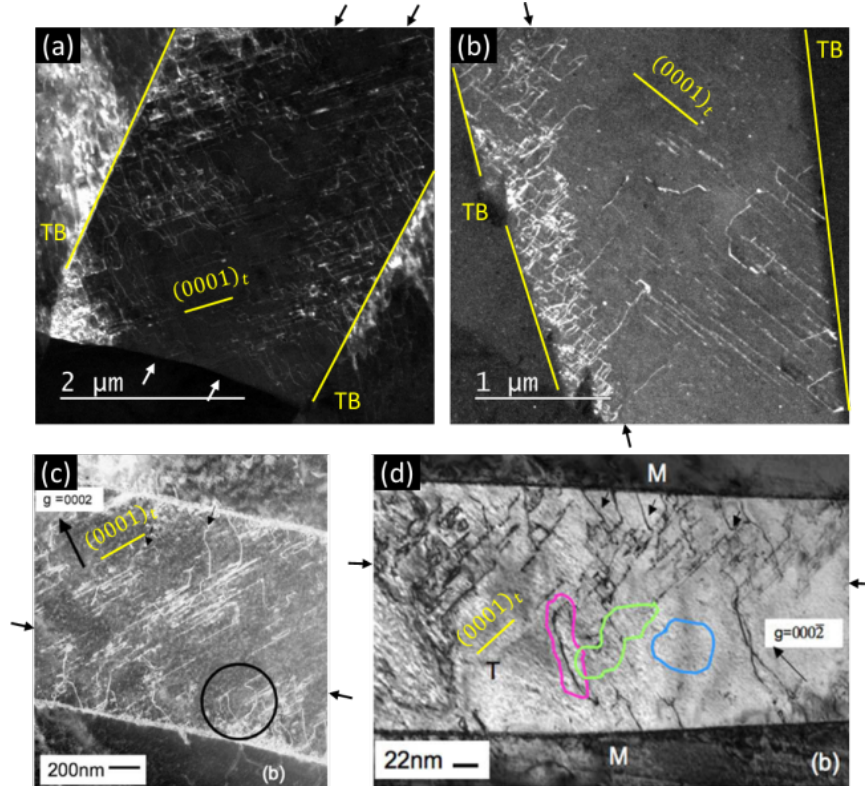


Figure 4.4. Dislocation substructure in  $(10\bar{1}2)$  twins in polycrystalline samples. (a) and (b) are in Mg alloy AZ31 compressed along rolling direction of a rolled plate [12, 25]. (c) and (d) are in pure Zr rolled plate undergone in-plane compression (IPC) [18].

#### 4.4 Discussions and conclusion

Whereas a consistent dislocation substructure has been found in  $(10\bar{1}2)$  twins, within a number of hexagonal metals, the origins of the abundant  $[c]$ -containing dislocations and large  $I_1$  faults still deserve further consideration. Both  $[10\bar{1}0]$  compression of the current single crystal and in-plane compression of textured polycrystalline plates (Figure 4.4) promote twinning activity. As the twin boundary advances, it is expected to interact with pre-existing dislocations in the parent crystal. According to the aforementioned reactions [9, 12], interaction of  $\langle a \rangle$  dislocations in the matrix with TB can result in  $\langle c + a \rangle$  dislocations in twin. Perfect dislocations

with  $[c]$  Burgers vector may form either directly at the TB [26] or via decomposition of  $\langle c + a \rangle$  dislocations [17, 27]. In the case of non-ideally oriented grains within polycrystals, both basal dislocation slip and  $\{10\bar{1}2\}$  twinning activity are expected [6]. For the current single crystal, even if one considers the very low CRSS of the basal slip mode (on the order of 0.5 – 1 MPa [20, 28]), little basal slip activity is expected. Nevertheless, grown-in basal dislocations are expected. Therefore, the heterogeneous distribution of dislocations in twins raises an interesting possibility. Perhaps the initial forward propagation results in a relatively defect free twin, whereas subsequent lateral twin growth (thickening) leads to the dislocation twin boundary reactions discussed above. Consider the twins in Figure 4.2 (a) and Figure 4.4 (a) and (c), which have the  $[c]$ -containing defects near both TBs. This indicates that both TBs have advanced, whereas those in Figure 4.4 (b) and (d) only have abundant defects near one of the TBs, suggesting that the twins in the latter cases grew laterally (thickened) in only one direction.

The large  $I_1$  faults in the  $(10\bar{1}2)$  twins can arise from several origins. Firstly, as-grown crystals naturally contain  $I_1$  faults as a result of defective crystal growth or condensation of vacancies or self-interstitials on basal planes, as reported in the seminal paper by Berghezan et al. [29]. In fact, the interaction of  $I_1$  faults with TB has been examined by the current authors in [30], for a case where the population of  $I_1$  faults was firstly enhanced by  $[c]$ -axis compression of single crystal sample [24, 31, 32], and then swept by advancing  $\{10\bar{1}2\}$  TBs induced by  $[10\bar{1}0]$  compression. It is noted that there is no direct geometrical (lattice) correspondence between  $I_1$  faults in the matrix and the twin (and they lie on orthogonal planes). If there is a correlation between the two, it would require vacancy transport between the matrix and twin and therefore is not viewed as the most likely explanation during room temperature deformation.



The second possible origin of  $I_1$  faults is the dissociation of edge  $\langle c + a \rangle$  dislocations on basal plane, which is an attractive explanation, considering the abundance of  $[c]$ -containing dislocations in the observed twins. The dissociation of a single  $\langle c + a \rangle$  dislocation into two partial dislocations enclosing a basal fault,  $1/3\langle 1\bar{2}13 \rangle \rightarrow 1/6\langle 2\bar{2}03 \rangle + 1/6\langle 0\bar{2}23 \rangle$ , is energetically favorable. The equilibrium size of  $I_1$  fault is determined by a force balance involving the repulsion of the bounding partial dislocations and the attraction arising from stacking fault, e.g. 37 nm given the known  $I_1$  stacking fault energy  $\gamma_{I_1} = 11.3 \text{ mJ/m}^2$  [27]. For this dissociation reaction to explain the wide faults observed, it would require extensive climb motion of the partial dislocations, since their Burgers vectors are out of the basal plane. Further, these partial dislocations would have been driven far beyond their equilibrium spacing without any obvious driving force provided by the applied stress [27, 33].

Thirdly,  $I_1$  faults may nucleate from incoherent twin boundaries, as was reported recently based upon both molecular dynamics (MD) simulation [34] and high resolution TEM [35]. The formation of  $I_1$  faults from  $\{10\bar{1}2\}$  TBs had not previously received much attention, aside from the proposed formation mechanisms of generic basal fault by emission of partial dislocation from the incoherent facets of a migrating TB [36]. Using the same crystallographic basis of the lattice correspondence [9], a possible mechanism is proposed. Similar to the transformation of two  $\langle a \rangle$  to a unit  $\langle c + a \rangle$  plus a small residual interfacial defect, one basal  $\langle a \rangle$  dislocation could be transformed to  $1/2\langle c + a \rangle$  (or  $1/6\langle 1\bar{2}13 \rangle$ ) in the twin lattice plus an even smaller residual defect. Subsequent glide of this partial dislocation or motion of the TB would result in a *high energy fault on a non-basal plane* [37].

On the other hand, the  $\langle a \rangle$  dislocation could transform directly to  $1/6\langle 2\bar{2}03 \rangle$  within the twin, plus small residual defects in the twin boundary (including the  $1/6\langle \bar{1}010 \rangle$  difference from

$1/2\langle c + a \rangle$ ). In fact,  $1/6\langle \bar{1}010 \rangle$  is an admissible vector on  $\{10\bar{1}2\}$  twin interface [38]. Given the low stress at which twin boundaries move, it is likely that the  $1/6\langle 2\bar{2}03 \rangle$  partial dislocation would be sessile and a basal  $I_1$  fault would thusly form. One end of the fault would be bounded by the  $1/6\langle \bar{1}010 \rangle$  dislocation in the TB and the other would be anchored by the  $1/6\langle 2\bar{2}03 \rangle$  partial dislocation in the twin. Because the bounding partial is sessile, the fault may become very wide as the TB migrates away from it. Careful evaluation of this possible interfacial reaction is underway, using MD simulation.

It is noted that there is another twin-dislocation feature which has been of significant interest to researchers, both theoretical [39] and experimental [40]. This effect concerns the observed relaxation of twin-induced stresses, where twins intersect internal interfaces (grain boundaries, other twin boundaries, and phase boundaries). Here, we have restricted the attention to the interactions between dislocations and twin boundaries far from other internal interfaces, and the processes observed presently appear to operate in both pure single crystals and polycrystalline alloys.

To summarize, a characteristic dislocation substructure inside  $\{10\bar{1}2\}$  twins is identified within a pure Mg single crystal compressed along the  $[10\bar{1}0]$  direction to promote  $\{10\bar{1}2\}$  twinning activity. Abundant  $c$ -containing defects were present in the wake of advancing twin boundaries, in the form of non-basal  $[c]$  and  $\langle c + a \rangle$  perfect dislocations and basal  $I_1$  stacking faults with widths approaching 100nm. This dislocation substructure has been previously reported in polycrystal Mg alloys as well as other hexagonal metals, demonstrating its wide applicability. It is significant for the discussion of plasticity for three reasons. (1) The twin contains defects that are not easily activated in matrix; (2) the high local density of  $[c]$ -containing defects in the vicinity of TB may create a hard environment for other slip modes as

well as twin boundary migration in either the forward or the backward direction (twin thickening and detwinning, as observed in [41, 42]); and (3) potential slip activity of these dislocations, especially the non-basal  $\langle c + a \rangle$  dislocations, could accommodate strain along  $[c]$ -axis within the twins. Considering the ubiquity of  $\{10\bar{1}2\}$  twins and recent evidence that the dislocation structure in and around twins plays a significant role in determining the flow stress [43] and twin boundary mobility more generally [41, 42], subsequent plasticity models of hexagonal metals should take account of the possible effects of this characteristic dislocation substructure.

## References

- [1] D. Brown, S. Agnew, M. Bourke, T. Holden, S. Vogel, C. Tome, *Mater. Sci. Eng. A* 399 (2005) 1-12.
- [2] X. Lou, M. Li, R. Boger, S. Agnew, R. Wagoner, *Int. J. Plas.* 23 (2007) 44-86.
- [3] S. Asgari, E. El-Danaf, S. Kalidindi, R. Doherty, *Metall. Mater. Trans. A* 28A (1997) 1781.
- [4] A. Salem, S. Kalidindi, R. Doherty, *Acta Mater.* 51 (2003) 4225-4237.
- [5] A. Jain, S. Agnew, *Mater. Sci. Eng. A* 462 (2007) 29-36.
- [6] B. Clausen, C. Tome, D. Brown, S. Agnew, *Acta Mater.* 56 (2008) 2456-2468.
- [7] P. Wu, X. Guo, H. Qiao, S. Agnew, D. Lloyd, J. Embury, *Acta Mater.* 122 (2017) 369-377.
- [8] Z. Basinski, M. Szczerba, M. Niewczas, J. Embury, S. Basinski, *Rev. de Metall.* 94 (1997) 1034-1044.
- [9] M. Niewczas, *Acta Mater.* 58 (2010) 5848-5857.
- [10] M. Yoo, C. Wei, *Phil. Mag.* 14 (1966) 573-587.
- [11] D. Tomsett, M. Bevis, *Phil. Mag.* 19 (1969) 129-140.
- [12] F. Wang, S. Agnew, *Int. J. Plas.* 81 (2015) 63-86.
- [13] H. El Kadiri, A. Oppedal, *J. Mech. Phys. Sol.* 58 (2010) 613-624.
- [14] N. Bertin, C. Tome, I. Beyerlein, M. Barnett, L. Capolungo, *Int. J. Plas.* 62 (2014) 72-92.
- [15] A. Oppedal, H. El Kadiri, C. Tome, G. Kaschner, S. Vogel, J. Baird, M. Horstemeyer, *Int. J. Plas.* 30-31 (2012) 41-61.
- [16] S. Morozumi, M. Kikuchi, H. Yoshinaga, *Trans. JIM* 17 (1976) 158-164.
- [17] D. Tomsett, M. Bevis, *Phil. Mag.* 19 (1969) 533-537.
- [18] D. Bhattacharyya, E. Cerreta, R. McCabe, M. Niewczas, G. Gray III, A. Misra, C. Tome,

- Acta Mater. 57 (2009) 305-315.
- [19] K. Molodov, T. Al-Samman, D. Molodov, Mater. Sci. Eng. A 651 (2016) 63-68.
- [20] E. Kelley, W. Hosford Jr., Trans. Metall. Soc. AIME 242 (1968) 5-13.
- [21] C. Mo, B. Wisner, M. Cabal, K. Hazeli, K.T. Ramesh, H. El Kadiri, T. Al-Samman, K.D. Molodov, D.A. Molodov, A. Kotsos, Materials 9 (2016) 662.
- [22] N. Chetty, M. Weinert, Phys. Rev. B 56 (1997) 10844.
- [23] D. Hull, D. Bacon, Introduction to Dislocations, Elsevier Science, 2011.
- [24] J. Geng, M.F. Chisholm, R.K. Mishra, K.S. Kumar, Phil. Mag. Lett. 94 (2014) 377-386.
- [25] F. Wang, S. Agnew, Dislocation-twin interactions in magnesium alloy AZ31, in: Magnesium Technology 2015, John Wiley & Sons, Inc., Hoboken, NJ, 2015, pp. 139-144.
- [26] D. Westlake, Acta Metal. 9 (1961) 327-331.
- [27] Z. Wu, W. Curtin, Nature 526 (2015) 62-67.
- [28] B. Wonsiewicz, W. Backofen, Trans. Metall. Soc. AIME 239 (1967) 1422.
- [29] A. Berghezan, A. Fourdeux, S. Amelinckx, Acta Metal. 9 (1961) 464-490.
- [30] F. Wang, C. Barrett, K. Hazeli, K. Molodov, T. Al-Samman, A. Oppedal, D. Molodov, A. Kotsos, K. Ramesh, H. El Kadiri, S. Agnew, The Effect of {10-12} Twin Boundary on the Evolution of Defect Substructure, in: Magnesium Technology 2017, Springer International Publishing, 2017, pp. 175-180.
- [31] P. Price, J. Appl. Phys. 32 (1961) 1750-1757.
- [32] J. Geng, M.F. Chisholm, R.K. Mishra, K.S. Kumar, Phil. Mag. 95 (2015) 3910-3932.
- [33] S. Agnew, L. Capolungo, C. Calhoun, Acta Mater. 82 (2015) 255-265.
- [34] H. Fan, J. El-Awady, J. Appl. Mech. 82 (2015) 101006.
- [35] Q. Sun, X. Zhang, Y. Shu, L. Tan, Q. Liu, Mater. Lett. 185 (2016) 355-258.
- [36] J. Tu, X. Zhang, J. Wang, Q. Sun, Q. Liu, C. Tome, Appl. Phys. Lett. 103 (2013) 051903.
- [37] Z. Wu, M. Francis, W. Curtin, Modelling Simul. Mater. Sci. Eng. 23 (2015) 015004.
- [38] C. Barrett, H. El Kadiri, Scr. Mater. 84-85 (2014) 15-18.
- [39] M. Kumar, A. Kanjarla, S. Niezgoda, R. Lebensohn, C. Tome, Acta Mater. 84 (2015) 349-358.
- [40] H. Abdolvand, A.J. Wilkinson, Int. J. Plas. 84 (2016) 160-182.
- [41] Y. Xin, L. Lv, H. Chen, C. He, H. Yu, Q. Liu, Mater. Sci. Eng. A 662 (2016) 95-99.
- [42] Y. Cui, Y. Li, Z. Wang, Q. Lei, Y. Koizumi, A. Chiba, Int. J. Plas. 99 (2017) 1-18.
- [43] L. Lv, Y. Xin, H. Yu, R. Hong, Q. Liu, Mater. Sci. Eng. A 636 (2015) 389-395.

## CHAPTER 5    DISLOCATION INDUCED TWIN GROWTH AND FORMATION OF BASAL STACKING FAULTS IN $(10\bar{1}2)$ TWINS IN PURE MAGNESIUM

### 5.1 Introduction

The interactions of the  $\{10\bar{1}2\}$  twin boundary (TB) with matrix  $\langle a \rangle$  dislocations are primary interactions in hexagonal metals, as both defects are easily generated during deformation via the operation of  $\{10\bar{1}2\}$  twinning and basal dislocation slip. With respect to a  $(10\bar{1}2)$  twinning plane, the  $\langle a \rangle$  dislocations fall into two categories: (1) the  $1/3[\bar{1}2\bar{1}0]$  Burgers vector,  $[a_2]$ , is the co-zone axis of the matrix and the twin and is hence parallel to the interface, and (2) the  $1/3[2\bar{1}\bar{1}0]$  and  $1/3[\bar{1}\bar{1}20]$  Burgers vectors,  $[a_1]$  and  $[a_3]$ , are at  $60^\circ$  to the intersection line of the basal slip plane and twinning plane. The crystallographic transformations of  $\langle a \rangle$  dislocations at the  $(10\bar{1}2)$  interface in zinc have been derived and discussed by Yoo and Wei in 1966 [1]. When transformed from the matrix to the twin, the  $[a_2]$  Burgers vector is unchanged, leaving no residual defect at the interface and therefore not causing the twin boundary motion, whereas the  $[a_1]$  or  $[a_3]$  Burgers vector corresponds to a  $1/2[c \pm a_2]$  vector in the twin with a

difference vector in the twinning shear direction. The latter transformation further poses the possibility that a unit  $\langle c + a \rangle$  dislocation can be produced in the twin by incorporating two  $[a_1]$  or  $[a_3]$  basal dislocations. The vector transformation is then [2]

$$2 \times [a_{1,3}]_m = [c \pm a_2]_t + b_t$$

with a difference vector of exactly one twinning dislocation (disconnection)  $b_t = \frac{3-\gamma^2}{3+\gamma^2} [\bar{1}011]$  [3], whose gliding on the  $(10\bar{1}2)$  twinning plane would displace the interface by  $2d_{10\bar{1}2}$  parallel to the plane normal.

The transformation of the  $[a_1]$  or  $[a_3]$  at  $(10\bar{1}2)$  TB has been a topic of continuing interest, motivated by its potential ability to modulate the defects in the twin crystal as well as the TB migration via the generation of  $[c \pm a_2]$  and  $b_t$  dislocations respectively. To distinguish it from generic interfacial dislocation transformations, this specific transformation is referred to as dislocation transmutation reaction [2, 4]. Based on the prior experimental studies in Mg, Zn and Zr [2, 5-8], a characteristic dislocation substructure in the  $(10\bar{1}2)$  twins is identified [9] that the twins have abundant  $[c]$ -containing defects in the form of perfect  $[c]$  and  $\langle c + a \rangle$  dislocations on non-basal planes, and  $I_1$  stacking faults (SF) on basal planes presumably as a result of the dissociation of  $\langle c + a \rangle$  dislocations. The Burgers vectors of the defects inside twin are consistent with the dislocation transmutation reaction. In terms of the effect of the dislocation-TB interactions on the structure and motion of the interface, the seminal atomistic simulations by Serra and Bacon [10] suggested that the  $60^\circ$  dislocations  $[a_1]$  or  $[a_3]$  are absorbed by the interface and decompose into multiple twinning dislocations (TD) and a step that is intermediate between the basal plane in the matrix and prismatic plane in the twin and can be a source of TDs under stress. Many studies since then employed molecular dynamics (MD) simulations to investigate the structure of the  $(10\bar{1}2)$  interface as a result of dislocation-TB interaction and the

effect of basal-prismatic (BP) or prismatic-basal (PB) interfaces on twin boundary migration [11-14]. The experimental evidence of dislocations induced formation of TDs was reported by Lay and Nouet [15] from transmission electron microscopy (TEM) observations. The high resolution TEM (HRTEM) studies in Mg, Ti and Co [16-18] revealed that the  $(10\bar{1}2)$  interfaces consist terraces of coherent twin boundary (CTB) and BP/PB interfaces at atomic scale, which very recently were correlated to the dislocation-twin interactions by Zhang et al. [19].

On top of the previous experimental and modeling endeavors, a few gaps remain in understanding the dislocation interaction with  $(10\bar{1}2)$  TB. Regarding the dislocations inside the twins, the formation of the defects at the interface cannot be directly concluded from the post mortem experimental studies. Whether the interfacial dislocation transformation corresponds to slip transfer or a dislocation incorporation and emission process is unclear. The recent study conducted in a single crystal pure Mg involving compression along the  $[10\bar{1}0]$  direction [9] created a scenario of TB being driven by the applied loading to migrate toward the unstressed dislocations in the matrix, and dislocations consistent with the transmutation reaction were found in the wake of the advancing TB. It seems to suggest that dislocation slip is not necessary to invoke the interfacial reaction. Regarding the influence of the dislocation-TB interaction on twin growth, either promotive by inducing the generation of TDs or inhibitive by creating interfacial serrations, the effects are convoluted in the polycrystalline environment where both basal dislocation slip and twinning are promoted simultaneously by the external loading during deformation, e.g. in-plane compression of a rolled plate. Whether TDs are generated from the dislocation-TB interaction, or the ratio of TDs per gliding dislocation remain to be examined experimentally.

The current work aims to elucidate the dislocation transformation interaction at the  $(10\bar{1}2)$  TB by *in situ* observations during tension straining in TEM. The oriented single crystal specimens were employed, such that a relatively controlled loading geometry was achieved. The interpretation of the vector transformation process is further aided by MD simulations and topological analyses of defects across the twin interface. The migration of the twin interface and the evolution of the interface structure are analyzed. An attempt is made to correlate the observed twin growth with the incorporation of slip dislocations at the twin interface.

## 5.2 Experimental methods

The *in situ* tension experiments were carried out using a Gatan 671 single tilt straining holder in a FEI Tecnai F30 TEM operating at 300 kV. The tensile specimen was produced similar to the conventional 3 mm diameter disk sample for TEM, but with a width of 2.5 mm in order to fit the straining holder. The thin foil was then glued onto a thin Cu plate with 11.5 mm in length and 2.5 mm in width, which was fixed by screws on the holder. Tension strain was applied by displacing the mobile crosshead at a speed of 0.1  $\mu\text{m/s}$ . Dynamic deformation process was recorded by a Gatan charge-coupled device camera at a rate of 10 frames/s. In some instances, the thin foils were retrieved after the straining experiments by immersing the sample complex in acetone. They were suitable for post mortem analysis on a double tilt holder.

The tensile specimen is designed to allow 1) straining at a defined orientation and 2) convenient access to suitable diffraction conditions, preferentially for both the matrix and twin crystals simultaneously. The tensile specimens were from a pure Mg single crystal sample containing preferentially activated tension twin variants  $(10\bar{1}2)$  and  $(\bar{1}012)$  after compression along the  $[10\bar{1}0]$  direction to 1.1% true strain [9]. Slabs of 2.5 mm width were machined by



diamond cutting saw from the  $(\bar{1}2\bar{1}0)$  plane of the bulk material, with the longitudinal direction parallel to the  $[10\bar{1}1]$  direction. The slabs were then annealed at 200°C for 50 minutes and furnace cooled overnight in order to decrease the dislocation density from prior deformation. Thin foils with areas of electron transparency were prepared by mechanical thinning, rim-punching and electro-polishing. The electrolyte and polishing parameters are detailed in [2].

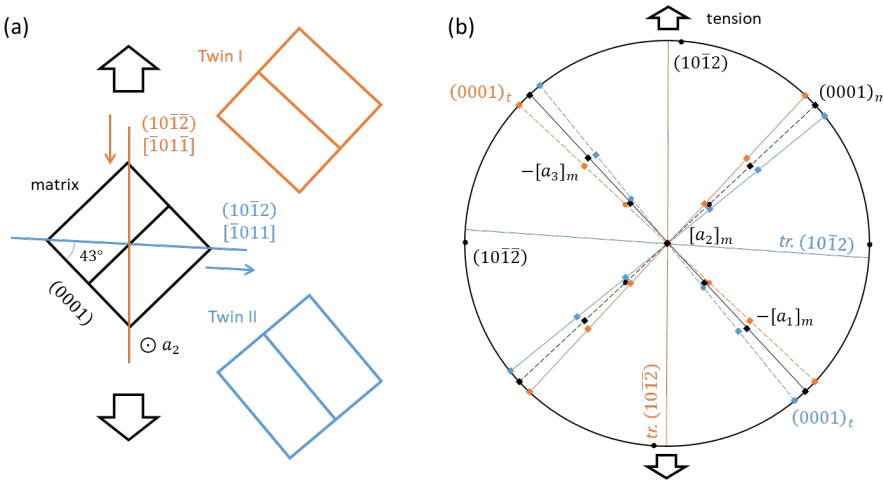


Figure 5.1. Orientations of the matrix and the two twin variants in the single crystal tensile specimen. During the *in situ* straining, the tension strain is applied in the vertical direction, which is also the axis of sample tilting, and the electron beam is perpendicular to the plane of the paper. (a) is the projected hexagonal lattices of the crystals. (b) is the stereographic projection of important plane poles and directions of the matrix and twins. The solid lines indicate the trace of basal planes, and the dash lines indicate the trace of  $(10\bar{1}0)$  prismatic planes.

The tensile specimens produced thus are positioned on the straining holder with the  $[10\bar{1}1]$  direction parallel to the tension axis and  $(\bar{1}2\bar{1}0)$  plane facing upward (Figure 5.1). At this orientation, the applied loading promotes the  $\lceil a_{1,3} \rceil$  basal dislocation slip in the matrix (Schmid factor  $m = 0.43$ ), but has minimal resolved shear stress on the twinning shear system of the two pre-existing twin variants ( $m = 0$  and  $0.06$ ), because the principle straining direction is

either parallel or nearly perpendicular ( $\sim 86^\circ$ ) to the twinning shear direction of the twin variants. Note deviations from the exact orientation were inevitably introduced during sample preparation or loading on the *in situ* tension holder. The viewing direction during the *in situ* experiments is close to the common  $[a_2]$  zone axis of the twin and the matrix. For the interest of diffraction contrast of TEM observation, a slight deviation away from the zone-axis is actually favored, which allows access to the  $(0002)_t$  and  $(10\bar{1}0)_m$  Kikuchi diffraction band simultaneously on the single tilt straining holder. All the results presented subsequently are obtained at this diffraction condition, so the visible dislocations in twin are  $[c]$ -containing, and the visible gliding basal dislocations in matrix are  $[a_1]$  and  $[a_3]$ .

### 5.3 Molecular dynamics simulation

To investigate the details of the interfacial reaction, MD simulations were carried out using LAMMPS [20] with an embedded-atom method potential developed by Wu et al. [21]. The simulation box was a bicrystal with a  $(10\bar{1}2)[\bar{1}011]$  twinning relationship, with periodic boundary conditions in the twinning shear direction (x axis), and shear plane normal (y axis). Free surfaces were imposed along the twinning plane normal (z axis). The simulation box is 55 nm long along z axis, and is restricted to 3.8 nm in the direction normal to the plane of shear (y axis). After relaxing the TB using a conjugate gradient method, mixed character basal dislocations with Burgers vector  $[a_3]$  were inserted in the matrix crystal using the anisotropic elastic solution for the displacement field [22, 23]. The line direction of the dislocations is parallel to the shear plane normal, namely the  $[a_2]$  direction of the matrix crystal. The inserted dislocations are thus of  $60^\circ$  mixed character.

Representative previous MD simulations studied the dislocation interaction with TB by moving the interface into the dislocations, which was induced by a shear strain in the twinning plane and along the shear direction [10, 12, 13]. Based on the loading condition of the *in situ* experiments (orientation I in Figure 5.1), the current simulations additionally applied a tensile strain parallel to the twinning shear direction. The exact loading conditions are detailed in Section 5.5.

## 5.4 Experimental results

### 5.4.1 Local twin growth induced by dislocation impingement

The time-resolved images in Figure 5.2 show the twin growth of a twin at orientation II. At the beginning of the captured image sequence (Figure 5.2 (a)), the TB is already serrated by small steps during prior straining, but remains mostly straight and close to the inclination of CTB, which is determined approximately from the traces of the basal planes in matrix and twin in the images ( $\sim 43^\circ$  to basal plane). As straining ensues, basal dislocations in matrix were stressed to glide toward the TB, evidenced by the dark contrast developed parallel to the basal plane traces. It is observed through Figure 5.2(a-c) that the TB in region I has advanced, accompanied by the formation of a straight boundary to its left. With further advancement of the boundary till Figure 5.2(f), the length of the boundary is extended, and it appears to be orthogonal to the basal plane traces in matrix. Presumably, the straight boundary is comprised mostly of PB facets (named after the close alignment with the prismatic plane in matrix and basal plane in twin), which are commonly observed on the  $\{10\bar{1}2\}$  TB but on the length scale of tens of nanometers [16-19]. In the following, such large boundaries are more appropriately referred to as PB serrations. The difference images in Figure 5.2(g) and (f) demonstrate that the boundary extends its length

upward, accompanied by the TB advancement on its right side, and does not migrate/glide laterally. Through Figure 5.2 (d-f), the TB in region II bulges up and forms a convex-shaped interface, preceded by dark strain contrast in the proximate matrix arising from basal dislocation slip activity. Besides the above two occasions of TB advancement, all other segments of the TB do not undergo noticeable migration at the current length scale. Therefore, the local twin growth is attributed to the interaction of gliding basal dislocations with TB rather than the external applied stress.

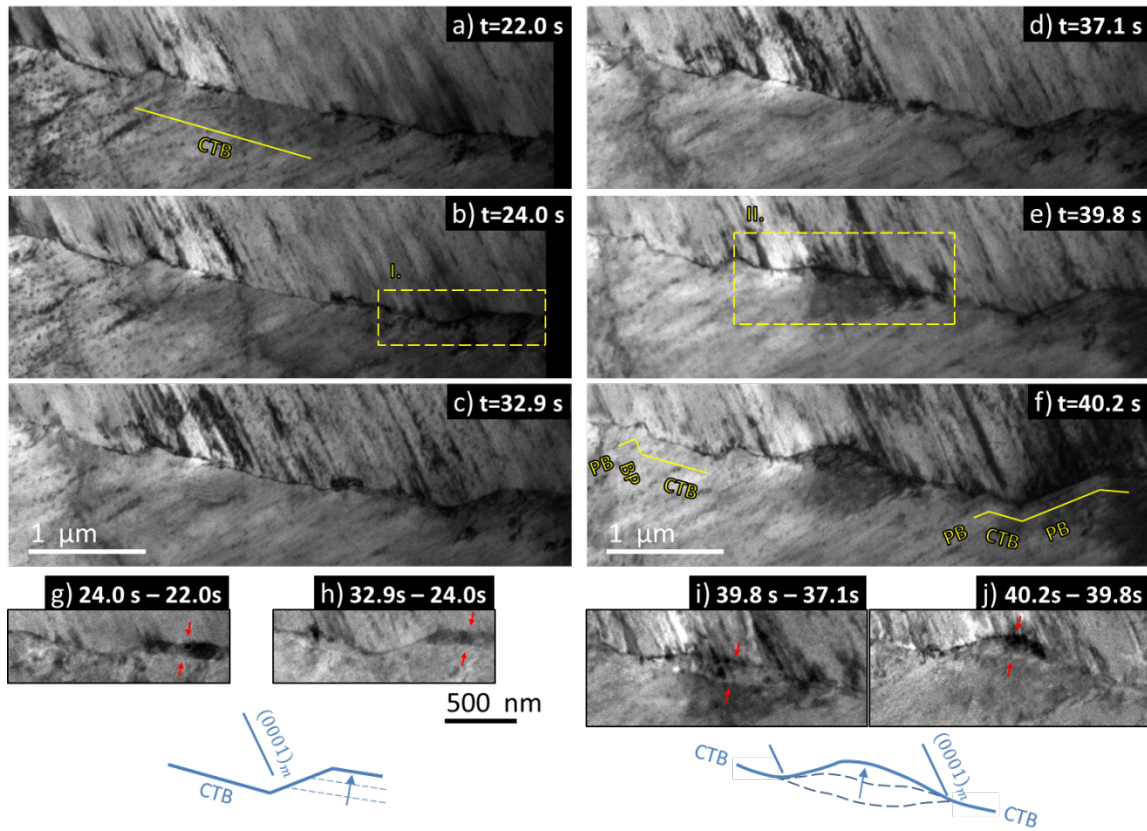


Figure 5.2. Captured image sequence showing the local twin growth in two regions along the same TB, (a-c) and (d-f) respectively. The twin is the lower crystal in the images and the matrix the upper crystal. The dashed boxes in (b) and (e) highlight the regions of interest. (g) and (h) are

difference images between (a), (b) and (c) for region I, and (i) and (j) are those between (d), (e) and (f) for region II. Schematics of the TB advancement are shown below.

---

The video was compiled from the raw time resolved image sequence recorded at a rate of 10 frames per second. The images were registered using the TrakEM2 plugin in the image processing program ImageJ, by firstly automatic batch alignment process using the least square method and allowing only rotation and displacement of the images, and then manual alignment of specific frames when necessary. The user identifies that certain features in the image are stationary and can be used as fiducial marks. This second step was always necessary to obtain an accurate difference image from two frames at different times. The difference images were obtained by overlaying an inverted previous frame with a semi-transparent latter frame. Note that the existing add or subtract functions do not give the best contrast of the resulting image.

---

Figure 5.3 presents the evolution of the TB for another twin at orientation II. Similar to the case in Figure 5.2(d-f), a convex-shaped interface (Figure 5.3(b)) emerges from the initially flat interface (Figure 5.3(a)). Interestingly, the grown region exhibits a distinct contrast than the original twin. Such contrast is in fact also present in Figure 5.2(e) and (f) but is vague due to the short exposure time during video recording. Weak beam dark field (WBDF) condition refines the diffraction contrast to the near proximity of defects and reveals that the grown region contains profuse basal defects with  $[c]$ -component (Figure 5.3(c)). An important feature is that these defects are confined in the grown region, not exceeding the original position of the TB. To further investigate the origin of the distinct contrast, diffraction patterns (DP) were captured from the pertinent regions. The DP in Figure 5.3(e) is from the matrix and the grown region. It describes the typical  $\{10\bar{1}2\}$  twinning relationship, with the coincident spots representing the common twinning plane. The orientation of the CTB is therefore determined from the DP and is found to be parallel to the long segment of the bounding interface of the grown region (Figure

5.3(b)). The front short segment is closely aligned with the basal plane trace, corresponding to a BP serration. When the DP is obtained from the matrix, the grown region and the original twin, a third set of diffraction spots emerge (Figure 5.3(f)), corresponding to the original twin. Clearly, the DP of the original twin does not share coincident spots with the matrix, and there is an in-plane rotation of  $\sim 3^\circ$  between the grown region of the twin and the original twin. Note that all the diffraction spots are sharp, indicating that each diffracting region has a distinct orientation with little misorientation within each region.

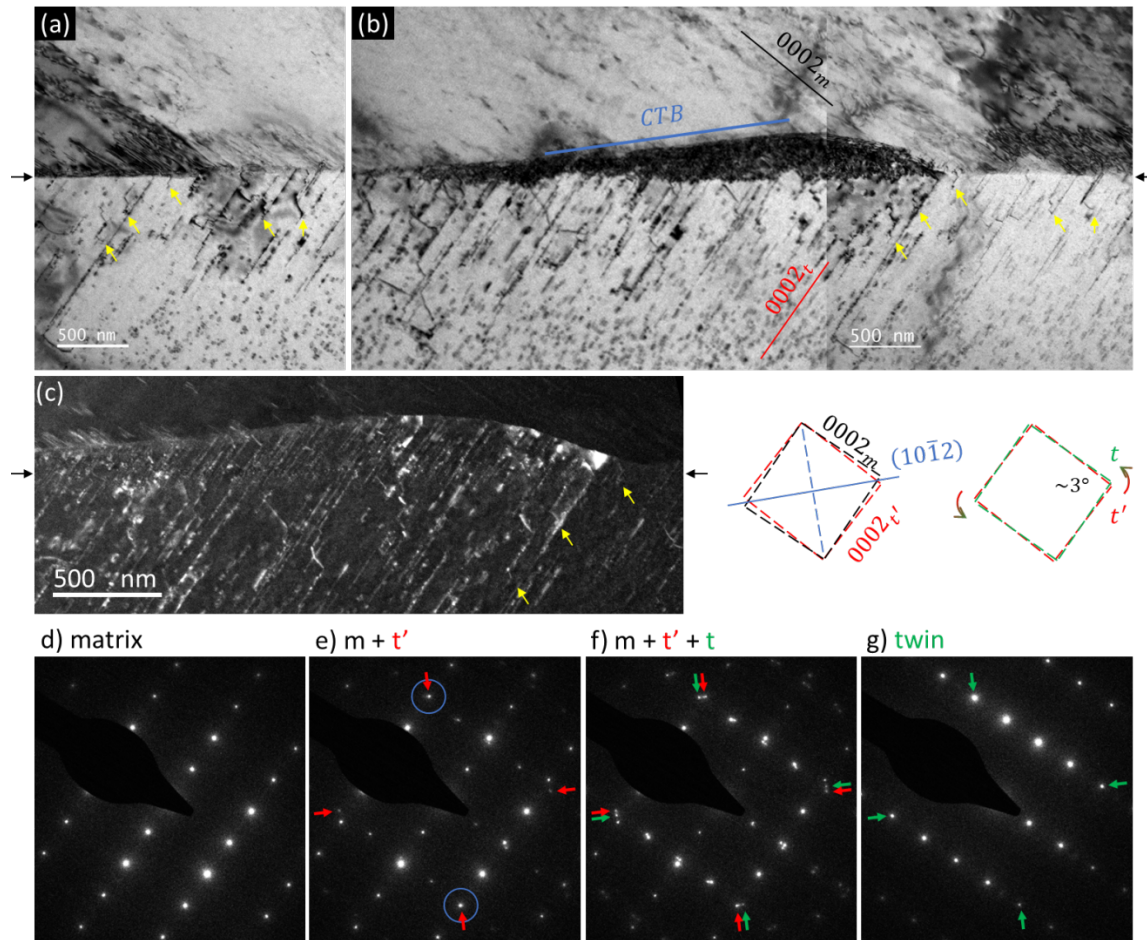


Figure 5.3. Static images of a TB (a) before and (b) after the tensile loading in the vertical direction. The yellow arrows point to the same features in the two images, which conveniently function as fiducial markers. (c) is the WBDF image with  $g = 0002_t$  focusing on the grown

region of the twin in (b). The position of the original flat TB is denoted by arrows outside the image frames. The diffraction patterns are obtained at state (b) from different regions: (d) the matrix – m, (e) matrix and the grown region – t', (f) matrix, the grown region and the original twin – t, and (g) the original twin. The circles in (e) highlight the coincident diffraction spots of matrix and the grown region. The red and green arrows point to the spots of the grown region and the original twin respectively.

In the two cases above, the TB develops convex-shaped interfaces after the impingement of gliding dislocations for the twin variants at orientation II. For a twin variant at orientation I, the TB is observed to develop concave-shaped interfaces (Figure 5.4). The twin was initially bounded by straight TBs and possessed a few  $[c]$ -containing dislocations in the twin interior. The regions in the vicinity of TB are relatively clear of defects (Figure 5.4(a)). During the straining, concentrated dislocation slip activity in the matrix was developed, as evidenced by the strong contrast parallel to the basal plane (Figure 5.4(b)). This is a common occurrence of localized plasticity in TEM thin foil sample, frequently induced by the stress concentration at irregularities around the hole of the sample [24]. Toward the impingement point of the gliding dislocations at TB, a wedge-shaped extrusion of the twin is formed. The difference image comparing the initial and final position of the interface reveals that the interface recessed on one side of the planar dislocation flow and progressed on the other side (Figure 5.4(d)). Along the same TB and away from the impingement point of the concentrated gliding dislocations (Figure 5.4(c)), the TB migrated less severely and is only serrated by small interfacial steps.

Dark contrast is observed inside the wedge-shaped twin extrusion (Figure 5.4(b)), similar to Figure 5.3(b). And again, the defects are confined only in the grown area (Figure 5.4(d)), indicating that they are generated by the advancing interface. The local defects are more clearly presented in Figure 5.5 obtained by post mortem characterization on a double tilt holder. Figure



5.5(a) is at the two-beam condition of  $g = 0002_t$ , where basal planes in twin are edge-on. All the visible defects in twin are  $[c]$ -containing, lying mostly on basal planes and with a few short segments on non-basal planes. When the twin is tilted to the two-beam condition of  $g = 10\bar{1}0_t$  (Figure 5.5 (b) and (c)), parallel fringes contrast is observed on the inclined basal planes, characteristic of stacking faults. The high local defect density renders it difficult to determine the bounding partial dislocations of the SFs, but they are suggested as  $I_1$  type based on the  $[c]$ -component of these basal faults. At this length scale, the interface bounding the twin extrusion is observed to be curved, deviating from the exact orientation of CTB (inclined  $\sim 43^\circ$  to the basal plane trace when both are edge on). Nevertheless, the straight segments of the interface are very close to the BP boundary and CTB, as delineated in Figure 5.5(a).

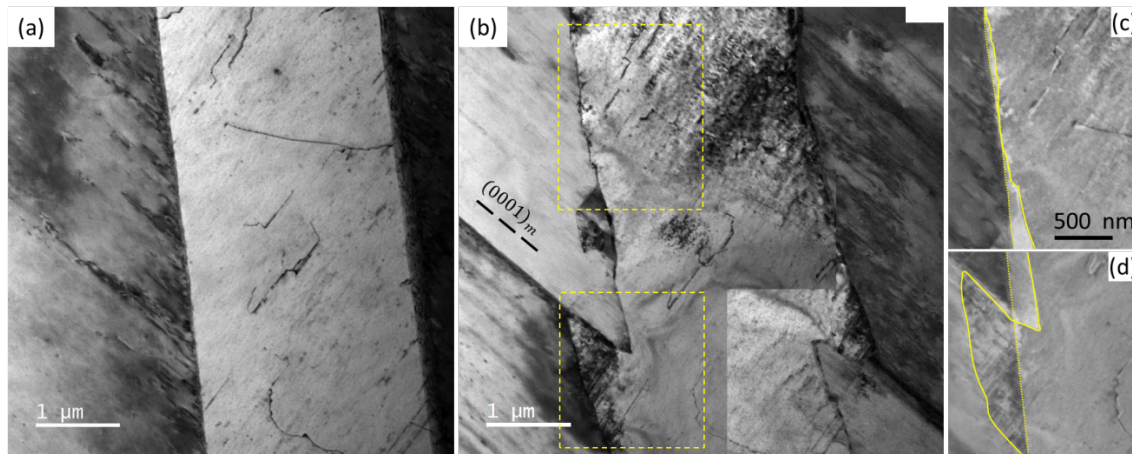


Figure 5.4. Snapshots of the same twin (a) before and (b) after the impingement of localized basal dislocations from the matrix. (c) and (d) are the difference images of two areas along the TB, with the dashed line indicating the initial position of the TB and solid line the final position.



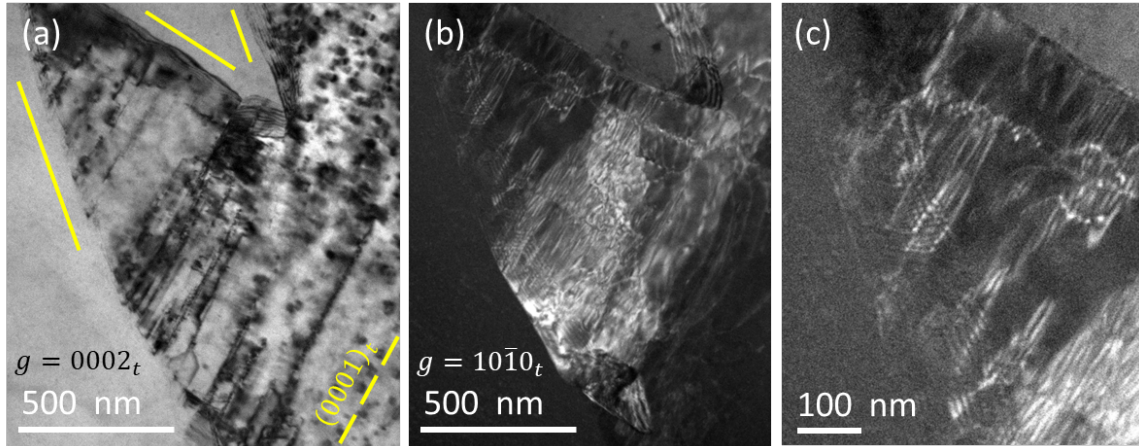


Figure 5.5. Defects inside the wedge-shaped twin extrusion from the twin in Figure 5.4. (a) and (b) are two-beam BF and WBDF images respectively using the diffraction vector  $g = 0002_t$  and  $g = 10\bar{1}0_t$ . (c) is a magnified view of (b), highlighting the fringe contrast of faults. The traces of the straight segments of the twin interface are shown by yellow lines aside the interface.

#### 5.4.2 Stacking faults in the wake of the advancing TB

Profuse basal stacking faults behind the advancing TB seem to be an important product of the dislocation – TB interaction in the above cases of local twin growth. Figure 5.6 shows a twin at orientation II after the straining. The TB is wavy on the length scale of  $10\ \mu\text{m}$  with some segments close to the traces of CTB and BP boundary. There is clearly a straight line behind the wavy TB demarcating regions of higher and lower defects density. The morphological features on one hand are consistent with those in Figure 5.2 and Figure 5.3, and on the other hand suggest that the TB has grown significantly while continuously interacting with the matrix dislocations. Note there are also many short non-basal dislocations in the grown region in Figure 5.6.

In order to determine the identity of the basal faults, diffraction contrast analyses were performed at a series of two-beam conditions near the zone axis of  $[1\bar{2}10]$  (Figure 5.7). The stacking faults are either edge-on (Figure 5.7(a)) or inclined (Figure 5.7(b-d)), exhibiting linear contrast at the former and parallel fringe contrast with bounding partial dislocations at the latter.

The tilting of the sample is suitably controlled such that the projection of the basal plane is as wide as possible but in the meantime overlapping of the faults on parallel basal planes is avoided. The faults are elliptical in shape on the highly inclined basal planes and are enclosed by two partial dislocation loops, e.g. SF 5 in Figure 5.7(c2). Such morphology is consistent with the previous characterizations of  $I_1$  faults in hexagonal metals [25, 26]. The upper and lower segments of the partial dislocation loops are close to the electron beam direction and therefore appear short, the remaining segments are long and curved in the projected view. Noticeably, the contrast of the partial dislocations is convoluted by the parallel fringes contrast of the immediate faulted area. Several faults are selected that show discernable contrast at the outer or inner periphery of the faults. For instance, the upper half loop of SF 4 is enclosed by a bright outer periphery in Figure 5.7 (d1), which is clearly invisible in Figure 5.7 (c1). The inner periphery of SF 4 is bright in Figure 5.7 (c1) but is relatively less defined in Figure 5.7 (d1). The same visibilities at the two diffraction conditions can be found for SFs 1, 5, and 6 as well. At the two-beam condition of  $g = (10\bar{1}0)_t$ , the parallel fringes are not enclosed by bright outer or inner peripheries, i.e. both partial dislocation loops are out of contrast.

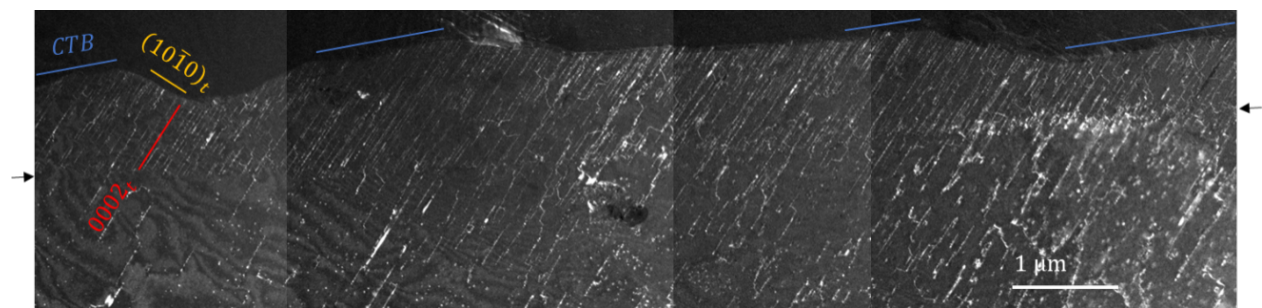


Figure 5.6. Montaged WBDF images at  $g = 0002_t$  two-beam condition showing the TB and defects inside twin after tensile straining of the twin in the vertical direction. The lower crystal in the images is the twin.

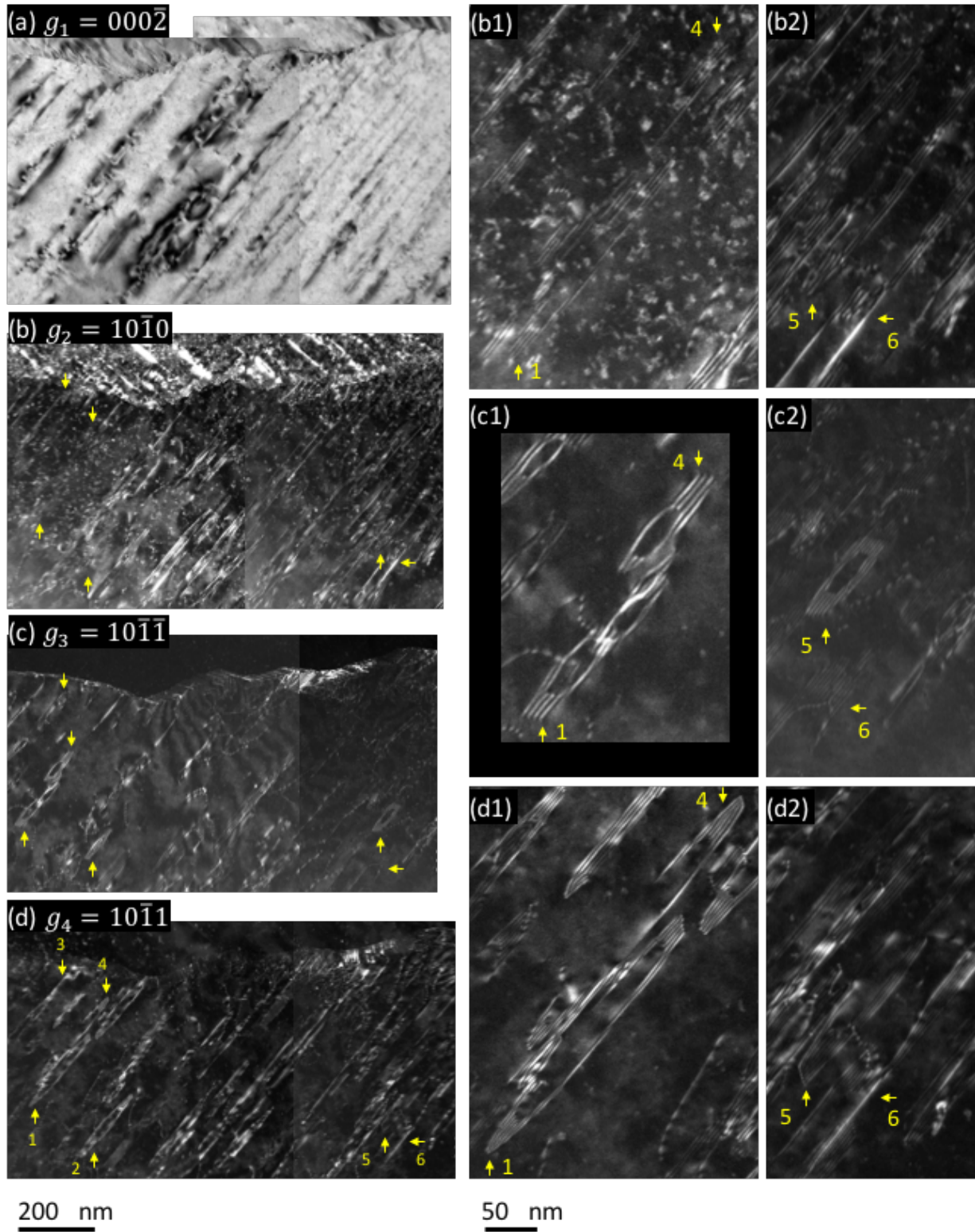


Figure 5.7. WBDF images of basal stacking faults in the wake of an advanced TB. The respective diffraction vectors  $g$  are (a)  $(000\bar{2})$ , (b)  $(10\bar{1}0)$ , (c)  $(10\bar{1}\bar{1})$  and (d)  $(10\bar{1}\bar{1})$ . (a-d) are

montaged images of the same area with the arrows pointing to the same features. Selected SFs are presented in magnified views at the latter three diffraction conditions: (b1, c1 & d1) focus on SFs 1 and 4, and (b2, c2 & d2) focus on SFs 5 and 6.

Table 5.1. The  $g \cdot b$  values of the partial dislocations of  $I_1$  stacking fault at the four two-beam conditions. The Burgers vectors of the partial dislocations are arranged in dissociated pairs of perfect  $\langle c + a \rangle$  dislocations. The  $g \cdot b$  values smaller or equal than  $1/3$  are underlined.

$b \setminus g$		$g_1 = 000\bar{2}$	$g_2 = 10\bar{1}0$	$g_3 = 10\bar{1}\bar{1}$	$g_4 = 10\bar{1}1$
$\langle c + a \rangle$	$I_1$ partials				
$1/3[11\bar{2}3]$	$1/6[20\bar{2}3]$	-1	0.67	<u>0.17</u>	1.17
	$1/6[02\bar{2}3]$	-1	<u>0.33</u>	<u>-0.17</u>	0.83
$1/3[1\bar{2}13]$	$1/6[2\bar{2}03]$	-1	<u>0.33</u>	<u>-0.17</u>	0.83
	$1/6[0\bar{2}23]$	-1	<u>-0.33</u>	-0.83	<u>0.17</u>
$1/3[\bar{2}113]$	$1/6[\bar{2}203]$	-1	<u>-0.33</u>	-0.83	<u>0.17</u>
	$1/6[\bar{2}023]$	-1	-0.67	-1.17	<u>-0.17</u>
$1/3[11\bar{2}\bar{3}]$	$1/6[20\bar{2}\bar{3}]$	1	0.67	1.17	<u>0.17</u>
	$1/6[02\bar{2}\bar{3}]$	1	<u>0.33</u>	0.83	<u>-0.17</u>
$1/3[1\bar{2}1\bar{3}]$	$1/6[2\bar{2}0\bar{3}]$	1	<u>0.33</u>	0.83	<u>-0.17</u>
	$1/6[0\bar{2}2\bar{3}]$	1	<u>-0.33</u>	<u>0.17</u>	-0.83
$1/3[\bar{2}11\bar{3}]$	$1/6[\bar{2}20\bar{3}]$	1	<u>-0.33</u>	<u>0.17</u>	-0.83
	$1/6[\bar{2}02\bar{3}]$	1	-0.67	<u>-0.17</u>	-1.17

The Burgers vectors of the partial dislocation loops are determined by the  $g \cdot b = 0$  invisibility criterion, which is adjusted to  $|g \cdot b| \leq 1/3$  in practice [27] and is especially suitable

for partial dislocations that have small magnitudes of Burgers vectors. The bounding partial dislocations are both  $[c]$ -containing and  $\langle a \rangle$ -containing, based on their contrast at the diffraction condition of  $g_1$  and  $g_2$ . The stacking faults are enclosed by two bounding partial dislocations of different diffraction contrast, e.g. at  $g_3$  and  $g_4$  respectively, suggesting that firstly the partial dislocations add up to a perfect Burgers vector that does not disturb the stacking sequence of the lattice, and secondly, they are not simply opposite signed. Therefore, the bounding partial dislocations are of  $1/6\langle 20\bar{2}3 \rangle$  type with the summation of a pair to be a perfect  $\langle c + a \rangle$  Burgers vector. With this constraint, the two-beam conditions listed in Table 5.1 are sufficient to determine that the Burgers vectors of the double dislocation loops constitute only the  $[c \pm a_2]$  variants of all the  $\langle c + a \rangle$  Burgers vectors, the ones that are closely aligned with the  $[a_{1,3}]$  Burgers vectors in the matrix as dictated by the twinning relationship.

## 5.5 MD simulations of the dislocation – TB interaction

The *in situ* experimental results show twin growth in the impingement region of the gliding  $\langle a \rangle$  dislocations, accompanied by interfacial facet formation and profuse  $I_1$  stacking faults in the wake of the advanced interface. MD simulations were performed to further reveal the detailed procedures of the interfacial reaction at smaller length scale and time resolution, and interpret the evolution of defects.

The global coordinates and the crystal axes are shown in Figure 5.8. In tensorial form, the simulation box is subject to a stress of

$$\boldsymbol{\sigma} = \begin{pmatrix} \sigma_{xx} & 0 & \sigma_{xz} \\ 0 & 0 & 0 \\ \sigma_{xz} & 0 & 0 \end{pmatrix}$$

The basal  $[a_3]$  dislocation with line direction  $[-y]$  experiences a Peach-Koehler force of

$$\mathbf{F} = (\boldsymbol{\sigma} \cdot \mathbf{b}) \times \boldsymbol{\xi} = \left( \boldsymbol{\sigma} \cdot a \begin{pmatrix} \frac{\sqrt{3}}{2} \cos 43^\circ \\ 1/2 \\ -\frac{\sqrt{3}}{2} \sin 43^\circ \end{pmatrix} \right) \times \begin{pmatrix} 0 \\ -1 \\ 0 \end{pmatrix} = \frac{\sqrt{3}a}{2} \begin{pmatrix} \cos 43^\circ \sigma_{xz} \\ 0 \\ -\cos 43^\circ \sigma_{xx} + \sin 43^\circ \sigma_{xz} \end{pmatrix}$$

So the resolved glide force perpendicular to the line direction and toward the TB is

$$F_{glide} = \mathbf{F} \cdot \begin{pmatrix} \cos 43^\circ \\ 0 \\ -\sin 43^\circ \end{pmatrix} = \frac{\sqrt{3}a}{2} \cdot \left( \frac{\sin 86^\circ}{2} \sigma_{xx} + \cos 86^\circ \sigma_{xz} \right) \approx \frac{\sqrt{3}a}{4} \sigma_{xx}$$

Therefore, the applied shear stress ( $\sigma_{xz}$ ) acts to drive the TB upward into the basal dislocation, and the tension stress ( $\sigma_{xx}$ ) acts to direct the basal dislocation toward the TB in the resistance of the repulsive force from the interface and the image force from the upper free surface in the same direction, e.g. the image force is estimated to be  $\sim 22$  MPa/a for a screw dislocation 20 nm away from the surface. Simulations were carried out at different loading combinations, and it was found that both tension and shear stresses are necessary to induce the dislocation incorporation and transformation, with stress values as low as 100 MPa tension ( $\sigma_{xx}$ ) and 180 MPa shear ( $\sigma_{xz}$ ). Tension or shearing alone cannot induce the dislocation transmutation reaction even at high stress values.

In Figure 5.8, the sequential incorporation and transformation of a basal dislocation at the twin interface is presented from the perspective of the co-zone of the matrix and twin  $[\bar{1}2\bar{1}0]$ . The basal planes in both crystals and the twin boundary are at edge-on orientation. As the front dislocation approaches the interface, a PB interface is firstly developed in response to the stress field of the dislocation (Figure 5.8 (b)). When the dislocation is by-passed by the interface, it transforms to a sessile partial dislocation inside the twin crystal, staying at the position of incorporation, and a residual defect on the interface (Figure 5.8 (c)). As the TB migrates upward, the sessile dislocation trails a basal SF in the twin, the residual defect is observed to be glissile,

traversing on the twin interface while the SF is extended (Figure 5.8 (d-f)). Closer inspection of the faulted area reveals a stacking sequence of ABAB|CBCB (Figure 5.8 (g)), corresponding to  $I_1$  SF. Using the RH/SF convention with respect to a closed circuit in the perfect crystal, a Burgers circuit around the trailing partial dislocation produces a projected closure failure of  $1/2[0001] + 1/6[10\bar{1}0]$  from the perspective of  $[\bar{1}2\bar{1}0]$ , corresponding to a partial dislocation of either  $1/6[2\bar{2}03]$  or  $1/6[02\bar{2}3]$  Burgers vector. The migration of the twin interface appears to be not inhibited by the interfacial reaction. The interface is able to gradually resume a nearly flat configuration after the complete incorporation of the  $[a_3]$  dislocation (Figure 5.8 (f)), until the incorporation of the second basal dislocation occurs.

The MD simulation results are consistent with the *in situ* observation. A single  $[a_3]$  dislocation transforms to a sessile partial dislocation in the twin crystal, bounding a  $I_1$  SF that lengthens with the advancing TB. Repetitions of this unit process by dislocations from parallel basal planes in the matrix are expected to leave an array of sessile dislocations at the original position of the TB and produce abundant defects in the grown region, forming a heterogeneous defect distribution inside the twin, e.g. Figure 5.3 (b), Figure 5.4 (b) and Figure 5.6. At the immediate step after the dislocation transmutation (Figure 5.8 (d)), a concave shaped interface is formed, similar to the experimentally observed interface of a twin at orientation I in Figure 5.4. The serrated interface is readily relaxed subsequently during the simulation by the applied shear stress in the twinning shear system.



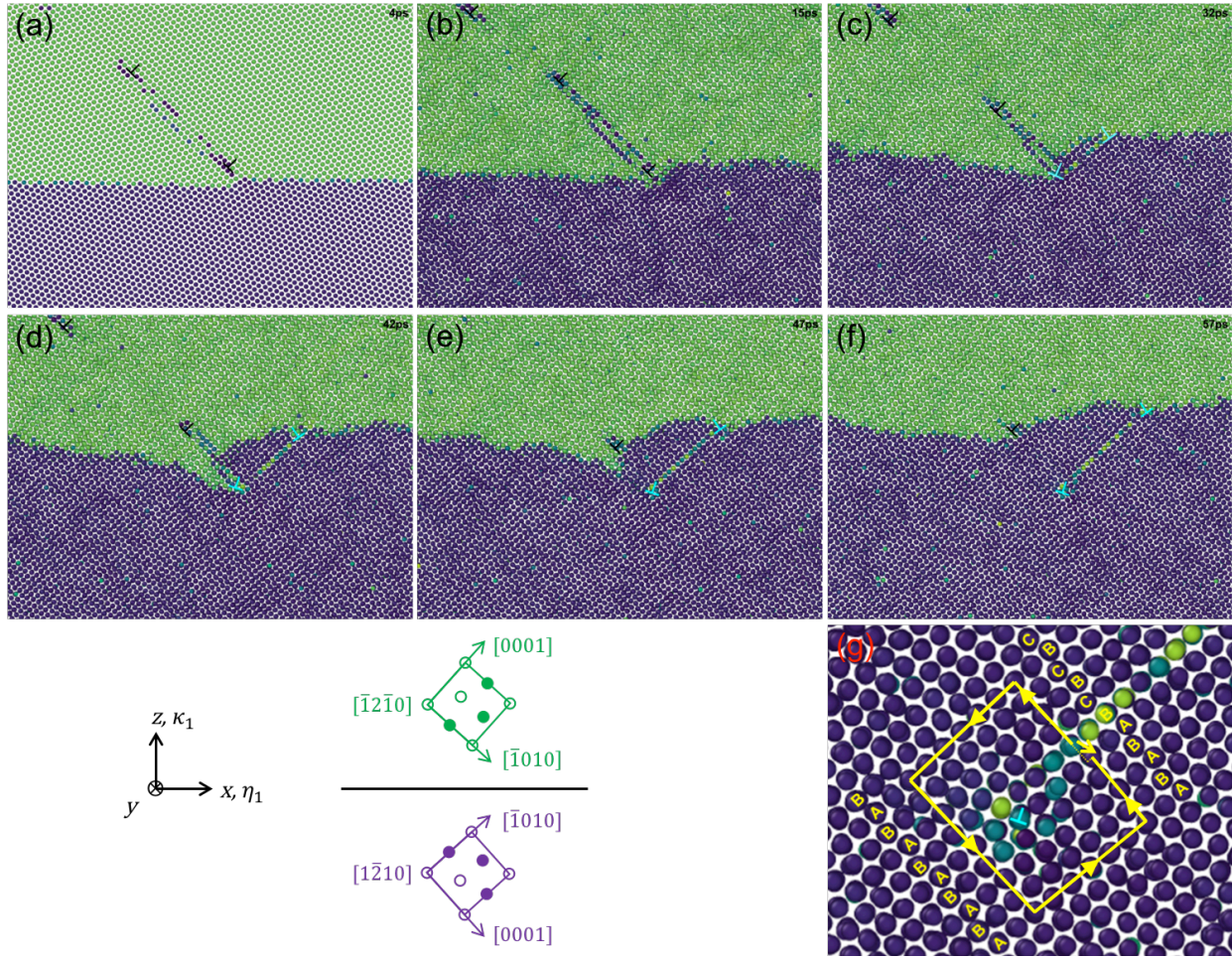


Figure 5.8. Time-resolved sequences of dislocation interaction with TB by MD simulation. The  $(10\bar{1}2)$  TB is horizontal in the images with the matrix above and the twin below. The atoms are colored based on the component of the normalized local  $c$ -axis along the vertical direction of the simulation box (the basal plane vector method [28]). The positions of the dislocations are indicated. The results shown correspond to a temperature of 50K, which, owing to minimal thermal fluctuation, facilitated the identification and analysis of defects structures.

## 5.6 Discussions

The current *in situ* tension experiments and MD simulations studied the interaction of  $60^\circ$  basal dislocations in the matrix with  $(10\bar{1}2)$  TB. It is observed that local twin growth is induced in the impingement region of the gliding dislocations at the interface. The grown region



is bounded on one side by a straight interface at a length around 500 nm and close to the PB/BP orientation and on the other side by an interface close to CTB. Abundant large  $I_1$  basal SFs are observed in the wake of the advanced interface. They are confined only in the grown region defined by the original position of the twin interface. In the following sections, we first analyze the defects involved in the interfacial reaction. Then we quantitatively evaluate the observed twin growth using the dislocation transmutation reaction. Finally, we discuss the evolution of the interfacial structure as a result of the slip-twin interaction with respect to the twin boundary mobility.

#### 5.6.1 Defects analyses of the interfacial reaction

The trichromatic pattern constructed by the interpenetrating projected lattices of the matrix ( $\mu$ , black), twin ( $\lambda$ , white) and a third imaginary lattice ( $\kappa$ , red) is a convenient tool to correlate the defects across an interface. It is recognized that the PB interface formed in response to the stress field of the incoming dislocation is only intermittent (Figure 5.8 (b)), so the vector transformation through the twin interface is resolved using the trichromatic pattern including the CTB (Figure 5.9) created using the  $\mu$  and  $\lambda$  lattices, and adding a  $\kappa$  lattice which is oriented the same as the  $\lambda$  lattice but with the ABAB basal stacking sequence changed to ACAC. The  $\kappa$  and  $\lambda$  lattices are essentially the twin lattice on either side of an  $I_1$  SF. This type of trichromatic pattern was recently used by Ostapovets [29] to describe the relationship of  $I_1$  faults to a  $\{10\bar{1}1\}$  twin boundary.

When a  $[a_3]$  dislocation is incorporated by the CTB, it finds the closest step vector  $b_{0/-1}^\kappa$  in the red lattice, and the two incompatible step vectors are connected by a residual disconnection  $[-b_{-1/-1}]$

$$[a_3] = b_{-1/0}^{\mu} = b_{0/-1}^{\kappa} - b_{-1/-1}^{\mu\kappa}$$

The step vector  $b_{0/-1}^{\kappa}$  connects two lattice spots across a  $1/2[c]$  plane. Since the  $\kappa$  and  $\lambda$  lattices have the stacking sequence of ACACAC and ABABAB respectively, the vector  $b_{0/-1}^{\kappa}$  represents a shift in the stacking sequence of the twin lattice and bounds a  $I_1$  stacking fault.

As shown in the MD simulation results (Figure 5.8), the fault created by the sessile partial dislocation keeps extending as TB migrates away from it. In order to enclose the continuously growing fault and therefore end the increase of energy associated with the fault, another partial dislocation has to be formed at the anchoring point of the fault on TB, which necessitates the transformation of a second  $[a_3]$  dislocation. For the second dislocation, although the vector  $b_{0/-1}^{\kappa}$  is the closest candidate, it cannot enclose the fault that is created by the first  $b_{0/-1}^{\kappa}$  vector since they do not add up to a perfect translation vector in the twin lattice. Instead, if the  $[a_3]$  dislocation transforms to the second closest vector  $b_{0/-1}^{\lambda}$  by

$$[a_3] = b_{0/-1}^{\lambda} + b_{-1/-1}^{\mu\lambda}$$

the two consecutive reactions are effectively

$$\begin{aligned} 2 \times [a_3] &= (b_{0/-1}^{\kappa} - b_{-1/-1}^{\mu\kappa}) + (b_{0/-1}^{\lambda} + b_{-1/-1}^{\mu\lambda}) = (b_{0/-1}^{\kappa} + b_{0/-1}^{\lambda}) + (b_{-1/-1}^{\mu\lambda} - b_{-1/-1}^{\mu\kappa}) \\ &= b_{0/-2}^{\lambda} + b_{2/2} \end{aligned}$$

As shown by the parallelogram in Figure 5.9(b), both step vectors  $b_{0/-1}^{\kappa}$  and  $b_{0/-1}^{\lambda}$  are partial dislocations in the twin lattice ( $\lambda$ ), they are able to enclose a fault with a total vector of a perfect  $[c + a_2]$  dislocation. Note the  $[a_2]$  component is not revealed in the trichromatic pattern, because it is perpendicular to the projection plane. The disconnections  $b_{-1/-1}$  are the residual defects in the twin interface. As shown in the simulated results, the disconnection generated by the first transformation process is able to glide on the migrating interface, trailing the basal SF.

More importantly, the combination of the two disconnections generated by the successive transformation of  $[a_3]$  dislocations results in a twinning disconnection  $b_t = b_{2/2}$ , whose glide on the twin interface produces boundary migration.

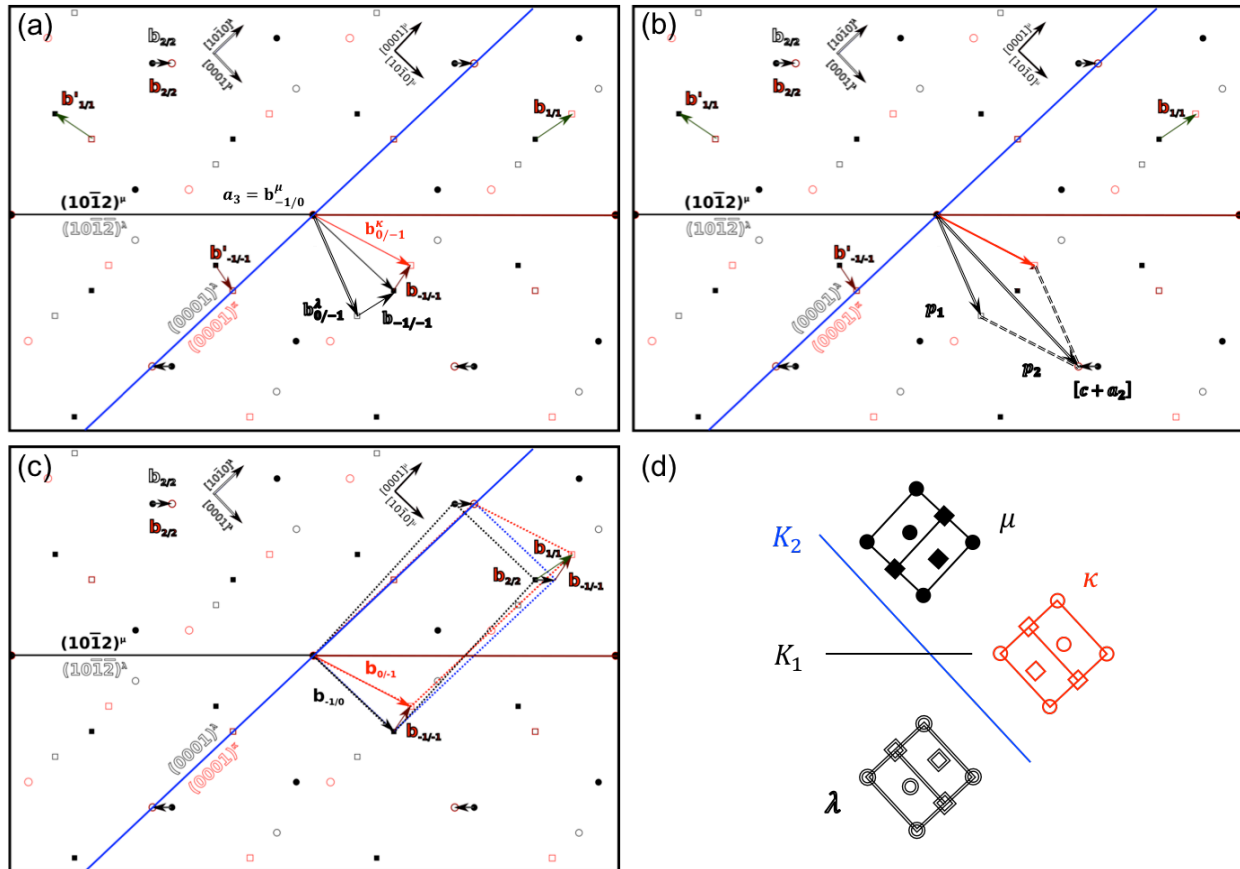


Figure 5.9. Trichromatic pattern of the matrix ( $\mu$ ), the twin ( $\lambda$ ) and the third ( $\kappa$ ) lattices projected along the co-zone axis  $[a_2]$ . The horizontal black lines indicate the CTB, and the inclined blue lines the coherent plane between the  $\lambda$  and  $\kappa$  lattices. The dissociation of the matrix  $[a_3]$  dislocation is shown in (a). (b) and (c) show the total resultant Burgers vector in the twin crystal ( $[c + a_2]$ ) and the interface ( $b_{2/2}$ ) respectively after the transformation of two matrix dislocations. (d) is the schematic of the three lattices and their orientation relationships with respect to the twinning plane  $K_1$  and conjugate plane  $K_2$ .

Overall, the reaction is consistent with the crystallography based vector transformation involving perfect dislocations of  $2 \times [a_{1,3}] \rightarrow b_t + [c \pm a_2]$ . The interfacial defects analyses help to elucidate the unit reaction that one basal dislocation transforms at twin interface to a partial dislocation of  $I_1$  fault. The fault is anchored by the sessile partial dislocation at the trailing end and terminates at the interface by a glissile disconnection. The interface therefore is not restricted by the residual interfacial defect and can migrate under an appropriate stress and lengthen the fault as it advances. The fault produced thus can be very wide, increasing the total fault energy while it grows, until the transformation of a second basal dislocation occurs. As discussed above, in order to stop the continuous growth of the fault, the second dislocation would preferably transform to the conjugate partial dislocation that is able to enclose it. The fault is then bounded by two different partial dislocations, the summation of which is either  $[c + a_2]$  or  $[c - a_2]$  depending on the Burgers vector of the incoming matrix dislocation. This is consistent with the experimentally determined Burgers vectors of the  $I_1$  stacking faults in Figure 5.7.

The above processes implicitly require that the two basal dislocations are of the same Burgers vector and the second one approaches the close vicinity of the terminating point of the fault at interface. The first requirement is expected to be readily fulfilled since dislocations of the same Burgers vector systematically glide in the same direction under external loading according to the Schmid law. The second requirement seems geometrically rigid. In fact, the twin interfaces in Figure 5.5(b) and Figure 5.7(c, d) are observed to trail faults that are still attached to the interface, presumably not yet enclosed by the transformed second matrix dislocation. On the other hand, given the abundance of gliding dislocations on parallel basal planes in the matrix, the termination of a fault by the second partial dislocation is considered frequent from a statistical point of view, as evidenced by the profuse faults scattered in a band behind the TB (Figure 5.6

and Figure 5.7). The evaluation of the above process as well as the double looped morphology of the SFs should be performed in 3 dimensions involving the complete line length of the dislocations. A continuing work is devoted to the analyses.

Whereas the unit reaction produces a sessile dislocation in the twin, it is identified that TB advancement is necessary for the continuous occurrence of the reaction. Imagine the TB is stationary when the dislocation arrives, e.g. the transient state between Figure 5.8(b) and (c), the sessile partial dislocation remains in the interface and cannot trail a fault unless the interface moves away from it. In this regard, it is not a slip transfer process. Representative previous simulations of dislocation-TB interaction [10, 12, 13] reported complete absorption of the matrix dislocation at interface, forming an interfacial step that can be a source of twinning dislocations and in such a way contributes to subsequent twin growth. The current simulations differ from the previous work firstly by a boundary condition that enforces the matrix dislocation to interact with TB. In addition to a shear stress that motivates interface advancement as in the previous studies, the current simulation box is subject to a tension stress in the twinning shear direction, giving rise to a positive RSS on the matrix dislocation. Secondly, the current work employs a new interatomic potential for Mg introduced by Wu et al. [21]. The potential accurately describes the  $I_1$  stacking fault energy, which is intimately associated with the interfacial reaction, and therefore is a determining factor to well reproduce the dislocation transmutation reaction.

### 5.6.2 Slip-assisted twin growth model

In light of the fact that the dislocation reaction at TB overall abides the dislocation transmutation reaction, its contribution to twin growth is evaluated and compared with the experimentally observed local twin growth.

Figure 5.3 presents an instance of local twin growth from a flat twin interface. The interface is conveniently extracted from the recorded image according to the straight traces of the interfaces (Figure 5.10), and the grown region is approximated as a triangle, with a measured area of  $5.213 \times 10^5 \text{ nm}^2$ . The diffraction pattern in Figure 5.3(e) shows that the grown region maintains the coherent twinning orientation relationship with the matrix, and the long segment of the interface bounding the grown region is aligned with the trace of CTB. Acknowledging that the growth is carried out by successive glide of twinning dislocations on parallel  $(10\bar{1}2)$  twinning planes, the area of the triangle gives an effective CTB elevation ( $H$ ) of 227 nm.

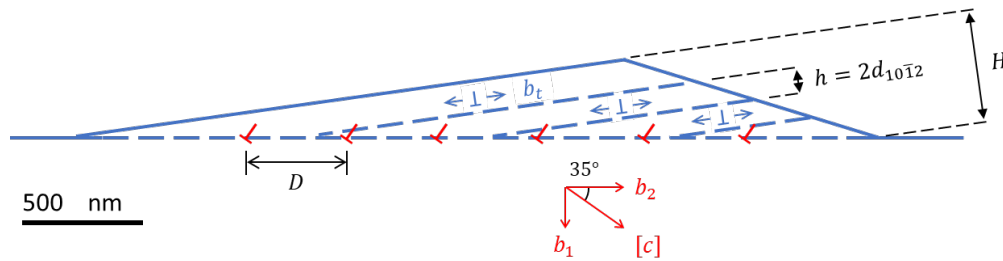


Figure 5.10. The outline of the twin interface extracted from Figure 5.3(b). The length scale and the inclination of plane traces and vectors reflect the original experimental image. The parallel dashed lines represent the coherent  $(10\bar{1}2)$  twinning planes, with the twinning dislocation  $b_t$  and the step height  $h$  drawn schematically.

In the following, the occurrence of the interfacial dislocation reactions is firstly derived from the orientation of the grown region; the expected twin growth is then computed assuming the dislocation transmutation reaction. As shown by both the experimental observations and MD simulations, gliding basal dislocations from the matrix transform to sessile dislocations inside the twin. As a result, they are confined only in the grown region, giving rise to a misorientation of the region from the original twin. By simple Schmid analysis for the orientation in Figure 5.1,

the external applied loading drives  $[-a_1]_m$  and  $[a_3]_m$  dislocations to glide toward the TB. The transmuted defects in twin can be in the form of  $I_1$  partial dislocations or perfect dislocations, but effectively have the Burgers vectors of either  $[c - a_2]_t$  or  $[c + a_2]_t$ . The  $[a_2]_t$  components of the transmuted dislocations are perpendicular to the plane of image, whereas the  $[c]_t$  components are contained in the plane of image and inclined to the twinning plane (Figure 5.10). Therefore, the  $[c]_t$  components are the ones that constitute the in-plane rotation exhibited in the diffraction pattern in Figure 5.3(f).

In order to compute the total number of the effective  $[c \pm a_2]_t$  dislocations in the grown region, a low angle tilt boundary is constructed at the original position of the TB by equally spaced  $[c]$  dislocations, which virtually represent all the defects in the grown region. If the  $[c]$  Burgers vector is further resolved to the components perpendicular and parallel to the boundary  $b_1 = b \sin 35^\circ$  and  $b_2 = b \cos 35^\circ$ , the  $b_1$  dislocations constitute a vertical array (Burgers vector perpendicular to the boundary), i.e. a symmetric tilt boundary, and are hence responsible for the  $3^\circ$  in-plane rotation between the grown region and the original twin; the  $b_2$  dislocations constitute a horizontal array (Burgers vector parallel to the boundary) and do not produce lattice rotation. Using the symmetric low angle tilt boundary model [30], the average spacing  $D$  of the dislocations is computed from the measured tilt angle  $\theta = 3^\circ = \pi/60$  as

$$D = \frac{b_1}{\theta} = 5.71 \text{ nm}$$

The total number of dislocations in the wall with a measured length of 3310 nm is then estimated to be 580. According to the transmutation equation, an equivalent number of twinning dislocations are produced by the dislocation-twin interaction. The glide of each twinning dislocation on  $(10\bar{1}2)$  plane brings a step height of  $h = 2d_{10\bar{1}2} = 0.38 \text{ nm}$ . Therefore, these twinning dislocations can elevate the twin interface by  $580 \times 0.38 \text{ nm} = 220 \text{ nm}$ .

The amount of twin boundary advancement induced by the dislocation transmutation reaction agrees well with the experimentally determined value with only a slight deviation, suggesting that the local twin growth is completely induced by the mechanism. Admittedly, the above analysis ignores the intermittent stages of the transformation of dislocations at interface, but in a collective manner, it is determined that the transformation of every two basal dislocations leads to one twinning dislocation that can effectively contribute to twin boundary migration. To the authors' knowledge, the current results are the first experimental verification in Mg of the twin growth mechanism proposed by Yoo and Wei in 1966 [1].

The dislocation transmutation reaction functions as a source mechanism for twinning dislocations and contributes thus to twin growth. The local twin growth phenomena in the current *in situ* experiments are attributed to the successive generation of twinning dislocations in the region. The twinning dislocations glide on the twin interface, driven by the repulsive near field stress of the incoming basal dislocations. Due to the lack of sufficient global shear stress, their glide activity is limited and therefore only leads to local boundary migration.

On the other hand, it is accepted that the  $\{10\bar{1}2\}$  deformation twinning is not a source limited mechanism and twin growth is predominantly slip independent [31, 32]. While the growth induced by dislocation-twin interaction may not be sufficient to account for all the twin volume that is needed to accommodate the macroscopic plastic strain [31], it is an effective mechanism when twinning is not promoted by the global stress state. Since the incident slip dislocations induce the forward migration of TB by repelling the locally generated twinning dislocations, the TB is able to continuously absorb the dislocations in front of it and in such a way relax any potential dislocations pile-up. In this regard, it is an accommodation process that dissipates the near field stress in the matrix side of the TB. For instance, the TB in Figure 5.2



absorbs the incident dislocations and responds by forward migration, and the grown region in Figure 5.3(b) has in its vicinity only scattered basal dislocations rather than dislocations pile-up after the slip-twin interaction.

### 5.6.3 Formation of interfacial facets

The dislocation-twin interaction effectively regulates the development of interfacial facets. The glides of locally generated twinning dislocations advance the interface via the elevation of  $\{10\bar{1}2\}$  twinning planes, the grown regions therefore are bounded partially by CTBs. In the meantime, the accumulation of twinning dislocations and the lack of global shear stress in the twinning system lead to the buildup of twinning dislocations pile-up, which can relax into atomic scale BP/PB facets [33]. Short facets are indeed present in the current observations, e.g. in Figure 5.7(c), but more strikingly are the development of straight and long serrations close to the BP/PB orientations after slip-twin interaction.

The formation of different facets was studied by Serra et al. [11] based on the absorption of incident basal dislocations of different signs using atomistic simulations. The *in situ* experiments in this work stimulate the dislocation interaction with the  $\{10\bar{1}2\}$  TBs of two variants. Simple Schmid analysis informs that basal  $\langle a \rangle$  dislocations of the same sign will be driven to TB by the applied tension. In the coordinate system of the matrix (Figure 5.1),  $[-a_3]$  and  $[+a_1]$  dislocations glide toward the interface and  $[+a_3]$  and  $[-a_1]$  away from the interface (Figure 5.11(a, b)). However, the half plane of the edge component of the forward dislocation is at an acute angle with the twinning shear direction for twin variant I and a blunt angle for twin variant II. The two situations essentially represent the interaction of positive and negative dislocations interacting with the same twinning shear system. The interface structures after the

dislocation impingement are extracted from Figure 5.4, Figure 5.6 and Figure 5.3, representing variant I and variant II respectively, and are presented schematically in Figure 5.11(c, d). The current experimental results show similar boundary structure with those by atomistic simulations [11, 13, 34], but the observed serrations are on the length scale of 500 nm to 1  $\mu\text{m}$ . For the interaction of both positive and negative dislocations, basal-prismatic serrations are preferred. More generally, positive dislocations induce the formation of concave-shaped serrations, and negative dislocations induce convex-shaped serrations. Such phenomena can occur on different twin variants during the straining of a grain in a polycrystalline material, a similar situation as the current single crystal. It is also expected to occur on the same twin during uniaxial cyclic loading or non-proportional loading where the principle stress direction is changed, namely the situation in Figure 5.11(c, d).

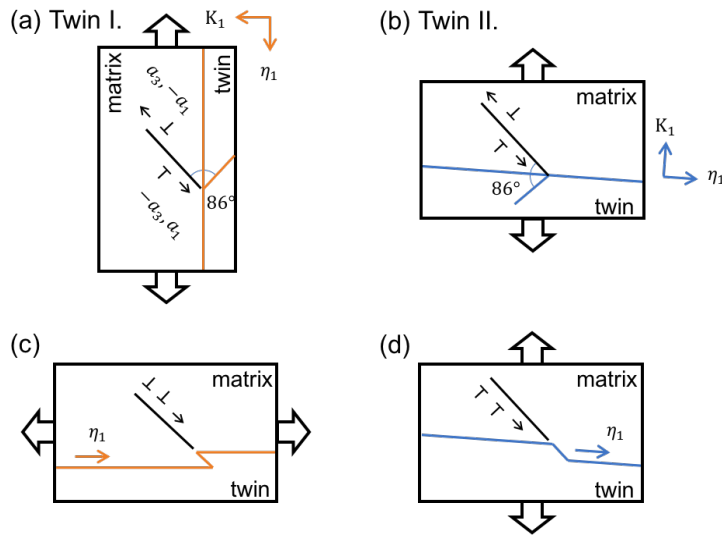


Figure 5.11. (a) and (b) show schematically the slip direction of opposite basal dislocations in the matrix with respect to the two twinning systems. (c) and (d) are the corresponding interface structure extracted from Figure 5.4, Figure 5.6 and Figure 5.3 after the dislocation-twin interaction. Note for the purpose of comparison, (c) is rotated from (a) such that the twinning shear direction ( $\eta_1$ ) is aligned with that in (d).

The fact that TB is able to advance for hundreds of nanometers during the *in situ* experiments demonstrates its ability to continuously incorporate gliding dislocations, even though it deviates from the CTB by microscale BP/PB serrations or the nanoscale facets. This may provide a physical interpretation of the small Hall-Petch coefficient associated with twinning [35]. On the other hand, the effect of the large serrations on TB mobility is worthy of further considerations. It was shown by atomistic simulations [13] that when a gliding twinning dislocation on the CTB merges onto a BP/PB facet at one end, the facet tends to maintain a stable length of 10 basal atomic layers by emitting a twinning dislocation at the other end, whose continuous glide further induces boundary migration. The flattening of the atomic scale concave facet in Figure 5.8(d) during subsequent straining demonstrates that TDs are able to glide through various twin interfaces and lead to boundary migration as a whole. The wavy TB across a length scale of 10  $\mu\text{m}$  in Figure 5.6 has advanced about 1  $\mu\text{m}$  from the initial position, with the profuse defects in its wake being a signature of extensive dislocation-twin interactions and marking the path of boundary migration. This behavior also appears to support the glide of twinning dislocations across the serrated boundary consisting of CTB and BP/PB facets. However, when the BP/PB facets are extended beyond the stable length, misfit dislocations are formed at both ends of the facet to compensate the lattice misregistry [36]. In Figure 5.2, the TB on the right side of the PB serration keeps advancing throughout the recorded video, accompanied by the extension of the serration on the upper end due to the pile-up and merge of twinning dislocations. On the other hand, the TB at the lower end is stationary, absent of twinning dislocation activity. This is likely related to the fact that such large serrations must be stabilized by misfit dislocations, which impede the passage of the twinning dislocations. The

large concave serration developed in Figure 5.4 is also expected to be a strong obstacle, since it involves defects on the boundaries that are at acute angles. Cyclic deformations involving twinning in Mg and other hexagonal metals have shown cleavage cracking along the TB with serrated crack profile [37], or even fragmentation of the twin [38]. The large serrations developed due to the extensive dislocation-twin interaction may be a cause for such behaviors.

## 5.7 Conclusions

*In situ* tension TEM were performed using oriented pure Mg single crystal specimens to study the dislocation slip induced  $\{10\bar{1}2\}$  twin growth, the formation of  $I_1$  stacking faults in twin, and the evolution of TB structures. The crystal defects were investigated by diffraction contrast at the length scale of conventional TEM, exhibiting consistent structures and mechanisms that are commonly studied by atomistic simulations or HRTEM. The current study therefore should contribute to the understanding of collective grain-scale mechanics. The major findings are summarized below:

Local twin growth is observed at the region of gliding basal dislocation impingement, and is evaluated to be completely induced by the dislocation transmutation reaction with a ratio of one twinning dislocation per transformation of two  $60^\circ$  basal dislocations. The locally generated twinning dislocations glide under the near field stress of the incident dislocations and therefore result in the migration of the interface.

The transformation of basal dislocations at the  $\{10\bar{1}2\}$  TB is not a slip transfer process, it occurs only when the TB advances. Profuse  $I_1$  basal stacking faults are observed in the wake of the locally advanced TB, with a few short non-basal  $[c]$ -containing dislocations. MD simulations and interfacial topological analyses reveal that as the unit process of dislocation-twin interaction,

each matrix dislocation transforms to a partial dislocation inside the twin crystal, trailing a  $I_1$  SF when the TB advances. Because of the sessile nature of the bounding partial dislocation and the low stacking fault energy, the fault formed in such a way can be very large. The partial dislocations are dissociation products of  $[c \pm a_2]$  dislocations (not  $[c \pm a_1]$  or  $[c \pm a_3]$ ), as determined by the diffraction contrast analyses in TEM as well as the topological analyses. Their correlation to the perfect  $[c \pm a_2]$  dislocations frequently observed in  $(10\bar{1}2)$  twins is the subject of further investigation.

Large interfacial serrations on the order of 500 nm to 1  $\mu\text{m}$  and close to the orientation of PB/BP boundaries are developed as a result of the localized dislocation-twin interactions. The large size suggests their ability to continuously incorporate basal dislocations from the matrix. The serrations appear to be barriers for the passage of twinning dislocations, but on the other hand do not stop the boundary motion.

## References

- [1] M. Yoo and C. Wei, *Phil. Mag.*, vol. 14, pp. 573-587, 1966.
- [2] F. Wang and S. Agnew, "Dislocation transmutation by tension twinning in magnesium alloy AZ31," *Int. J. Plas.*, vol. 81, pp. 63-86, 2016.
- [3] A. Serra, D. Bacon and R. Pond, "The crystallography and core structure of twinning dislocations in H.C.P. metals," *Acta Metall.*, vol. 36, pp. 3183-3203, 1988.
- [4] H. El Kadiri and A. Oppedal, "A crystal plasticity theory for latent hardening by glide twinning through dislocation transmutation and twin accommodation effects," *Journal of the Mechanics and Physics of Solids*, vol. 58, pp. 613-624, 2010.
- [5] D. Westlake, "Twinning in Zirconium," *Acta Metal.*, vol. 9, pp. 327-331, 1961.
- [6] D. Tomsett and M. Bevis, "The incorporation of basal slip dislocations in  $\{10\text{-}12\}$  twins in zinc crystals," *Philosophical Magazine*, vol. 19, no. 157, pp. 129-140, 1969.
- [7] S. Morozumi, M. Kikuchi and H. Yoshinaga, "Electron microscope observation in and around  $\{1\text{-}102\}$  twins in magnesium," *Trans. JIM*, vol. 17, pp. 158-164, 1976.
- [8] D. Bhattacharyya, E. Cerreta, R. McCabe, M. Niewczas, G. Gray III, A. Misra and C.

- Tome, "Origin of dislocations within tensile and compressive twins in pure textured Zr," *Acta Materialia*, vol. 57, pp. 305-315, 2009.
- [9] F. Wang, K. Hazeli, K. Molodov, C. Barrett, T. Al-Samman, D. Molodov, A. Kontsos, K. Ramesh, H. El Kadiri and S. Agnew, "Characteristic dislocation substructure in {10-12} twins in hexagonal metals," *Scripta Mater.*, vol. 143, pp. 81-85, 2018.
- [10] A. Serra and D. Bacon, *Phil. Mag.*, vol. 73, pp. 333-343, 1996.
- [11] A. Serra, D. Bacon and R. Pond, "Dislocations in interfaces in the H.C.P. metals - I. defects formed by absorption of crystal dislocations.," *Acta Mater.*, vol. 47, pp. 1425-1439, 1999.
- [12] A. Serra and D. Bacon, *Phil. Mag.*, vol. 90, pp. 845-861, 2010.
- [13] H. El Kadiri, C. Barrett, J. Wang and C. Tome, *Acta Mater.*, vol. 85, pp. 354-361, 2015.
- [14] B. Xu, L. Capolungo and D. Rodney, "On the importance of prismatic/basal interfaces in the growth of (-1012) twins in hexagonal close packed crystals," *Scripta Mater.*, vol. 68, pp. 901-904, 2013.
- [15] S. Lay and G. Nouet, "Interaction of slip dislocations with the (01-12) twin interface in zinc," *Philosophical Magazine A*, vol. 70, pp. 1027-1044, 1994.
- [16] Y. Li, Y. Chen, J. Walmsley, R. Mathinsen, S. Dumouлина and H. Roven, "Faceted interfacial structure of {10-11} twins in Ti formed during equal channel angular pressing," *Scripta Mater.*, vol. 62, pp. 443-446, 2010.
- [17] J. Tu, X. Zhang, C. Lou and Q. Liu, "HREM investigation of {10-12} twin boundary and interface defects in deformed polycrystalline cobalt," *Philos. Mag. Lett.*, vol. 93, pp. 292-298, 2013.
- [18] J. Tu, X. Zhang, Y. Ren, Q. Sun and Q. Liu, "Structural characterization of {10-12} irregular-shaped twinning boundary in hexagonal close-packed metals," *Mater. Charact.*, vol. 106, pp. 240-244, 2015.
- [19] J. Zhang, G. Xi, X. Wan and C. Fang, "The dislocation-twin interaction and evolution of twin boundary in AZ31 Mg alloy," *Acta Mater.*, vol. 133, pp. 208-216, 2017.
- [20] S. Plimpton, "Fast parallel algorithms for short-range molecular dynamics," *J. Comput. Phys.*, vol. 117, pp. 1-19, 1995.
- [21] Z. Wu, M. Francis and W. Curtin, "Magnesium interatomic potential for simulating plasticity and fracture phenomena.," *Modelling and Simulation in Materials Science and Engineering*, vol. 23, p. 015004, 2015.
- [22] D. Barnett and J. Lothe, "Consideration of the existence of surface wave (Rayleigh wave) solutions in anisotropic elastic crystals," *J. Phys. F: Metal Phys.*, vol. 4, p. 671, 1974.
- [23] D. Barnett and J. Lothe, "An image force theorem for dislocations in anisotropic bicrystals," *J. Phys. F: Metal Phys.*, vol. 4, p. 1618, 1974.
- [24] A. Couret, J. Crestou, S. Farenc, G. Molenat, N. Clement, A. Coujou and D. Caillard, "In situ deformation in TEM: recent developments," *Microsc. Microanal. Microstruct.*, vol. 4,

- pp. 153-170, 1993.
- [25] A. Berghezan, A. Fourdeux and S. Amelinckx, "Transmission electron microscopy studies of dislocations and stacking faults in a hexagonal metal: Zinc," *Acta Metal.*, vol. 9, pp. 464-490, 1961.
  - [26] J. Geng et al., "The structure of  $\langle c+a \rangle$  type dislocation loops in magnesium," *Phil. Mag. Lett.*, vol. 94, pp. 377-386, 2014.
  - [27] B. Fultz and J. Howe, *Transmission electron microscopy and diffractometry of materials*, New York: Springer, 2001.
  - [28] C. Barrett, M. Tschopp and H. El Kadiri, "Automated analysis of twins in hexagonal close-packed metals using molecular dynamics," *Scripta Mater.*, vol. 66, pp. 666-669, 2012.
  - [29] A. Ostapovets and A. Serra, "Slip dislocation and twin nucleation mechanisms in hcp metals," *Journal of Materials Science*, vol. 52, p. 533-540, 2017.
  - [30] P. Anderson, J. Hirth and J. Lothe, *Theory of Dislocations*, Cambridge University Press, 2017.
  - [31] L. Capolungo, I. Beyerlein and C. Tome, "Slip-assisted twin growth in hexagonal close-packed metals," *Scripta Mater*, vol. 60, pp. 32-35, 2009.
  - [32] P. Price, "Nucleation and growth of twins in dislocation-free zinc crystals," *Proceedings of the Royal Society of London. Series A, Mathematical and Physical Sciences*, Vols. 260-262, p. 251, 1961.
  - [33] C. Barrett and H. El Kadiri, "Impact of deformation faceting on  $\{10\text{-}12\}$ ,  $\{10\text{-}11\}$  and  $\{10\text{-}13\}$  embryonic twin nucleation in hexagonal close-packed metals," *Acta Mater.*, vol. 70, pp. 137-161, 2014.
  - [34] J. Wang, L. Liu, C. Tome, S. Mao and S. Gong, "Twinning and de-twinning via glide and climb of twinning dislocations along serrated coherent twin boundaries in hexagonal-close-packed metals," *Mater. Res. Lett.*, vol. 1, pp. 81-88, 2013.
  - [35] C. Caceres, P. Lukac and A. Blake, "Strain hardening due to  $\{10\text{-}12\}$  twinning in pure magnesium," *Phil. Mag.*, vol. 88, pp. 991-1003, 2008.
  - [36] C. Barrett and H. El Kadiri, "The roles of grain boundary dislocations and disclinations in the nucleation of  $\{10\text{-}12\}$  twinning," *Acta Mater.*, vol. 63, pp. 1-15, 2014.
  - [37] Q. Yu, J. Zhang and Y. Jiang, "Fatigue damage development in pure polycrystalline magnesium under cyclic tension-compression loading," *Mater. Sci. Eng. A*, vol. 528, pp. 7816-7826, 2011.
  - [38] P. Partridge, "Cyclic twinning in fatigued close-packed hexagonal metals," *Philos. Mag.*, vol. 12, pp. 1043-1054, 1965.

## CHAPTER 6    $\langle c + a \rangle$ DISLOCATION IN $(10\bar{1}2)$ TWIN: A KINEMATIC REQUIREMENT

### 6.1 Introduction

In Mg alloys and many other hexagonal metals, the  $\{10\bar{1}2\}$  twinning is an important deformation mode that strongly influences the texture and hardening [1]. Under appropriate loading, such as compression along the principle working direction of a wrought material (e.g. the extrusion direction of an extruded bar or the in-plane direction of a rolled plate), the  $\{10\bar{1}2\}$  twins contribute significantly to the initial yielding and the immediate plateau regime in the stress-strain curve. The twins grow pervasively, inducing twin-twin intersections [2, 3] and interactions of gliding basal  $\langle a \rangle$  dislocations in the matrix with the migrating TB. The latter includes the obstruction of dislocation slip via a weak Hall-Petch effect [4-8] and dislocation transformations at the interface [11-13]. As a result of the fast twin growth, a considerable volume fraction of the material is consumed by twins early in the deformation, e.g. 80% volume fraction up to 6% strain in a rolled Mg alloy AZ31 [12]. The twin crystals therefore govern the subsequent stress-strain response of the polycrystalline aggregates. The  $\{10\bar{1}2\}$  twinning instantaneously reorients the crystals at hard orientations with respect to the external straining



axis. Before the onset of the hard deformation modes in the  $\{10\bar{1}2\}$  twins, the twins deform like elastic inclusions, causing a rapid rise of the macroscopic stress proportional to the volume fraction of the twins [13]. It was predicted by crystal plasticity modeling studies [16-18] that, in order to plastically accommodate the imposed strain, extensive pyramidal  $\langle c + a \rangle$  slip activity is necessitated in the twins.

The knowledge of the dislocation substructure inside the  $\{10\bar{1}2\}$  twins is therefore essential for understanding and predicting the straining response of the twinning dominated deformation of Mg alloys. It has been identified experimentally in several hexagonal metals [9, 10, 17-19] that the twins contain both perfect  $\langle c + a \rangle$  dislocations and basal  $I_1$  stacking faults (SF), whose bounding partial dislocations are dissociation products of  $\langle c + a \rangle$  dislocations. Such dislocation substructures were observed in polycrystalline Mg alloy AZ31 compressed along the rolling direction of a rolled plate to a global stress of about 100 MPa [10], as well as in a single crystal pure Mg compressed parallel to the basal plane to a global stress of only 5 MPa [13]. The generation of the abundant  $\langle c + a \rangle$  dislocations at low stresses were attributed to the transformations of  $\langle a \rangle$  dislocations from the matrix at the TB, as suggested by the crystallography based concept of Yoo and Wei [20] in 1966,

$$2 \times [a_{1,3}]_m = [c \pm a_2]_t + b_t \quad (1)$$

where  $[a_{1,3}]_m$  represents either the  $[a_1]$  or  $[a_3]$  Burgers vector in the matrix with respect to a  $(10\bar{1}2)$  TB,  $[c \pm a_2]_t$  represents the transformed Burgers vector in the twin and  $b_t$  represents the twinning dislocation. The above dislocation transformation is not energetically favorable if simply evaluated using the Frank's rule. Whereas a unit  $\langle a \rangle$  dislocation may correspond to a  $1/2\langle c + a \rangle$  in the twin, the latter is not a complete translation vector in the lattice and may create either a high energy fault in the twin or remain sessile at the TB. In either case, the combination

of two  $\langle a \rangle$  dislocations of the same Burgers vector at TB is expected to require a high local stress, e.g. from a dislocations pile-up, if they approach the TB from the same basal slip plane [10, 21]. Recently, it was observed during *in situ* straining experiments in TEM that extensive interactions of gliding  $\langle a \rangle$  dislocations with  $\{10\bar{1}2\}$  TB produced predominantly  $I_1$  SFs in the wake of the advancing interface. The study revealed that the unit process of the dislocation transformations is each  $\langle a \rangle$  dislocation transforming to one partial dislocation of  $I_1$  SF in the twin, and suggested that potentially the products of the successive transformations of two dislocations can add to a perfect  $\langle c + a \rangle$  Burgers vector and thereby enclose the fault.

On the other hand, the formations of the commonly observed  $\langle c + a \rangle$  dislocations were not captured during the experiments and remains unsolved from the 2-dimensional atomistic simulation. It is the goal of the current study to propose and examine a formation mechanism of the  $\langle c + a \rangle$  dislocations in the  $\{10\bar{1}2\}$  twins. While the  $I_1$  SFs could function as potential nucleation sites for  $\langle c + a \rangle$  dislocations [22, 23], the dissociation of a perfect  $\langle c + a \rangle$  dislocation to two partial dislocations is an intrinsically preferred process in Mg [24]. The relationship of the dissociated  $I_1$  SF and perfect  $\langle c + a \rangle$  dislocation in the vicinity of the TB will be explained. Evidences from *in situ* tension experiments in TEM will be presented to support the proposed mechanism and inform the subsequent evolution of the  $\langle c + a \rangle$  dislocations.

## 6.2 Proposed procedures of the formation of $\langle c + a \rangle$ dislocations in twin

### 6.2.1 The sequential transformations of basal $\langle a \rangle$ dislocations

The 2-dimensional MD simulations revealed that when one matrix dislocation arrived at TB, it transforms to a sessile partial dislocation in the twin crystal. As the TB migrates away, a fault is trailed in its wake with one end anchored at the sessile partial dislocation and the other

end attached to the TB by a residual defect. The reaction is described in terms of the interfacial disconnections as

$$b_{-1/0} = b_{0/-1} + b_{-1/-1} \quad (2)$$

For the  $(10\bar{1}2)$  twin,  $b_{-1/0}$  is the  $[a_{1,3}]$  dislocation in the matrix,  $b_{0/-1}$  is the  $1/6\langle 20\bar{2}3 \rangle$  type  $I_1$  partial dislocation in the twin, and  $b_{-1/-1}$  is the residual dislocation at interface. The use of an infinitely long straight dislocation facilitates the interpretation of the interfacial reaction and identification of the Burgers vectors. However, for the understanding of the subsequent evolutions of the defects, the complete dislocation line in 3-dimensions should be considered.

Figure 6.1(a) to (e) describe the transformation of the first matrix dislocation, and the formation of basal SF in twin, as informed by the 2D MD simulation. When part of the gliding dislocation reaches the TB, it is virtually the  $I_1$  partial dislocation in the twin crystal but stays on the TB because of its sessile nature (Figure 6.1(b)), the other segments of the curved  $\langle a \rangle$  dislocation remain in the matrix and are represented by discretized straight lines at right angles in the schematic for the interest of simplicity. The TB advances via the gliding of twinning dislocation  $b_t$  on TB (Figure 6.1(c)). Assuming weak dislocation interactions, the partial dislocation is unaltered by the passage of the  $b_t$ , whereas a jog will be created on the  $\langle a \rangle$  dislocation segments after the intersection with  $b_t$  (Figure 6.1(d)). The matrix  $\langle a \rangle$  dislocation is eventually displaced out of the original basal plane after successive gliding of twinning dislocations, and is incorporated by the TB while maintaining the continuity of dislocation line across the interface with the sessile partial dislocation (Figure 6.1(e)). A fault is therefore formed behind the advancing TB, and is bounded by the partial dislocation on the basal plane of the twin and a residual  $b_{-1/-1}$  type interfacial step on TB. Note that the  $\langle a \rangle$  Burgers vector is out of the twinning plane and is not considered to be admissible on the interface. It may decompose into an

interfacial step characterized by  $b_{5/6}$  and a number of twinning dislocations ( $b_{-2/-2}$ ) according to the atomistic simulations of Serra and Bacon [25, 26]

$$b_{-1/0} = 3b_{-2/-2} + b_{5/6} \quad (3)$$

Both decomposition products are able to glide on the boundary under stress. In the following discussions, the  $\langle a \rangle$  dislocations that are displaced on the TB are referred to in general as  $b_{TBa}$ .

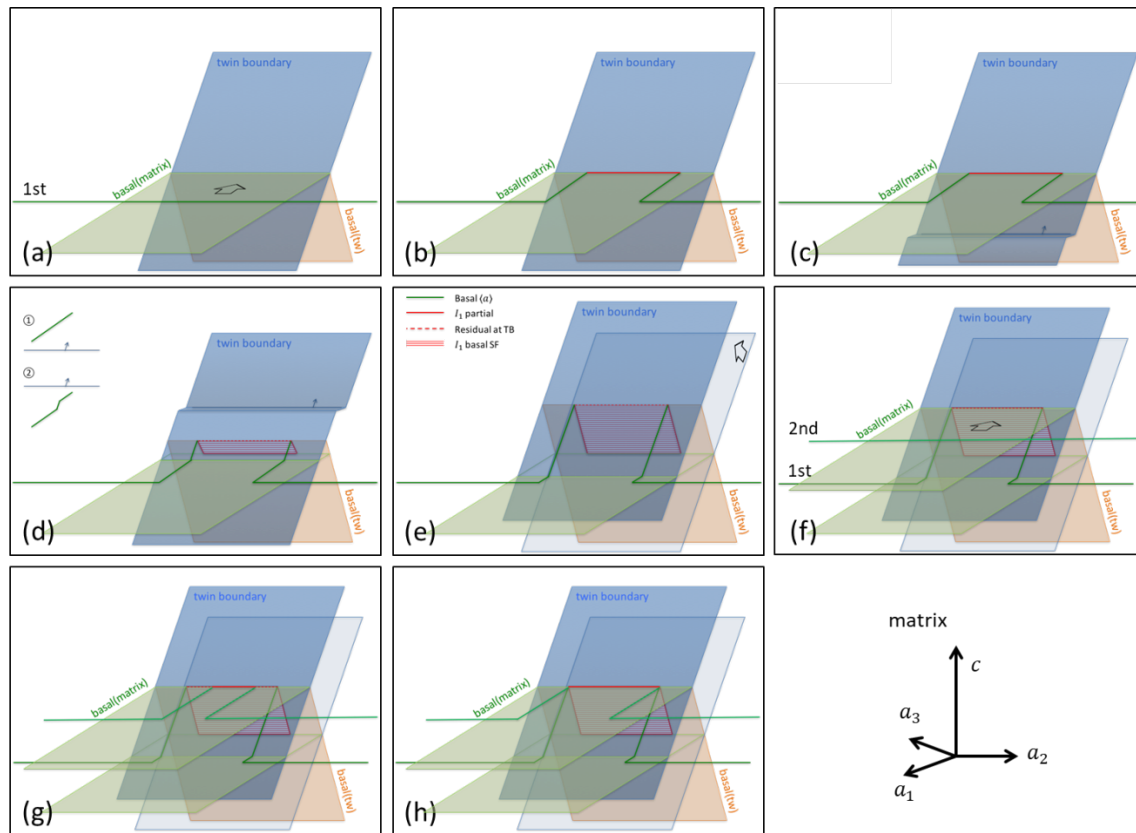


Figure 6.1. Proposed procedures of the incorporation of matrix dislocations by a moving TB and the evolution of defects in twin. The matrix crystal is in the front left in the perspective view, and the twin crystal in the back right. The basal plane in the matrix (green) and that in twin (orange) are at an angle of 86°, with the bisecting TB (blue) in between. The TB is depicted as a flat plane, ignoring the nanoscale interfacial steps. The step created by  $b_t$  is exaggerated in (c) and (d) to illustrate the jog of the matrix dislocation. Dislocations with different Burgers vectors are represented by different colors as indicated in the insets.

The fault is expected to grow continuously with the advancing TB, until a second matrix dislocation glides to the anchoring segment of the fault on TB, or probably in its vicinity on atomic length scale. In Figure 6.1(g) and (h), the second dislocation is depicted to impinge at the middle of the anchoring segment on TB. In reality, it could certainly impinge at the left or right part of the anchoring segment, which merely creates an asymmetric geometry than the ones depicted here and does not greatly alter the essence of the dislocation interactions discussed subsequently. The second dislocation transforms to the conjugate partial dislocation of the existing one according to Equation (2), such that the two partial dislocations add up to a perfect Burgers vector in the twin lattice. The stacking fault is then enclosed either partially or completely, depending on the extent of the incorporation of the second dislocation (Figure 6.1(g) and (h)), which further depends on the relative rate of TB migration and basal dislocation slip. For instance, if the TB migrates before the second dislocation has extended the length of the anchoring segment of the fault, the fault is partially enclosed; if dislocations are strongly stressed to glide to TB, the fault can be completely enclosed before further TB migration occurs. The  $b_{-1/-1}$  type residual defects on the TB generated by the transformations of two matrix dislocations can combine into a twinning dislocation  $b_t = b_{-2/-2}$ , and the total two-step dislocations transformation that encloses a  $I_1$  SF is

$$2 \times b_{-1/0} = (p_1 + p_2) + b_{-2/-2} \quad (4)$$

where  $p_1$  and  $p_2$  are the  $b_{0/-1}$  type conjugate partial dislocations (as in Equation (2)) of a perfect  $\langle c + a \rangle$  dislocation. For example,  $1/6[\bar{2}203] + 1/6[02\bar{2}3] = 1/3[\bar{1}2\bar{1}3]$ .

A rigid geometric relationship between the two dislocations is required for the concerted dislocation transformations described above. This is not an assumption, but rather a probabilistic

occurrence. Acknowledging that  $\langle a \rangle$  dislocations are driven by the external applied stress to glide toward TB on all basal planes, the ones gliding on other parallel basal planes or impinging the boundary at positions outside the anchoring segment of the existing fault are expected to transform independently and repeat the process of one dislocation as from Figure 6.1(a) to (e), producing SFs bounded by a single partial dislocation. It is only the dislocation meeting the geometric requirement that will enclose the existing fault. As long as basal dislocation slip is active in the matrix and the TB continues to migrate toward the gliding dislocations, the concerted incorporation of the second dislocation would occur, depending on the distribution of dislocations in front of the TB.

### 6.2.2 Formation of $\langle c + a \rangle$ dislocations from the advancing TB

In the following, the defect evolutions during further TB migration are discussed for the scenario of partial enclosure of the fault (Figure 6.1(g)) and the scenario of complete enclosure of the fault (Figure 6.1(h)). Two alternatives of the dislocations evolutions are identified: the extension model and the constriction model. The preference of either model is evaluated based on the simplified geometric construction of discrete dislocation segments.

For the first scenario, as the TB advances from Figure 6.2 (a), the second matrix dislocation is displaced out of basal plane, resulting in segments lying on TB in the form of glissile interfacial dislocations  $b_{TBa}$ . It is a similar process as illustrated in Figure 6.1(c) to (d). The interfacial segments of the first matrix dislocation as well as the partial dislocations in twin are extended by the boundary (Figure 6.2(a-c)). Alternatively, the two partial dislocations could at any moment constrict to a single node at the junction on TB via the gliding of interfacial dislocations  $b_{TBa}$  (Figure 6.2(d) or (e)). The TB advancement would automatically create  $\langle c +$

$a$ ) dislocations with one end at the enclosed  $I_1$  SF and the other end at the TB. The local configurations of extension and constriction at the junction on TB is depicted in Figure 6.2(b1) and (d1) respectively. Note that  $b_{TBa}$  is the decomposition product of  $\langle a \rangle$  on the interface, so the Burgers vector is conserved for the constriction, i.e.  $\langle a \rangle_m + b_{TBa} = \langle c + a \rangle_t + b_t = (p_1 + p_2)_t + b_t$ . For the interest of clarity, the twinning dislocation is not depicted at the junction on TB, because it can readily glide away on TB.

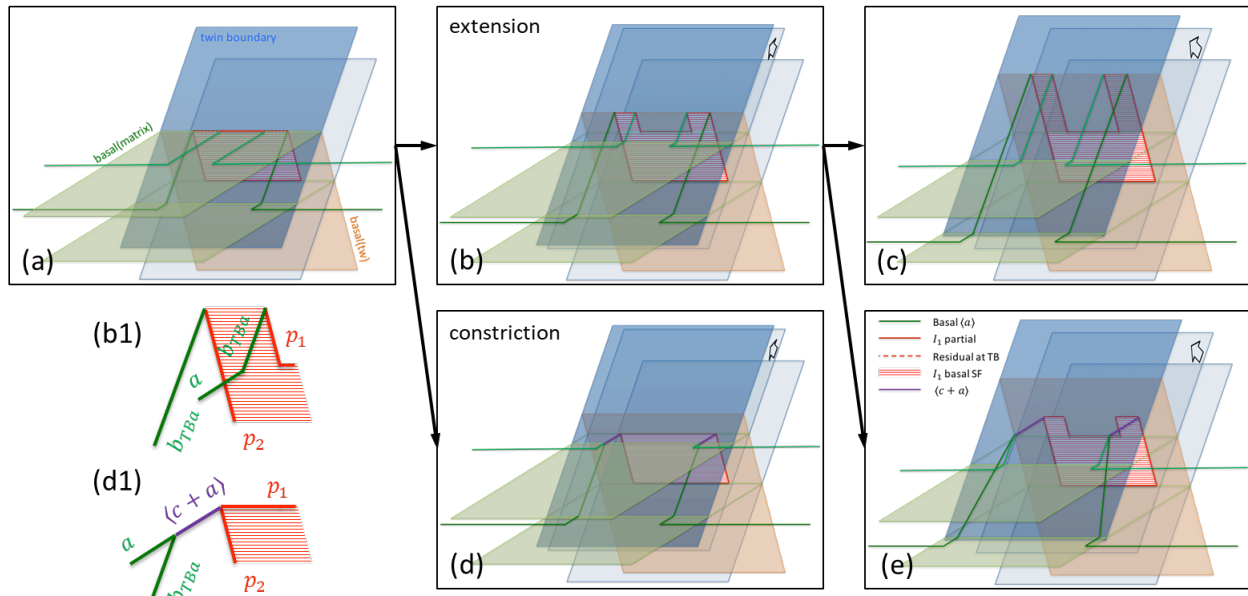


Figure 6.2. Extension of the fault with further TB advancement based on the scenario of Figure 6.1(g). (b) and (d) are two alternatives after (a). (c) and (e) are alternatives after (b). (b1) and (d1) depict the local dislocation configurations around the junction at TB in (b) and (d) respectively.

For the second scenario where the fault is completely enclosed (Figure 6.1(h)), a node is formed at TB, comprising one  $\langle a \rangle$  dislocations in the matrix, an interfacial dislocation  $b_{TBa}$  and two partial dislocations in the twin. When the gliding twinning dislocation intersects the two  $\langle a \rangle$  dislocations, both dislocations are displaced out of the basal plane, and the bounding partial

dislocations in the twin are extended in order to maintain the continuity of dislocations (Figure 6.3(b) and (b1)). It therefore creates a similar configuration as that in Figure 6.2(b) and (b1). Alternatively, a  $\langle c + a \rangle$  dislocation may be directly extended between the node of the two partial dislocations and the node of the two  $\langle a \rangle$  dislocations on TB (Figure 6.3(c)). And further TB migration lengthens only the  $\langle c + a \rangle$  dislocations (Figure 6.3(d)).

In general considerations, it is expected that with continuous forward migration of the TB, the increase of the energy due to the extension of the line lengths of (1) the interfacial dislocations  $b_{TBa}$  and (2) the partial dislocations in the twin as well as (3) the area of the SF becomes so large that beyond certain stage, constriction of the dislocations to perfect  $\langle c + a \rangle$  dislocations in the twin may be preferred such that the migrating TB would lengthen only the  $\langle c + a \rangle$  dislocations.

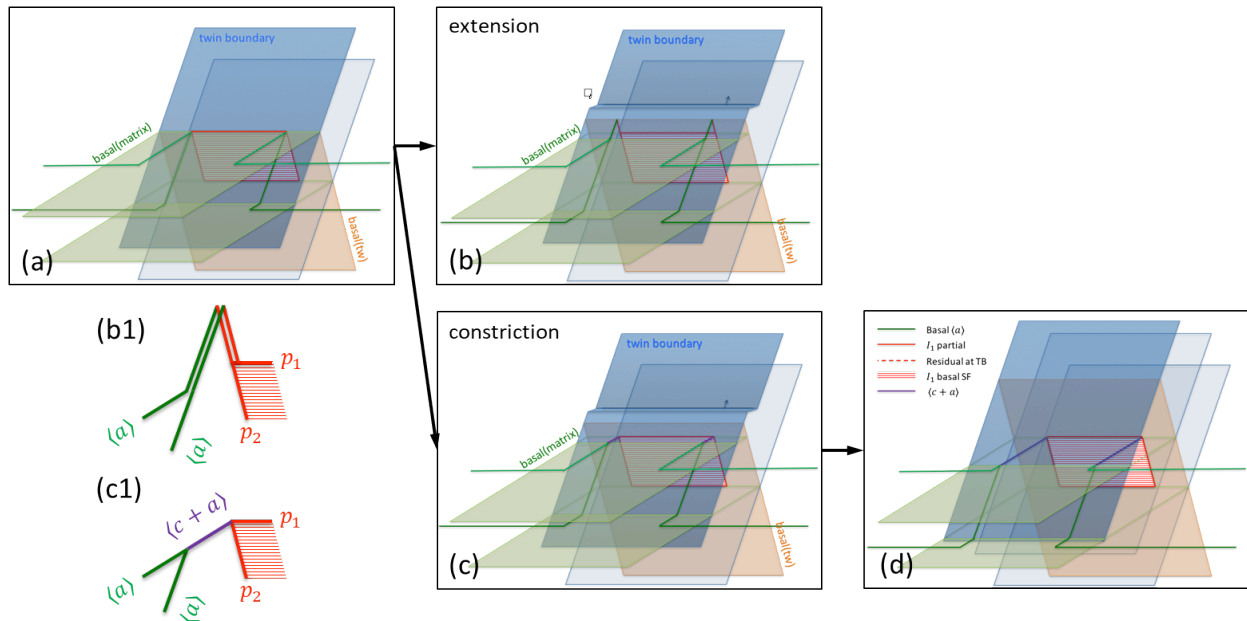


Figure 6.3. Extension of the fault with further TB advancement based on the scenario of Figure 6.1(h). (b) and (c) are two alternatives as TB advances. (b1) and (c1) presents the detailed dislocation lines and Burgers vectors connected to the nodes at TB in (b) and (c) respectively.



It is admitted that the above evolution is a dynamic process, but in order to assess a possible transition between the two alternatives of extension and constriction, the static state energies of the two representative configurations of Figure 6.2(b) and (d) are evaluated in the following. Straight dislocation segments are considered, and the energy of the system is the sum of the elastic self-energy  $E_{self}$  of all the dislocation lines, the interaction energy  $E_{int}$  between each dislocation and the stacking fault energy  $E_{fault}$ . Because Mg crystal is nearly elastically isotropic [27], the isotropic dislocation theory is employed for the energy calculations. For a dislocation line with length  $l$ , and Burgers vector  $b$ , the dislocation self-energy is obtained from

$$E_{self} = l \frac{\mu b^2}{4\pi} \left( \cos^2 \beta + \frac{\sin^2 \beta}{1-\nu} \right) \ln \left( \frac{R}{r_0} \right) \quad (5)$$

where the shear modulus  $\mu = 16.5$  GPa and Poisson's ratio  $\nu = 0.35$ .  $\beta$  is the angle between the Burgers vector and the line direction, describing the character of a dislocation line. The logarithmic term normally takes a value of 10, representing a large cut-off radius ( $R$ ) of the strain field of dislocation with respect to the core radius of dislocation ( $r_0$ ). The interaction energy between any two dislocation segments denoted by 1 and 2 is obtained from [28]

$$E_{int} = \left[ -\frac{\mu b}{2\pi} (b_1 \times b_2) \cdot (\xi_1 \times \xi_2) + \frac{\mu}{4\pi} (b_1 \cdot \xi_1)(b_2 \cdot \xi_2) \right] \int_{x_i}^{x_f} dx \times \int_{y_i}^{y_f} \frac{dy}{R} + \frac{\mu}{4\pi(1-\nu)} (b_1 \times \xi_1) \cdot T \cdot (b_2 \times \xi_2) \quad (6)$$

In this equation,  $b$  and  $\xi$  are the Burgers vector and line direction of each dislocation, and the interaction energy is integrated over the whole length of a dislocation segment, from the initial coordinates of  $(x_i, y_i)$  to the final coordinates of  $(x_f, y_f)$ , described in a local non-orthogonal coordinate system where the  $x$  and  $y$  axes are aligned with the two dislocations.  $T$  is a second-

rank tensor whose explicit expression is provided in [28], specifically for the parallel and perpendicular dislocation lines as used in the current simplified geometry. The stacking fault energy is the product of the faulted area ( $A$ ) and the stacking fault energy  $\gamma_{I_1} = 11.3 \text{ mJ/m}^2$  [29]

$$E_{\text{fault}} = A \cdot \gamma \quad (7)$$

The geometry adopted to demonstrate the relative rank of energy of the extension model and constriction model is presented in Figure 6.4. The important geometric parameters include the width of the first partial dislocation loop in the twin of  $800a$ , where  $a$  is the lattice parameter (0.321 nm), and the height between the first and the second partial dislocations of  $200a$ , which equals the height between the basal planes in the matrix where the two  $\langle a \rangle$  dislocations originally lie on. The width ( $L$ ) of the second partial dislocation loop in the twin is treated as variable, representing different extent of the incorporation and transformation of the second  $\langle a \rangle$  dislocation from the matrix. During forward migration of the TB, the extension model increases the height ( $H$ ) of the dislocation junctions at TB, and therefore the length of the associated dislocation segments as well as the faulted area between the two partial dislocations. On the other hand, the alternative constriction model only increases the length of the two  $\langle c + a \rangle$  dislocation segments between the SF and the TB, which is correlated to the value of  $H$ .

The energies of each model are plotted in Figure 6.4(c) for a range of  $L$  and  $H$  values. The energy of the extension model increases proportional to the amount of extension ( $H$ ) enforced by the TB advancement, and depends weakly on the horizontal width ( $L$ ) of the inner partial dislocation loop. The energy of the constriction model increases much more slowly than that of the extension model, arising only from the increasing line length of the two  $\langle c + a \rangle$  dislocations. Therefore, at small values of TB migration (small  $H$ ), the extension model is of lower energy, which is essentially consistent with the general preference of the dissociated

partial dislocations bounding a fault than a perfect dislocation. With increasing TB migration, the extension model brings a rapid increase of energy that the constriction model actually becomes the energetically preferred option. The projection of the energy surface in Figure 6.4(d) shows clearly that the transition of the energy rank occurs mostly at the sensible value of  $H \approx 375a$ , corresponding to a TB migration of about 120 nm. Based on the above comparison of the end states with simplified geometry and arbitrary dimensions, an opportunity is presented that the extension of perfect  $\langle c + a \rangle$  dislocations could be an energetically preferred path for a large distance of TB advancement. It is recognized that there exist numerous combinations of geometric parameters that would change the preference of either the extension and constriction model within certain range, e.g. the size of the first and the second partial dislocation loops, the distance between the two partial dislocation loops and the distance of TB migration. A parametric study exploring the multi-dimensional space of the variables may be necessary for the pursuit a low energy path of the transient stages of the dislocation evolutions.

In summary, it is demonstrated that the concerted incorporations and transformation of two matrix dislocations on different basal planes eventually can enclose a basal  $I_1$  SF in twin and produce a configuration of two  $\langle c + a \rangle$  dislocations extending between the sessile SF and the advancing TB. It is worth mentioning that the two  $\langle c + a \rangle$  dislocations have the same Burgers vector but opposite line directions, they hence constitute a dislocation dipole.

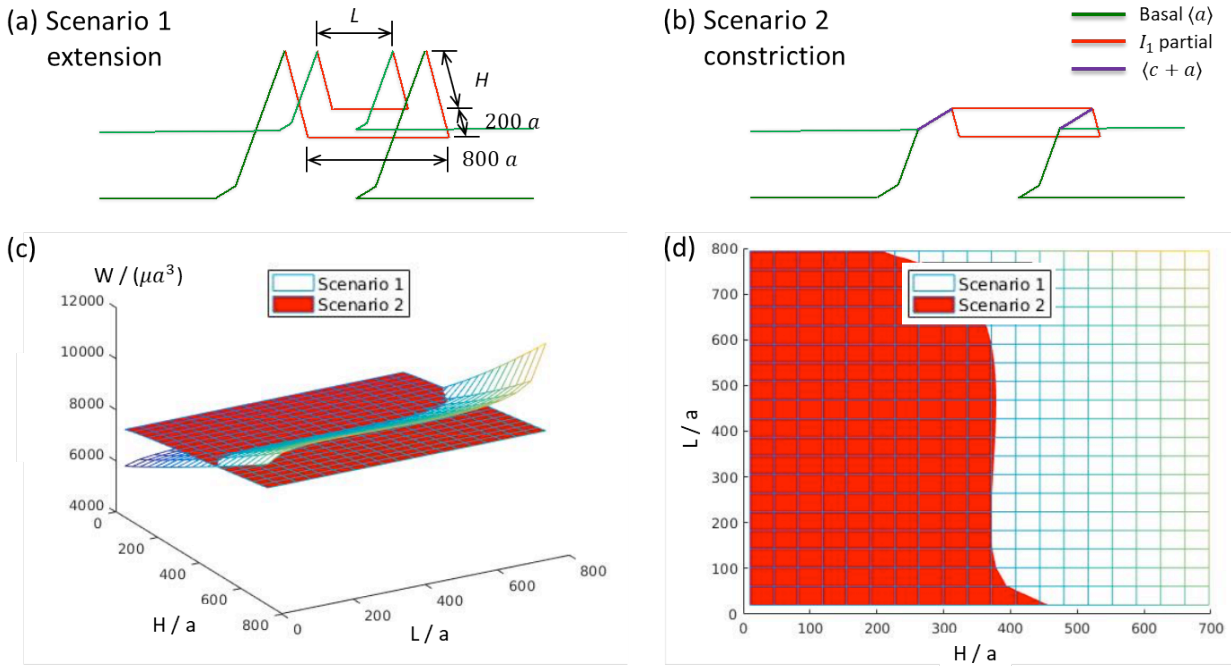


Figure 6.4. The dislocations configurations representing the two alternatives of (a) extension and (b) constriction. (c) is the total energy of the systems at various lengths of  $H$  and  $L$ . (d) is the projection of the energy surfaces, showing the intersection line in two-dimensions. The lengths are in the unit of lattice parameter  $a = 0.321$  nm.

### 6.3 *In situ* TEM observations of the $\langle c+a \rangle$ dislocations in twin

In order to evaluate the proposed formation mechanism of  $\langle c+a \rangle$  dislocations in twin from the interfacial reaction, *in situ* tension experiments were performed in TEM. The samples were produced from a pure Mg single crystal containing pre-existing  $\{10\bar{1}2\}$  twins, and was annealed to decrease the dislocation density. The preparation of the TEM tensile specimen and the experimental procedures are detailed in the previous paper. All the characterizations were performed near the co-zone axis,  $[1\bar{2}10]$  direction, of the matrix and twin, and at the two-beam diffraction condition of  $(0002)_t$  and  $(10\bar{1}0)_m$  simultaneously. Therefore, the basal plane in the

twin is edge-on, and that in matrix and the TB are only slightly inclined. The visible dislocations in twin are  $[c]$ -containing, and the visible basal dislocations in matrix are either  $[a_1]$  or  $[a_3]$ .

In Figure 6.5, basal dislocations are motivated to glide toward the TBs by the applied tension in the vertical direction. The movement of the basal dislocations are so fast that individual dislocations are not captured in two consecutive frames at the current length scale with a recording rate of 10 frames per second. The basal slip activity is identified by the emergence of the slip traces parallel to the basal plane, e.g. in Figure 6.5(b). The TB is expected to be weakly stressed at this orientation by the applied tension, it is yet observed to homogeneously migrate forward, presumably due the variation of the principle stress direction in this specific region of the thin foil sample [30]. The advancing boundary trails both basal defects and non-basal dislocations with  $[c]$ -component. Based on the previous detailed analysis of the defects in  $(10\bar{1}2)$  [11-13] and the tendency of the basal segments of  $\langle c + a \rangle$  dislocations to dissociate [23, 24], the defects are assumed to be mostly basal  $I_1$  SFs, and perfect  $\langle c + a \rangle$  or  $[c]$  dislocations on non-basal planes. The non-basal dislocations are long and slightly curved. Many appear to lengthen by the advancing boundary with line directions closely aligned with the basal plane traces in matrix, e.g. the ones attached to the TB as indicated by yellow arrows in Figure 6.5(b) and (c).

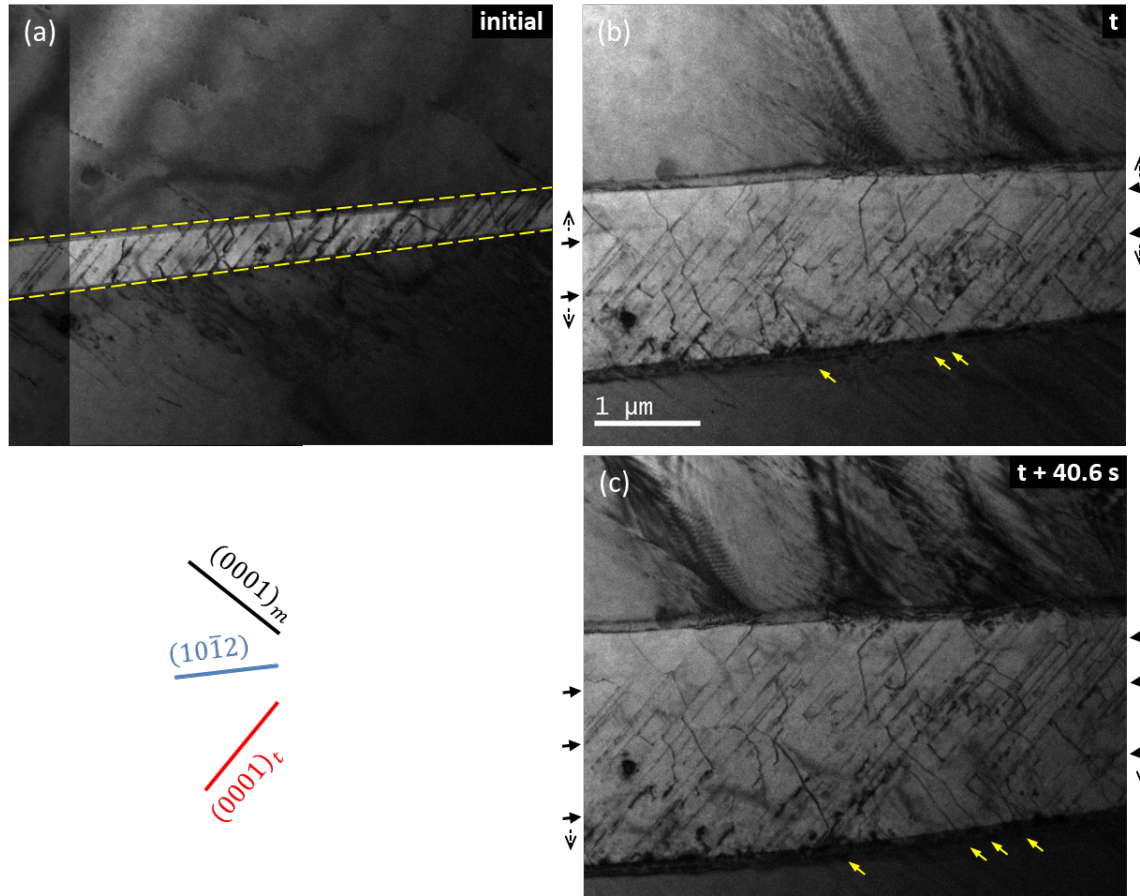


Figure 6.5. Homogeneous TB migration and the evolution of defects in twin under a tension in the vertical direction. The twin is roughly horizontal in the middle of the images, with the matrix above and below it. The black arrows outside the frames in (b) and (c) indicate the position of TB at previous times. The yellow arrows point to the same dislocations that are extended by the boundary through (b) to (c).

The evolutions of several dislocations in the twin are presented in detail in Figure 6.6. The dislocations A, A', B, B' and C are firstly elongated with one end attached to the advancing TB and the other end anchored at basal SFs (Figure 6.6(a) to (b)). They maintain a projected length of more than 500 nm, while the dislocations A and A' even approach 1  $\mu\text{m}$ . With further TB advancement (Figure 6.6(c)), the long dislocations A and A' disappear, and two new dislocations A1 and A1' emerge below the original ones, with the lower end attached to the TB

and the upper end at the basal SF. The slightly curved dislocations B and B' form a semi-loop with the upper two ends connected to the basal SF, suggesting that the two original dislocations are of the same Burgers vector. It therefore corresponds to the pinch-off of a dislocation dipole. Accompanying the formation of the semi-loop, two new dislocations B1 and B1' emerge below it. The semi-loop vanishes at a later time (Figure 6.6(d)), leaving only a basal SF. The difference image in Figure 6.6(e) overlays the original and new dislocations in Figure 6.6(b) and (c) respectively and suggests a continuation of the dislocations after the upper segments vanished. It is inferred from the pinch-off of the dislocation dipoles B and B' into a semi-loop and its subsequent collapse into basal SF that the same process may have occurred for dislocations A and A' as well between Figure 6.6(b) and (c), however, the transient stage was not captured. The dislocation C is observed to elongate with the advancing TB (Figure 6.6(a) and (b)) and subsequently detach the boundary (Figure 6.6(c)). All the non-basal dislocations are roughly perpendicular to the edge-on basal planes in twin, which is conveniently delineated by the straight defect contrast on them. On the other hand, the long projected length suggests that the dislocations are contained in the TEM thin foil such that they are not intersected by the upper or lower foil surfaces while elongating. Therefore, the line direction of the majority of the long dislocations should be close to the  $[c]$  direction and the dislocations are thus more screw type.

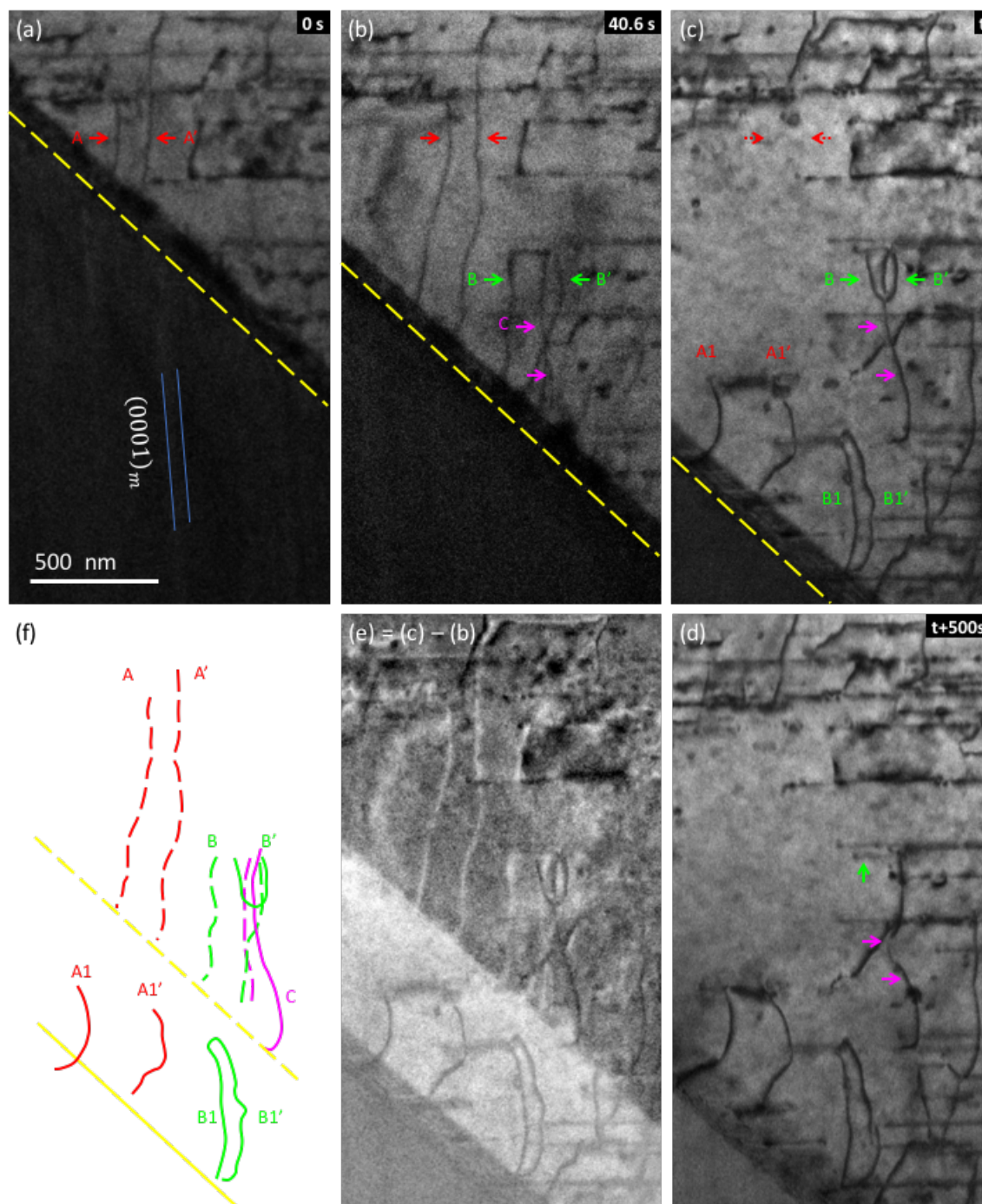


Figure 6.6. Evolution of the dislocations in twin in the wake of the advancing TB. The images are rotated from Figure 6.5 such that the basal plane in twin is horizontal and that in matrix is almost vertical. (a-d) are taken at increasing times. (e) is the difference image of (c) and (b), with the white features represent those in (b) and dark features those in (c). The dislocation lines are extracted in (f) showing the original dislocations (dashed lines) and new dislocations (solid lines).



Figure 6.7 presents the collective dislocation slip activity of the screw-like  $[c]$  or  $\langle c + a \rangle$  dislocations observed within a time period of 500s. The dislocations are able to glide for a projected distance of more than 100 nm, e.g. dislocations 1, 3, 9 and 14. Note that the  $(10\bar{1}0)$  prismatic plane that is closely aligned with the basal plane in the matrix and presumably the plane where the  $\langle c + a \rangle$  dislocations are initially formed has a narrow projected length, as indicated at the bottom of Figure 6.7 for each column of images. The traces of the basal plane in twin and the TB are measured from the respective images. The prismatic plane trace is taken as perpendicular to the measured basal plane trace and the projected width is determined by the intersected length of the edge-on basal plane with the inclined TB. The projected glide distances of dislocations 1 and 3 are larger than the width of the prismatic plane in the images, which suggests that they are gliding on non-basal planes that are less inclined in the TEM foil, e.g. the pyramidal planes. The dislocations 5 and 13 are examples of dislocation dipoles attached to the TB. For the dipole 5, the impingement points of the two dislocations at TB are along the basal plane trace in the twin (Figure 6.7(b) and (f)), and their line directions are close to the  $[c]$  axis while slightly curved towards each other. It therefore presents a typical dislocation dipole structure lying on the  $(10\bar{1}0)$  prismatic plane. Their mutually attractive motions are expected to result in dislocations annihilation and thereafter the pinch-off to loops, similar to the evolution of dislocations B and B' in Figure 6.6.

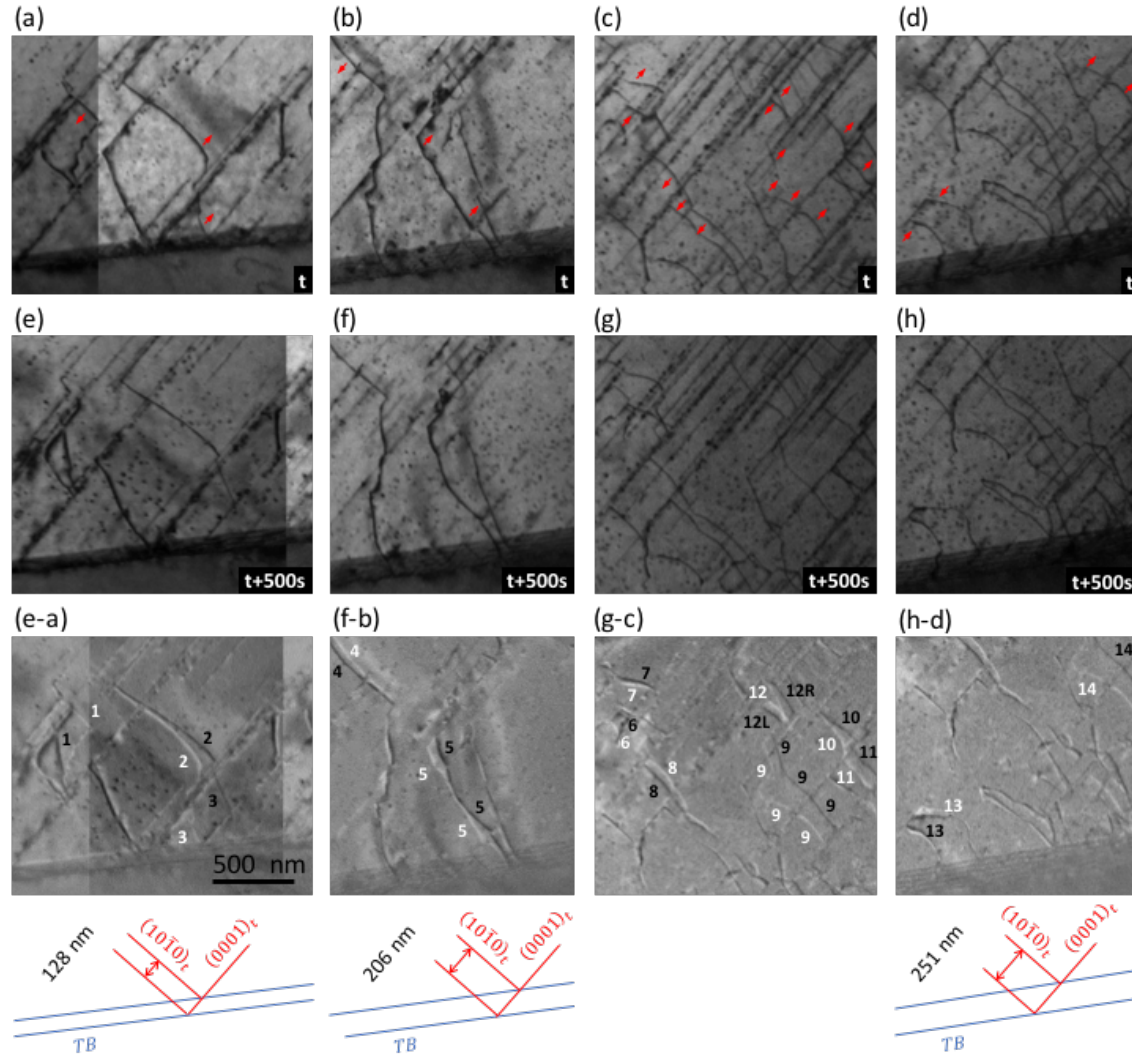


Figure 6.7. Collective slip activity of the  $[c]$  and  $\langle c+a \rangle$  dislocations on non-basal planes in twin. (a-d) are the initial dislocation structure in four different regions, and (e-h) are the respective final structure after being strained by the tension in the vertical direction for 500s. The difference images reveal the direction and distance of the dislocation movements, with the white representing the initial dislocations and the black the final dislocations. The directions of the dislocation movements are indicated by red arrows. (a) and (e) are montaged images and therefore possess vertical stripes of different brightness.

The *in situ* deformation results present the extension of perfect dislocations in twin by the advancing TB, with one end attached to the TB and the other end to the basal SFs in twin. The

dislocations appear long and have a line direction close to the  $[c]$  axis of the twin. The experimental observations are consistent with the final stages of the proposed formation mechanism in Figure 6.2(d, e) and Figure 6.3(d). Furthermore, the glissile nature the dislocations and the observed pinch-off of dipoles stimulate the discussions of the subsequent defect evolutions in twin.

#### 6.4 The evolution and morphology of the $I_1$ SFs in twin

The proposed mechanism suggests that the as-formed  $\langle c + a \rangle$  dislocations constitute a dislocation dipole (Figure 6.2(d, e) and Figure 6.3(d)). In both cases, the  $\langle c + a \rangle$  dislocation forms a node with the two partial dislocations on basal plane and has the other end attached to the TB, as shown schematically in Figure 6.8(a). Assuming a dislocation line direction of  $[c]$ , as observed for the long dislocations during the *in situ* observations, the transformed  $[c \pm a_2]$  dislocations are glissile on the prismatic plane in the twin. When the  $\langle c + a \rangle$  dislocation dipole is elongated by the advancing TB, the two dislocations can pinch-off due to the mutual attractive force between them, forming a semi-loop on prismatic plane attached to the TB and dislocation segments on the basal plane still connected to the node with the bounding partial dislocations of the SF. The basal segments are edge dislocations and tend to dissociate into the  $I_1$  partial dislocations [23, 24]. It therefore corresponds to the unzipping of the node of perfect dislocation and partial dislocations from Figure 6.8(b) to (c). The final stage of the evolution is a perfect  $\langle c + a \rangle$  semi-loop attached to the TB and an independent double looped basal  $I_1$  stacking fault whose total Burgers vector is the same as the  $\langle c + a \rangle$  dislocation.

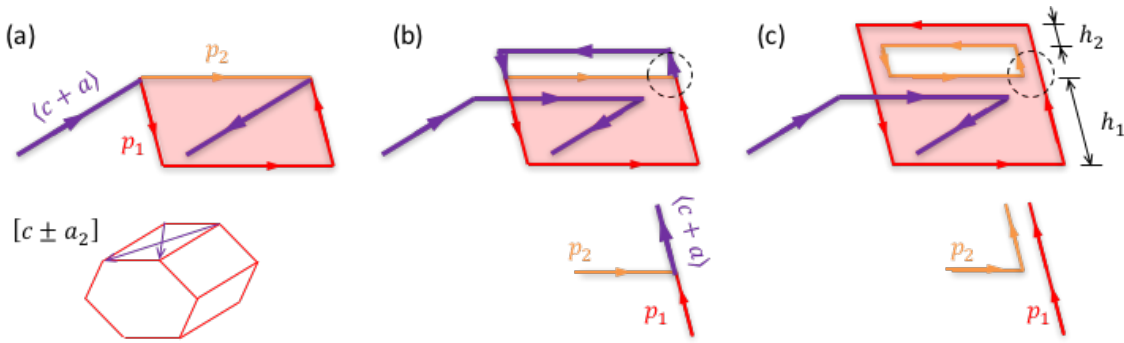


Figure 6.8. The pinch-off of the  $\langle c + a \rangle$  dislocation dipole and the subsequent dissociation of the segments on basal plane. The partial dislocations  $p_1$  and  $p_2$  enclose an  $I_1$  fault on basal plane. The dislocation line directions are indicated by the arrows along the line.

The shape of the fault depicted in Figure 6.8 are idealized by straight segments of the bounding partial dislocations. The distance between the two partial dislocations at the lower part of the fault ( $h_1$ ) equals the spacing of the two parallel basal planes of the matrix dislocations based on the geometry described in Figure 6.1. The dissociation reaction of each straight  $\langle c + a \rangle$  segment involves the climb motion of the  $1/6\langle 20\bar{2}3 \rangle$  type partial dislocations on basal plane, which may not require the diffusion of vacancies or interstitials from the surrounding as suggested by the atomistic simulation [24]. The initial separation distance of the partial dislocations at the upper part of the double looped fault ( $h_2$ ) may represent the equilibrium spacing of 20 nm or 37 nm as estimated using different  $I_1$  stacking fault energies [23, 24].

The basal  $I_1$  SFs generated as a result of the interaction of matrix dislocation with TB are presented in Figure 6.9. Both independent double looped faults as well as partially emitted faults with one end attached to the TB are observed. The former corresponds to the final proposed configuration in Figure 6.8(c), and the latter corresponds to an earlier stage where only one partial dislocation is formed and bounds the fault as in Figure 6.1(e). The image was obtained near the co-zone axis  $[\bar{1}2\bar{1}0]$  of the matrix and the twin, so the basal plane in twin is steeply

inclined to the image plane. Since the through thickness direction gives a very short projected length of the true dimension, the dimensions of the faults are measured only along the in-plane direction. As seen in Figure 6.9, the partially emitted faults are extended very long by the TB. For the independent double looped faults, the widths of the faults are not the same at the side further from the TB ( $h_1$  in Figure 6.8(c)) and the side closer to the TB ( $h_2$  in Figure 6.8(c)), whereas both are much larger than the equilibrium value. As discussed above, the separation distance of the inner and outer partial dislocation loops firstly depends on the distance of TB migration until a second partial dislocation is transformed from a matrix dislocation. The width of the fault can further be adjusted by the climb motions of the two loops in pursuit of lower interaction energy between all the dislocation segments. Since the  $I_1$  SF is essentially a layer of vacancies or interstitials on basal plane with a height of  $1/2[c]$ , the climb motions of the loops are expected to be facilitated by the local diffusion within the fault while the total area is maintained (in the absence of global diffusion). By the symmetry of the interactions between the two partial dislocation loops, a final configuration of a fault with approximately concentric loops is possible, such as those reported in [31] and in the previous paper.

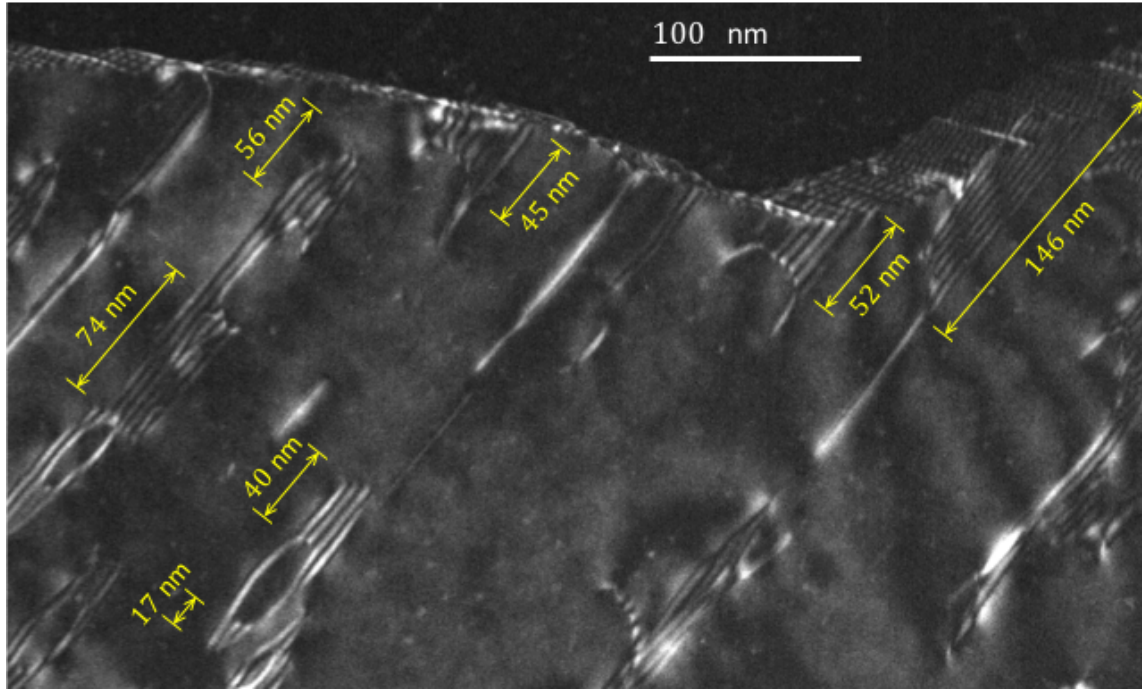


Figure 6.9. WBDF image of basal  $I_1$  SFs inside a twin after extensive dislocation-TB interactions, as evidenced by the curvature of the TB. The diffraction condition is  $g = (10\bar{1}\bar{1})_t$ . The twin is the lower crystal in the image, the matrix is the upper one but does not exhibit diffraction contrast.

## 6.5 Conclusions and outlook

The current work proposes a formation mechanism of  $\langle c + a \rangle$  dislocations from the  $(10\bar{1}2)$  TB. It is based on the transformation reaction of one  $[a_{1,3}]$  dislocation in the matrix to an  $I_1$  partial dislocation in the  $(10\bar{1}2)$  twin as investigated in the previous work. Due to the sessile nature of the partial dislocation, the formation of the  $\langle c + a \rangle$  dislocation necessitates the advancement of TB and the concerted transformation of two matrix dislocations from parallel basal planes. The crystallographic relationship of the  $(10\bar{1}2)$  twin with the matrix creates a favorable condition for the constriction of the  $I_1$  partial dislocations to a perfect  $\langle c + a \rangle$  dislocation at the interface, which is normally an uphill process in terms of energy.

The *in situ* observations in TEM during tension deformation provide evidences of the final stages of the proposed mechanism. The observed slip activity and the pinch-off of dislocation dipoles further suggest that  $I_1$  stacking faults in a double looped morphology can be produced from the perfect  $\langle c + a \rangle$  dislocations.

The formation of the glissile  $\langle c + a \rangle$  dislocations and large sessile  $I_1$  SF inside the  $(10\bar{1}2)$  twin is revealed experimentally in pure Mg single crystal where both basal slip and twinning are operating. The microstructural features and the evolutions of the dislocation structure should be applicable to other alloys systems, unless the movement of TB or the energetics of the  $\langle c + a \rangle$  dislocation and  $I_1$  SF are greatly modified, for instance, by solute atoms or precipitates [32-34]. These defects are important for the plasticity of the  $(10\bar{1}2)$  twins. According to the Orowan's equation, the shear strain  $\gamma = \rho bl$ , where  $\rho$  and  $b$  are the density and Burgers vector of the gliding dislocations and  $l$  is the slip distance. The collective slip activity of the abundant  $\langle c + a \rangle$  dislocations generated at the twin interface is expected to produce an appreciable amount of plastic strain. It could relax the stress in the near vicinity of the TB, which is suggested to be influential on the TB migration, e.g. [35, 36]. The large sessile  $I_1$  SFs are potential obstacles for the subsequent dislocation slip. However, the exact interactions with dislocations of different Burgers vectors, especially with the  $\langle c + a \rangle$  dislocation, should be subject to future investigation, probably following a similar approach as in [37].

Careful assessments of the critical stages and the transition paths of the proposed mechanism should be carried out in future research endeavors on the scale of both atomistic and discrete dislocation simulations, for instance, the interaction of the basal  $\langle a \rangle$  dislocation with gliding twinning dislocations, the force experienced by the second incoming  $\langle a \rangle$  dislocation from

the existing configuration of the first  $\langle a \rangle$  dislocation, and the constriction of the interfacial steps that are the decomposition products of  $\langle a \rangle$  dislocation on TB, to list just a few.

## References

- [1] M. Yoo, "Slip, twinning, and fracture in hexagonal close-packed metals," *Metallurgical transactions A*, vol. 12A, pp. 409-418, 1981.
- [2] Q. Yu, J. Wang, Y. Jiang, R. McCabe and C. Tome, "Co-zone  $\{-1012\}$  Twin Interaction in Magnesium Single Crystal," *Mater. Res. Lett.*, vol. 2, pp. 82-88, 2014.
- [3] P. Juan, C. Pradalier, S. Berbenni, R. McCabe, C. Tome and L. Capolungo, "A statistical analysis of the influence of microstructure and twin–twin junctions on twin nucleation and twin growth in Zr," *Acta Mater.*, vol. 95, pp. 399-410, 2015.
- [4] S. Asgari, E. El-Danaf, S. Kalidindi and R. Doherty, *Metall Mater Trans A*, vol. 28A, p. 1781, 1997.
- [5] E. El-Danaf, S. Kalidindi and R. Doherty, *Mdtall Mater Trans A*, vol. 30, p. 1223, 1999.
- [6] S. Kalidindi, A. Salem and R. Doherty, *Adv Eng Mater*, vol. 5, p. 229, 2003.
- [7] A. Salem, S. Kalidindi and R. Doherty, "Strain hardening of titaniu: role of deformation twinning," *Acta Mater.*, vol. 51, pp. 4225-4237, 2003.
- [8] A. Salem, S. Kalidindi, R. Doherty and S. Semiatin, *Metall Trans A*, vol. 37, p. 259, 2006.
- [9] D. Bhattacharyya, E. Cerreta, R. McCabe, M. Niewczas, G. Gray III, A. Misra and C. Tome, "Origin of dislocations within tensile and compressive twins in pure textured Zr," *Acta Materialia*, vol. 57, pp. 305-315, 2009.
- [10] F. Wang and S. Agnew, "Dislocation transmutation by tension twinning in magnesium alloy AZ31," *Int. J. Plas.*, vol. 81, pp. 63-86, 2016.
- [11] F. Wang, K. Hazeli, K. Molodov, C. Barrett, T. Al-Samman, D. Molodov, A. Kontsos, K. Ramesh, H. El Kadiri and S. Agnew, "Characteristic dislocation substructure in  $\{10-12\}$  twins in hexagonal metals," *Scripta Mater.*, accepted.
- [12] D. Brown, S. Agnew, S. Abeln and et al., "The role of texture, temperature, and strain rate in the activity of deformation twinning," *Mater. Sci. For.*, Vols. 495-497, pp. 1037-1042, 2005.
- [13] P. Wu, X. Guo, H. Qiao, S. Agnew, D. Lloyd and J. Embury, "On the rapid hardening and exhaustion of twinning in magnesium," *Acta Mater.*, vol. 122, pp. 369-377, 2017.
- [14] G. Proust, C. Tome, A. Jain and S. Agnew, "Modeling the effect of twinning and detwinning during strain-path changes of magnesium alloy AZ31," *Int. J. Pla.*, vol. 25, pp. 861-880, 2009.



- [15] B. Clausen, C. Tome, D. Brown and S. Agnew, "Reorientation and stress relaxation due to twinning: modeling and experimental characterization of Mg," *Acta Mater.*, vol. 56, pp. 2456-2468, 2008.
- [16] P. Juan, S. Berbenni, M. Barnett, C. Tome and L. Capolungo, "A double inclusion homogenization scheme for polycrystals with hierarchical topologies: application to twinning in Mg alloys," *Int. J. Plas.*, vol. 60, pp. 182-196, 2014.
- [17] D. Tomsett and M. Bevis, "The formation of stacking faults in {10-12} twins in zinc as a result of slip dislocation-deformation twin interactions," *Phil. Mag.*, vol. 19, pp. 533-537, 1969.
- [18] D. Tomsett and M. Bevis, "The incorporation of basal slip dislocations in {10-12} twins in zinc crystals," *Philosophical Magazine*, vol. 19, no. 157, pp. 129-140, 1969.
- [19] S. Morozumi, M. Kikuchi and H. Yoshinaga, "Electron microscope observation in and around {1-102} twins in magnesium," *Trans. JIM*, vol. 17, pp. 158-164, 1976.
- [20] M. Yoo and C. Wei, *Phil. Mag.*, vol. 14, pp. 573-587, 1966.
- [21] H. Fan and J. El-Awady, "Molecular dynamics simulations of orientation effects during tension, compression and bending deformations of Magnesium nanocrystals," *Journal of Applied Mechanics*, vol. 82, p. 101006, 2015.
- [22] S. Sandloebes, S. Zaeferrer, I. Schestakow, S. Yi and R. Gonzalez-Martinez, "On the role of non-basal deformation mechanisms for the ductility of Mg and Mg-Y alloys," *Acta Mater.*, vol. 59, pp. 429-439, 2011.
- [23] S. Agnew, L. Capolungo and C. Calhoun, *Acta Materialia*, vol. 82, pp. 255-265, 2015.
- [24] Z. Wu and W. Curtin, "The origin of high hardening and low ductility in magnesium," *Nature*, vol. 526, pp. 62-67, 2015.
- [25] A. Serra and D. Bacon, *Phil. Mag.*, vol. 90, pp. 845-861, 2010.
- [26] A. Serra and D. Bacon, *Phil. Mag.*, vol. 73, pp. 333-343, 1996.
- [27] L. Capolungo, I. Beyerlein and Z. Wang, *Modell. Simul. Mater. Sci. Eng.*, vol. 18, p. 085002, 2010.
- [28] P. Anderson, J. Hirth and J. Lothe, *Theory of dislocations*. 3rd ed., Cambridge University Press, 2017.
- [29] Z. Wu, M. Francis and W. Curtin, "Magnesium interatomic potential for simulating plasticity and fracture phenomena," *Modelling and Simulation in Materials Science and Engineering*, vol. 23, p. 015004, 2015.
- [30] A. Couret, J. Crestou, S. Farenc, G. Molenat, N. Clement, A. Coujou and D. Caillard, "In situ deformation in TEM: recent developments," *Microsc. Microanal. Microstruct.*, vol. 4, pp. 153-170, 1993.
- [31] J. Geng et al., "The structure of <c+a> type dislocation loops in magnesium," *Phil. Mag. Lett.*, vol. 94, pp. 377-386, 2014.

- [32] J. Nie, Y. Zhu, J. Liu and X. Fang, "Periodic segregation of solute atoms in fully coherent twin boundaries," *Science*, vol. 340, pp. 957-960, 2013.
- [33] S. Sandloebes, Z. Pei, M. Friak, L.-F. Zhu, F. Wang, S. Zaefferer, D. Raabe and J. Neugebauer, "Ductility improvement of Mg alloys by solid solution: Ab initio modeling, synthesis and mechanical properties," *Acta Mater.*, vol. 70, pp. 92-104, 2014.
- [34] W. Wang, S. Shang, Y. Wang, Z. Mei, K. Darling, L. Kecskes, S. Mathaudhu, X. Hui and Z. Liu, "Effects of alloying elements on stacking fault energies and electronic structures of binary Mg alloys: a first-principles study," *Materials Research Letters*, vol. 2, pp. 29-36, 2014.
- [35] M. Kumar, A. Kanjarla, S. Niezgoda, R. Lebensohn and C. Tome, *Acta Mater.*, vol. 84, pp. 349-358, 2015.
- [36] H. Abdolvand and A. Wilkinson, *Int. J. Plas.*, vol. 84, pp. 160-182, 2016.
- [37] N. Bertin, C. Tome, I. Beyerlein, M. Barnett and L. Capolungo, "On the strength of dislocation interactions and their effect on latent hardening in pure Magnesium," *Inter. J. Plasticity*, vol. 62, pp. 72-92, 2014.

## CHAPTER 7    COMPREHENSIVE SUMMARY AND RECOMMENDATIONS FOR FUTURE WORK

### 7.1    Motivations

In Mg alloys and many other hexagonal metals, the  $\{10\bar{1}2\}$  twinning is an important deformation mode. Under appropriate loading, the  $\{10\bar{1}2\}$  twins are activated early during the deformation and grow pervasively such that a large volume fraction of the material is consumed by twin. The deformation behavior of the twins dominates the subsequent stress-strain response of the polycrystalline aggregates. *Therefore, it is critical to investigate the dislocation substructure in the  $\{10\bar{1}2\}$  twins.* On the other hand, the interactions of the  $\{10\bar{1}2\}$  twin boundary (TB) with matrix  $\langle a \rangle$  dislocations are primary interactions in hexagonal metals, as both defects are easily generated during deformation via the operation of  $\{10\bar{1}2\}$  twinning and basal dislocation slip. A crystallography-based concept of dislocation transformation at the TB was proposed more than five decades ago. It provided an opportunity to generate the hard  $\langle c + a \rangle$  dislocations which are necessary for the plastic deformation of the  $\{10\bar{1}2\}$  twins and are in general considered to be essential for the homogeneous and ductile deformation of Mg. *The processes of the transformation and the types of defects generated at the interface have not been*

*systematically studied experimentally.* The present study therefore aims to address the fundamental problems of the transformation and interactions of both perfect and partial dislocations near twin boundary.

## 7.2 Major conclusions

In a common Mg alloy AZ31B rolled plate that was deformed in such a way that twinning dominated the strain accommodation, the crystallography based dislocation transformation reaction was confirmed by diffraction contrast analyses in TEM. The reaction involves either  $[a_1]$  or  $[a_3]$  matrix dislocation that “transmutes” into  $[c - a_2]$  or  $[c + a_2]$  dislocation, respectively, in the  $(10\bar{1}2)$  twin. Collective observations of a number of twins in different grains further showed that the  $(10\bar{1}2)$  twins contain only  $\langle c \pm a_2 \rangle$  among all six possible  $\langle c + a \rangle$  dislocations, and the dislocations form a particular distribution inside twin, preferentially populating the region near the twin boundary. Besides the perfect  $\langle c + a \rangle$  dislocations, perfect  $[c]$  dislocations on non-basal planes and  $[c]$ -containing  $I_1$  stacking faults on basal plane were also observed.

Through further experimentation and literature survey, the observed dislocation substructure in the polycrystalline Mg alloy AZ31 was identified to be characteristic of  $\{10\bar{1}2\}$  twins in hexagonal metals. A pure Mg single crystal was compressed along the  $[10\bar{1}0]$  direction to promote  $\{10\bar{1}2\}$  twinning activity. At a global stress of only 5 MPa, abundant  $[c]$ -containing defects were present in the wake of advancing twin boundaries, in the form of non-basal  $[c]$  and  $\langle c + a \rangle$  perfect dislocations and basal  $I_1$  stacking faults with widths approaching 100 nm. The single crystal deformation experiment suggests that TB migration into stationary matrix  $\langle a \rangle$

dislocations is able to induce the dislocation transformations. Previous researchers presented similar evidence from Zr and Zn (low and high  $c/a$  ratio hexagonal metals, respectively).

In order to elucidate the process of the dislocation transformations at TBs and assess its effect on TB motion, *in situ* tension tests were performed in the TEM using oriented pure Mg single crystal specimens where basal  $\langle a \rangle$  dislocations are motivated to glide toward the unstressed TB. (1) Local twin growth is observed on unstressed TB subsequent to the impingement of gliding basal dislocations. The boundary motion is evaluated to be completely induced by the dislocation transmutation reaction with a ratio of one twinning dislocation per transformation of two basal dislocations. (2) The advancing TB trails profuse  $I_1$  basal stacking faults in its wake, with a few short non-basal  $[c]$ -containing dislocations. (3) MD simulations and interfacial topological analyses reveal that the unit process of dislocation-twin interaction involves a matrix dislocation which transforms to a sessile partial dislocation inside the twin crystal, trailing a  $I_1$  SF, if only the TB advances. Because of the sessile nature of the bounding partial dislocation and the low  $I_1$  stacking fault energy, the resulting fault can be very large. The successive transformations of two  $\langle a \rangle$  dislocations are expected to enclose the SF by two partial dislocations, whose net Burgers vector is equivalent to  $[c \pm a_2]$ .

A formation mechanism of perfect  $\langle c + a \rangle$  dislocations is proposed. It necessitates the advancement of TB which results in the correlated transformation of two matrix dislocations from distinct basal planes. The resulting geometry creates a favorable condition for the two  $\langle a \rangle$  dislocations to meet at a single point. When this junction is swept by twinning dislocations, it results in the production of a  $\langle c + a \rangle$  dislocation at the interface, which is normally an energetically uphill process. Once formed it continues to be lengthened by the growth of the twin (a la threading dislocations in thin films or solidification). The *in situ* observations in TEM

during tensile deformation support the proposed mechanism and furthermore show that the  $\langle c + a \rangle$  dislocations formed at the interface are glissile. The pinch-off of dislocation dipoles could be responsible for the observed large  $I_1$  SFs in a double looped morphology.

Furthermore, the interactions of gliding dislocations with TB shed lights on the understanding of twinning behavior. The TB appears to readily absorb the incident dislocations and respond by forward migration. The twinning dislocations generated by the slip-twin interaction maintain the coherency of the interface. However, in the absence of sufficient shear stress on the twinning shear system, the twinning dislocations would pile up and form large interfacial serrations, which impede the passage of twinning dislocations across the serrated interface but do not stop the neighboring boundary migration.

### 7.3 Significance of the work

The current study identified a characteristic dislocation substructure inside the  $\{10\bar{1}2\}$  twins which result from interfacial dislocation transformations. It is observed to be applicable to pure Mg and the most common commercial wrought Mg alloy, AZ31, as well as other hexagonal metals (Zn and Zr). It is significant for the discussion of plasticity for four reasons. (1) The twin contains defects that are not easily activated in matrix; (2) the slip activity of the glissile  $\langle c + a \rangle$  dislocations could accommodate subsequent strain along the  $[c]$ -axis of the twins; (3) the  $[c]$ -containing  $I_1$  stacking faults larger than 100 nm are essentially a plate of vacancies or interstitials on basal plane and are sessile, they could act as obstacles to gliding dislocations and be related to void formation; and (4) the high local density of  $[c]$ -containing defects in the vicinity of TB may create a hard environment for other slip modes as well as twin boundary migration in either the forward or the backward direction (twin thickening and detwinning). Considering the ubiquity of

$\{10\bar{1}2\}$  twins, the work revealed a defect substructure that could establish the basis for subsequent full-field plasticity modeling and should be appropriately accounted for within mean-field modeling schemes.

The processes of the interfacial dislocation transformations are elucidated and formulated based on a crystallography based concept proposed more than 5 decades ago. The topic of slip- $\{10\bar{1}2\}$  twin interactions has been previously studied mostly by atomistic simulations. The current work provides the experimental evidences by performing *in situ* straining in TEM and complements such modeling endeavors. The phenomena revealed in this work cover multiple length scales, from the atomistic scale generally investigated by using HRTEM or MD simulations to dislocation scale and to subgrain level. The work can contribute to the development of physically-based constitutive equations of plasticity and hence of predictive models for the accurate description of material deformation behavior and design of materials with superior mechanical properties.

The broader impacts of this research are that the fundamental knowledge of dislocation-twin boundary interaction can potentially be applied to all hexagonal metals, and provide insights to other materials where twinning and dislocation transfer through interface are of interest, e.g. twinning-induced plasticity (TWIP) steel and shape memory alloys.

#### **7.4 Recommendations for future work**

While this work provides rich information of defect interactions in the vicinity of twin boundaries, it also raises more questions and opportunities for future studies. The crux of this study is the transformation of basal dislocations  $[a_1]$  and  $[a_3]$  at the  $(10\bar{1}2)$  TB when TB migrates forward (twin thickening)

$$2 \times [-a_1]_m = 1/6[2\bar{2}03]_t + 1/6[0\bar{2}\bar{2}3]_t + b_t = [c - a_2]_t + b_t$$

$$2 \times [a_3]_m = 1/6[\bar{2}203]_t + 1/6[02\bar{2}3]_t + b_t = [c + a_2]_t + b_t$$

where the  $1/6\langle 2\bar{2}03 \rangle$  type dislocation is the bounding partial dislocation of the  $I_1$  stacking fault and  $b_t$  is the twinning dislocation at the TB. As the TB migrates into the matrix where the dislocation density keeps increasing, a heterogeneous distribution of dislocations is formed in the twin, as shown in the large-scale observations.

#### 7.4.1 Implementing the dislocation transformations in crystal plasticity (CP) models

Naturally, the interfacial process revealed in this work should be implemented in a dislocation density (DD) based model, e.g. that developed by Beyerlein and Tome [1], to account for the different types of dislocations and correlate the evolution of the dislocation densities in the matrix and in the twin. In such models, dislocation density is taken as a state variable that influences the critical resolved shear stress (CRSS), a parameter defining the activation stress of dislocation slip activity that produces shear strain.

The dislocation transformation reaction should be implemented when any  $\{10\bar{1}2\}$  twin variant grows in a grain during straining. The transformation reactions for all the six twin variants are listed in Table 7.1. The coordinate systems of the matrix and the twin lattices are correlated by  $180^\circ$  rotation around the twin shear direction  $\eta_1 \parallel \langle \bar{1}011 \rangle$  (see Section 3.3). When a twin grows and consumes the volume of the matrix, the original basal  $\langle a \rangle$  dislocations in the volume should be transformed to corresponding dislocations in the twin, with the ratio and Burgers vectors defined by these equations. The transformations are in two types: direct transmission without changing the Burgers vector and transmutation producing  $\langle c + a \rangle$



dislocations. Since the latter is a special source mechanism for the hard dislocations, the evolution of the  $\langle c + a \rangle$  dislocation density in twin is detailed in the following.

Table 7.1. Dislocation transformation reactions for all the  $\{10\bar{1}2\}$  twin variants. The twinning dislocation  $b_t$  is the corresponding positive twinning shear vector of each twin variant.

Twin variant	Direct transmission	Transmutation
$(01\bar{1}2)[0\bar{1}11]$	$[a_1]_m = [-a_1]_t$	$2 \times [-a_2]_m = 1/6[\bar{2}203]_t + 1/6[\bar{2}023]_t + b_t = [c - a_1]_t + b_t$ $2 \times [a_3]_m = 1/6[2\bar{2}03]_t + 1/6[20\bar{2}3]_t + b_t = [c + a_1]_t + b_t$
$(0\bar{1}12)[01\bar{1}1]$	$[a_1]_m = [-a_1]_t$	$2 \times [a_2]_m = 1/6[2\bar{2}03]_t + 1/6[20\bar{2}3]_t + b_t = [c + a_1]_t + b_t$ $2 \times [-a_3]_m = 1/6[\bar{2}203]_t + 1/6[\bar{2}023]_t + b_t = [c - a_1]_t + b_t$
$(10\bar{1}2)[\bar{1}011]$	$[a_2]_m = [-a_2]_t$	$2 \times [-a_1]_m = 1/6[2\bar{2}03]_t + 1/6[0\bar{2}23]_t + b_t = [c - a_2]_t + b_t$ $2 \times [a_3]_m = 1/6[\bar{2}203]_t + 1/6[02\bar{2}3]_t + b_t = [c + a_2]_t + b_t$
$(\bar{1}012)[10\bar{1}1]$	$[a_2]_m = [-a_2]_t$	$2 \times [a_1]_m = 1/6[\bar{2}203]_t + 1/6[02\bar{2}3]_t + b_t = [c + a_2]_t + b_t$ $2 \times [-a_3]_m = 1/6[2\bar{2}03]_t + 1/6[0\bar{2}23]_t + b_t = [c - a_2]_t + b_t$
$(1\bar{1}02)[\bar{1}\bar{1}01]$	$[a_3]_m = [-a_3]_t$	$2 \times [-a_1]_m = 1/6[02\bar{2}3]_t + 1/6[20\bar{2}3]_t + b_t = [c - a_3]_t + b_t$ $2 \times [a_2]_m = 1/6[0\bar{2}23]_t + 1/6[\bar{2}023]_t + b_t = [c + a_3]_t + b_t$
$(\bar{1}\bar{1}02)[1\bar{1}01]$	$[a_3]_m = [-a_3]_t$	$2 \times [a_1]_m = 1/6[0\bar{2}23]_t + 1/6[\bar{2}023]_t + b_t = [c + a_3]_t + b_t$ $2 \times [-a_2]_m = 1/6[02\bar{2}3]_t + 1/6[20\bar{2}3]_t + b_t = [c - a_3]_t + b_t$

Full-field models, e.g. one within a finite element (FE) framework developed by Knezevic et al. [2], are suitable to describe the heterogeneous distribution of the dislocations inside the twin. As shown in Figure 7.1, when a twin is initially generated inside a grain, it has a dislocation density of  $\rho_T(t_0)$ . The twin grows at each time step  $t_1$  and  $t_2$ , increasing the volume fraction of the twin by  $\Delta f(t_1)$  and  $\Delta f(t_2)$ . In the meantime, dislocation transformation occurs, transforming the  $\langle a \rangle$  dislocations in the twinned volume to  $\langle c + a \rangle$  dislocations

$$\Delta f(t) \cdot \rho_{T,c+a}(t) = 1/2 \cdot \Delta f(t) \cdot \rho_{M,a}(t - 1)$$

Since the dislocation density of the  $\langle a \rangle$  dislocations in the matrix  $\rho_{M,a}$  evolves with time, the twinned volume inherits different densities. The twin at any time step of simulation is a composite body comprising regions of different dislocation densities and hence different hardening behaviors.

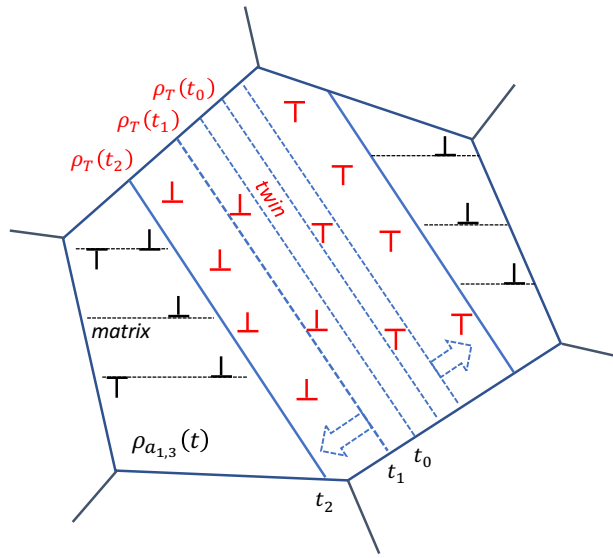


Figure 7.1. Schematic illustration of the dislocation density in the matrix ( $\rho_M$ ) and in the growing twin ( $\rho_T$ ). The twin grows by the lateral migration of both TBs from the time  $t_0$  to  $t_1$  and to  $t_2$ . Different regions of the twin have different dislocation densities resulting from the dislocation transformation mechanism.

In mean-field models, the collective behavior of all the dislocations in the twin is taken into account. The total dislocation density in the twin at any time step ( $t$ ) is the average value of the density at the previous time step ( $t-1$ ) and that in the incremented twin volume fraction  $\Delta f(t)$ ,

$$\rho_{T,c+a}(t) = \frac{f(t-1) \cdot \rho_{T,c+a}(t-1) + 1/2 \cdot \Delta f(t) \cdot \rho_{M,a}(t-1)}{f(t-1) + \Delta f(t)}$$

In contrast to the twin in the full-field scheme, the twin is a homogeneous body whose effective dislocation density is updated at every time step.

Additionally, it is recognized that the  $\langle c + a \rangle$  dislocations in the twin as a result of the dislocation transformations can be in the form of either perfect dislocation or dissociated partial dislocations. The population of either type of defect may be influenced by the kinetics of the

dislocation slip relative to the TB migration, as discussed in Chapters 5 and 6. A fraction ( $x \in [0, 1]$ ) can be assigned in the model and be treated as a free parameter

$$\rho_{T,c+a}(t) = x \cdot \rho_{T,perfect}(t) + (1 - x) \cdot \rho_{T,partial}(t)$$

Furthermore, since the dislocation transformation mechanism is a source mechanism for  $\langle c + a \rangle$  dislocations, it is expected that probably a new CRSS value needs to be adopted only for those in the twin.

The above discussion concerns the evolution of the density and type of dislocations in a simulation volume (or element in a finite element sense) when it is transformed from matrix to twin. This information can be used in the constitutive equations of the slip systems in each volume/element. On the other hand, the effect of the interface was not accounted. To the author's knowledge, the effect of the internal boundary and the interaction of neighboring grains have not been directly accounted in many simulations of polycrystal deformation, except for Lee et al. [3] and Lim et al. [4]. The authors [3, 4] developed a DD-based FE model, where grains are treated in a finite element sense with many elements per grain. The model uses a two-scale method comprised of, firstly, a grain-scale simulation that computes inhomogeneous stress, strain and the local generation of dislocation density in each element and, secondly, a novel meso-scale simulation that redistributes the mobile dislocation density for each element. For the grain interior elements, a slip system is subject to the stress field of the net dislocation density in each element, which is obtained from the flux of dislocation density from one element to the adjacent element. For the boundary elements, a slip system is additionally subject to the obstacle stress of the boundary if the slip dislocation is able to be incorporated or transmitted by the boundary. In other words, the interactions of dislocation with internal boundary are accounted by considering

the effect of the heterogeneous distribution of dislocation density in the vicinity of the boundary and the obstacle strength of the boundary.

#### 7.4.2 Investigating the interactions of the defects in the twin

The current study reveals that a  $\{10\bar{1}2\}$  twin contains only two out of six  $\langle c + a \rangle$  variants as a result of dislocation transformation, e.g. perfect  $[c \pm a_2]$  dislocations as well as their dissociated partial dislocations in a  $(10\bar{1}2)$  twin. The dislocation interactions arising from the specific Burgers vectors should be investigated, in order to understand the strength of such interactions and their effect on the latent hardening of the twin crystals. The interactions between various types of perfect dislocations in Mg have been studied in a discrete dislocation dynamics (DDD) model in [5]. In order to investigate one specific interaction, a primary dislocation was loaded to glide through a forest of dislocations of prescribed Burgers vector and line direction.

Following the similar methodology, the current study suggests to investigate the hardening caused by the partial dislocations. A distribution of partial dislocation double loops should be built *a priori*, according to the TEM observation of the morphology of the  $I_1$  SFs. Basal  $\langle a \rangle$  dislocations and the transformed  $\langle c + a \rangle$  dislocations are then introduced in the built microstructure respectively and are loaded to glide, to induce one specific type of interaction. Again, the perfect  $\langle c + a \rangle$  dislocations and the prescribed partial dislocations should belong to the two transformed  $\langle c + a \rangle$  variants.

Furthermore, it is expected that the slip activity of the two  $\langle c + a \rangle$  variants in a twin could lead to shear strain along specific directions and, therefore, lead to strain localization and crack formation. This can be tested by loading a simulation box in DDD, where a microstructure is built containing the two  $\langle c + a \rangle$  variants and their dissociated partial dislocations. Since the

dissociation of the edge segments of the gliding  $\langle c + a \rangle$  dislocations on basal plane produces  $I_1$  SFs, which are plates of vacancies or interstitials, these point defects should be accounted, as they could be the precursor of crack formation.

#### 7.4.3 Investigating the critical dislocation configurations at the interface

Careful assessments of the critical stages of the proposed mechanism in Chapter 6 should be carried out in future research endeavors on the scale of both atomistic and discrete dislocation simulations, for instance, the interaction of the basal  $\langle a \rangle$  dislocation with gliding twinning dislocations, the force experienced by the second incoming  $\langle a \rangle$  dislocation from the existing configuration of the first  $\langle a \rangle$  dislocation, and the constriction of the interfacial steps that are the decomposition products of  $\langle a \rangle$  dislocation on TB as well as the constriction of the  $I_1$  partial dislocations at the junction at TB.

One critical scenario is the incorporation of the second basal dislocation at the TB that is subject to the stress field of the existing configuration of the first dislocation (Figure 7.2). For a fixed geometry of the first dislocation, the position of the second incoming dislocation is described by coordinates  $(x, z)$ , representing the horizontal distance of it from the  $I_1$  SF enclosed by the transformed partial dislocation in twin and the vertical distance of it from the bottom of the  $I_1$  SF. It is of interest to learn the resolved shear stress on the second dislocation in the  $[-x]$  direction, i.e. the stress attracting or repelling the second dislocation toward the TB, for any position  $(x, z)$ . The result can be a contour plot in the coordinate system in Figure 7.2, describing potential regions of attraction or repulsion. Note that only the second dislocation whose  $z$  coordinate is  $H$  is able to terminate the continuously growing fault with the advancing TB. The variation of the stress on the second dislocation along the dislocation line should also be

computed to explore which segment of the line is subject to the largest attractive/repulsive stress. This result can inform the most probable impingement position on TB.

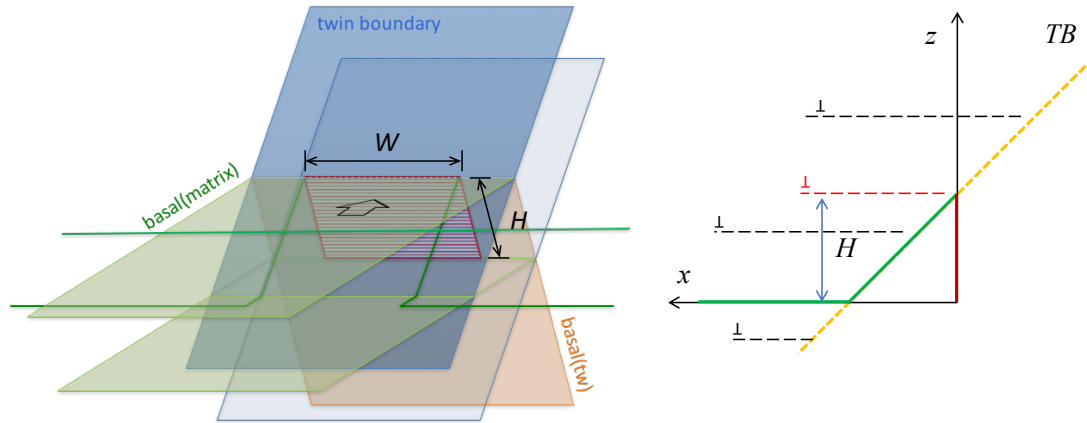


Figure 7.2. Geometry of the incorporation of two basal dislocations at TB.

On top of the above calculation, it is noted that the existing configuration of the first dislocation can be described by two variables, the height ( $H$ ) and the width ( $W$ ) of the SF. A sensitivity study should be carried out to explore how sensitive the stress computed above depends on each variable.

Another critical scenario is the energetic evaluation of the extension and constriction model in Section 6.2.2. Specific geometries with arbitrarily assigned dimensions are currently evaluated for the purpose of demonstrating the feasibility of the proposed mechanism. It is recognized that there exist a number of combinations of the pertinent geometric parameters ( $H_1$ ,  $H_2$ ,  $W_1$ ,  $W_2$  in Figure 7.3) that may change the preference of the proposed mechanism within certain range. And a preferred transition path may exist. Certainly, a dynamic modeling in a discrete dislocation model can be carried out to explore the evolution of the configuration, which presumably requires extensive computational expense. Alternatively, a comprehensive

parametric study could be performed by varying multiple geometric variables of the static dislocations configuration. The simulations would generate the energies of the competing configurations for each combination of the variables and thus constitute a multi-dimensional matrix of data. A minimum energy path of the transition may be sought by an algorithm similar to the nudged elastic band method with known initial and final states.

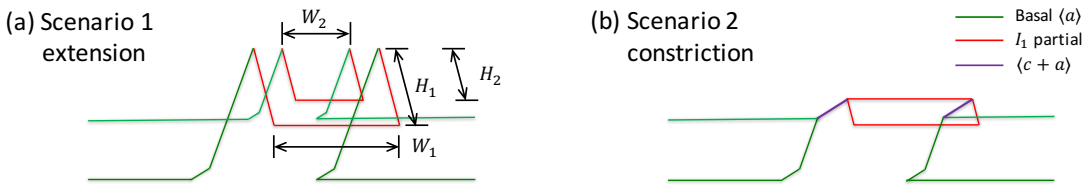


Figure 7.3. Possible geometric variables for the energetic evaluation of the two competing scenarios.

## References

- [1] I. Beyerlein and C. Tome, "A dislocation-based constitutive law for pure Zr including temperature effects," *International Journal of Plasticity*, vol. 24, pp. 867-895, 2008.
- [2] M. Knezevic, R. McCabe, R. Lebensohn, C. Tome, C. Liu, M. Lovato and B. Mihaila, "Integration of self-consistent polycrystal plasticity with dislocation density based hardening laws within an implicit finite element framework: Application to low-symmetry metals," *Journal of the Mechanics and Physics of Solids*, vol. 61, pp. 2034-2046, 2013.
- [3] M. Lee, H. Lim, B. Adams, J. Hirth, R. Wagoner, "A dislocation density-based single crystal constitutive equation," *International Journal of Plasticity*, vol. 26, pp. 925-938, 2010.
- [4] H. Lim, M. Lee, J. Kim, B. Adams, R. Wagoner, "Simulation of polycrystal deformation with grain and grain boundary effects," *International Journal of Plasticity*, vol. 27, pp. 1328-1354, 2011.
- [5] N. Bertin, C. Tome, I. Beyerlein, M. Barnett and L. Capolungo, "On the strength of dislocation interactions and their effect on latent hardening in pure Magnesium," *Inter. J. Plasticity*, vol. 62, pp. 72-92, 2014.